Detaillierte Untersuchungen der Oxidationschemie verschiedener konventioneller und alternativer Brennstoffe und Brennstoffgemische

Dissertation
zur Erlangung des Doktorgrades
der Naturwissenschaften

Universität Bielefeld
Fakultät für Chemie

vorgelegt von
Julia Pieper

März 2018

Danksagung

Die vorliegende Arbeit wurde im Zeitraum von Juli 2015 bis März 2018 in der Arbeitsgruppe *Physikalische Chemie I* der Fakultät für Chemie an der Universität Bielefeld unter der Leitung von Frau Prof. Dr. Katharina Kohse-Höinghaus angefertigt. Ihr möchte ich herzlich für die gute Betreuung, die Bereitstellung spannender Forschungsthemen und -projekte und die stetige Unterstützung danken. Darüber hinaus konnte ich während dieser Zeit an einigen internationalen Messkampagnen und Konferenzen teilnehmen, die meine persönliche Entwicklung stark vorangebracht haben. Für die Vielzahl dieser Möglichkeiten möchte ich mich aufrichtig bedanken.

Bei Prof. Dr. Thomas Hellweg möchte ich mich für die freundliche Übernahme des Zweitgutachtens und die schnelle Bearbeitung bedanken.

Großer Dank gilt der Arbeitsgruppe PC I, in der ich mich in all der Zeit immer sehr wohlgefühlt habe. Ein überaus guter Zusammenhalt und ein mehr als angenehmes Arbeitsklima haben die vielen Stunden in Form von Kaffeepausen, KuDo's, Betriebsausflügen und Weihnachtsfeiern geradezu wie im Flug vergehen lassen. Ein besonderer Dank gilt meinen Mitstreitern der Massenspektrometrie-Gruppe Eike Bräuer, Lena Ruwe, Steffen Schmitt und Julia Wullenkord, sowie den ehemaligen Mitgliedern Patrick Oßwald, Marina Schenk, Kai Moshammer, Daniel Felsmann und Christian Hemken für stetige Hilfs- und Diskussionsbereitschaft.

Auf der experimentellen Seite gilt mein Dank vor allem Harald Waterbör für technische Hilfe jeglicher Art und der elektronischen und mechanischen Werkstatt für die allseits zügige Hilfe in Notlagen. Außerdem möchte ich mich bei meinen Forschungspraktikanten und Masteranden Steffen Schmitt und Raphael Dalpke für die außerordentlich gut geleistete Arbeit im Labor bedanken.

Regine Schröder möchte ich für die viele organisatorische Hilfe in jeglicher Hinsicht danken.

Für die stetige Hilfe bei IT-Problemen, der Programmierung von kleinen Helfer-Routinen und den immer wieder anregenden und aufmunternden Gesprächen danke ich Michael Letzgus-Koppmann herzlich. Ohne dich wären wir hier alle verloren.

Im Rahmen dieser Arbeit sind einige Veröffentlichungen entstanden, die ohne die tolle Zusammenarbeit mit vielen nationalen und internationalen Partnern nicht möglich gewesen wäre. Deshalb möchte ich mich besonders bei Luc-Sy Tran und Hanfeng Jin

bedanken. Darüber hinaus gilt mein Dank Christian Hemken, Rene Büttgen und Alexander Heufer vom Institut für *Physical Chemical Fundamentals of Combustion* (PCFC) der *RWTH Aachen*, sowie Julia Krüger, Gustavo Garcia und Laurent Nahon vom *Synchrotron SOLEIL*. Für einen spannenden und sehr lehrreichen aber auch spaßigen Aufenthalt an der *Advanced Light Source* (ALS) in Berkeley, USA, möchte ich dem *Flame Team* und insbesondere Nils Hansen danken.

Für eine immer sehr angenehme Stimmung im Büro und nicht zuletzt den Gewinn einer tollen Freundin danke ich Lena Ruwe von Herzen.

Weiterhin möchte ich mich bei Mona Remmers und Isabelle Graf für das Korrekturlesen dieser Arbeit bedanken.

Abschließend danke ich meiner Familie für die stetige Unterstützung und das Verständnis seit Beginn meines Studiums, zu dessen Gelingen ihr letztendlich einen großen Teil beigetragen habt. Meinem Mann Matthias Pieper danke ich insbesondere für die bisherige tolle Zeit und blicke gespannt auf unsere gemeinsame Zukunft. Ohne dich wäre ich jetzt nicht hier.

Abstract

It is well known that emissions from combustion processes are harmful and dangerous for climate, air quality, environment and health. However, a significant increase of anthropogenic CO_2, particulate matter, and soot has been measured over the past years. Since more than 80 % of the global primary energy is still covered by fossil energy sources, an immediate substitution by renewable energy is not yet possible and efficient and cleaner alternatives are needed for the transition period in the next 10-20 years.

To achieve such cleaner combustion goals, several changes in different fields should be considered, while in engine combustion two main approaches are pursued. These suggested developments include the technical approach of a homogeneous low-temperature combustion, which is supposed to lead to a lower emission of pollutants, as well as the use of alternative fuels (e.g. alcohols, ethers, esters) with a proposed cleaner emission than prototypical fuels. However, due to their different molecular structures including heteroatoms, they often exhibit a very different species distribution in their combustion. The respective chemical composition can lead to the emission of toxic species or pollutants that can have negative influences on human health and the atmosphere by photochemical reactions. Therefore, the combustion behavior of these types of fuels needs to be analyzed in more detail to gain understanding of their complex reaction pathways, especially in the low-temperature regime.

Technical studies often analyze global parameters of combustion as e.g. ignition delay times, flame speeds or the concentration of unburnt hydrocarbons at the tailpipe. However, from the chemical point-of-view, the combustion process is highly complex. Therefore, the aim of this work was to achieve detailed knowledge about specific reaction pathways in the combustion process of different fuels and fuel mixtures to help evaluating the potential of possible alternative fuels and fuel additives. For this purpose, laminar premixed low-pressure flames and a laminar flow reactor were used as model experiments on a laboratory scale to cover a broad range of the relevant phase space including temperature, pressure and stoichiometry. The species distributions in different oxidation processes were analyzed by molecular-beam mass spectrometry serving as a universal technique to measure a multitude of species at the same time. A combination of different ionization techniques covering electron impact ionization, photoionization and photoelectron/photoion coincidence spectroscopy has been used to cross-validate the obtained data and to gain complementary information for a detailed structure analysis of species occuring in the oxidation processes. Therefore measurements at *Bielefeld University* were combined with several measurements at large-scale setups using synchrotron-generated vacuum-ultraviolet radiation from the *Advanced Light Source* in Berkeley, USA, the *National Synchrotron Radiation Laboratory* in Hefei, China

and the *SOLEIL Synchrotron* in Gif-sur-Yvette, France. Furthermore, the experimental data has been complemented by specific and internally consistent reference measurements, theoretical calculations and kinetic modeling as a connection between laboratory-scale experiments and technical processes.

The main focus of this work was the investigation of alternative fuels and their influences on the combustion process of mixtures, as these are already used on the road (e.g. E10, biodiesel). Adding alternative fuels to prototypical compounds can have a significant impact on the reacitivity and the reaction pathways of the oxidation leading to interaction between species rising from the oxidation process. Currently, only little information is available on these mixing effects. Therefore, several pure fuels as well as mixtures of prototypical and alternative fuel candidates have been analyzed in the low- and high-temperature environment to investigate the influence of fuel additives and interactive effects in mixtures. As a fundamental result of this work it could be confirmed that a combination of several experimental techniques together with theoretical calculations and kinetic modeling is very important and necessary to obtain the complex information needed on the combustion process of fuels. The results revealed that the molecular structure of the fuel molecules as well as the oxidation environment are of significant influence for the reaction pathways and therefore the formation of possible pollutants. For the addition of alcohols and ethers very strong and partially contrary influences on the fuels reactivity and the resulting species distribution could be observed for the low- and high-temperature regime. While in a high-temperature environment only small effects and mainly on the formation of soot precursors were found, the reactivity of the mixtures was dramatically influenced in a low-temperature environment leading to a different species distribution, enabling the possibility to influence the combustion process by changing the oxidation environment and a selective addition of specific components. Furthermore, the experimental results of this work have contributed to the further development and validation of several kinetic models by detecting new species and possible reaction pathways that have not been included in simulations before, but can be used to improve the predictability of such mechanisms in the future.

Publikationsliste

Wissenschaftliche Veröffentlichungen

[1] J. Pieper, S. Schmitt, C. Hemken, E. Davies, J. Wullenkord, A. Brockhinke, J. Krüger, G.A. Garcia, L. Nahon, A. Lucassen, W. Eisfeld, K. Kohse-Höinghaus, Isomer Identification in Flames with Double-Imaging Photoelectron/Photoion Coincidence Spectroscopy (i^2PEPICO) using Measured and Calculated Reference Photoelectron Spectra, *Z. Phys. Chem.* **232**(2), 153-187, 2018.

[2] D. Felsmann, A. Lucassen, J. Krüger, C. Hemken, L.S. Tran, J. Pieper, G.A. Garcia, A. Brockhinke, L. Nahon, K. Kohse-Höinghaus, Progress in Fixed-Photon-Energy Time-Efficient Double Imaging Photoelectron/Photoion Coincidence Measurements in Quantitative Flame Analysis, *Z. Phys. Chem.* **230**(8), 1067-1097, 2016.

[3] L.S. Tran, J. Pieper, H.-H. Carstensen, H. Zhao, I. Graf, Y. Ju, F. Qi, K. Kohse-Höinghaus, Experimental and kinetic modeling study of diethyl ether flames, *Proc. Combust. Inst.* **36**, 1165-1173, 2017.

[4] L.S. Tran, J. Pieper, M. Zeng, Y. Li, X. Zhang, W. Li, I. Graf, F. Qi, K. Kohse-Höinghaus, Influence of the biofuel isomers diethyl ether and *n*-butanol on flame structure and pollutant formation in premixed *n*-butane flames, *Combust. Flame* **175**, 47-59, 2017.

[5] H. Jin[1], J. Pieper[1], C. Hemken, E. Bräuer, L. Ruwe, K. Kohse-Höinghaus, Chemical interaction of dual-fuel mixtures in low-temperature oxidation, comparing *n*-pentane/dimethyl ether and *n*-pentane/ethanol, *Combust. Flame*, zur Veröffentlichung akzeptiert, 2018.

[6] J. Pieper, C. Hemken, R. Büttgen, I. Graf, N. Hansen, K.A. Heufer, K. Kohse-Höinghaus, A high-temperature study of 2-pentanone oxidation: experiment and kinetic modeling, *Proc. Combust. Inst.*, eingereicht, positiv begutachtet, 2018.

1 geteilte Erstautorenschaft

Eigene Beiträge zu den wissenschaftlichen Veröffentlichungen

Alle Veröffentlichungen sind ein gemeinschaftliches Werk mehrerer Wissenschaftler und Wissenschaftlerinnen. Im Folgenden sind meine persönlichen Beiträge zu den jeweiligen Arbeiten aufgelistet.

[1] Ich habe die Messkampagne am *Synchrotron SOLEIL* geplant und in Kooperation mit Mitgliedern unserer Arbeitsgruppe die Experimente durchgeführt. Die aufgenommenen Daten habe ich federführend ausgewertet. Ich habe das Manuskript weitgehend selbst geschrieben.

[2] Ich habe an der Messkampagne am *Synchrotron SOLEIL* teilgenommen, Messungen durchgeführt und bei der Auswertung der Daten unterstützt. Das Manuskript wurde von mir kommentiert.

[3] Ich habe in enger Zusammenarbeit mit L.S. Tran die EI-MBMS- und GC-Messungen in Bielefeld durchgeführt und ausgewertet. Für das Manuskript habe ich Abbildungen erstellt und meine Kommentare und Anmerkungen in das finale Manuskript eingearbeitet.

[4] Ich habe in enger Zusammenarbeit mit L.S. Tran die EI-MBMS- und GC-Messungen in Bielefeld durchgeführt und ausgewertet. Für das Manuskript habe ich Abbildungen erstellt und meine Kommentare und Anmerkungen in das finale Manuskript eingearbeitet.

[5] Ich habe in enger Zusammenarbeit mit H. Jin die Messungen am laminaren Strömungsreaktor begleitet und ausgewertet. Ich habe wesentliche Teile des Manuskriptes erstellt.

[6] Ich habe die Durchführung und Auswertung der EI-MBMS-Experimente in Bielefeld und der PI-MBMS-Experimente an der *Advanced Light Source* und federführend das Schreiben des Manuskriptes vorgenommen.

Konferenzbeiträge

Der präsentierende Autor ist jeweils gekennzeichnet.

- I. Graf, J. Pieper, A. Brockhinke, Temperature measurements and their semi-empirical modelling in low-pressure hydrocarbon flames (Poster), 117. Hauptversammlung der Deutschen Bunsen-Gesellschaft für Physikalische Chemie, Hannover, Deutschland, 10.-12. Mai 2018.
- J. Pieper, S. Schmitt, J. Krüger, G.A. Garcia, L. Nahon, W. Eisfeld, A. Brockhinke, K. Kohse-Höinghaus, Isomer selective combustion analysis by double-imaging fixed-photon-energy photoelectron/photoion coincidence (i^{2}PEPICO) spectroscopy (Poster), International Bunsen Discussion Meeting *Chemistry and Diagnostics for Clean Combustion*, Bielefeld, Deutschland, 21.-23. Juni 2017.

- H. Jin, E. Bräuer, J. Pieper, L. Ruwe, C. Hemken, L.S. Tran, K. Kohse-Höinghaus, Chemical interaction of dual-fuel mixtures in low-temperature oxidation, comparing *n*-pentane/dimethyl ether and *n*-pentane/ethanol (Poster), International Bunsen Discussion Meeting *Chemistry and Diagnostics for Clean Combustion*, Bielefeld, Deutschland, 21.-23. Juni 2017.
- C. Hemken, U. Burke, J. Pieper, R. Büttgen, K.A. Heufer, K. Kohse-Höinghaus, Effect of the carbonyl group in the oxidation of small methyl ketones (Vortrag), 116. Hauptversammlung der Deutschen Bunsen-Gesellschaft für Physikalische Chemie, Kaiserslautern, Deutschland, 25.-27. Mai 2017.
- S. Schmitt, J. Pieper, J. Krüger, G.A. Garcia, L. Nahon, W. Eisfeld, A. Brockhinke, K. Kohse-Höinghaus, Double-imaging fixed-photon-energy photoelectron/photoion coincidence (i^2PEPICO) spectroscopy for combustion analysis (Poster), 116. Hauptversammlung der Deutschen Bunsen-Gesellschaft für Physikalische Chemie, Kaiserslautern, Deutschland, 25.-27. Mai 2017.
- L.S. Tran, J. Pieper, H.-H. Carstensen, H. Zhao, I. Graf, Y. Ju, F. Qi, K. Kohse-Höinghaus, Experimental and kinetic modeling study of diethyl ether flames (Vortrag), 36th International Symposium on Combustion, Seoul, Korea, 31. Juli - 5. August 2016.
- J. Pieper, D. Felsmann, A. Lucassen, J. Krüger, G.A. Garcia, L. Nahon, A. Brockhinke, K. Kohse-Höinghaus, Fixed-photon-energy double-imaging photoelectron/photoion coincidence (i^2PEPICO) spectroscopy for combustion analysis (Poster), 36th International Symposium on Combustion, Seoul, Korea, 31. Juli - 5. August 2016.
- J. Pieper, L.S. Tran, M. Zeng, Y. Li, F. Qi, K. Kohse-Höinghaus, Chemistry of C4-fuel combinations: reaction pathways in *n*-butane flames upon addition of the biofuel isomers diethyl ether or *n*-butanol (Poster), 36th International Symposium on Combustion, Seoul, Korea, 31. Juli - 5. August 2016.
- J. Pieper, M. Zeng, L.S. Tran, I. Graf, K. Kohse-Höinghaus, Influence of the biofuel isomers diethyl ether and *n*-butanol on pollutant formation in premixed *n*-butane flames (Poster), 115. Hauptversammlung der Deutschen Bunsen-Gesellschaft für Physikalische Chemie, Rostock, Deutschland, 5.-7. Mai 2016.
- J. Pieper, M. Zeng, L.S. Tran, I. Graf, K. Kohse-Höinghaus, Structural effects of the biofuel isomers diethyl ether and *n*-butanol on the flame chemistry of premixed *n*-butane flames (Poster), KAUST Future Fuels Workshop, Thuwal, Saudi Arabien, 7.-9. März 2016.

Inhaltsverzeichnis

1 Einleitung **1**

2 Theoretische und experimentelle Grundlagen **5**
2.1 Verbrennungsprozesse 5
2.2 Modellexperimente 7
2.2.1 Vorgemischte laminare Niederdruckflamme 7
2.2.2 Laminarer Strömungsreaktor 9
2.3 Molekularstrahl-Massenspektrometrie 10
2.4 Datenauswertung und Quantifizierung 13
2.5 Kinetische Modellierungen 15

3 Identizierung von Isomeren in Flammen mittels Photoelektronen-Photoionen Koinzidenz-Spektroskopie **17**

4 Einfluss der Addition von Biokraftstoffen auf die Flammenstruktur und Schadstoffbildung in vorgemischten Niederdruckflammen **25**

5 Chemische Interaktion und synergistische Effekte in Brennstoffmischungen im Bereich der Niedertemperaturoxidation **35**

6 Untersuchung der Hochtemperaturoxidation von 2-Pentanon **45**

7 Zusammenfassung und Ausblick **53**

Literaturverzeichnis **55**

A Publikation 1 **67**

B Publikation 2 **105**

C Publikation 3 **139**

D Publikation 4 **151**

E Publikation 5 **167**

F Publikation 6 **219**

Die Ergebnisse dieser Arbeit sind bereits in den Publikationen [1–4] veröffentlicht, bzw. in Form der Manuskripte [5, 6] eingereicht und bereits akzeptiert bzw. positiv begutachtet. Im Folgenden werden daher die publizierten Ergebnisse zusammengefasst. Die Veröffentlichungen sowie die eingereichten Manuskripte sind im Anhang dieser Arbeit zu finden.

KAPITEL 1

Einleitung

Die aus Verbrennungsprozessen entstehenden Emissionen haben nachweislich einen schädlichen Einfluss auf das Klima, die Luftqualität, die Umwelt und die Gesundheit [7, 8]. Die globale Emission von CO_2 ist von 1990 bis 2015 um mehr als 60 % gestiegen, wobei 2015 der anthropogene CO_2-Anteil bereits bei 94 % lag [9]. Jedoch ist nicht nur der CO_2-Ausstoß relevant, auch die Emission von Feinstaub und Ruß hat einen signifikanten Einfluss auf das Klima [10], zählt zu den größten globalen Gesundheitsbedrohungen und führt nachweislich zu schweren Atemwegs- und Herz-Kreislauf-Erkrankungen [11–17]. Im Hinblick auf all diese Aspekte ist vor allem ein kritisches Überdenken der Strategien im Transportsektor notwendig, jedoch sind auch viele andere Bereiche für diese Entwicklung verantwortlich. Eine reine Umstellung auf Elektromobilität reicht somit nicht aus, da nicht zuletzt auch die Elektroenergie zum größten Teil aus fossilen Energieträgern produziert wird [18]. Heutzutage wird insgesamt immer noch mehr als 80 % des globalen Primärenergiebedarfs aus fossilen Energiequellen abgedeckt [7, 8, 19]. Eine vollständige Substitution durch erneuerbare Energie (z.B. aus Wind, Sonne, Wasser) ist zwar rein technisch möglich [20], jedoch aufgrund der starken Fluktuation im Hinblick auf die Verfügbarkeit solch natürlicher Ressourcen schwierig. Mit dem weiterhin steigenden Energiebedarf ist für die nähere Zukunft keine Prognose für eine vollständige Substitution fossiler Brennstoffe möglich [7, 8, 21]. Die Übergangszeit mit komplementärer Nutzung fossiler und erneuerbarer Energien wird daher noch mindestens die nächsten 10-20 Jahre andauern. Daher ist es besonders wichtig, auch im Flüssigbrennstoffbereich Alternativen zu erforschen, die über eine sauberere Verbrennung im Vergleich zu momentan genutzten Kraftstoffen verfügen. Dazu existieren bereits vielversprechende Ansätze und Konzepte, welche jedoch ein interdisziplinäres Wissen über Brennstoffe, Energieumsätze, technische Infrastruktur und die motorische Verbrennung kombinieren müssen [22].

Im Bereich der motorischen Verbrennung gibt es zwei wesentliche Ansatzmöglichkeiten, diese Ziele zu erreichen. Eine CO_2-Reduktion kann durch effizientere Verbrennungsstrategien sowie durch Brennstoffe mit verringerter Kohlenstoffsignatur ermöglicht werden. Zum einen ist die technisch relevante homogenisierte Niedertemperaturverbrennung zu nennen,

bei der durch eine möglichst gleichmäßige Vormischung von Brennstoff und Oxidator sowie einer Reduktion der Verbrennungstemperatur eine effiziente Verbrennung erreicht sowie der Ausstoß von Schadstoffen signifikant verringert werden soll. Dasselbe Ziel kann mithilfe der Nutzung alternativer Kraftstoffe verfolgt werden, die aufgrund von unterschiedlichen Molekülstrukturen ein verändertes Emissionsverhalten im Vergleich zu herkömmlichen Kraftstoffen aufweisen.
Im technischen Bereich werden dazu vorrangig Messungen von globalen Parametern der Verbrennung, wie z.B. Zündverzugszeiten, Flammengeschwindigkeiten oder der Konzentration von Kohlenwasserstoffgemischen am Auspuff unter verschiedenen Bedingungen durchgeführt, um wesentliche Erkenntnisse für eine technische Andwendbarkeit und Nutzbarkeit von alternativen Kraftstoffen zu erhalten. Der Verbrennungsprozess ist jedoch aus chemischer Sicht sehr komplex. Daher wurden in dieser Arbeit spezifische Details der Verbrennung in Umgebungen untersucht, die auch tatsächlich chemisch analysiert werden können. Dazu wurden Modellexperimente eingesetzt, die dazu dienen, ein umfassendes chemisches Verständnis komplexer Verbrennungsprozesse und Reaktionswege zu erhalten. Dies ist insbesondere im Hinblick auf das noch nicht ausreichend erforschte Schadstoffbildungspotential alternativer Kraftstoffe und Kraftstoffzusätze wichtig, da diese oftmals ein sehr unterschiedliches Emissionsverhalten im Vergleich zu momentan genutzten Kraftstoffen aufweisen und auch Schadstoffe emittieren, die ebenfalls kritisch im Bezug auf Klima, Atmosphäre und Gesundheit betrachtet werden müssen und unter Umständen bisher gesetzlich nicht reguliert sind [23].

Im Rahmen dieser Arbeit wurden mit der laminaren vorgemischten Niederdruckflamme und dem laminaren Strömungsreaktor zwei verschiedene Modellexperimente verwendet, die einen größeren Bereich des relevanten Phasenraums aus Druck, Temperatur und Stöchiometrie abdecken. Als Bindeglied zwischen Laborexperimenten und technisch relevanten Prozessen werden üblicherweise kinetische Modelle verwendet. Solche Modelle können mithilfe experimenteller Ergebnisse, wie sie in dieser Arbeit vorgestellt werden, weiterentwickelt werden. Bisher sind solche Modelle vorrangig für den Bereich von Molekülen mit ein bis vier Kohlenstoffatomen gut entwickelt und erprobt [23–25], für größere Moleküle und Mischungen verschiedener Brennstoffmoleküle sind jedoch weiterhin eine Vielzahl experimenteller Daten zur Entwicklung und Validierung notwendig.

In dieser Arbeit wurde die Molekularstrahl-Massenspektrometrie (*Molecular-beam mass spectrometry*, MBMS) als universelle Detektionsmethode eingesetzt, da sie durch die gleichzeitige Analyse einer Vielzahl an Spezies eine wertvolle und etablierte Methode in vielen Bereichen, wie z.B. Pyrolyse, Photolyse und Oxidation darstellt [26–34]. Damit können auch im Verbrennungsbereich nützliche Informationen für die Modellentwicklung und die Erprobung neuer Betriebsbedingungen gewonnen werden [35, 36]. Die Nutzung verschiedener Ionisationstechniken ist dabei sowohl im Hinblick auf die Kombination unterschiedlicher Erkenntnisse als auch eine Kreuzvalidierung verschiedener Experimente sinnvoll. Daher wurden zunächst quantitative Messungen an der *Universität Bielefeld* mit der relativ einfach anwendbaren Elektronenstoßionisation (EI) [37, 38] durchgeführt, die jedoch aufgrund einer breiten Elektronenverteilung keine scharf definierte Ionisationsenergie liefert und damit über die reine Detektion der Masse keine Isomere voneinander getrennt werden können. Dies ist hingegen mithilfe der Photoionisation (PI) möglich [26, 27, 39], da dabei mittels synchrotrongenerierter Vakuumultravioletstrahlung Photonen mit einer sehr schmalen

Energieverteilung erzeugt werden und somit eine zusätzliche Identifizierung und Separation von Isomeren ermöglicht wird. Solche Messungen wurden an der *Advanced Light Source* (ALS), Berkeley, USA und dem *National Synchrotron Radiation Laboratory*, Hefei, China durchgeführt und ebenfalls für die Ergebnisse dieser Arbeit genutzt. Auch eine Quantifizierung der beobachteten Spezies mittels PI ist möglich, jedoch gelangt auch diese Methode bei Spezies mit nah beieinanderliegenden Ionisationsenergien an ihre Grenzen. Eine zusätzliche Kombination mit Messungen der doppelt abbildenden Photoelektronen-Photoionen Koinzidenz-Spektroskopie (i^{2}PEPICO), die am *Synchrotron SOLEIL*, Gif-sur-Yvette, Frankreich durchgeführt wurden, liefert eine weitere Identifizierungsmöglichkeit über die Messung individueller Photoelektronenspektren (PES) [40]. Die Nutzung dieser Methode ist erst kürzlich in den Fokus der Verbrennungsdiagnostik gerückt und die aktuelle Forschung liefert vielversprechende Ergebnisse [2, 41–43]. All diese Methoden liefern eine Vielzahl von Informationen zur Analyse von Verbrennungsprozessen, sowohl qualitativ als auch quantitativ, und eine Kombination mehrerer Analysemethoden ist im Bereich komplexer Prozesse nicht nur sinnvoll, sondern unbedingt notwendig. Darüber hinaus gilt zu beachten, dass zur Identifizierung und Quantifizierung von in der Verbrennung relevanten Spezies komplexe Informationen sowie Literaturdaten in Form von Ionisationsquerschnitten oder Photoelektronenspektren bekannt sein müssen, die oft bisher nicht gemessen wurden. Eine theoretische Berechnung solcher Parameter ist zwar ebenfalls möglich, aber nicht weniger zeitintensiv.

In dieser Arbeit wurde daher eine Kombination aus EI-MBMS-, PI-MBMS-Experimenten und PEPICO-Messungen zur zusätzlichen Identifizierung spezifischer Isomere genutzt. Dazu wurden die Photoelektronenspektren einer Vielzahl von möglichen Referenzsubstanzen gemessen und teilweise auch theoretisch berechnet. Die Ergebnisse dieser Arbeiten dienen insbesondere dem detaillierten Verständnis der während der Verbrennung ablaufen Reaktionsmechanismen und konnten für die Verbrennung von Cyclopenten, *iso*-Pentan und Diethylether wertvolle Erkenntnisse für die weitere Modellentwicklung liefern. In Kap. 3 sind einige der in [1] veröffentlichten Ergebnisse zusammengefasst.

Ein zentraler Fokus dieser Arbeit lag auf der Analyse alternativer Kraftstoffe. In diesem Bereich sind besonders Stoffklassen wie Alkohole, Ether und Ester im Gespräch [23, 35, 44], da sie zum Teil aus Biomasse produziert werden können und nachweislich weniger Schadstoffe emittieren als herkömmliche Kraftstoffe [23, 45–47]. Durch ihre veränderte molekulare Struktur werden jedoch auch signifikante Unterschiede in der Verbrennung erhalten, welche insbesondere durch enthaltene Sauerstoffatome zu einem erhöhten Ausstoß von toxischen Carbonylverbindungen führen [48–50] und einen signifikanten Einfluss auf photochemische Reaktionen in der Atmosphäre haben können [51]. Im Fokus dieser Arbeit standen insbesondere Mischungen alternativer und prototypischer Kraftstoffe, da selbige schon in Form von E10 und Biodiesel im Alltag relevant sind. Ein interessanter Kraftstoff mit technisch relevanten Eigenschaften ist Diethylether. Dieser wurde zunächst individuell und anschließend auch in Mischungen in laminaren vorgemischten Niederdruckflammen untersucht. Im Hinblick auf die Auswirkung der Brennstoffstruktur auf die Schadstoffbildung wurden dann die Isomere Diethylether und *n*-Butanol - ebenso ein vielversprechender Kraftstoff - in Mischungen mit *n*-Butan analysiert. Die in [3, 4] veröffentlichten Ergebnisse sind in Kap. 4 zusammengefasst.

Im Anschluss an die im Hochtemperaturbereich analysierten Niederdruckflammen wurden die Auswirkungen von Kraftstoffadditiven ebenfalls im Niedertemperaturbereich untersucht. Viele motorische Anwendungen beruhen auf dem Konzept der homogenisierten Niedertemperaturverbrennung [52, 53]. Durch eine niedrigere Temperatur kann eine Reduktion der Rußbildung sowie der NO_x-Emission erzielt werden [54, 55], wobei durch die langsamer ablaufenden Reaktionen vorrangig die Reaktionen der Brennstoffradikale mit Sauerstoff zu Peroxylradikalen dominieren [56–58]. Durch diese Einflüsse ergeben sich deutlich veränderte Reaktionswege über sogenannte Niedertemperaturspezies, deren Strukturen und Bildungswege detaillierter erforscht werden müssen. In Gemischen sind zudem in diesem Temperaturbereich komplexe Interaktionen der Verbrennungsreaktionen möglich, die die Zündung beeinflussen und die bisher nur sehr wenig erforscht wurden. Brennstoffstrukturspezifische, nicht regulierte Schadstoffe sind möglicherweise die Konsequenz der langsamen Reaktionszeiten. In dieser Arbeit wurde detalliert die Auswirkung der Addition zweier potentieller Biokraftstoffe, nämlich Dimethylether und Ethanol, auf die Niedertemperaturoxidation eines Kohlenwasserstoffes untersucht. Die Ergebnisse wurde bereits in Form des Manuskripts [5] zur Veröffentlichung akzeptiert und sind in Kap. 5 zusammengefasst.

Die Entwicklung möglichst schadstoffarmer Biokraftstoffe ist ein sehr aktuelles Thema. Die Verbrennung von kleinen Methylketonen ist kürzlich in den Fokus der Diskussionen gerückt, da diese eine hohe Klopffestigkeit aufweisen und oft mikrobiologisch herstellbar sind [59, 60]. So wurde z.B. 2-Butanon vom Exzellenzcluster "Maßgeschneiderte Kraftstoffe aus Biomasse"(*Tailor-Made Fuels from Biomass*, TMFB) der *RWTH Aachen* als möglicher Zukunftsbrennstoff vorgestellt. Bisherige Untersuchungen zu diesem Brennstoff [61–63] zeigten vielversprechende Ergebnisse im Hinblick auf eine niedrige Schadstoffbildung wie z.B. die Reduktion von Ruß, NO_x und unverbrannten Kohlenwasserstoffen [46, 61]. Aufgrund seiner höheren Energiedichte ist 2-Pentanon interessant, obwohl es bisher nicht aus Biomasse herstellbar ist. Daher wurde in dieser Arbeit die Hochtemperaturkinetik von 2-Pentanon in einer laminaren vorgemischten Niederdruckflamme besonders im Hinblick auf mögliche Unterschiede in der Verbrennungskinetik zu 2-Butanon untersucht. Die Ergebnisse sind zur Veröffentlichung eingereicht [6] und in Kap. 6 zusammengefasst.

KAPITEL 2

Theoretische und experimentelle Grundlagen

In diesem Kapitel werden die zum Verständnis der Arbeit benötigten theoretischen Grundlagen zu den untersuchten Verbrennungsprozessen sowohl im Hochtemperatur- als auch im Niedertemperaturbereich erläutert sowie die experimentellen Untersuchungsobjekte und die verwendete Molekularstrahl-Massenspektrometrie kurz vorgestellt. Außerdem wird eine kurze Übersicht über die Datenauswertung und die Quantifizierung für die verschiedenen Experimente gegeben. Da viele der experimentellen Ergebnisse mit kinetischen Modellierungen verglichen werden, werden abschließend die verwendeten Simulationsmethoden beschrieben.

2.1 Verbrennungsprozesse

Bei einer Verbrennung wird ein Brennstoff mit einem Oxidator in einer schnell ablaufenden Folge exothermer, meist radikalischer Kettenreaktionen zu den Verbrennungsprodukten umgesetzt [64]. Je nach Verhältnis von Brennstoff und Oxidator wird die Verbrennung brennstoffreich oder brennstoffarm genannt, während die stöchiometrische Verbrennung den Fall beschreibt, in dem Brennstoff und Oxidator stöchiometrisch zueinander vorliegen und bei der Verbrennung eines Kohlenwasserstoffes damit vollständig zu Kohlendioxid und Wasser reagieren [56]. Eine bespielhafte verallgemeinerte Reaktionsgleichung dieser Art zeigt Gl. 2.1. Die daraus resultierende Stöchiometrie ϕ der Oxidation gibt das Verhältnis von Brennstoff zu Oxidator normiert auf den stöchiometrischen Fall an (s. Gl. 2.2).

$$C_{\mathrm{x}}H_{\mathrm{y}}O_{\mathrm{z}} + \beta\ \mathrm{O_2} \rightarrow x\ \mathrm{CO_2} + 0.5 \cdot y\ \mathrm{H_2O} \tag{2.1}$$

$$\text{mit } \beta = x + 0.25 \cdot y - 0.5 \cdot z$$

$$\phi = \frac{\frac{n_{\mathrm{Brennstoff}}}{n_{\mathrm{Oxidator}}}}{\frac{n_{\mathrm{Brennstoff,stöch.}}}{n_{\mathrm{Oxidator,stöch.}}}} = \frac{n_{\mathrm{Brennstoff}}}{n_{\mathrm{Oxidator}}} \cdot \beta \quad \text{mit } n\text{: Stoffmenge} \tag{2.2}$$

Die ablaufenden Kettenreaktionen bei der Verbrennung unterscheiden sich im Allgemeinen stark in Abhängigkeit von den vorliegenden Umgebungsbedingungen (Druck und insbesondere Temperatur). Dies führt zu sehr unterschiedlichen Reaktionsmechanismen in verschiedenen Temperaturbereichen. Die sich dabei hauptsächlich unterscheidenden Reaktionswege sind in Abb. 2.1 nach [65, 66] schematisch und verallgemeinert dargestellt. Typische Reaktionsklassen für beide Bereiche werden im Folgenden kurz erläutert.

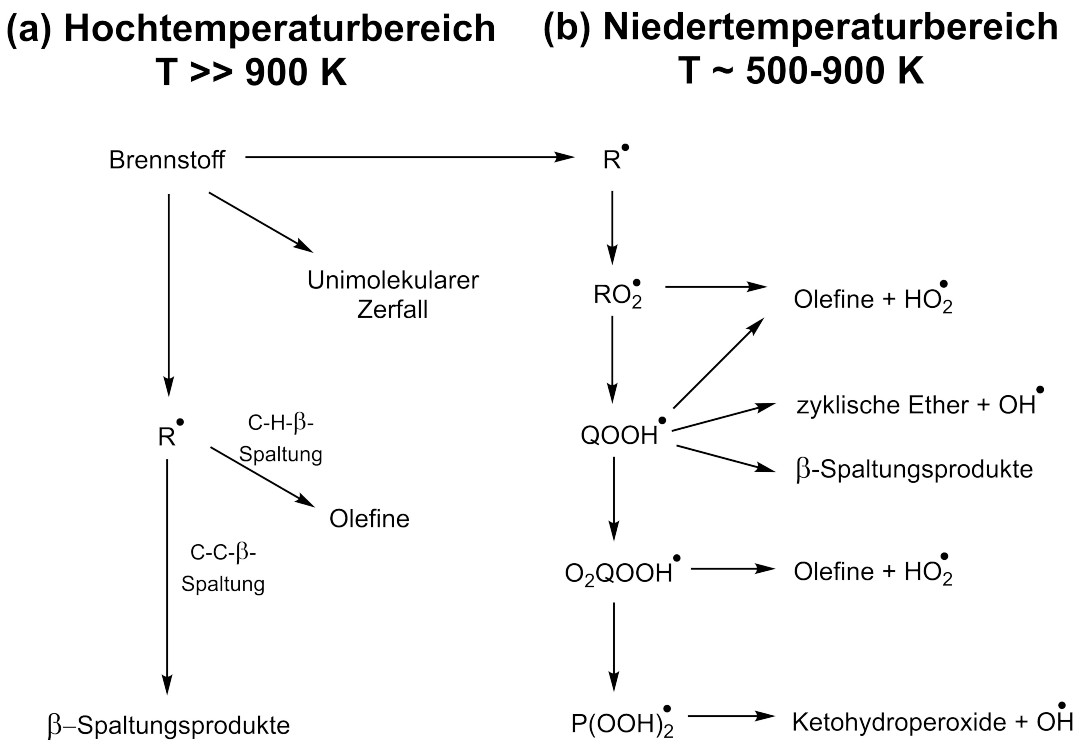

Abbildung 2.1: Reaktionswege für den (a) Hochtemperatur- und (b) Niedertemperaturbereich, Reaktionsklassen adaptiert aus [65, 66].

Im Hochtemperaturbereich, der für die hier untersuchten Systeme deutlich oberhalb von 900 K beginnt, findet zunächst eine H-Abstraktion vom Brennstoffmolekül vorrangig durch H- und OH-Radikale statt. Durch anschließende C-H- bzw. C-C-β-Spaltung werden dann entweder Olefine oder andere Spaltungsprodukte (stabile Spezies + Radikal) gebildet. Im Niedertemperaturbereich (hier ca. 500-900 K) findet die erste H-Abstraktion hauptsächlich durch OH- und HO_2-Radikale statt. Für eine anschließende β-Spaltung ist bei niedrigerer Temperatur jedoch nicht genügend Energie vorhanden, weshalb es hier vorrangig zu einer Anlagerung eines Sauerstoffmoleküls kommt. Das daraus gebildete Peroxylradikal RO_2 kann dann über mehrere in Abb. 2.1 dargestellte Reaktionswege weiter reagieren, die die Gesamtreaktivität des Systems steigern oder verringern können, je nachdem ob und wie viele weitere Radikale dabei gebildet werden. Zum Beispiel werden durch die Reaktion über das Isomerisierungsprodukt QOOH zum Ketohydroperoxid und dessen anschließende Spaltung der Peroxidgruppe mehr OH-Radikale produziert, als für die initiale H-Abstraktion vom Brennstoff benötigt werden, was zu einer erheblichen Steigerung der Gesamtreaktivität des Systems führt. Die Stabilität solcher peroxidischen Spezies ist jedoch sehr gering und wird durch eine Erhöhung der Temperatur stark reduziert. In diesem Fall kommt es vermehrt zu Kettenabbruchreaktionen wie der Bildung von Olefinen sowie zu weniger reaktiveren HO_2-Radikalen. Im Bereich von ca. 800-1200 K spricht man von einem Übergangsbereich, da hier sowohl die Reaktionsklassen der Hoch- als auch der Niedertemperaturkinetik auftreten können. Die Auswirkungen dieser unterschiedlichen Reaktionswege sind in Abb. 2.2 dargestellt.

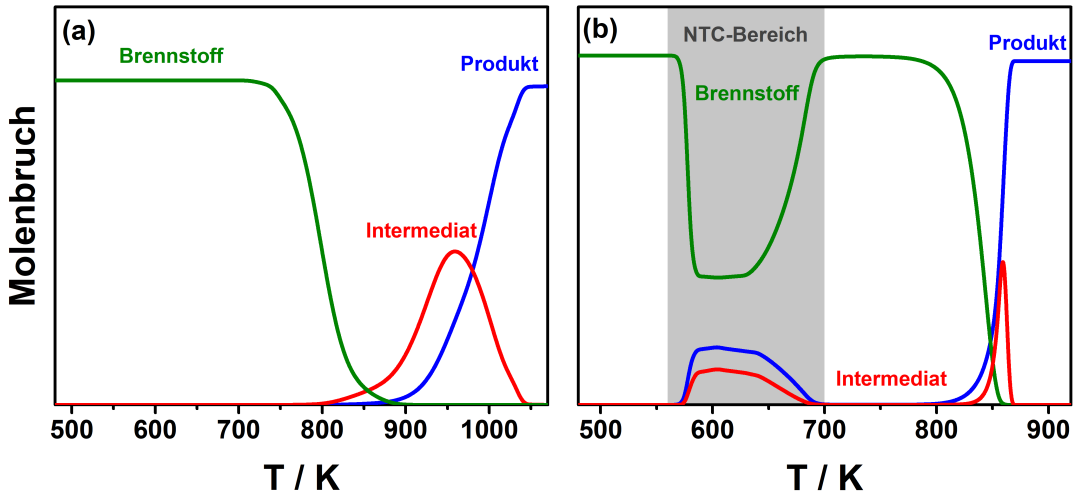

Abbildung 2.2: Typische Edukt-, Produkt- und Intermediatverläufe für die Oxidation eines Brennstoffs (a) ohne und (b) mit Niedertemperaturkinetik.

Zündunwillige Brennstoffe mit einer hohen Oktanzahl[1] zeigen erst bei höheren Temperaturen eine Reaktivität und somit einen Brennstoffumsatz (Abb. 2.2a), während Brennstoffe mit einer niedrigen Oktanzahl bereits eine ausgeprägte Kinetik im Niedertemperaturbereich aufweisen und einen sogenannten NTC-Bereich (NTC: *Negative Temperature Coefficient*) zeigen können. Dies bedeutet, dass mit steigender Temperatur der Brennstoffabbau zunächst zurückgeht und die Reaktivität des Systems abnimmt (s. Abb. 2.2b).

Aufgrund der hier vorgestellten unterschiedlichen Reaktionsabläufe ist es wichtig, den Brennstoffabbau unter verschiedenen Konditionen (Druck, Temperatur, Stöchiometrie) zu untersuchen, um ein möglichst breites Parameterfeld abzudecken.

2.2 Modellexperimente

In dieser Arbeit wurden zwei verschiedene Modellexperimente verwendet, die jeweils stark unterschiedliche Randbedingungen darstellen. Die vorgemischte laminare Niederdruckflamme wird bei niedrigem Druck p (hier 40 mbar) untersucht und spiegelt vorrangig Reaktionen des Hochtemperaturbereichs wider, da die vorliegende Flammentemperatur T im Bereich von 1000-2000 K liegt. Um hingegen die Niedertemperaturchemie zu untersuchen, wurde ein laminarer Strömungsreaktor verwendet, der bei einem Umgebungsdruck von 970 mbar und in einem Temperaturbereich von 450-1100 K betrieben wird. Im Folgenden werden die verwendeten Systeme und ihre Spezifikationen kurz vorgestellt.

2.2.1 Vorgemischte laminare Niederdruckflamme

Die vorgemischte laminare Niederdruckflamme eignet sich für die Untersuchung von Verbrennungsprozessen im Hochtemperaturbereich besonders gut, da sie parallel zur Austrittsöffnung eine konstante Intermediatkonzentration gewährleistet. Idealerweise ist durch diese

1 Klassifizierung der Zündunwilligkeit von Brennstoffen, meist Angabe als RON (*Research Octane Number*). Definitionsgemäß ist die RON für 2,2,4-Trimethylpentan (”Isooktan”) mit einem Wert von 100 maximal und liegt für n-Heptan bei 0. Die RON gibt an, wieviel Isooktan in einer Mischung mit n-Heptan vorliegen muss, um die gleiche Klopffestigkeit wie der zu prüfende Kraftstoff aufzuweisen [67].

Geometrie der Ausströmung die Flussgeschwindigkeit des Reaktionsgemisches an jeder Stelle der Flamme identisch und die Konzentration von Edukten, Produkten und Verbrennungsintermediaten daher nur eine Funktion der Reaktionszeit. Die Position h (Höhe oberhalb der Brenneroberfläche) innerhalb der Flamme korreliert somit direkt mit dem Reaktionsfortschritt, wodurch quasi-eindimensionale Molenbruchprofile erhalten werden können. Ein solches Beispiel ist in Abb. 2.3 dargestellt.

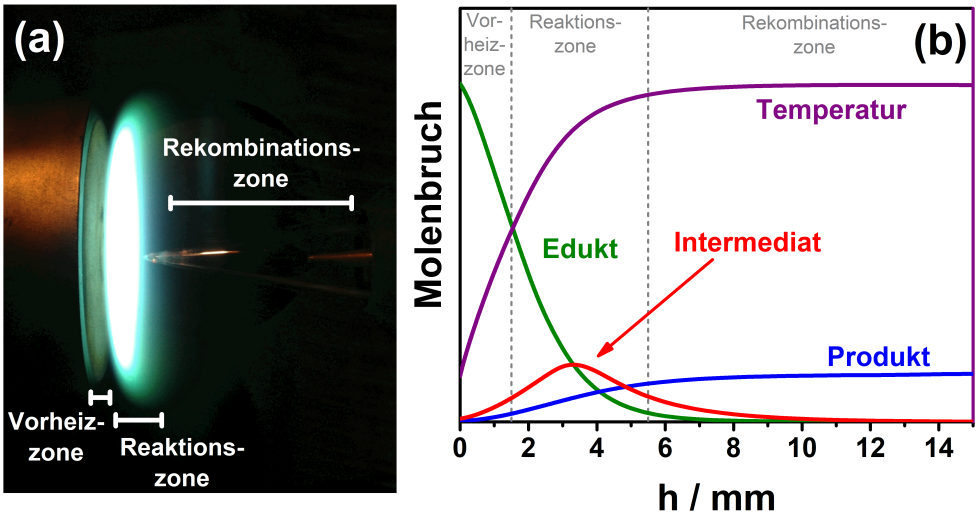

Abbildung 2.3: (a) Foto einer brennstoffreichen vorgemischten Niederdruckflamme und schematische Darstellung der darin vorliegenden Zonen. (b) Typische Konzentrationsprofile von Edukten, Intermediaten und Produkten und der Verlauf der Flammentemperatur in Abhängigkeit von der Höhe über der Brenneroberfläche h (horizontal dargestellt).

Die laminare Vormischflamme kann grob in die drei Zonen aus Abb. 2.3a unterteilt werden. In der Vorheizzone direkt oberhalb der Brenneroberfläche liegen Brennstoff und Oxidator vor. In der sich anschließenden Reaktionszone finden die eigentlichen chemischen Reaktionen über die Bildung von Intermediaten statt. Im weiteren Reaktionsverlauf finden in der Rekombinationszone Kettenabbruchreaktionen statt und stabile Produkte werden gebildet. In der vergleichsweise heißen und druckarmen Umgebung dieser Flammen werden in der Regel Hochtemperaturspezies über die Reaktionswege in Abb. 2.1a gebildet. Die Detektion von typischen Niedertemperaturspezies (vgl. Abb. 2.1b) ist aufgrund der rasch ansteigenden Temperatur eher nicht zu erwarten, jedoch wurden oxygenierte Spezies, die z.B. den zyklischen Ethern zugeordnet wurden, auch in der Vorheizzone der Flamme (die mit einer niedrigeren Temperatur korreliert, vgl. Temperaturprofil in Abb. 2.3b) gefunden [37, 61]. Solche Spezies können zwar detektiert werden, dominieren die Flammenchemie jedoch nicht.

Messungen in laminaren vorgemischten Niederdruckflammen wurden im Rahmen dieser Arbeit sowohl an der *Universität Bielefeld* als auch an der *Advanced Light Source* (ALS) in Berkeley, USA und dem *National Synchrotron Radiation Laboratory* in Hefei, China durchgeführt. Alle drei Systeme folgen einem sehr ähnlichen Aufbau, sodass die erhaltenen Ergebnisse aller Apparaturen gut miteinander vergleichbar sind. Die Flamme wird dabei jeweils auf einer Brennermatrix innerhalb einer Brennerkammer stabilisiert,

wobei ein konstanter Druck vorgegeben wird. Brennstoff und Oxidator werden unterhalb der Brennerkammer partiell vorgemischt und strömen anschließend gleichmäßig durch die Brennermatrix in die Brennerkammer. Gasförmige Brennstoffe werden dazu über Masseflussregler mit einer Ungenauigkeit von ca. 5% des eingestellten Masseflusses direkt eingeleitet, während flüssige Brennstoffe zunächst über ein Verdampfungssystem konstant in die Gasphase überführt werden. Um die in Abb. 2.3b gezeigten Speziesprofile über den entsprechenden Höhenbereich über der Brenneroberfläche zu erhalten, kann der Brenner mit einem Schrittmotor verfahren werden. Dadurch kann die Probenahme an verschiedenen Orten in der Flamme erfolgen und die Zusammensetzung der Spezies in Abhängigkeit vom Reaktionsfortschritt analysiert werden.

2.2.2 Laminarer Strömungsreaktor

Im Rahmen dieser Arbeit wurden Messungen am laminaren Strömungsreaktor an der *Universität Bielefeld* durchgeführt. Ein solches System eignet sich besonders gut für die gezielte Untersuchung von einigen der in Abb. 2.1b vorgestellten Niedertemperaturspezies und bietet aufgrund seiner einfachen Geometrie eine vergleichsweise einfach zu beschreibende Strömungsdynamik, was insbesondere für die Modellierbarkeit von großer Bedeutung ist. Eine schematische Darstellung des in dieser Arbeit verwendeten laminaren Strömungsreaktors kann Abb. 2.4a entnommen werden. Der eigentliche Reaktor besteht aus einem Quarzglasrohr mit einer Länge von 1.30 m, einem Innendurchmesser von 8 mm und einem Außendurchmesser von 10 mm, welches durch acht unabhängig voneinander regelbare Ni-Cr/Ni-Thermoelemente an der Außenseite auf Temperaturen im Bereich von 448-1173 K (175-900 °C) geheizt werden kann. Die Thermoelemente sind mit einem Fehler von 0.4 % behaftet, jedoch haben interne Kalibrationsmessungen und Vergleiche mit Modellierungen ergeben, dass die Temperatur im Reaktor aufgrund von Inhomogenitäten eher mit einer Ungenauigkeit von ± 15 K angenommen werden muss. Das in Abb. 2.4b gezeigte Temperaturprofil über die Länge des gesamten Reaktors zeigt außerdem, dass der Reaktor im Wesentlichen in drei Zonen unterteilt werden kann (Vorheizzone 0-0.14 m, Reaktionszone 0.14-1.25 m, Abkühlzone 1.25-1.30 m). Dies ist besonders für die Berücksichtigung des Wärmetransfers bei der Modellierung des Reaktors wichtig (s. Kap. 2.5).

Um die Konzentrationen der durch Oxidationsreaktionen entstehenden Spezies messen zu können, werden Brennstoff und Sauerstoff, wie in Abb. 2.4a dargestellt, jeweils unabhängig voneinander mit dem Verdünnungsgas Argon vorgemischt und anschließend über ein Y-Konnektorstück zusammengeführt. Im Reaktor wird das Gemisch auf die von außen eingestellte Temperatur erhitzt und durch den kontinuierlich nachströmenden Fluss durch das Quarzglasrohr hindurchgeleitet. Für dieses System ist bei einer Flussrate von bis zu 0.5 slm (Standard Liter pro Minute, bei 273.15 K und 1 atm) von einer sogenannten *Plug-Flow*-Strömung auszugehen. Das bedeutet, dass sich das Gemisch wie eine Scheibe durch den Reaktor bewegt und Reibung an der Reaktorwand vernachlässigt werden kann. Durch die zusätzliche Vernachlässigung von Rückdiffusionsprozessen kann so eine homogene Konzentrationsverteilung an jeder Position des Reaktors angenommen werden, was zu einer deutlich vereinfachten Modellierung des Reaktorsystems führt. Am Ende des Quarzglasrohrs erfolgt dann die Probenahme und die anschließende Detektion und Analyse der Spezieszusammensetzung bei der jeweils eingestellten Temperatur, sodass Temperatur-Konzentrations-Profile wie in Abb. 2.2 erhalten werden.

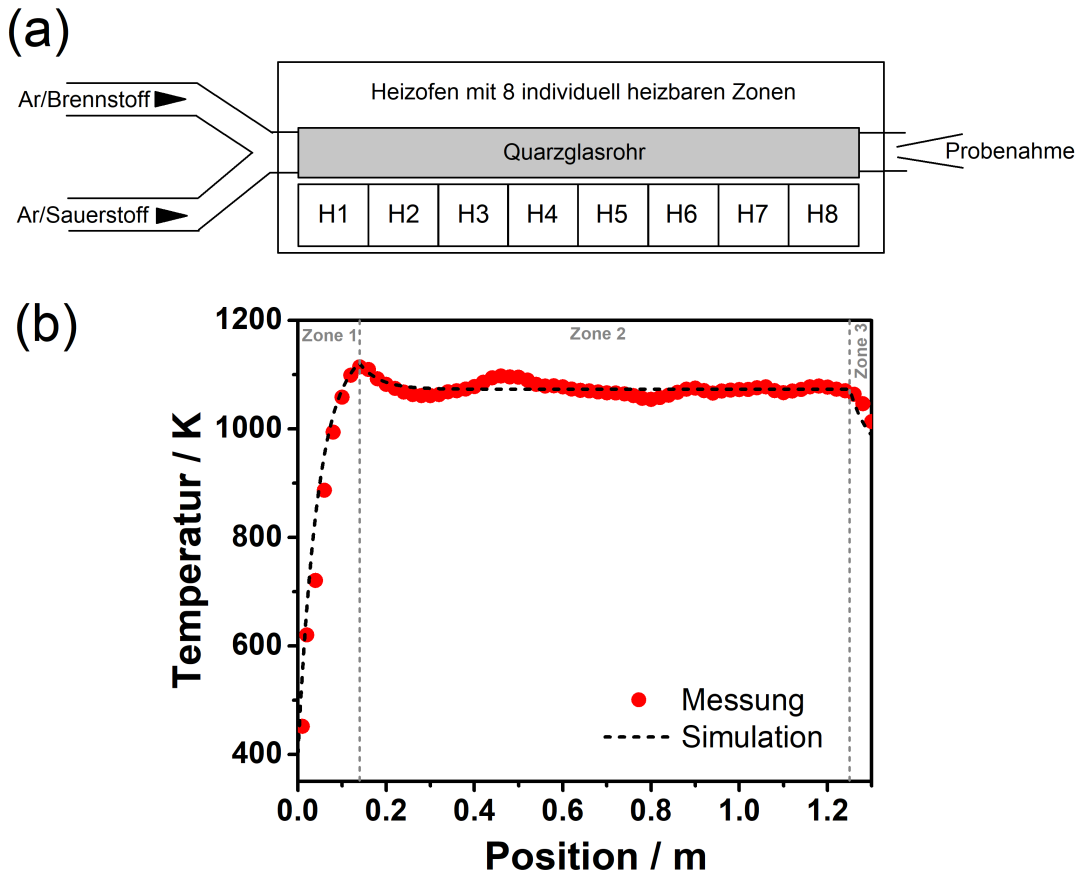

Abbildung 2.4: (a) Schematische Darstellung des laminaren Strömungsreaktors. (b) Temperaturprofil von Argon über die Reaktorlänge mit Vorheizzone (Zone 1), Reaktionszone (Zone 2) und Abkühlzone (Zone 3).

2.3 Molekularstrahl-Massenspektrometrie

In dieser Arbeit wurde zur Probenahme und Detektion der bei der Oxidation entstehenden Spezies die Molekularstrahl-Massenspektrometrie (*Molecular-beam mass spectrometry*, MBMS) eingesetzt. Dabei wird zunächst eine Quarzglasdüse mit einer sehr kleinen Öffnung (hier 50-500 µm; Öffnungswinkel Bielefeld: 25°, ALS: 40°, Hefei: 30°) an den Ort der Probenahme gebracht. Mithilfe einer zweistufigen Expansion über einen Druckgradienten bildet sich ein sogenannter Molekularstrahl aus, was bedeutet, dass die mittlere freie Weglänge der Teilchen so stark zunimmt, dass Stöße untereinander stark reduziert werden und somit näherungsweise eine Konservierung der Speziesverteilung am Probenahmeort gewährleistet wird. Dies trifft auch auf Radikale zu, die mithilfe dieser Technik identifiziert werden können. Die Überführung aus der ersten in die zweite Druckstufe erfolgt dabei über einen Skimmer (Bielefeld: Kupfer, ALS: Nickel, Hefei: keine zweite Druckstufe) mit einer Öffnung von ca. 1-2 mm, um ausschließlich den zentralen Teil des Molekularstrahls auszuschneiden. Eine schematische Darstellung dieses Verfahrens ist in Abb. 2.5 gegeben.

Der gebildete Molekularstrahl wird anschließend mit einem Elektronen- oder Photonenstrahl gekreuzt und die Moleküle werden dadurch ionisiert. Nach der Beschleunigung in ein

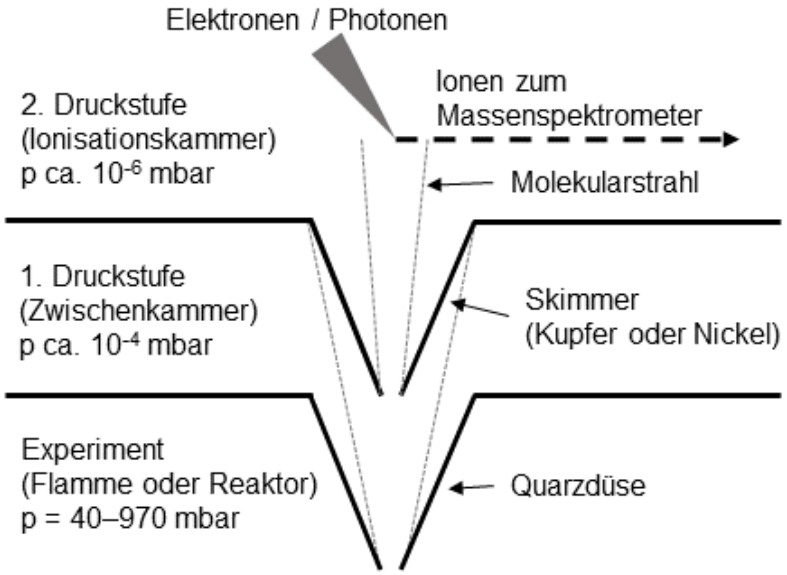

Abbildung 2.5: Schematische Darstellung des Molekularstrahl-Probenahmeverfahrens.

angrenzendes Flugzeit-Massenspektrometer und der Detektion über eine *Multichannel Plate* (MCP) kann ein Massenspektrum der Speziesverteilung am Probenahmeort erhalten werden. Zur Ionisation können unterschiedliche Techniken genutzt werden, wozu die in dieser Arbeit verwendeten Methoden der Elektronenstoßionisation (EI) und Photoionisation (PI) sowie die Photoelektronen-Photoionen Koinzidenz-Spektroskopie (PEPICO) als spezielle Form der Photoionisation gehören. Die drei Methoden werden im Folgenden kurz vorgestellt.

Elektronenstoßionisation

Bei der Elektronenstoßionisation (EI) werden Elektronen durch Anlegen eines Stroms aus einem Filament (hier Wolframdraht) erzeugt. Dies bietet den großen Vorteil einer besonders einfachen und kostengünstigen Ionisation, führt jedoch zu einer sehr breiten Energieverteilung der erzeugten Elektronen (*Full Width at Half Maximum* (FWHM) ca. 1 eV). Daraus resultiert die gleichzeitige Ionisation vieler Spezies, auch mit Ionisationsenergien oberhalb der eingestellten Elektronenenergie, wodurch keine Trennung von Isomeren erfolgen kann. In dieser Arbeit wurden EI-MBMS-Messungen an zwei Massenspektrometern in Bielefeld durchgeführt, die jeweils mit dem laminaren Strömungsreaktor und der laminaren Niederdruckflamme kombiniert sind. Beide Massenspektrometer bieten mit Massenauflösungen $\frac{m}{\Delta m}$ von ca. 2000 (Strömungsreaktor-MS) bzw. 4000 (Niederdruckflammen-MS) die Möglichkeit, nicht nur die Nominalmasse, sondern im untersuchten Massebereich von 2-120 amu auch die exakte C/H/O-Zusammensetzung einer Spezies zu bestimmen. Weitere Details zu den verwendeten EI-MBMS-Systemen können der Literatur entnommen werden [37, 38, 62, 68].

Photoionisation

Die Photoionisation (PI) bietet gegenüber der Elektronenstoßionisation den Vorteil einer extrem schmalen Energieverteilung. Daher werden nur Spezies ionisiert, deren Ionisationsenergie unterhalb der verwendeten Photonenenergie liegt, was eine Separation von Isomeren ermöglicht, sofern sich die Ionisationsenergien der Isomere ausreichend unterscheiden. Ein

wesentlicher Nachteil besteht jedoch in der aufwändigen Zugänglichkeit, da die dazu benötigten, über einen weiten Energiebereich durchstimmbaren Strahlungsquellen wie z.B. Synchrotrons als Großanlagen nur mit begrenzter Messzeit zur Verfügung stehen.
Im Rahmen dieser Arbeit konnten Messungen in einer laminaren Niederdruckflamme am PI-MBMS unter Verwendung von Synchrotronstrahlung der *Advanced Light Source* (ALS) in den *Lawrence Berkeley Laboratories* (Berkeley, Kalifornien, USA) durchgeführt werden. Das verwendete Massenspektrometer erlaubt mit einer Massenauflösung von $\frac{m}{\Delta m} > 4000$ ebenfalls eine eindeutige Bestimmung der Summenformel (C/H/O-Zusammensetzung). Die Energieauflösung der durch die Synchrotronstrahlung generierten Photonen ist mit $\Delta E = \pm 0.05$ eV angegeben. Weitere Details zum ursprünglichen Aufbau des verwendeten PI-MBMS-System können der Literatur entnommen werden [69]. Es sei jedoch darauf hingewiesen, dass nach Veröffentlichung der angegebenen Publikation durch die Integration eines Reflektrons die Massenaufllösung des Systems von damals 400 auf >4000 erhöht wurde.
Weiterhin wurden Messungen am PI-MBMS am *National Synchrotron Radiation Laboratory* (NSRL) der *University of Science and Technology of China* in Hefei, China durchgeführt. Das dort verwendete Massenspektrometer weist eine Massenauflösung von ca. 2500 auf, während die verwendete Synchrotronstrahlung eine Energieauflösung $\frac{E}{\Delta E}$ von etwa 4000 besitzt. Weitere Informationen zum Aufbau des Systems sowie der Speziesidentifizierung und Quantifizierung der erhaltenen Daten können der Literatur entnommen werden [27, 70–72].

Photoelektronen-Photoionen Koinzidenz-Spektroskopie

Für die Photoelektronen-Photoionen Koinzidenz-Spektroskopie (PEPICO) werden ebenfalls am Synchrotron generierte Photonen zur Ionisation genutzt. Bei dieser Methode werden jedoch zusätzlich zur Detektion der Ionen in Form des Massenspektrums auch die aus dem Ionisationsprozess entstehenden Elektronen in Koinzidenz detektiert, sodass die zur Ionisation benötigte Energie und daraus resultierend zusätzlich ein Photoelektronenspektrum (PES) erhalten werden kann. Damit können Isomere zusätzlich durch ihre charakteristischen Photoelektronenspektren identifiziert werden. Im Rahmen dieser Arbeit wurden Messungen in laminaren Niederdruckflammen an der *Beamline DESIRS* am *Synchrotron SOLEIL* (Gif-sur-Yvette, Frankreich) durchgeführt. Dazu wurde eine wie oben beschriebene Brennerkammer mit zweistufiger Expansion und Molekularstrahl-Probenahme an das vor Ort vorhandene *DELICIOUSIII* Spektrometer gekoppelt. Dieses bietet die Möglichkeit, detektierte Ionen und Elektronen aus einem Ionisationsprozess mithilfe einer Multi-Start/Multi-Stop-Technik miteinander in Koinzidenz zu bringen. Die Elektronen werden von einem zweidimensionalen *Velocity Map Imaging* (VMI) Spektrometer mit einer Energieauflösung von ca. 30 % in der Detektormitte (langsame Elektronen) und ca. 3-4% am Detektorrand (schnelle Elektronen) aufgenommen, was bei einer kinetischen Überschussenergie der Elektronen (eingestellte Photoelektronenenergie abzüglich der für den Ionisationsprozess benötigten Energie) im Bereich von 0-3.6 eV zu einer Energieauflösung von 30-140 meV in den daraus resultierenden Photoelektronenspektren führt. Für die hier vorgestellten Messungen wurde dabei größtenteils der sogenannte *Fixed-Photon-Energy Mode* verwendet, bei dem bei einer fest eingestellten Photonenenergie gemessen wird und durch den zweidimensionalen Detektor Elektronen unterschiedlicher kinetischer Energie anhand ihres Aufschlagortes unterschieden werden können, sodass aus einer einzelnen festfrequenten Messung ein Photoelektronenspektrum in einem Energiebereich von der eingestellten Photonenenergie bis ca. 3-4 eV darunter erhalten wird. Wird hingegen ein

sogenanntes *Threshold Photoelectron Spectrum* (TPES) aufgenommen, werden mehrere Messungen variierender Photonenenergie durchgeführt und für jede Messung jeweils die Elektronen ohne kinetische Überschussenergie (*Zero Kinetic Electrons*, ZKE) ausgewertet. Aufgrund der Abfolge mehrerer Messungen wird hierfür jedoch mehr Zeit benötigt (ca. 12 h *vs.* ca. 1 h für eine festfrequente Messung, vgl. [43]). Die Ionen werden mithilfe eines Wiley-McLaren-Flugzeit-Massenspektrometers mit einer Massenauflösung von $\frac{m}{\Delta m} < 1700$ detektiert. Durch die angekoppelte Brennerkammer und die Molekularstrahl-Probenahme wird diese jedoch auf ca. 300 reduziert. Ausführliche Informationen zur Ankopplung der Brennerkammer [1, 2, 43], der DESIRS-Beamline [73] und dem *DELICIOUSIII* Spektrometer [74, 75] können der jeweiligen Literatur entnommen werden.

2.4 Datenauswertung und Quantifizierung

Da die Auswertung und Quantifizierung der erhaltenen Daten für die verschiedenen Experimente generell einer vergleichbaren Prozedur folgt und sich für die verwendeten Experimente lediglich in wenigen Aspekten unterscheidet, wird im Folgenden zunächst die allgemeine Vorgehensweise erläutert. Im Anschluss daran werden die Besonderheiten für die einzelnen Experimente zusammengefasst.
Zur Quantifizierung der detektierten Signale im Massenspektrum wird zunächst die erhaltene Flugzeit der Ionen mithilfe einer quadratischen Anpassung von Kalibrationsmessungen in das Masse-zu-Ladungsverhältnis umgerechnet. Eine anschließende Integration über die gaußförmigen Signale liefert die zugehörige Signalintensität S_i. Diese ist jedoch nicht nur vom Molenbruch x_i der entsprechenden Spezies, sondern auch von einigen weiteren Parametern abhängig. Dieser Zusammenhang ist in Gl. 2.3 gegeben.

$$S_\mathrm{i} = x_\mathrm{i} \cdot \mathrm{c} \cdot \mathrm{D}(\mathrm{M_i}) \cdot SW \cdot \varphi \cdot \mathrm{FKT}(T) \cdot \int dE\ \sigma_\mathrm{i}(E) \cdot f(E) \tag{2.3}$$

Dabei ist c eine Gerätekonstante, $\mathrm{D}(\mathrm{M_i})$ der Massendiskriminierungsfaktor, SW (sweeps) die Anzahl der jeweils aufsummierten Spektren, φ die Zahl der Elektronen bzw. Photonen, $\mathrm{FKT}(T)$ eine temperaturabhängige Gerätefunktion, $\sigma_\mathrm{i}(E)$ der Ionisationsquerschnitt der Spezies bei der Energie E und $f(E)$ die Energieverteilung der Elektronen bzw. Photonen. Die Quantifizierung der Molenbrüche basiert anschließend auf unterschiedlichen Methoden je nach Art der Ionisation.

Auswertung der EI-MBMS-Daten

Da bei der Elektronenstoßionisation Elektronen mit einer breiten Energieverteilung erzeugt werden, wird auch das Verdünnungsgas Argon bei jeder Messung ionisiert, sodass es als Referenz zur Kalibration und Quantifizierung genutzt werden kann. Da somit jede Spezies und Argon aus derselben Messung verwendet werden, können die energieabhängigen und gerätespezifischen Faktoren in einem Kalibrationsfaktor $k_\mathrm{i/Ar}(E)$ zusammengefasst werden und Gl. 2.3 vereinfacht sich wie folgt:

$$\frac{S_\mathrm{i}}{S_\mathrm{Ar}} = \frac{x_\mathrm{i}}{x_\mathrm{Ar}} \cdot k_\mathrm{i/Ar}(E) \tag{2.4}$$

Zu den sogenannten Hauptspezies zählen alle Spezies mit einem Molenbruch von mindestens 0.01 (Brennstoff, Sauerstoff, Argon, Kohlenstoffmonoxid, Wasserstoff, Kohlenstoffdioxid

und Wasser). Für ihre Quantifizierung werden Bilanzgleichungen aufgestellt, für die angenommen wird, dass zu Beginn der Oxidation ausschließlich Brennstoff, Sauerstoff und Argon und nach vollständiger Oxidation nur noch die Produkte Kohlenstoffdioxid, Kohlenstoffmonoxid, Wasserstoff und Wasser und das Verdünnungsgas Argon vorliegen. Als zusätzliche Größe zur Lösung dieses Gleichungssystems wird das CO/CO_2-Signalverhältnis aus einer Kalibrationsmessung bestimmt. Somit können die Kalibrationsfaktoren $k_{\mathrm{i/Ar}}$ aller Hauptspezies und daraus letztendlich deren Molenbrüche für jede Spezieszusammensetzung bestimmt werden.
Zur Quantifizierung der in geringeren Mengen vorliegenden Intermediate der Oxidation werden die erhaltenen Rohsignale zunächst fragment- und isotopenkorrigiert. Anschließend wird der entsprechende Kalibrationsfaktor entweder direkt aus einer Referenzmessung der entsprechenden Spezies mit Argon oder über theoretische Abschätzungen bestimmt. Zu letzteren zählen zum Beispiel die Signalsimulation basierend auf der Faltung des Ionisationsquerschnitts mit der Energieverteilung der Elektronenenergie (*Convolution*-Methode) oder der Vergleich und die entsprechende Skalierung des Ionisationsquerschnitts mit strukturell sehr ähnlichen Spezies (*Relative Ionisation Cross Section*, *RICS*-Methode). Während der Molenbruchfehler bei den Hauptspezies auf ca. 10-15 % geschätzt wird, ist er für die Intermediate von der Art der gewählten Kalibrationsmethode abhängig. Für die direkte Kalibration liegt er in etwa bei einem Faktor von 2, während die *Convolution*- und die *RICS*-Methode je nach Verfügbarkeit und Qualität der verwendeten Ionisationsquerschnitte einen Fehler bis zu einem Faktor von 4 aufweisen können.
Eine detailliertere Beschreibung der vollständigen Quantifizierung und der unterschiedlichen Kalibrationsmethoden kann den Referenzen [37, 38] entnommen werden.

Auswertung der PI-MBMS-Daten

Aufgrund der schmalen Energieverteilung bei der Photoionisation wird Argon mit einer Ionisationsenergie von 15.763 eV [76] bei Messungen mit niedrigerer Photonenenergie nicht ionisiert und kann daher nicht als Referenz verwendet werden. Die Quantifizierung erfolgt somit nach Gl. 2.3, welche sich aufgrund der als Delta-Distribution angenäherten Energieverteilung wie folgt vereinfacht:

$$S_{\mathrm{i}} = x_{\mathrm{i}} \cdot \mathrm{c} \cdot \mathrm{D}(\mathrm{M_i}) \cdot SW \cdot \varphi \cdot \mathrm{FKT}(T) \cdot \sigma_{\mathrm{i}}(E) \tag{2.5}$$

Dabei werden die Anzahl der zur Ionisation verwendeten Photonen φ mithilfe einer kalibrierten Photodiode und die Massendiskriminierungsfaktoren $\mathrm{D}(\mathrm{M_i})$ durch Messungen von definierten Kalibrationsmischungen über einen großen Massebereich bestimmt. Das Produkt $\mathrm{c} \cdot \mathrm{FKT}(T)$ wird nach der Quantifizierung der Hauptspezies aus dem Argonmolenbruch bestimmt. Um geräteabhängige Schwankungen zwischen den Messungen bei unterschiedlichen Photonenenergien auszugleichen, werden Messungen aufeinanderfolgender Energien mithilfe eines sogenannten *Scanfaktors* korrigiert. Aus Gl. 2.5 folgt, dass ausschließlich Spezies quantifiziert werden können, für die ein Ionisitationquerschnitt $\sigma_{\mathrm{i}}(E)$ bekannt ist. Die Quantifizierung der Hauptspezies erfolgt analog der Elektronenstoßionisation über die bereits genannten Bilanzgleichungen. Im Wesentlichen unterscheidet sich die Methode dadurch, dass für jede Spezies eine Messung mit einer oberhalb der Ionisationsenergie liegenden Photonenenergie und der entsprechende Ionisationsquerschnitt der Spezies verwendet werden müssen. Dies gilt auch für die Quantifizierung der Intermediate. Der Fehler des Molenbruchs ist hier somit insbesondere von der Qualität der verwendeten Ionisations-

querschnitte abhängig und liegt ebenfalls im Bereich von einem Faktor 2-4.
Zur Quantifizierung von Isomeren können Messungen bei unterschiedlichen Photonenenergien (jeweils knapp oberhalb der Ionisationsenergie der entsprechenden Isomere) verwendet werden. Dabei wird zunächst eine Energie verwendet, bei der nur ein Isomer vorliegen kann und dieses quantifiziert. Durch Subtraktion des von diesem Isomer rührenden Signals in der Messung bei einer höheren Photonenenergie kann der Beitrag eines weiteren Isomers zum Gesamtsignal ermittelt und dieses quantifiziert werden. Um eine eindeutige Zuordnung der Isomere zu erhalten, können außerdem sogenannte Photoionisationseffizienzkurven (PIE-Kurven) aufgenommen werden, bei denen mit zunehmender Photonenenergie ein Signalanstieg gemessen wird. Durch Anpassung der bekannten Ionisationsquerschnitte an diese Signale kann eine Identifizierung und relative Quantifizierung (Isomerenverhältnis) erfolgen.

Auswertung der PEPICO-Daten

Wie bei den EI- und PI-MBMS-Messungen werden bei den PEPICO-Messungen ebenfalls Massenspektren der Spezieszusammensetzung am Probenahmeort gemessen. Darüber hinaus kann auch für jede Masse ein zweidimensionales Bild der mit diesen Ionen koinzidenten Elektronen erhalten werden. Durch eine inverse Abel-Transformation [77] kann die ursprüngliche Kugelverteilung der Elektronen berechnet und daraus ein Photoelektronenspektrum generiert werden. Felsmann *et al.* [2] konnten bereits zeigen, dass mit einem vergleichbaren Prinzip wie dem der PI-MBMS-Auswertung auch eine Quantifizierung der Spezies aus den Massenspektren erfolgen kann. In dieser Arbeit wurden jedoch keine absoluten Quantifizierungen vorgenommen, vielmehr wurden die erhaltenen Photoelektronenspektren zur Identifizierung von bis zu vier auftretenden Isomeren bei einer Masse genutzt. Durch die zusätzliche Aufnahme von Referenz-Photoelektronenspektren der reinen Komponenten kann sowohl eine Speziesidentifizierung als auch eine relative Quantifizierung (Isomerenverhältnis) durch Anpassung der Referenzspektren erfolgen. Dies ist insbesondere in Ergänzung zu bereits vorliegenden und quantifizierten EI-MBMS-Messungen hilfreich, da so der Molenbruch einer Summenformel in die Anteile der entsprechenden auftretenden Isomere zerlegt werden kann und zusätzliche Informationen gewonnen werden.

2.5 Kinetische Modellierungen

Die im Rahmen dieser Arbeit gemessenen Daten wurden jeweils mit den Ergebnissen kinetischer Modellierungen[1] verglichen. Diese wurden für die laminaren Niederdruckflammen unter Verwendung eines gemessenen Temperaturprofils mithilfe von sogenannten *Burner Stabilized Premixed Flame* Modulen geeigneter Software (LOGEsoft [78], CHEMKIN-PRO [79] und OPENSMOKE++ [80]) durchgeführt. Das Modellexperiment der laminaren Niederdruckflamme ist in diesen Modulen bereits unter Berücksichtigung von thermischer Diffusion und Mehrkomponenten-Transporteigenschaften hinterlegt und nur die Flussbedingungen der Flamme und ein gestörtes Temperaturprofil müssen als Eingabeparameter verwendet werden. Letzteres wird aus dem Druckprofil in der ersten Expansionsstufe der Molekularstrahl-Probenahme über den gesamten Flammenbereich unter Kalibration auf eine gemessene Abgastemperatur erhalten [4, 37, 81], welche mithilfe von OH-pLIF-

1 Modellierungen für die untersuchten Systeme erfolgten in Kooperation mit den jeweiligen in den Originalpublikationen genannten Partnern.

Messungen[1] (pLIF: planare laserinduzierte Fluoreszenz) bestimmt wird [82].
Da für die Simulation des laminaren Strömungsreaktors kein Modul zur Verfügung steht, das die Eingabe eines Temperaturprofils erlaubt, wurde die von Hemken *et al.* [62] vorgestellte Prozedur verwendet, in der die Zerlegung der Modellierung in die drei Zonen des Reaktors (Vorheizzone, Reaktionszone und Abkühlzone, vgl. Kap. 2.2.2) erfolgt und mithilfe eines gemessenen, dem nicht reaktiven Zustand entsprechenden Temperaturprofils von Argon (s. Abb. 2.4b) ein Wärmetransferkoeffizient vorgegeben wird. Diese Prozedur nutzt die Simulationssoftware LOGEsoft [78] und kombiniert die modellierten Temperaturprofile für die drei Reaktorzonen.

Für die Modellierungen der durchgeführten Experimente wurden jeweils brennstoffspezifische kinetische Modelle aus der Literatur verwendet (Reaktionsmechanismen, thermochemische Eigenschaften und Transporteigenschaften) oder aufbauend auf der Literatur in Kooperation mit verschiedenen Arbeitsgruppen mit neu entwickelten Submechanismen kombiniert. Die Details dazu sind in den jeweiligen Abschnitten zu den entsprechenden Experimenten angegeben.
Obwohl es sich bei den Ergebnissen der Simulationen um theoretische Berechnungen handelt, die in jedem Fall ebenso wie experimentelle Daten mit einem Fehler behaftet sind, ist es schwierig, diesen für die erhaltenen Molenbrüche zu quantifizieren. Dies stellt beim Vergleich mit experimentellen Daten immer wieder ein Problem dar, jedoch konnte bisher noch keine einheitliche Möglichkeit zur Fehlerquantifizierung solcher Modellierungen etabliert werden. Ein vielversprechender Ansatz dazu wurde bereits von Wang und Sheen [83] vorgestellt, ist jedoch noch nicht vollständig für die Verwendung in kinetischen Modellen etabliert.

1 Die Messungen der Abgastemperatur wurden von Isabelle Graf an der *Universität Bielefeld* durchgeführt.

KAPITEL 3

Identizierung von Isomeren in Flammen mittels Photoelektronen-Photoionen Koinzidenz-Spektroskopie

Die Photoelektronen-Photoionen Koinzidenz-Spektroskopie (PEPICO) bietet in der Gasphasenanalytik eine besonders wertvolle Methode der Speziesidentifizierung. Die häufig verwendeten Methoden der Elektronenstoßionisation und Photoionisation sind bei zunehmender Komplexität der untersuchten Brennstoffe und der hohen Anzahl möglicher bei ihrer Oxidation auftretender Isomere schnell an ihren Grenzen angelangt. Eine zusätzliche Möglichkeit der Zuordnung und gleichzeitige Kreuzvalidierung vorhergehender Experimente durch die für jede Spezies spezifischen Photoelektronenspektren (PES) ist daher besonders nützlich. Eine eindeutige Identifizierung von Spezies kann dabei nur unter Kenntnis der entsprechenden Referenzspektren auftretender Spezies erfolgen, die jedoch in der Literatur oft fehlen. Im Rahmen der Veröffentlichung [1] wurden laminare Niederdruckflammen, die vorher mittels EI- und PI-MBMS untersucht wurden, im Hinblick auf spezielle Probleme der Isomerentrennung untersucht. Zur Zuordnung der erwarteten Spezies wurden dazu die PES von 18 Referenzsubstanzen gemessen und von zwei nicht verfügbaren Spezies mithilfe von theoretischen Berechnungen[1] bestimmt. Im Folgenden sollen exemplarisch Teile der veröffentlichten Ergebnisse kurz zusammengefasst werden.

Messung von Referenzspektren

Zur Identifizierung der Isomere bestimmter Masse-zu-Ladungsverhältnisse, die in dieser Arbeit untersucht wurden, ist die Kenntnis der entsprechenden Photoelektronenspektren unumgänglich. Um fehlende Referenzspektren zu erhalten und darüber hinaus eine gute Vergleichbarkeit der einzelnen Komponenten mit den Ergebnissen aus Flammenmessungen zu erreichen, wurden die PES von 18 Reinsubstanzen mit dem gleichen experimentellen Aufbau wie die Flammenmessungen aufgenommen. Somit haben die Spektren der puren Substanzen die gleiche spektrale Auflösung wie die Spektren aus den Flammen und es muss keine Verschiebung der Energieskala vorgenommen werden, um die experimentellen Ungenauigkeiten anderer Systeme auszugleichen. Dieser Ansatz wurde in einem kürzlich erschienen *Review*-Artikel von Baer und Tuckett [40] als signifikanter Vorteil herausgestellt. Die gemessenen PES umfassen Spezies der Summenformeln C_5H_6, C_5H_8, C_5H_{10} und C_4H_8O und sind in Abb. 3.1 dargestellt.
Für die in Abb. 3.1a,b gezeigten Komponenten sind die gemessenen PES relativ unterschiedlich und daher in Isomerenmischungen gut unterscheidbar. Für C_5H_{10} (Abb. 3.1c)

1 Diese Berechnungen erfolgten durch Steffen Schmitt und Wolfgang Eisfeld in Kooperation mit der Arbeitsgruppe *Theoretische Chemie* der *Universität Bielefeld*.

sehen sich die Spektren von 3-Methyl-1-buten und 1-Penten jedoch sehr ähnlich und liegen zusätzlich im gleichen Energiebereich, sodass hier eine Unterscheidung der Spezies in einer Mischung schlecht möglich ist. Selbiges gilt für die Spektren der oxygenierten C_4H_8O Isomere *n*-Butanal, *iso*-Butanal, 3-Buten-2-ol, 3-Buten-1-ol und *iso*-Butenol (Abb. 3.1d), welche zudem auch kaum eine Vibrationsstruktur aufweisen.

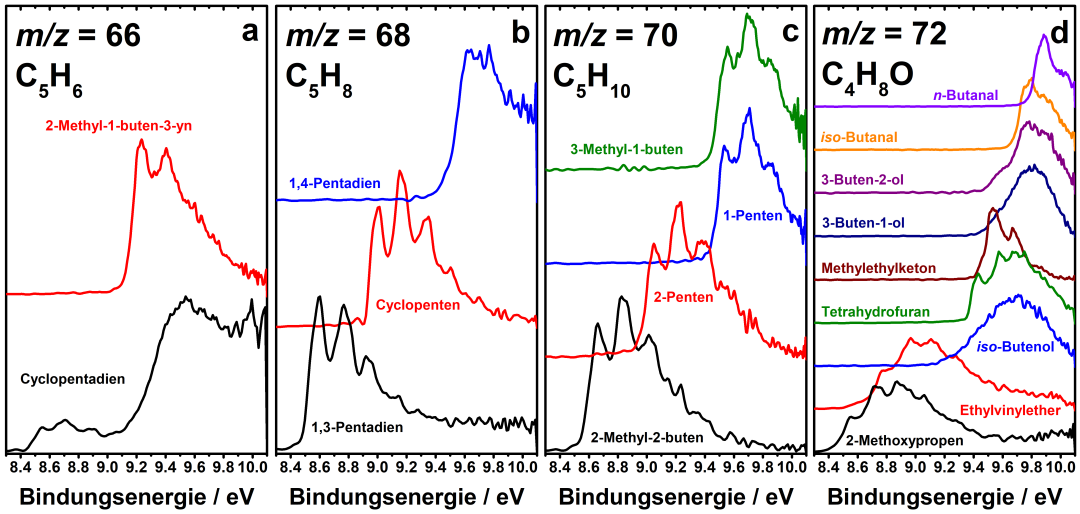

Abbildung 3.1: Gemessene Photoelektronenspektren für verschiedene molekulare Strukturen der Summenformeln (a) C_5H_6, (b) C_5H_8, (c) C_5H_{10} und (d) C_4H_8O. Alle Spektren wurden bei einer festen Photonenenergie von 10.1 eV gemessen. Zur besseren Übersicht wurden alle Spektren normiert und als Linien ohne Fehlerbalken übereinander dargestellt. Adaptiert von [1].

C_5H_{10}-Isomere in der Verbrennung von *iso*-Pentan

Eine brennstoffreiche *iso*-Pentanflamme ($\phi = 1.7$) wurde im Hinblick auf die ersten stabilen Intermediate aus dem Brennstoffabbau untersucht. Besonderes Augenmerk wurde dabei auf die Trennung der Isomere mit der Summenformel C_5H_{10} ($m/z = 70$) gelegt, da diese durch H-Abstraktion und direkt anschließende C-H-β-Spaltung aus dem Brennstoffmolekül entstehen und somit kritisch für die Modellentwicklung und -validierung sind. Durch vorhergehende Messungen der Flamme mittels EI-MBMS konnten bereits Molenbrüche für die jeweiligen Summenformeln erhalten werden, jedoch war eine Quantifizierung der Isomere nicht möglich. Die Verteilung der durch erneute Abfolge dieser Reaktionen gebildeten C_5H_8-Isomere ($m/z = 68$) wurde ebenfalls untersucht; die Ergebnisse werden hier nicht gezeigt, können aber in [1] nachgelesen werden. Gleiches gilt für die Ergebnisse vergleichbarer Messungen für eine *iso*-Pentanflamme mit einer Dimethyletherdotierung von 20 %.

In Abb. 3.2 sind die Strukturen und Ionisationsenergien einiger relevanter C_5H_{10}-Isomere zusammengefasst. Aus der bereits verzweigten Struktur des Brennstoffmoleküls *iso*-Pentan werden hauptsächlich die ebenfalls verzweigten Spezies 2-Methyl-2-buten, 2-Methyl-1-buten und 3-Methyl-1-buten erwartet. Hier ist insbesondere das Verhältnis der drei Isomere interessant. Lineare Moleküle wie 1- und 2-Penten können nicht direkt aus dem Brenn-

C_5H_{10}

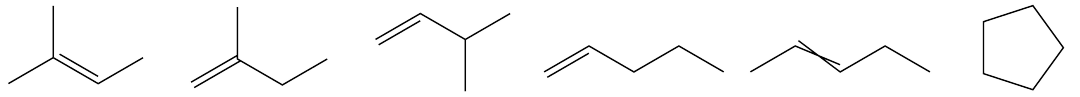

2-Methyl-2-buten IE 8.69 | 2-Methyl-1-buten IE 9.10 | 3-Methyl-1-buten IE 9.5 | 1-Penten IE 9.50 | 2-Penten IE 9.04/9.04 (*cis*/*trans*) | Cyclopentan IE 10.3

Abbildung 3.2: Strukturen und Ionisationsenergien [84–86] einiger für die Verbrennung von *iso*-Pentan relevanter C_5H_{10}-Isomere. Adaptiert von [1].

stoffabbau, sondern erst durch Rekombination kleinerer Abbauspezies entstehen, weshalb es ebenfalls interessant ist, ihre Existenz nachweisen oder ausschließen zu können. Die Bildung des zyklischen Moleküls Cyclopentan ist aufgrund seiner Ringstruktur kinetisch sowie thermodynamisch eher nicht favorisiert.

Zur Identifizierung der infrage kommenden Isomere wurde eine festfrequente Messung bei einer Photonenenergie von 10.1 eV in einer brennstoffreichen *iso*-Pentanflamme bei einer Höhe von 3.2 mm oberhalb der Brenneroberfläche (korrespondierend zum Maximum des Molenbruchs für C_5H_{10} aus den vorangegangenen EI-MBMS-Messungen) durchgeführt. In Abb. 3.3a ist das invertierte 2D-Elektronenbild für $m/z = 70$ dargestellt, woraus mithilfe der zuvor beschriebenen Auswerteroutine das zugehörige PES (Abb. 3.3b) erhalten wird. Zur Identifizierung der vorliegenden Isomere wurden ebenfalls die PES der erwarteten Spezies (2-Methyl-2-buten, 3-Methyl-1-buten, 1-Penten, 2-Penten) als Referenzsubstanzen gemessen (s. Abb. 3.1c). Das PES von 2-Methyl-1-buten wurde im Rahmen der Publikation [1] von Steffen Schmitt und Wolfgang Eisfeld mithilfe von Franck-Condon-Simulationen berechnet (vgl. Abb. 3.3c). Aufgrund von zuvor durchgeführten Simulationen mit dem kinetischen Modell für Pentane von Bugler *et al.* [87] und Gaschromatographie-Messungen (s. Supplementary Material 1 zu [1]) konnte die Präsenz von 1-Penten ausgeschlossen werden. Weiterhin kann aufgrund der Messung bei einer Photonenenergie von 10.1 eV kein Cyclopentan (IE 10.3 eV) detektiert werden. Deshalb wurden zur Anpassung der Referenzspektren ausschließlich die drei Methylbutene und 2-Penten berücksichtigt (vgl. Abb. 3.3c). Mithilfe einer Subtraktionsmethode [1, 2] konnten die Referenzspektren gewichtet und somit ihr Anteil am gesamten PES bestimmt werden. Die einzeln gewichteten Referenzspektren und das daraus resultierende Gesamtspektrum sind in Abb. 3.3d dargestellt. Mithilfe des zuvor aus EI-MBMS-Messungen bekannten Molenbruchs von C_5H_{10} konnten die Anteile somit in zugehörige Molenbrüche umgewandelt werden. Die Ergebnisse der Experimente und Simulation sind in Tab. 3.1 zusammengefasst. Als Hauptisomer kann 2-Methyl-1-buten mit einer guten Übereinstimmung zwischen Experiment (38.8 %) und Simulation (34.4 %) bestimmt werden. Die beiden weiteren Methylbutene wurden mit ca. 18-24 % im Experiment zu ähnlichen Teilen, aber mit größerer Abweichung zur Simulation (ca. 28-33 %) erhalten. Die Messung bestätigt ebenfalls die Präsenz von 2-Penten (18.5 %), allerdings mit einer noch größeren Abweichung zur Simulation (3.8 %), was auf Ungenauigkeiten bei der verwendeten Subtraktionsmethode sowie die starke Überlappung der PES von 2-Penten und 2-Methyl-1-buten zurückzuführen sein kann. Letztendlich sind aber auch die Ergebnisse der Modellierung nicht fehlerfrei und stark von den im Modell enthaltenen Reaktionen und Reaktionsraten abhängig, sodass hier auch Unterschiede zum Experiment auf Probleme im Modell hinweisen können.

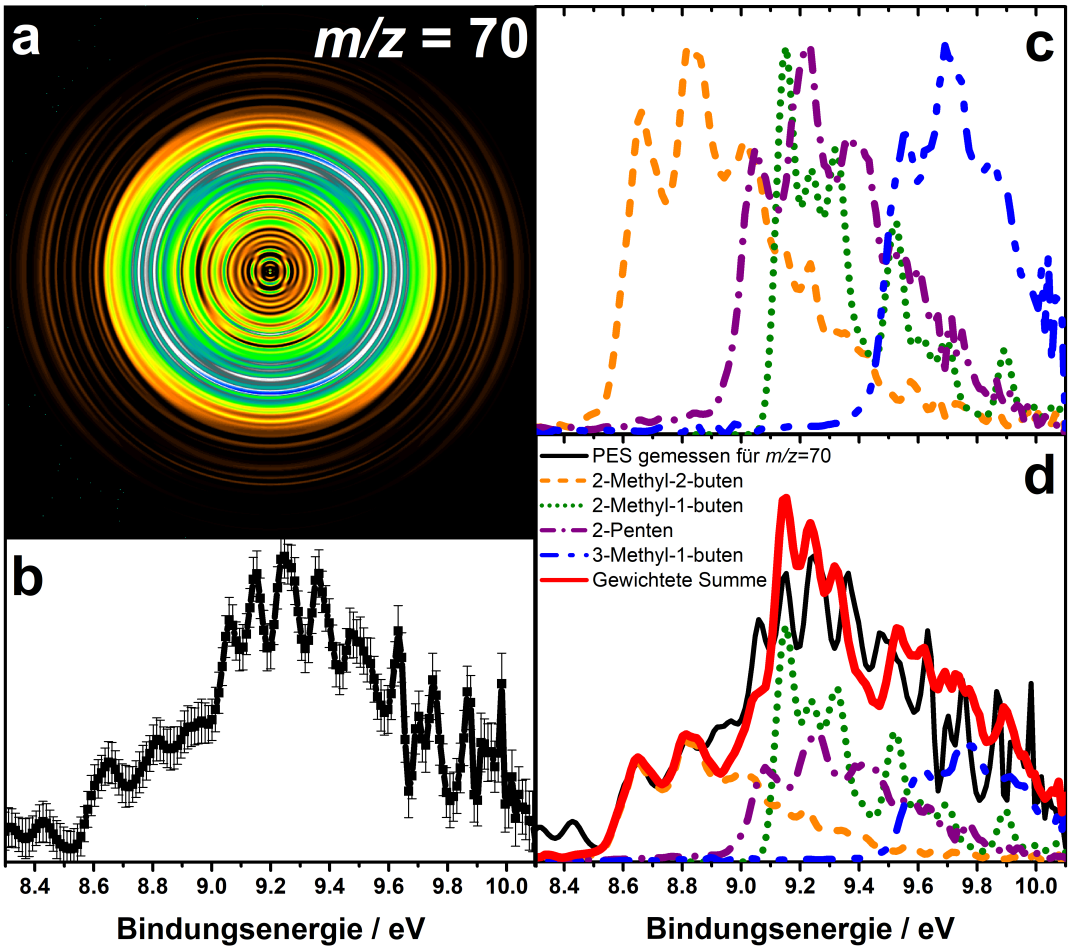

Abbildung 3.3: (a) Invertiertes 2D-Elektronenbild korrespondierend zu Ionen mit $m/z = 70$. (b) PES für $m/z = 70$ gemessen in einer brennstoffreichen *iso*-Pentanflamme mit einer Photonenenergie von 10.1 eV bei einer Höhe von 3.2 mm oberhalb der Brenneroberfläche. (c) Normierte Referenzspektren von 2-Methyl-2-buten, 3-Methyl-1-buten und 2-Penten (gemessen bei 10.1 eV) und 2-Methyl-1-buten (Franck-Condon-Simulation von Steffen Schmitt und Wolfgang Eisfeld, Geometrie-Optimierung auf CCSD(T)-F12a/aug-cc-pVDZ-Basis und Frequenzrechnung auf MP2/cc-pVDZ-Basis). (d) Vergleich des gemessenen PES mit der gewichteten Summe aller betrachteten Referenzspektren. Adaptiert von [1].

Tabelle 3.1: Anteile C (in %) und Molenbrüche x bei einer Höhe über der Brenneroberfläche von 3.2 mm in einer brennstoffreichen *iso*-Pentanflamme aus dem Experiment und der Simulation. n.q.: nicht quantifiziert. Die Referenzen der verwendeten Photoionisationsquerschnitte sind jeweils mit dem Speziesnamen gegeben (für 2-Penten wurde der Mittelwert des *cis*- und *trans*-Isomers verwendet).

	Experiment		**Simulation**	
Spezies	C	x	C	x
2-Methyl-2-buten [88]	18.6	$1.5 \cdot 10^{-4}$	32.8	$3.3 \cdot 10^{-4}$
2-Methyl-1-buten [88]	38.8	$3.0 \cdot 10^{-4}$	34.4	$3.4 \cdot 10^{-4}$
3-Methyl-1-buten [88]	24.1	$1.9 \cdot 10^{-4}$	28.5	$2.8 \cdot 10^{-4}$
2-Penten [89]	18.5	$1.4 \cdot 10^{-4}$	3.8	$3.8 \cdot 10^{-5}$
1-Penten [90]	n.q.	-	0.5	$4.5 \cdot 10^{-6}$
Summe C_5H_{10}	100	$7.8 \cdot 10^{-4}$	100	$9.9 \cdot 10^{-4}$

Identifizierung von Ethylvinylether in einer brennstoffreichen Diethylether-Flamme

In einer vorherigen Untersuchung von Tran *et al.* [3] wurde bereits eine brennstoffreiche Diethyletherflamme mithilfe von EI- und PI-MBMS-Experimenten untersucht. Aufgrund der hohen Massenauflösung der verwendeten Spektrometer konnte dabei eindeutig das C_4H_8O-Signal von dem der gleichen Nominalmasse entsprechenden C_5H_{12}-Signal separiert und auf einen Molenbruch von ca. $1.0 \cdot 10^{-5}$ quantifiziert werden. Aus der Messung einer Photoionisationseffizienzkurve (PIE-Kurve) konnte zudem ein deutlicher Anstieg im Bereich der von Ethylvinylether liegenden Ionisationsenergie (8.98 eV [91]) vermerkt werden. Aufgrund dieser Messungen wurde Ethylvinylether in den Diethylether-Submechanismus des kinetischen Modells integriert. Eine eindeutige Identifizierung dieser Spezies wäre darüber hinaus jedoch wünschenswert.

Im Rahmen dieser Arbeit wurden daher die Photoelektronenspektren von neun Referenzsubstanzen der Summenformel C_4H_8O mithilfe von festfrequenten PEPICO-Messungen aufgenommen (vgl. Abb. 3.1d). Darüber hinaus wurde in der brennstoffreichen Diethyletherflamme identischer Bedingungen ein *Threshold Photoelectron Spectrum* (TPES, vgl. Kap. 2.3) bei einer Höhe von 2.3 mm aufgenommen, da dort in den vorangegangenen Messungen die höchste Konzentration an C_4H_8O gemessen wurde. Dabei wurde nicht bei einer fest eingestellten Energie gemessen, sondern die Energie in einem Bereich von 8.35-9.35 eV variiert. Dadurch konnte eine erhöhte Energieauflösung von etwa 10 meV im Vergleich zu den festfrequenten Messungen (30-70 meV im untersuchten kinetischen Überschussenergiebereich von 0-1.75 eV) erzielt werden, was in diesem Fall aufgrund der nahe beieinanderliegenden PES der Referenzsubstanzen eine übersichtlichere Trennung ermöglichen sollte. Das gemessene TPES ist in Abb. 3.4a zusammen mit den PES der Referenzsubstanzen 2-Methoxypropen, Ethylvinylether und *iso*-Butenol dargestellt. Die weiteren gemessenen Referenzspektren liegen außerhalb des hier untersuchten Energiebereichs und tragen daher nicht zum gemessenen Signal im TPES bei. Der erste leichte Anstieg des TPES bei ca. 8.55 eV und die bei 8.70 eV stärker steigende Tendenz stimmt sehr gut mit dem Verlauf des PES von Ethylvinylether überein, während die Präsenz von

2-Methoxypropen durch einen fehlenden Anstieg bei 8.40 eV ausgeschlossen werden kann. Beiträge von *iso*-Butenol können nicht explizit ausgeschlossen werden, sind im Rahmen dieser Messung aber auch nicht quantifizierbar. Dazu, und auch zum Nachweis oder Ausschluss weiterer Isomere der Summenformel C_4H_8O mit jeweils höherer Ionisationsenergie, müssten zusätzliche Messungen bei höheren Photonenenergien durchgeführt werden. Dies gestaltet sich jedoch schwierig, da ab einer Energie von 9.51 eV [92] auch das Brennstoffmolekül Diethylether ionisiert wird und aufgrund seiner hohen Konzentration im Massenspektrum zu einem Überlappen der Signale der Masse-zu-Ladungsverhältnisse von 72 (C_4H_8O) und 74 ($C_4H_{10}O$, Diethylether) führen würde. Es sei jedoch darauf hingewiesen, dass weitere Strukturen mit C_4H_8O nicht direkt aus dem Brennstoffabbau gebildet werden können, sondern zunächst aus kleineren Abbauprodukten über Rekombinationsreaktionen entstehen müssen. Dies findet meist jedoch nur in sehr kleinen (schwer nachweisbaren) Mengen statt, weshalb die bevorzugte Bildung von Ethylvinylether naheliegt.

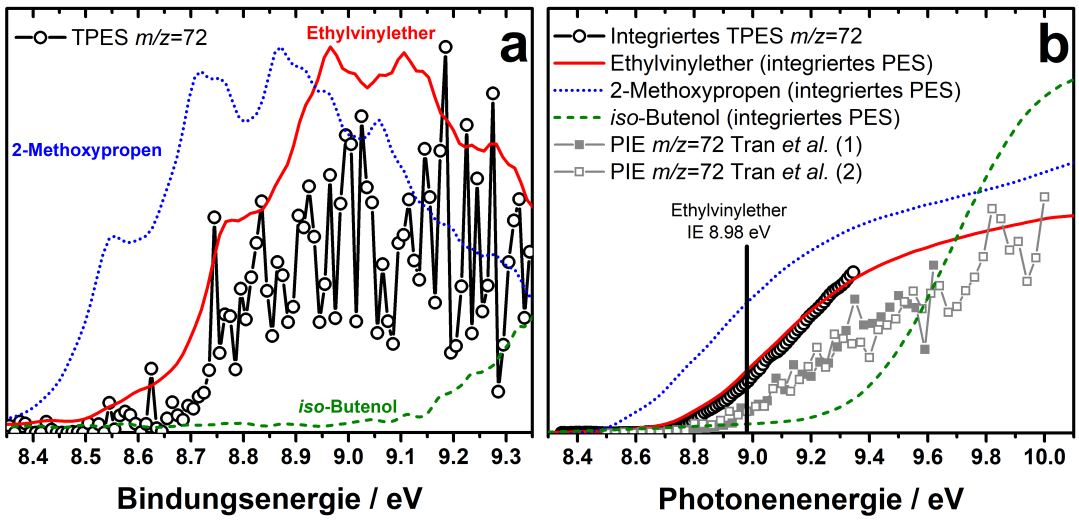

Abbildung 3.4: (a) Gemessenes TPES im Bereich von 8.35-9.35 eV (ΔE = 10 meV) für m/z = 72 bei einer Höhe von 2.3 mm in einer brennstoffreichen Diethyletherflamme zusammen mit den PES von 2-Methoxypropen, Ethylvinylether und *iso*-Butenol, gemessen bei einer festen Photonenenergie von 10.1 eV. (b) Integriertes TPES und integrierte PES aus (a) zusammen mit den PIE-Kurven identischer Flammenmessungen von Tran *et al.* [3], zweifache Messung (1,2). Zum Vergleich ist die tabellierte Ionisationsenergie von Ethylvinylether als vertikale Linie eingezeichnet [91]. Adaptiert von [1].

Da das TPES in Abb. 3.4a aufgrund einer geringen C_4H_8O-Konzentration und knapper Messzeit nur ein geringes Signal-zu-Rausch-Verhältnis aufweist, wurde mittels Integration die entsprechende PIE-Kurve bestimmt. Diese ist für das in der Flamme gemessene TPES und die PES der Referenzsubstanzen in Abb. 3.4b zusammen mit den PIE-Kurven aus den vorherigen PI-MBMS-Messungen von Tran *et al.* [3] dargestellt. Es kann eine exzellente Übereinstimmung zwischen dem integrierten TPES und dem intergrierten PES von Ethylvinylether mit einem Anstieg bei ca. 8.75 eV festgestellt werden. Die besonders hohe Qualität des integrierten TPES aus dem geringen Signal-zu-Rausch-Verhältnis unterstreicht erneut den Vorteil der PEPICO-Technik, auch in kurzer Messzeit qualitativ hochwertige Daten zu erhalten. Beim Vergleich mit den PIE-Kurven von Tran *et al.* [3] kann eine Verschiebung

von ca. 0.1 eV festgestellt werden. Dies spricht insbesondere dafür, Referenzspektren zur eindeutigen Identifizierung immer zusammen mit den eigentlichen Messungen wie in dieser Arbeit am selben experimentellen Aufbau durchzuführen. Trotz des minimalen Versatzes kann jedoch für jede Methode an sich eine hohe Reproduzierbarkeit erreicht werden. Insgesamt konnte mit diesen Ergebnissen eindeutig Ethylvinylether als Hauptisomer der Summenformel C_4H_8O in der Verbrennung von Diethylether identifiziert werden.

Zusammenfassung

Mithilfe der in diesem Abschnitt vorgestellten Ergebnisse aus [1] konnte die enorme Fähigkeit der Photoelektronen-Photoionen Koinzidenz-Spektroskopie als wertvolle Methode zur Trennung spezifischer komplexer Isomerensituationen in der Gasphasenanalytik von Brennstoffen mit fünf schweren Atomen gezeigt werden. Der Ansatz der eindeutig unterscheidbaren individuellen Photoelektronenspektren wurde in [1] auf laminare Niederdruckflammen der Brennstoffe Cyclopenten, Diethylether und *iso*-Pentan (pur und mit Dimethylether dotiert) für spezielle, nicht mit anderen Methoden zugängliche Informationen einzelner Massen angewendet. Dazu wurden in [1] zur Identifizierung einzelner Spezies die Referenzspektren von 18 Strukturen der Summenformeln C_5H_6, C_5H_8, C_5H_{10} und C_4H_8O am gleichen experimentellen Aufbau unter identischen Messbedingungen aufgenommen, sowie von zwei Molekülen mittels Franck-Condon-Simulationen berechnet. Einige wichtige Beispiele aus [1] wurden in dieser Arbeit vorgestellt.

Bei der Untersuchung des Brennstoffes *iso*-Pentan konnten die Anteile der bei einem Masse-zu-Ladungsverhältnis von $m/z = 70$ (C_5H_{10}) und $m/z = 68$ (C_5H_8) auftretenden Isomere quantifiziert und mithilfe vorangegangener Messungen mittels Elektronenstoßionisation auch die entsprechenden Molenbrüche bestimmt werden. Für C_5H_{10} konnte eine bevorzugte Bildung verzweigter Strukturen (Methylbutene) festgestellt werden, was mit der verzweigten Struktur des Brennstoffmoleküls in Einklang steht. Jedoch wurde auch ein Beitrag des linearen Isomers 2-Penten eindeutig identifiziert. Während das kinetische Modell nur geringfügige Mengen an 2-Penten und die Methylbutene in vergleichbaren Anteilen vorhergesagt hat, konnten in der Messung ein höherer Anteil an 2-Penten gemessen werden und 2-Methyl-1-buten eindeutig als Hauptisomer identifiziert werden. Für C_5H_8 wurde, wie aus der ebenfalls verzweigten Struktur erwartet, Isopren als dominantes Isomer gefunden, jedoch wurden auch Beiträge von Cyclopenten und Pentadienen quantifiziert. Einige dieser Spezies waren zuvor nicht im kinetischen Modell enthalten und sollten daher auf der experimentellen Grundlage dieser Ergebnisse in Zukunft im verwendeten Reaktionsmechanismus berücksichtigt werden. Insgesamt konnten die Ergebnisse somit einen wertvollen Beitrag für die Optimierung des Modells liefern. Zusätzliche Messungen des Brennstoffes *iso*-Pentan mit einer Dotierung von 20 % Dimethylether als oxygeniertem Brennstoff mit stark unterschiedlichen Verbrennungseigenschaften konnten zeigen, dass die Zugabe von geringen Mengen unter den analysierten Bedingungen von hoher Temperatur und niedrigem Druck kaum Einfluss auf die ersten brennstoffspezifischen Abbauwege des *iso*-Pentans haben. In einem niedrigeren Temperaturbereich wird jedoch für beide Brennstoffe eine frühe peroxidbildende Oxidation erwartet, dessen Auswirkung im Mischungsfall besonders interessant ausfallen könnte.

In der Verbrennung von Diethylether konnte mithilfe der hier vorgestellten Messungen und Ergebnisse die dominante Bildung von Ethylvinylether eindeutig beobachtet werden. Mithilfe eines präzise aufgenommenen Photoelektronenspektrums und entsprechenden Referenzspektren vieler möglicher Strukturen konnte die Bildung anderer Isomere weitestgehend ausgeschlossen und vorherige Messungen mittels Elektronenstoßionisation und Photoionisation bestätigt und um eindeutig identifizierende Photoelektronenspektren ergänzt werden. Die eindeutige Identifizierung von Ethylvinylether ist für einen neu entwickelten Submechanismus von Diethylether besonders für die kinetische Modellierung interessant, da diese Spezies zuvor nicht in bereits existierenden Modellen enthalten war.

Abschließend lässt sich festhalten, dass insgesamt mehrere experimentelle Methoden mit entsprechenden Referenzmessungen zusammen mit theoretischen Berechnungen und kinetischen Modellierungen nur in Kombination Aufschluss über komplexe Probleme in der Verbrennungsanalytik bieten. Die Photoelektronen-Photoionen Koinzidenz-Spektroskopie konnte dabei als wertvoller Baustein zur spezifischen Isomerentrennung für die Weiterentwicklung und Validierung kinetischer Modelle zur Vorhersage von Verbrennungseigenschaften unterschiedlichster Brennstoffe genutzt und vorgestellt werden.

KAPITEL 4

Einfluss der Addition von Biokraftstoffen auf die Flammenstruktur und Schadstoffbildung in vorgemischten Niederdruckflammen

Während der Energiebedarf insbesondere im Transportsektor stark ansteigt, ist gleichzeitig eine Strategie zur Reduktion von Treibhausgasen notwendig, weshalb sich die Verbrennungsforschung zunehmend in die Richtung von erneuerbaren Kraftstoffen wie Alkoholen, Ethern und Estern orientiert [23, 35, 44]. Die Addition oxygenierter Biokraftstoffe zu erdölbasierten Kraftstoffen konnte bereits als vielversprechender Ansatz zur Reduktion von Rußemissionen charakterisiert werden [45, 93, 94]. Sowohl *n*-Butanol [95–97] als auch sein Isomer Diethylether [98–100] (beide $C_4H_{10}O$) wurden aufgrund ihrer positiven physikochemischen Eigenschaften im Hinblick auf die motorische Verbrennung sowie die Möglichkeit der Produktion aus Fermentationsprozessen bzw. Bioethanol bereits als mögliche Alternativen zu herkömmlichen Kraftstoffen diskutiert. Daher wurden in dieser Arbeit die Auswirkungen der Addition von *n*-Butanol und Diethylether auf die Verbrennung eines einfachen Kohlenwasserstoffes im Hinblick auf die Schadstoffbildung untersucht. Als möglichst einfaches Untersuchungsobjekt wurde dazu eine bereits gut bekannte vorgemischte Niederdruckflamme des Brennstoffes *n*-Butan herangezogen. Diese Untersuchungen, die auf ersten orientierenden Vorarbeiten aus meiner Masterarbeit [101] aufbauen und in den Publikationen [3] und [4] veröffentlicht sind, werden im Folgenden kurz zusammengefasst.

Flammenmessungen

Brennstoffreiche vorgemischte laminare Niederdruckflammen der Brennstoffe *n*-Butan (Bu), *n*-Butanol (BuOH) und Diethylether (DEE), sowie 50:50-Mischungen von *n*-Butan mit *n*-Butanol oder Diethylether, wurden unter identischen Bedingungen (Druck 40 mbar, Argonverdünnung 25 %, Kaltgasgeschwindigkeit 73 cm/s bei 333 K und 40 mbar, C/O-Verhältnis 0.52) mittels Molekularstrahl-Massenspektrometrie (MBMS) unter Verwendung von Elektronenstoßionisation (EI) untersucht. Darüber hinaus wurden für alle fünf Flammen einige stabile Isomere mithilfe eines an das System gekoppelten Gaschromatographen (GC-MS) getrennt. Die reine DEE-Flamme sowie die Bu/DEE Mischung wurden von Luc-Sy Tran zusätzlich mittels PI-MBMS am *National Synchrotron Radiation Laboratory* der *University of Science and Technology of China* in Hefei, China untersucht. Der Übersicht halber sind alle Flammen in Tab. 4.1 zusammengefasst.

Tabelle 4.1: Flammenbedingungen der untersuchten laminaren Niederdruckflammen. slm: Standard Liter pro Minute (bei 273.15 K und 1 atm), ṁ: Massefluss bei Einlass. * Leicht andere Bedingungen mit einem Argonfluss von 1.00 slm wurden im PI-MBMS-Experiment verwendet.

Flamme (Abkürzung)	Gasflussrate (slm)					ṁ	Verhältnis		ϕ
	Ar	O_2	DEE	*n*-Butanol	*n*-Butan	(g/cm^2/s)	C/H	C/O	
n-Butan (Bu)	1.14	2.71			0.71	0.004013	0.40	0.52	1.70
n-Butan/DEE (Bu/DEE)*	1.14	2.67	0.37		0.37	0.004174	0.40	0.52	1.75
	1.00	2.35	0.33		0.33	0.004174	0.40	0.52	1.75
DEE (DEE)*	1.14	2.63	0.79			0.004355	0.40	0.52	1.80
	1.00	2.31	0.70			0.004355	0.40	0.52	1.80
n-Butan/*n*-Butanol (Bu/BuOH)	1.14	2.67		0.37	0.37	0.004174	0.40	0.52	1.75
n-Butanol (BuOH)	1.14	2.63		0.79		0.004355	0.40	0.52	1.80

Kinetische Modellierung

In der Publikation [3] wurde zunächst nur auf Basis der Daten der DEE-Flamme in Zusammenarbeit mit dem *Laboratory for Chemical Technology* der *Ghent University*, Belgien ein neuer Submechanismus für die kinetische Modellierung des Brennstoffes DEE entwickelt. Dabei wurden im Vergleich zu einem vorherigen DEE-Mechanismus [102] zusätzliche Reaktionen der direkt aus dem Brennstoff entstehenden Radikale berücksichtigt, sowie neue Ratenkonstanten für die primären Reaktionen unter Verwendung genauerer theoretischer Berechnungen auf *CBS-QB3*-Basis bestimmt. Das optimierte DEE-Modell wurde mithilfe der gemessenen Flammendaten sowie Messungen von laminaren Flammengeschwindigkeiten unter hohem Druck validiert und konnte die gemessenen Daten gut wiedergeben.
Das entwickelte und validierte DEE-Modell konnte anschließend in der Publikation [4] genutzt werden, um ein kombiniertes Modell für die Beschreibung aller drei untersuchten Brennstoffe und deren Mischungen zu erstellen. Dazu wurde zunächst die Reaktionsdatenbank des *Combustion Chemistry Center* der *National University of Ireland Galway* (NUIG) [103, 104] als Basismodell verwendet. Hierarchisch gewachsen, baut diese auf den AramcoMech 1.3 [105] auf und beinhaltet bereits einen Großteil der in der Verbrennung relevanten Reaktionen und Spezies im Bereich von C_0 bis C_6, unter anderem auch die brennstoffspezifischen Reaktionen für *n*-Butan. Um auch die potentiellen Rußvorläufermoleküle Toluol und Ethylbenzol vorhersagen zu können, wurden die brennstoffspezifischen Reaktionen dieser Spezies zur Konsistenz ebenfalls von dieser Gruppe übernommen [106]. Einen Submechanismus für *n*-Butanol und Diethylether gibt es dort bisher jedoch nicht, weshalb diese von Sarathy *et al.* [107] für *n*-Butanol und, wie oben beschrieben, von Tran *et al.* [3] für Diethylether verwendet wurden. Dabei wurde auf interne Konsistenz der Ratenkonstanten, Thermo- und Transporteigenschaften von Spezies aus mehreren dieser Mechanismen geachtet und diese, wann immer möglich, aus dem Basismodell verwendet. Alle verwendeten Reaktionsmechanismen sind bereits zuvor durch zahlreiche Experimente über ein weites Parameterfeld validiert worden.

Brennstoffabbau und primäre Zerfallsprodukte

Um einen genaueren Überblick über die Abbauwege der verschiedenen Brennstoffe zu erhalten und mögliche Gemeinsamkeiten und Unterschiede zu ermitteln, wurden sogenannte *Rate of Production Analyses* (ROP) für alle analysierten Brennstoffe bei einer Höhe über der Brenneroberfläche von 2.1-2.2 mm (korrespondierend zu einer Temperatur von 1100 K und einem Brennstoffumsatz von 78 %) durchgeführt. Diese sind in Kombination für alle

drei Brennstoffe in Abb. 4.1 dargestellt. Um Gemeinsamkeiten besonders herauszuarbeiten, wurden die auftretenden Spezies mit verschiedenen Boxen umrahmt; primäre Abbauspezies, die von allen drei Brennstoffen gebildet werden, sind mit einer dreifachen Linie (rot) umrandet, während Spezies, die aus dem Basisbrennstoff *n*-Butan und einem der oxygenierten Brennstoffe gebildet werden, mit einer zweifachen Linie (grün) und Spezies, die nur aus einem Brennstoff entstehen, mit nur noch einer Linie (blau) umrahmt sind. Zusätzlich wurden die C-H-Bindungsenergien für alle drei Brennstoffe aus den thermodynamischen Daten des kinetischen Modells berechnet und sind jeweils unterhalb des Brennstoffmoleküls angegeben.

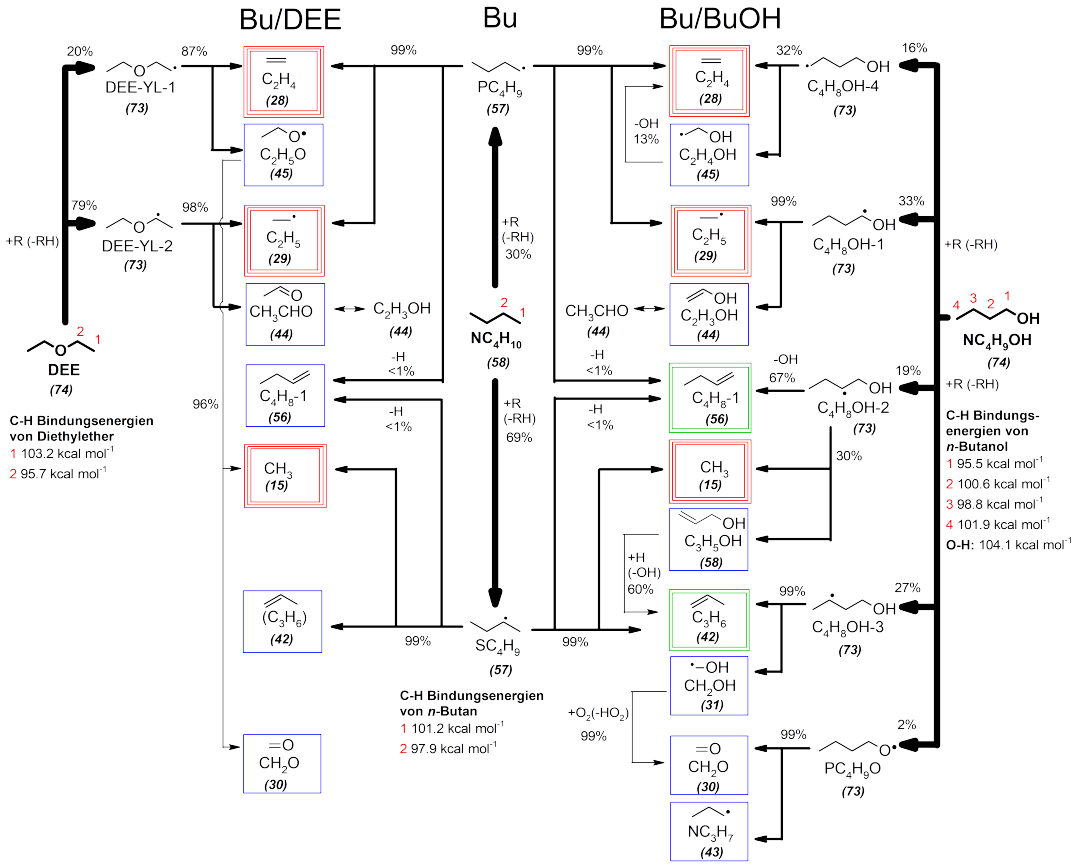

Abbildung 4.1: *Rate of Production Analyses* (ROP) für den Brennstoffabbau von *n*-Butan (NC_4H_{10}, Bu), Diethylether (DEE) und *n*-Butanol (NC_4H_9OH, BuOH) für eine Höhe über der Brenneroberfläche von 2.1-2.2 mm, korrespondierend zu einer Flammentemperatur von 1100 K und einem Brennstoffumsatz von 78 %. Die prozentualen Angaben sind relative Verbrauchsraten der entsprechenden Spezies. Die Intensität der Pfeile charakterisiert spezifische Reaktionsschritte (dick: H-Abstraktion vom Brennstoffmolekül, mittel: β-Spaltung der Brennstoffradikale, dünn: andere Reaktionen primärer Spezies). Isomerisierungen der Brennstoffradikale treten auf, sind jedoch der Übersicht halber nicht eingezeichnet. Dargestellte Bindungsenergien der Brennstoffmoleküle wurden mithilfe der thermodynamischen Daten aus dem in [4] verwendeten kombinierten Modell berechnet. Adaptiert von [4].

Aus der ROP in Abb. 4.1 kann entnommen werden, dass für alle drei Brennstoffmoleküle mindestens 97 % des initialen Brennstoffabbaus nur durch H-Abstraktion erfolgen. Für

die symmetrischen Moleküle *n*-Butan und DEE findet diese bevorzugt am C2 statt und weniger am C1, was entsprechend konsistent mit der niedrigeren C-H-Bindungsenergie am C2 ist. Beim unsymmetrischen *n*-Butanolmolekül kann die H-Abstraktion zu fünf Brennstoffradikalen führen, wobei die Abstraktion am C1 aufgrund der niedrigsten C-H-Bindungsenergie bevorzugt wird. Die sich in der Hochtemperaturkinetik üblicherweise an die H-Abstraktion anschließende β-Spaltung liefert für *n*-Butan ausschließlich Kohlenwasserstoffe, hauptsächlich Spezies mit drei Kohlenstoffatomen (C_3), aber auch C_1- und C_2-Spezies. C_4-Spezies, wie 1- und 2-Buten werden ebenfalls gebildet, jedoch zu weniger als 1 %. Wird nun DEE zu *n*-Butan addiert, wird der Speziespool durch zusätzliche Kohlenwasserstoffe, aber auch oxygenierte Spezies erweitert. Dies umfasst vor allem C_2- aber auch C_1-Spezies, die größtenteils aus dem Abbau von DEE entstehen. Erwartet wird somit eine Reduktion der C_3-Spezies bei einer gleichzeitigen Erhöhung der C_1- und C_2-Spezies. Wird hingegen *n*-Butanol zu *n*-Butan addiert, wird der Speziespool zwar auch durch Kohlenwasserstoffe und oxygenierte Spezies erweitert, jedoch im Gegensatz zu DEE nicht nur durch C_1- und C_2-Spezies, sondern vorrangig durch C_3- und C_4-Spezies. Um diese theoretischen Überlegungen experimentell zu bestätigen, werden in Abb. 4.2 die Molenbruchprofile einiger wichtiger erster auftretender Intermediate aus dem Diagramm in Abb. 4.1 für die verschiedenen untersuchten Flammen verglichen.

In Abb. 4.2a-c wird zunächst Ethen als Vertreter aus allen drei Brennstoffen verglichen. Dabei fällt auf, dass die Bildung von C_2H_4 für die Mischungen im Wesentlichen kaum von der Zugabe der oxygenierten Brennstoffe beeinflusst wird. Alle fünf Flammen sowohl der drei reinen Brennstoffe als auch der beiden Mischungen weisen vergleichbare Molenbrüche an Ethen auf. Dies liegt zum einen daran, dass es aus allen Brennstoffen auf direktem Weg gebildet werden kann, zum anderen aber auch für alle Brennstoffe als sekundäres Produkt aus dem weiteren Zerfall auftretender größerer Intermediate entsteht. Ähnliche Beobachtungen konnten auch für weitere kleine Spezies, die hier nicht gezeigt sind, gemacht werden. Zusätzlich kann festgehalten werden, dass für die DEE-Flamme und die Bu/DEE-Flamme eine sehr gute Übereinstimmung der Daten aus dem EI- und dem PI-Experiment zu beobachten ist, was für eine gute Kreuzvalidierung beider Experimente spricht.

Beispiele für Spezies, die sowohl aus dem Basisbrennstoff *n*-Butan und einem oxygenierten Brennstoff gebildet werden können, sind mit Propen (C_3H_6, Abb. 4.2d-f) und Buten (C_4H_8, Abb. 4.2g-i) gegeben. Beide Spezies weisen im Experiment für die Zugabe von *n*-Butanol entgegengesetzte Trends auf, welche auch vom kinetischen Modell sehr gut wiedergegeben werden. C_3H_6 bildet einen großen Anteil am Abbau von *n*-Butan, während der entsprechende Weg auf der Seite von *n*-Butanol nur einen kleineren Anteil ausmacht. Im Gegensatz dazu wird C_4H_8 nur in sehr geringen Mengen aus *n*-Butan erhalten, während der Weg aus *n*-Butanol deutlicher stärker ausgeprägt ist. Dadurch können die gegensätzlichen Trends im Experiment erklärt werden. Wird hingegen DEE zu *n*-Butan addiert, welches weder C_3H_6 noch C_4H_8 durch direkten Brennstoffabbau bilden kann, sinken die experimentell bestimmten Molenbrüche beider Spezies stark. Dies stimmt auch mit den Modellierungen überein.

Eine weitere interessante Spezies ist C_2H_4O (Abb. 4.2j-l), obwohl es keine Überlappung aus dem Zerfall der oxygenierten Brennstoffe mit dem Basisbrennstoff *n*-Butan gibt. Jedoch wird aus DEE das C_2H_4O-Isomer Acetaldehyd gebildet, während aus *n*-Butanol Vinylalko-

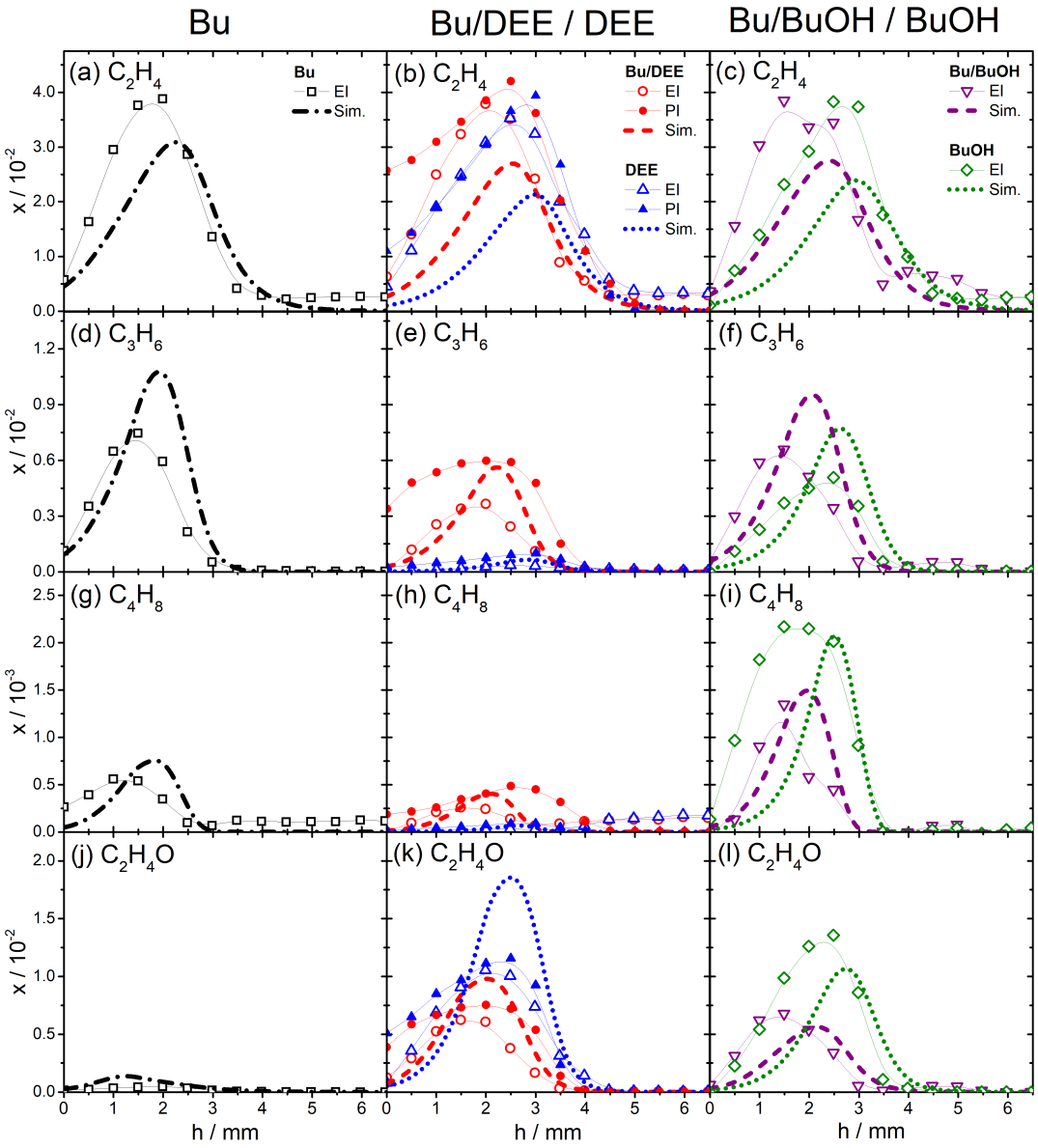

Abbildung 4.2: Molenbruchprofile ausgewählter Intermediate aus den ersten Stufen des Brennstoffabbaus. Links: *n*-Butanflamme, Mitte: *n*-Butan/Diethylether- und Diethyletherflamme, Rechts: *n*-Butan/*n*-Butanol- und *n*-Butanolflamme. Unausgefüllte Symbole: EI-MBMS-Experiment Bielefeld, Ausgefüllte Symbole: PI-MBMS-Experiment Hefei (nur für *n*-Butan/Diethylether- und Diethyletherflamme), Dicke Linien: Ergebnisse der kinetischen Modellierung mit dem kombinierten Modell, Dünne Linien: Verbindung der Messpunkte mit einer *Spline*-Funktion zur besseren Übersicht. Adaptiert von [4].

hol entsteht. Im für alle Flammen verwendeten EI-MBMS-Experiment können diese nicht unterschieden werden, während ihre Identifizierung durch das PI-MBMS-Experiment jedoch möglich war [4]. Beide Spezies werden in großen Mengen gebildet und der Vergleich der Summen zeigt daher für die Zugabe von DEE sowie für *n*-Butanol einen hohen Anstieg. Dies kann als eher negativer Aspekt der Biokraftstoffaddition festgestellt werden, da Aldehyde sowohl als gesundheitsgefährdend für den Menschen als auch als schädlich für die Umwelt und die Atmosphäre charakterisiert werden.

Einfluss der Addition von DEE und *n*-Butanol auf die Schadstoffbildung

Um die Trends und Effekte der Biokraftstoffaddition genauer zu untersuchen, werden im Folgenden ausschließlich die maximalen Molenbrüche einzelner Spezies in Abhängigkeit vom Zusatz des Additivs analysiert (0% Additiv: pure *n*-Butanflamme, 50% Additiv: 50:50-Mischungen von *n*-Butan und DEE oder *n*-Butanol, 100% Additiv: pure DEE- bzw. *n*-Butanolflamme). Dabei werden einige generelle Trends gefunden. Allgemein kann bei der Addition von DEE und *n*-Butanol ein starker Anstieg für toxische Carbonylverbindungen, insbesondere Aldehyde (hier vorrangig Formaldehyd und Acetaldehyd) beobachtet werden. Diese Tendenz potentieller Biokraftstoffe zur vermehrten Bildung von Aldehyden wurde bereits von Kohse-Höinghaus *et al.* [23] als bedenklich erwähnt und ist im Wesentlichen auf die vergleichsweise schnelle Bildung in wenigen Reaktionsschritten aus den meist oxygenierten Biokraftstoffmolekülen zurückzuführen. Werden hingegen die potentiellen Rußvorläuferspezies analysiert, können gegenläufige Tendenzen für die Addition von DEE und *n*-Butanol identifiziert werden. Mit der Zugabe von DEE wird ein signifikanter Rückgang der Bildung von Rußvorläuferspezies festgestellt, während für die Zugabe von *n*-Butanol nahezu keine Reduktionseffekte, für manche Spezies sogar ein deutlicher Anstieg gemessen wird. Diese beiden gegenläufigen Trends können auch mithilfe der kinetischen Modellierung erhalten werden und bestätigen die Erwartungen aus Abb. 4.1, da für die Bildung der als Rußvorläuferspezies genannten Strukturen größtenteils C_3- und C_4-Bausteine benötigt werden, die aufgrund der maximalen Kohlenstoffkette von zwei Atomen im Diethylethermolekül nicht aus dem direktem Brennstoffabbau entstehen können. Das Molekül *n*-Butanol hingegen weist mit einer C_4-Kette schon die entsprechenden Voraussetzungen auf, was somit zu einer möglichen Bildung von Strukturen im Bereich von C_4 bis C_8 führt. Zum Beispiel konnte mittels einer *Rate of Production Analysis* für Benzol die Radikalrekombination von C_3H_5 (Allyl) und C_3H_3 (Propargyl) als entscheidender Bildungsweg identifiziert werden (vgl. Tran *et al.* [4]). Beide Spezies werden aus den direkten β-Spaltungsprodukten C_3H_6 und C_4H_8 des *n*-Butanolabbaus (vgl. Abb. 4.1) gebildet und sind daher in großen Mengen verfügbar. Eine anschließende H-Abstraktion am Benzol liefert das Benzylradikal (C_6H_5), welches im weiteren Verlauf schnell mit anderen Radikalen wie z.B. C_2H_5 (Ethyl) zu Ethylbenzol oder CH_3 (Methyl) zu Toluol, aber auch mit weiteren größeren Radikalen rekombiniert und somit größere Strukturen aufbaut, die letztendlich zu Rußpartikeln führen können.

Zusätzlich zu den analysierten Trends sollte ebenfalls untersucht werden, ob die Bildung der betrachteten Intermediate ein rein kombinatorischer Effekt ist oder ob es zwischen den Speziespools zweier Brennstoffe zu Interaktionen kommt. Dazu wurde für jede Spezies der Mittelwert des detektierten Molenbruchs in der *n*-Butanflamme und der entpsprechenden Flamme des Biokraftstoffes berechnet und dann mit dem tatsächlich gemessenen Molenbruch in der Mischung verglichen. Die Auftragung der Abweichung des tatsächlich

gemessenen Wertes zum berechneten Mittelwert ist in Abb. 4.3 für einige relevante Spezies dargestellt. Unter der Annahme, dass eine tatsächliche Interaktion vorliegt, wenn diese Abweichung existiert, bzw. höher ist als der entsprechend zu berücksichtigende Fehler der Molenbrüche, können die Ergebnisse interpretiert werden. Dazu wurde der Fehler im Experiment mit 5 % angenommen (rote gestrichelte Linie in Abb. 4.3), da in diesem Fall alle Messungen unter identischen Bedingungen durchgeführt wurden und daher nicht der absolute Molenbruchfehler, sondern der relative Fehler innerhalb der Reproduzierbarkeit des Experiments entscheidend ist. Dieser wurde durch Wiederholung identischer Messungen auf unter 5 % bestimmt.

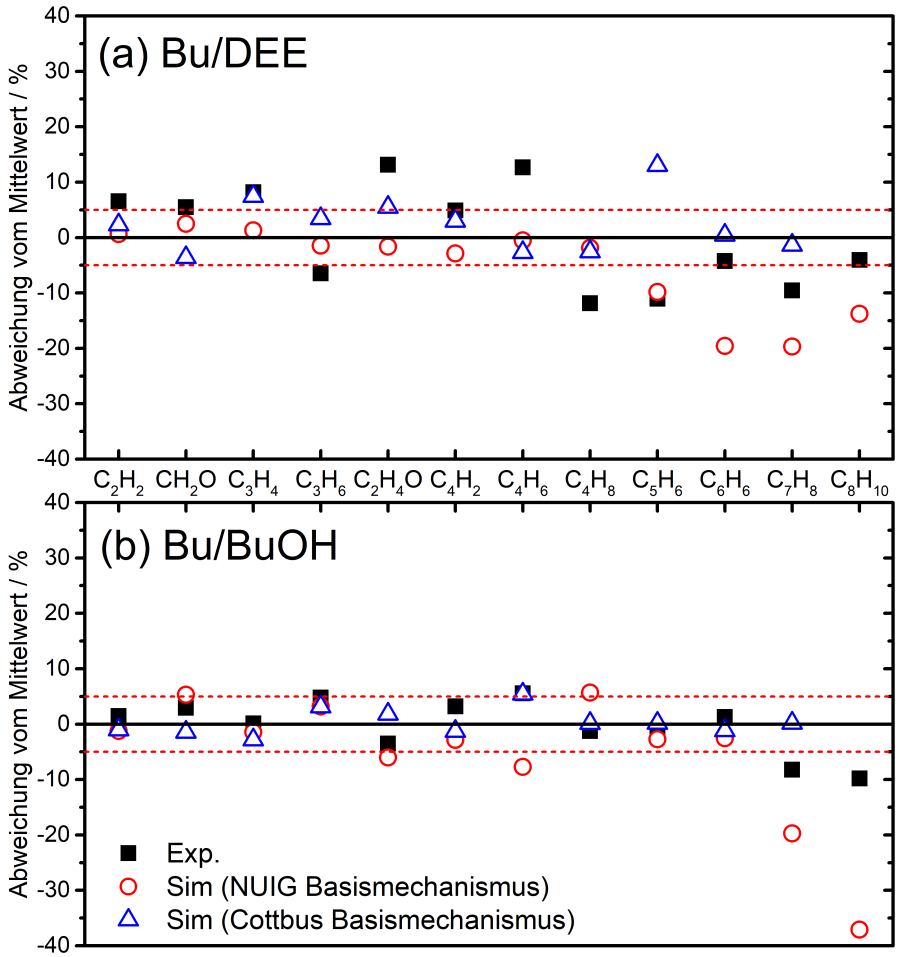

Abbildung 4.3: Abweichungen der maximalen Molenbrüche ausgewählter Kohlenwasserstoffspezies und Carbonylverbindungen in den Mischungsflammen vom berechneten Mittelwert der jeweils beiden puren Flammen in Prozent. Positive Werte zeigen an, dass die Spezies in der Mischung mehr gebildet wird als der Mittelwert der beiden puren Komponenten und andersherum. Oben: Mischung von *n*-Butan und Diethylether, unten: Mischung von *n*-Butan und *n*-Butanol. Die gleichen Berechnungen wurden für die Ergebnisse der Simulation mit zwei verschiedenen Basismechanismen durchgeführt (NUIG und Cottbus, Details zu den Mechanismen s. Text und [4]). Im Cottbus-Modell ist kein Ethylbenzol (C_8H_{10}) enthalten. Adaptiert von [4].

Die in Abb. 4.3 dargestellten Spezies der Klassen Rußvorläufer und Aldehyde wurden

besonders im Hinblick auf die mögliche Beschränkung der Nutzung der Biokraftstoffe aufgrund von Auswirkungen auf die Gesundheit sowie die Luftqualität und Atmosphärenchemie ausgewählt. Weiterhin sind in der Abbildung auch die Berechnungen für die Molenbrüche aus dem kinetischen Modell eingetragen, um einen direkten Vergleich zu ermöglichen. Dabei wurde sowohl das kombinierte Modell dieser Arbeit (basierend auf dem NUIG Basismechanismus) als auch zum Vergleich ein weiteres kombiniertes Modell mit einem anderen Basismechanismus des *Lehrstuhl Thermodynamik und Thermische Verfahrenstechnik* der *Brandenburgisch Technischen Universität Cottbus-Senftenberg* [37] verwendet.
Bei der Analyse der Abweichungen fällt auf, dass diese für viele der gezeigten Spezies, insbesondere kleinere Spezies bis in den C_4-Bereich, innerhalb oder um die Fehlergrenze liegen. Diskutable Abweichungen sind in der *n*-Butan/DEE-Mischung nur für C_4H_8 (nur im Experiment), C_5H_6 und C_7H_8 und in der *n*-Butan/*n*-Butanol-Mischung nur für Spezies über C_6 (C_7H_8 und C_8H_{10}) zu finden. Da aber gerade diese C_7-C_8-Spezies wichtige Schlüsselintermediate für die Rußbildung sind, ist es besonders interessant, dass die wenigen gefunden Interaktionen offensichtlich vorrangig diesen Bereich betreffen. Es fällt ebenso auf, dass alle diskutablen Abweichungen jeweils negativ sind, d.h. eine Interaktion führt zu einer Reduktion der Spezies im Vergleich zum theoretischen Mittelwert. Ein solcher Effekt kann jedoch sowohl auf thermische, als auch Transport- oder chemische Eigenschaften zurückzuführen sein. Letztere weisen dabei insbesondere auf Synergien zwischen den Reaktionswegen zweier Brennstoffe hin, welche detaillierter im Hinblick auf Unsicherheiten im Experiment, vor allem aber auch in den kinetischen Modellierungen analysiert werden müssen. Die zum Teil stark unterschiedlichen Abweichungen der zwei hier vorgestellten Modelle deuten darauf hin, dass die Ergebnisse solcher Simulationen stark abhängig vom verwendeten Mechanismus und folglich mit Vorsicht zu interpretieren sind.

Zusammenfassung

Der Einfluss der potentiellen Biokraftstoffe Diethylether und *n*-Butanol auf die Flammenstruktur einer laminaren Niederdruckflamme des Brennstoffes *n*-Butan wurde im Hinblick auf die Bildung erster Intermediatspezies als auch von Schadstoffen untersucht. Dazu wurden insgesamt mehr als 40 stabile und radikalische Spezies im Bereich von C_0 bis C_8 in fünf brennstoffreichen Flammen (*n*-Butan, Diethylether, *n*-Butanol und 50:50-Mischungen von *n*-Butan mit Diethylether oder *n*-Butanol) unter gleichbleibenden Flammenbedingungen aufgenommen und mithilfe von EI-MBMS und zum Teil auch PI-MBMS identifiziert und quantifiziert. Um die Ergebnisse entsprechend interpretieren zu können, wurde ein kinetisches Modell aus einem hinreichend validierten Basismechanismus und den Submechanismen der Additive Diethylether und *n*-Butanol kombiniert. Der Submechanismus für Diethylether wurde dabei auf Grundlage von theoretischen Berechnungen und den gemessenen Speziesprofilen in der laminaren Niderdruckflamme sowie gemessenen Flammengeschwindigkeiten neu aufgebaut.

Die Ergebnisse zeigen, dass die Bildung toxischer Carbonylverbindungen, insbesondere von Aldehyden, durch die Addition der Biokraftstoffe stark ansteigt. Die Analyse der untersuchten Rußvorläuferspezies fiel dahingegen unterschiedlich aus. Für die Addition von Diethylether zu *n*-Butan konnte eine signifikante Reduktion der Bildung von spezifischen Rußvorläuferspezies gefunden werden, während diese durch die Addition von *n*-Butanol zu

n-Butan kaum sinken, in einigen Fällen sogar ansteigen. Dies konnte sowohl im Experiment, als auch in den Ergebnissen der kinetischen Modellierung beobachtet werden. Der Effekt konnte im Wesentlichen auf die molekulare Brennstoffstruktur zurückgeführt werden, da die längste Kohlenstoffkette im Diethylethermolekül aus zwei Atomen besteht, während sie im *n*-Butanolmolekül vieratomig ist und dadurch wesentlich die entsprechenden brennstoffspezifischen Verbrennungsreaktionen beeinflusst. Die Analyse interaktiver Effekte zwischen den Verbrennungsabläufen zweier Brennstoffe ergab, dass diese im untersuchten Temperatur- und Druckbereich nur eingeschränkt vorliegen. Dies kann sowohl an Unsicherheiten im Experiment oder auch insbesondere in den kinetischen Modellen liegen, weshalb beides in Zukunft detaillierter analysiert werden sollte. Auch die Untersuchung solch interaktiver Effekte in einem niedrigeren Temperaturbereich scheint vielversprechend für weitere Experimente, da dort hochreaktive Spezies wie Peroxide gebildet werden, die die Zündwilligkeit und Reaktivität beeinflussen und somit eine starke Auswirkung auf interaktive Effekte haben können.

KAPITEL 5

Chemische Interaktion und synergistische Effekte in Brennstoffmischungen im Bereich der Niedertemperaturoxidation

In diesem Kapitel werden die Ergebnisse zu Untersuchungen von chemischen Interaktionen zwischen zwei Brennstoffen im Niedertemperaturbereich vorgestellt. Diese Arbeiten sind bisher nicht veröffentlicht, sind jedoch bereits in Form des Manuskripts [5] zur Veröffentlichung akzeptiert.
Ziel der Untersuchungen war die Analyse eines möglichen interaktiven Effekts in der Niedertemperaturoxidation von Brennstoffgemischen. In Kapitel 4 wurde bereits gezeigt, dass solche Interaktionen im Hochtemperaturbereich unter den hier untersuchten Randbedingungen nur wenig auftreten. Brennstoffadditive finden jedoch besonders im Bereich des intelligenten *Fuel Designs* Anwendung zur Kontrolle der Zündzeiten in zukünftigen Motorenkonzepten, immer mit dem Ziel einer saubereren Verbrennung und einer höheren thermischen Effizienz [52, 108]. Dazu fehlen jedoch bisher essentielle Informationen über mögliche synergistische Effekte und chemische Interaktionen der Brennstoffkomponenten im dabei relevanten Bereich der Niedertemperatur, in welchem die Selbstzündung stattfindet und beeinflusst werden kann. In solchen *Low-Temperature Combustion Engines* werden zum Beispiel Mischungen aus einem Brennstoff mit hoher Cetanzahl[1] und einem Brennstoff mit hoher Oktanzahl eingesetzt, um über eine interaktive Verbrennung die gewünschte höhere thermische Effizienz zu erreichen. Eine gute Übersicht über mögliche Strategien zur effizienteren Kontrolle von Motoren und Zündzeiten wurde von Saxena und Bedoya [53] zusammengestellt.
In dieser Arbeit wurden daher Untersuchungen zu möglichen Interaktionen prototypischer konventioneller und biobasierter Brennstoffe am laminaren Strömungsreaktor durchgeführt. Temperaturabhängige Speziesprofile wurden im Hinblick auf interaktive Effekte während des Oxidationsprozesses analysiert. Als Basis wurde hier das C_5-Alkan *n*-Pentan gewählt, da seine Oxidation vergleichsweise einfacher modelliert werden kann als die der technisch relevanteren Moleküle, wie z.B. das *Primary Reference Fuel n*-Heptan. Zur ersten Analyse überhaupt möglicher interaktiver Effekte ist es wichtig, die ablaufenden Reaktionen gut zu verstehen und entsprechend modellieren zu können. Mit größer werdenden Brennstoffmolekülen ist dies aber bisher aufgrund der exponentiell ansteigenden Zahl auftretender Spezies und ablaufenden Reaktionen noch nicht vollständig etabliert. *n*-Pentan ist daher ein guter Kompromiss zwischen Anwendbarkeit und Komplexität, da es eine bekannte

1 Die Cetanzahl beschreibt die Zündwilligkeit von Dieselkraftstoffen und -surrogaten und gibt an, dass sich ein Kraftstoff so verhält wie ein Gemisch aus dem als Cetanzahl angegebenen Volumentanteil des zündwilligen *n*-Hexadecan und dem zündträgen Methylnaphthalin. Je höher die Cetanzahl, desto zündwilliger das Gemisch, handelsübliche Dieselkraftstoffe weisen eine Cetanzahl von 51-56 auf [67].

Niedertemperaturkinetik aufweist, die durch Additive beeinflusst werden kann und seine Oxidationsreaktionen mithilfe aktueller kinetischer Modelle gut beschrieben werden können [109]. Als Additive wurden Dimethylether und Ethanol (beide C_2H_6O) gewählt, welche sich sowohl strukturell als auch in ihren Oxidationseigenschaften sehr stark unterscheiden. Für Dimethylether ist eine hohe Reaktivität im Niedertemperaturbereich bekannt, und ablaufende Reaktionen und auftretende Spezies sind bereits ausführlich untersucht worden [68, 110–114]. Darüber hinaus hat es eine hohe Cetanzahl und ist seit längerem als potentieller Biokraftstoff im Gespräch [23, 44]. Ethanol hat im Gegensatz eine hohe Oktanzahl und wird bereits als Kraftstoffadditiv verwendet (z.B. E10). Bisher konnte im Niedertemperaturbereich kaum Reaktivität gezeigt werden [111, 115]. Demzufolge werden unterschiedliche Effekte für die Addition von Dimethylether und Ethanol zu *n*-Pentan erwartet.

Reaktormessungen

Die Niedertemperaturoxidation von *n*-Pentan, Dimethylether (DME), Ethanol (EtOH) und entsprechenden Mischungen mit 25 bzw. 50 % der oxygenierten Komponente wurde im laminaren Strömungsreaktor (s. Kap. 2.2.2) in einem Temperaturbereich von 450-930 K unter konstanten Bedingungen untersucht. Dabei wurden für jede Messung eine Stöchiometrie von $\phi = 0.7$, ein Reaktordruck von 970 mbar, ein Gesamtfluss von 300 sccm (*standard cubic centimeters per minute* bei 273.15 K und 1 atm) und eine Argonverdünnung von 90 % verwendet. Alle Bedingungen sind in Tab. 5.1 zusammengefasst.
Temperaturabhängige Speziesprofile wurden mithilfe von EI-MBMS (vgl. Kap. 2.3) aufgenommen und wenn möglich quantifiziert. Interessante Spezies für die keine entsprechenden Literaturdaten zur Quantifizierung vorlagen wurden mithilfe einer Normierung auf die jeweiligen Eingangsbedingungen relativ untereinander verglichen, um Trends und interaktive Effekte zu visualisieren.

Tabelle 5.1: Experimentelle Bedingungen und Benennungen der Messungen am laminaren Strömungsreaktor. γ wird als Anteil von *n*-Pentan in den Mischungen definiert: $\gamma = x_{C5H12}/(x_{C5H12} + x_{C2H6O})$. sccm: *standard cubic centimeters per minute* bei 273.15 K und 1 atm.

					Gasfluss / sccm					
Brennstoff	Name	p / bar	ϕ	γ	Gesamt	Ar	O_2	C_5H_{12}	DME	EtOH
n-Pentan (C_5H_{12})	P100	0.97	0.7		300.0	270.0	27.59	2.414		
Dimethylether (DME)	D100	0.97	0.7		300.0	270.0	24.32		5.676	
Ethanol (EtOH)	E100	0.97	0.7		300.0	270.0	24.32			5.676
C_5H_{12}/DME	PD75	0.97	0.7	0.75	300.0	270.0	27.18	2.114	0.705	
Mischungen	PD50	0.97	0.7	0.50	300.0	270.0	26.61	1.694	1.694	
C_5H_{12}/EtOH	PE75	0.97	0.7	0.75	300.0	270.0	27.18	2.114		0.705
Mischungen	PE50	0.97	0.7	0.50	300.0	270.0	26.61	1.694		1.694

Kinetische Modellierung

Obwohl die experimentellen Ergebnisse in dieser Arbeit im Vordergrund stehen, wurden unterstützend Simulationen der Speziesprofile mithilfe kinetischer Modelle durchgeführt. Dazu wurde die in Kap. 2.5 vorgestellte Methode nach Hemken *et al.* [62] zur Beschreibung des laminaren Strömungsreaktors verwendet und der Wärmetransferkoeffizient des Systems mithilfe von Messungen für reines Argon (nicht reaktive Bedingungen) auf 10 $\mathrm{W \cdot m^{-2} \cdot K^{-1}}$ bestimmt. Als kinetische Modelle wurden die Mechanismen von Bugler *et al.* [109] (hier:

NUIG-Modell) und Ranzi *et al.* [116] (hier: Polimi-Modell) gewählt, da sie beide bereits alle drei untersuchten Brennstoffe und ihre jeweilige Kinetik enthalten. Im Folgenden werden die experimentellen Ergebnisse jedoch nur mit dem NUIG-Modell verglichen, für Vergleiche mit dem Polimi-Modell sei auf [5] verwiesen. Die kinetischen Modellierungen dienen hier vorerst der Unterstützung des Verständnisses möglicher interaktiver Effekte der Oxidationsprozesse zweier Brennstoffe. Es konnte festgestellt werden, dass weitere Parameter bei der Modellierung des laminaren Strömungsreaktors (Massenkonvektion, Diffusionsprozesse, Wärmefreisetzung des reagierenden Gases, thermische Leitfähigkeit, thermischer Austausch mit der Reaktorwand) berücksichtigt werden müssen und die Auswirkung der nicht detaillierten Berücksichtigung dieser Effekte konnte bisher noch nicht abschließend geklärt werden. Diese Überlegungen sind Gegenstand der aktuellen Forschung.

Reaktivität der Brennstoffgemische

Um mögliche Interaktionen der Oxidationsprozesse zweier Brennstoffe zu visualisieren, sind in Abb. 5.1 die Temperaturprofile für die jeweiligen Brennstoffumsätze gezeigt. Daran lässt sich erkennen, wie effizient und bei welchen Temperaturen der jeweilige Brennstoff umgesetzt wird und ob die Addition eines anderen Brennstoffes dieses Verhalten beeinflusst. In Abb. 5.1a ist der Umsatz von *n*-Pentan unter Zugabe von DME gezeigt (P100, PD75, PD50), während in Abb. 5.1b der Einfluss der Ethanoladdition dargestellt ist (P100, PE75, PE50). Um auch den Umsatz des jeweiligen Additivs auf Beeinflussung durch das *n*-Pentan zu analysieren, sind in Abb. 5.1c,d die Temperaturprofile für DME und Ethanol gezeigt (D100, PD50, PD75 bzw. E100 und PE75, PE50 ist nicht gezeigt, da dort noch keine Interaktion gemessen wurde und das Profil dem von E100 gleicht). Damit die jeweiligen Profile überhaupt miteinander verglichen werden können, wurden die quantifizierten Molenbrüche jedes Profils auf den jeweiligen Brennstoffmolenbruch der Gasmischung bei Einlassbedingungen normiert. Somit müssten alle Profile gleich aussehen, wenn keine Interaktion stattfinden würde. Jegliche Unterschiede in Form und Position sind demzufolge auf Mischungseffekte zurückzuführen.

In Abb. 5.1a kann für die Addition von DME zu *n*-Pentan ein geringfügiger Trend hin zu niedrigeren Temperaturen festgestellt werden. Außerdem ist ein stärkerer Brennstoffumsatz im Bereich zwischen 600 und 625 K zu sehen, der Unterschied ist jedoch sehr gering und liegt damit im Fehlerbereich des Experiments. Das Modell gibt den Brennstoffverbrauch für pures *n*-Pentan (P100) sowie die Trends unter DME-Addition sehr gut wieder, lediglich der Temperaturversatz wird etwas stärker vorhergesagt. Für die Addition von Ethanol in Abb. 5.1b wird ein gegenläufiger Trend erhalten. Der Brennstoffverbrauch von *n*-Pentan wird reduziert, zu leicht höheren Temperaturen verschoben und das NTC-Fenster (vgl. auch Abb. 2.2) wird schmaler. Auch dieses Verhalten kann vom Modell in Übereinstimmung mit dem experimentellen Befund dargestellt werden, lediglich für PE50 wird etwas weniger Inhibierung des Brennstoffumsatzes vorhergesagt als experimentell gemessen wurde.
Wird der Brennstoffumsatz aus Sicht des DME betrachtet (Abb. 5.1c), fällt auf, dass die Zugabe von *n*-Pentan den Umsatz von DME stark beeinflusst. Zwar ist ebenfalls nur ein kleiner steigernder Effekt auf den Umsatz zu erkennen, der Temperaturbereich ist jedoch mit 35 K bzw. 49 K für PD50 bzw. PD75 stark verschoben. Im Modell ist dieser Temperatureffekt etwas geringer. Für pures Ethanol (E100) ist in Abb. 5.1d kein messbarer Umsatz im Bereich von 600-650 K zu sehen. Durch Addition von *n*-Pentan kann jedoch auch für Ethanol eine

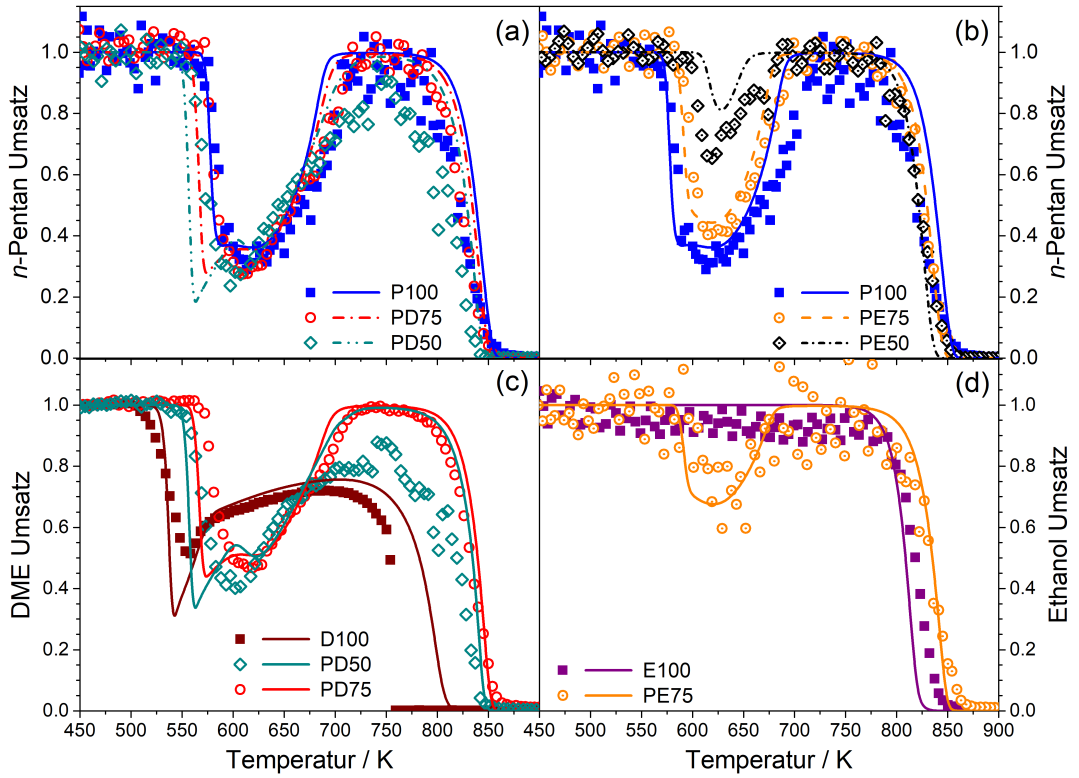

Abbildung 5.1: Reaktivität der reinen Brennstoffe und Brennstoffgemische anhand der Brennstoffumsätze. Experimentell erhaltene Molenbruchprofile (Symbole) und Ergebnisse der Modellierung (Linien), jeweils normiert auf den Anteil des jeweiligen Brennstoffes in der Mischung als Funktion der Temperatur. Adaptiert von [5].

verstärkte Reaktivität in diesem Bereich gemessen werden. Dieser Effekt ist jedoch erst bei 75 % *n*-Pentan signifikant genug und kann auch vom Modell sehr gut wiedergegeben werden.

Insgesamt kann für die Mischung von *n*-Pentan und DME ein interaktiver Effekt festgestellt werden. Dies lässt sich durch den intensiveren Umsatz beider Brennstoffe im Vergleich zum jeweils puren Fall bestätigen. In der Mischung von *n*-Pentan mit Ethanol wirkt Ethanol eher hemmend auf den *n*-Pentanumsatz, während umgekehrt *n*-Pentan die Reaktivität von Ethanol erhöht. Um diese Effekte zu verstehen, ist es nötig, die ablaufenden Reaktionen im Niedertemperaturbereich für die jeweiligen Brennstoffstrukturen miteinander zu vergleichen. Ein entscheidender Parameter für die Reaktivität eines Brennstoffes im Niedertemperaturbereich ist die OH-Bilanz, also die Differenz zwischen gebildeten und konsumierten OH-Radikalen. In Abb. 5.2 sind die Reaktionszyklen der drei untersuchten Brennstoffe im Hinblick auf die Bildung und den Verbrauch von OH dargestellt. Die dabei betrachteten hauptsächlich ablaufenden Reaktionen wurden bereits in Abb. 2.1b in Kap. 2.1 vorgestellt. Die beim Ablauf eines solchen Reaktionszyklus entstehenden OH-Radikale sind durch die durchgezogenen dicken Pfeile (türkis) hervorgehoben, während der Verbrauch von OH-Radikalen durch die H-Abstraktion am Brennstoffmolekül mit durchgezogenen dünnen Pfeilen (blau) dargestellt ist. Um die maximale OH-Bilanz zu bestimmen, dürfen jedoch nur die gebildeten OH-Radikale nach der zweiten O_2-Addition betrachtet werden,

da es sich nur dann um einen vollständigen Zyklus handelt und die vorherige Bildung von OH zu einem Kettenabbruch führen kann.

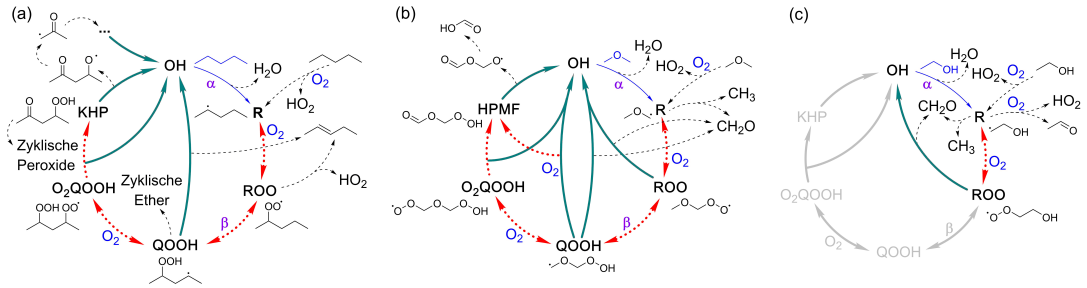

Abbildung 5.2: Schematische Darstellung der Hauptreaktionszyklen in der Niedertemperaturoxidation der untersuchten Brennstoffe *n*-Pentan (a), DME (b) und Ethanol (c). Durchgezogene dicke Pfeile: Reaktionen, die OH produzieren, durchgezogene dünne Pfeile: H-Abstraktion am Brennstoffmolekül, wodurch OH verbraucht wird, gestrichelte dicke Pfeile: Reaktionen, die den Reaktionszyklus begünstigen, gestrichelte dünne Pfeile: andere Produkte während des Oxidationsprozesses, durchgezogene hellgraue Pfeile: fiktiver Zyklus für Ethanol, der aufgrund der Struktur von Ethanol nicht stattfinden kann. KHP: Ketohydroperoxid, HPMF: Hydroperoxymethylformat (Ketohydroperoxid bei der Oxidation von DME). Adaptiert von [5].

Aus Abb. 5.2a kann ermittelt werden, dass die zweistufige Oxidation von *n*-Pentan maximal drei OH-Radikale produziert, während für den initialen Reaktionsschritt der Produktion von Pentylradikalen nur eins benötigt wird. Dieser sogenannte α-Schritt ist besonders wichtig, da er den gesamten Zyklus einleitet. Die für diesen Schritt zur Verfügung stehenden OH-Radikale sind das maßgebliche Kriterium für den Brennstoffumsatz jedes Brennstoffes. Wird ein weiterer Brennstoff addiert, kommt es an dieser Stelle zu Konkurrenz um die vorhandenen OH-Radikale. Ebenso ist die H-Abstraktion durch OH der dominanteste Prozess für die Verzweigung im DME. In Abb. 5.2b ist dies ebenfalls der einzige OH-Verbrauchsschritt, während aus dem weiter ablaufenden Zyklus wiederum maximal zwei OH-Radikale entstehen. Durch die Addition von DME zu *n*-Pentan können OH-Radikale aufgrund der höheren Niedertemperaturaktivität von DME schon bei niedrigerer Temperatur gebildet werden und somit auch für die Initialisierung des *n*-Pentanzyklus verwendet werden. Dadurch wird die Gesamtreaktivität im System erhöht. In Abb. 5.1a konnte jedoch gezeigt werden, dass der maximale Umsatz von *n*-Pentan durch die Zugabe von DME kaum erhöht wird. Dies deutet möglicherweise darauf hin, dass bei gleicher Stöchiometrie der Brennstoffe eine vergleichbare Konzentration der OH-Radikale vorliegt oder *n*-Pentan im Konkurrenzkampf um OH-Radikale die Oberhand gewinnt. Ebenso können möglicherweise weitere Radikale involviert sein oder es sich ausschließlich um einen Temperatureffekt handeln.
Bei Betrachtung von Abb. 5.2c wird schnell klar, warum Ethanol die Reaktivität von *n*-Pentan in der Mischung senkt. Die grauen Pfeile zeigen eine fiktive zweite O_2-Addition, die aufgrund der Molekülstruktur von Ethanol jedoch nicht stattfinden kann. Auch die erste O_2-Addition findet aufgrund von bevorzugt ablaufenden Konkurrenzreaktionen so gut wie nicht statt. Demzufolge wird für die initiale Erzeugung von Ethanolradikalen ein OH-Radikal benötigt, im weiteren Reaktionsverlauf des Brennstoffes jedoch keins erzeugt. Dies bedeutet, dass Ethanol dem Gesamtsystem nicht nur kein OH zur Verfügung stellt, sondern aktiv OH-Radikale verbraucht und sie aus dem Reaktionssystem entfernt. Dadurch

wird die Reaktivität im System stark verringert, was die experimentellen Befunde in Abb. 5.1b,d bestätigt und erklärt.
Für einen intensiveren Einblick in das Reaktionsverhalten der Brennstoffgemische im Niedertemperaturbereich werden im Folgenden ausgewählte Intermediate aus dem Oxidationsprozess im Hinblick auf eben diese Interaktion analysiert.

Interaktive Einflüsse auf die Intermediatbildung

Zur Analyse brennstoffspezifischer Intermediate im Niedertemperaturbereich ist in Abb. 5.3 und 5.4 eine stark eingeschränkte Auswahl der in Ref. [5] vorgestellten Spezies gezeigt. In Abb. 5.3 sind die für die Niedertemperaturoxidation von *n*-Pentan spezifischen Spezies $C_5H_{12}O_2$ (ROOH) und $C_5H_{10}O_3$ (Ketohydroperoxid) als Vertreter stabiler Intermediate dargestellt. Die jeweiligen Reaktionsdiagramme der untersuchten Brennstoffe sind im Detail in [5] abgebildet und folgen dem Schema aus Abb. 2.1 in Kap. 2.1. Die Abb. 5.4 zeigt Acetaldehyd (C_2H_4O) und Formaldehyd (CH_2O) als Vertreter wichtiger Schlüsselspezies bei der Analyse der Niedertemperaturoxidation, da ihr Auftreten aufgrund ihrer hohen Toxizität und Umweltschädlichkeit bei der Betrachtung alternativer Kraftstoffe besonders berücksichtigt werden sollte. Da beide Spezies jeweils aus vielen Brennstoffen entstehen können und typische Niedertemperaturspezies sind, ist ihre Herkunft aus unterschiedlichsten Reaktionen oft schwer zu beschreiben und ihr Verhalten in den Kraftstoffgemischen daher besonders interessant.

Hydroperoxyalkane entstehen durch eine Kettenabbruchreaktion aus den vorhergehenden ROO-Radikalen. Die Bildung von Hydroperoxypentanen ($C_5H_{12}O_2$) steht damit in direkter Konkurrenz zur Isomerisierung ROO $\longleftrightarrow$ QOOH [31]. Aus dem ROO-Radikal des *n*-Pentan können drei isomere Hydroperoxypentane gebildet werden, eine Isomerentrennung war in dem hier verwendeten EI-MBMS-Experiment jedoch nicht möglich. Aufgrund mangelnder Stoßquerschnitte konnte ebenso keine Quantifizierung der erhaltenen Signale erfolgen, in Abb. 5.3a,b sind daher relative Temperaturprofile, normiert auf die entsprechenden Einlassbedingungen des *n*-Pentan, dargestellt, um Trends und interaktive Effekte zu visualisieren. Für pures *n*-Pentan (P100) kann ein Maximum bei 585 K detektiert werden, welches gut mit dem Beginn des Brennstoffumsatzes in Abb. 5.1a übereinstimmt. Durch Zugabe von DME (Abb. 5.3a) wird das Maximum bei einer höheren Temperatur detektiert und die Bildung von $C_5H_{12}O_2$ aus C_5H_{12} steigt leicht an. Das Modell bestätigt diese Trends, überschätzt jedoch sowohl den Temperatureffekt, als auch die Umsatzsteigerung, wie bereits für den Brennstoffumsatz bemerkt wurde. Wird hingegen Ethanol zugesetzt (Abb. 5.3b), wird das Maximum zu höherer Temperatur verschoben und die Intensität nimmt stark ab. Für PE50 konnte bereits kein Signal mehr gemessen werden. Da $C_5H_{12}O_2$ ausschließlich aus *n*-Pentan gebildet wird, kann ein Anstieg oder eine Abnahme nicht aufgrund zusätzlicher Moleküle aus den Additiven erfolgen. Ein Einfluss durch Addition von DME und Ethanol auf die Reaktivität des *n*-Pentan kann damit klar bestätigt werden. Die Bildung von $C_5H_{12}O_2$ ist maßgeblich durch die initiale Produktion von Pentylradikalen gegeben. Da durch die Zugabe von DME mehr OH-Radikale ins System gelangen und somit die Produktion von Pentylradikalen gesteigert werden kann (vgl. Abb. 5.2 und entsprechende Diskussion im vorangegangenen Abschnitt) kann im Gegensatz zur Addition von Ethanol, welches OH-Radikale aus dem System entfernt, mehr $C_5H_{12}O_2$ gebildet werden.
Ein ähnliches Verhalten wird auch für die Bildung des Ketohydroperoxids ($C_5H_{10}O_3$)

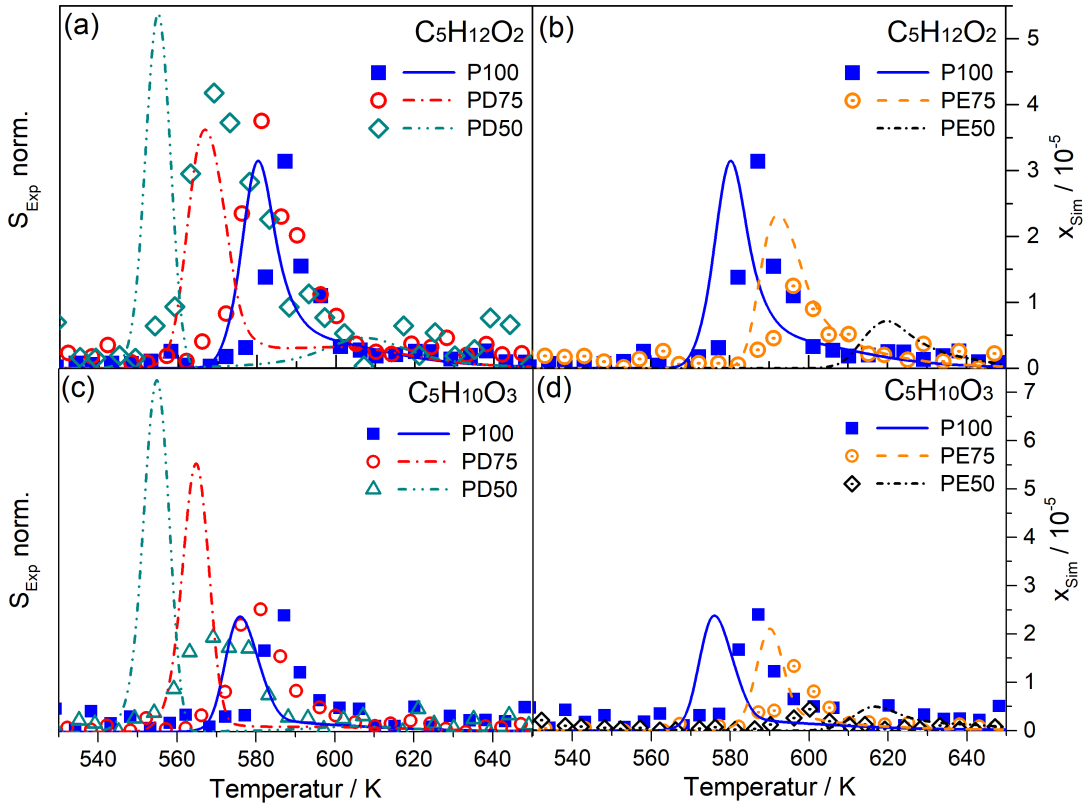

Abbildung 5.3: Signalintensitäten (Symbole, linke Achse, normiert auf den Anteil *n*-Pentan in der Mischung) und quantitative Molenbrüche aus der Modellierung (Linien, rechte Achse, ebenfalls normiert auf den Anteil *n*-Pentan in der Mischung) für $C_5H_{12}O_2$ (zugeordnet zu Hydroperoxypentanen, ROOH) und $C_5H_{10}O_3$ (zugeordnet zu Ketohydroperoxiden aus der *n*-Pentanoxidation) jeweils für die *n*-Pentan/DME-Mischungen (a,c) und *n*-Pentan/EtOH-Mischungen (b,d). Adaptiert von [5].

erwartet, da die Bildung mit dem gleichen Reaktionsablauf verknüpft ist und zunächst Pentylradikale zur Verfügung stehen müssen. Die Profile für $C_5H_{10}O_3$ sind in Abb. 5.3 für die Zugabe von DME (c) und Ethanol (d) dargestellt. Da auch hier nicht isomerenspezifisch gemessen werden konnte und keine Stoßquerschnitte verfügbar waren, ist ebenfalls ein relativer Vergleich über die Normierung auf die Einlassbedingungen gezeigt. Laut Rodriguez *et al.* [117] handelt es sich vorrangig um die Isomere 3-Hydroperoxypentanal und 1-Hydroperoxy-3-pentanon, wohingegen nach Messungen von Rodriguez *et al.* [117] das dritte mögliche Isomer 2-Hydroperoxy-4-pentanon eher weniger vertreten sein soll, obwohl es das chemisch stabilere und kinetisch wahrscheinlichste ist. Die Positionen der Maxima stimmen mit denen von $C_5H_{12}O_2$ überein und der Einfluss der Zugabe von DME und Ethanol auf die Temperatur ist vergleichbar. Allerdings kann kein deutlicher Anstieg der Intensität mit DME-Addition gefunden werden, während die Ethanoladdition trotzdem zu einer Reduktion führt. Im Rahmen der Fehlertoleranz sind die Intensitäten für P100, PD75 und PD50 in etwa gleich, das Modell sagt jedoch einen klaren Anstieg vorher. Eine mögliche Begründung für diesen Unterschied kann in den im Modell fehlenden Reaktionen liegen. Gerade für die Mischungen sind Niedertemperaturreaktionen zwischen beiden Reaktionswegen wie z.B. $RO_2 + R'O_2 \longrightarrow RO + R'O + O_2$ oder die H-Abstraktion durch die

RO_2-Radikale beider Brennstoffe besonders wichtig, jedoch nicht im Modell enthalten, da es sich hier nicht um ein Modell zur Simulation der Reaktionen von Brennstoffgemischen handelt. Eine Implementierung solcher Reaktionen könnte zur besseren Beschreibung der experimentellen Resultate führen.

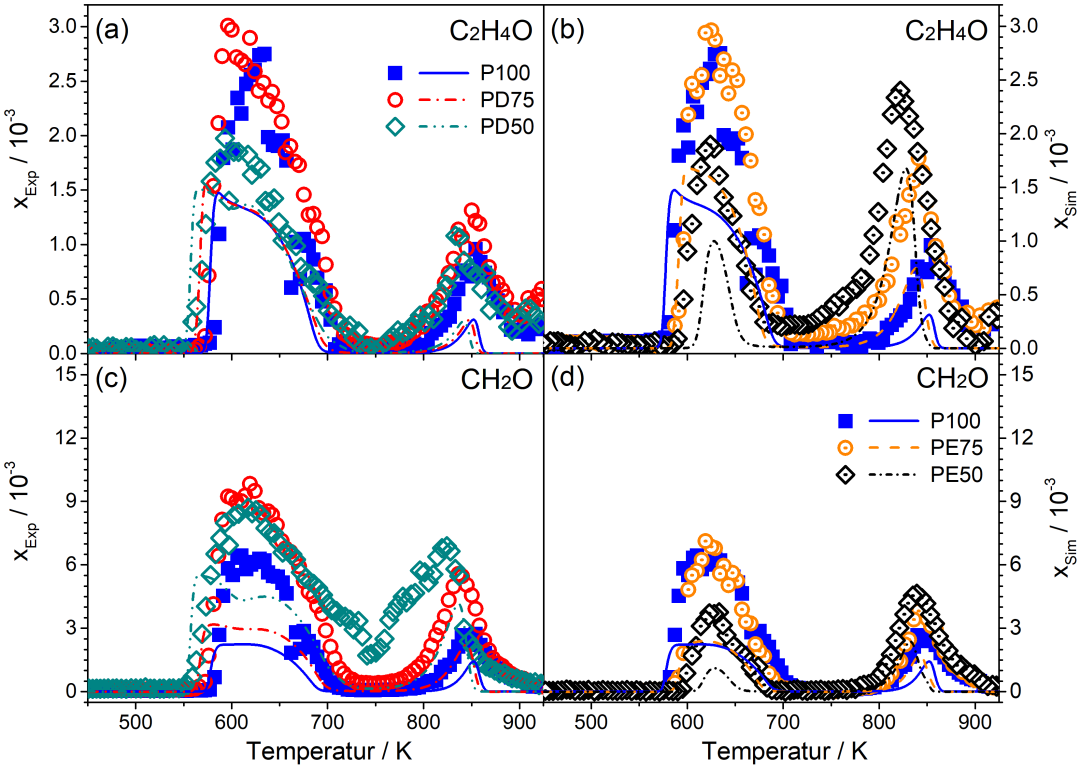

Abbildung 5.4: Quantitative Molenbrüche aus Experiment (Symbole) und Modellierung (Linien), jeweils normiert auf den Anteil *n*-Pentan in der Mischung für Acetaldehyd (C_2H_4O) und Formaldehyd (CH_2O) für die *n*-Pentan/DME-Mischungen (a,c) und *n*-Pentan/EtOH-Mischungen (b,d). Adaptiert von [5].

In Abb. 5.4 sind die Temperaturprofile von Acetaldehyd (C_2H_4O) und Formaldehyd (CH_2O) gezeigt. Für diese beiden Spezies kann eine Quantifizierung erfolgen, weshalb die Molenbrüche der Spezies bestimmt wurden. Damit trotzdem eine Vergleichbarkeit innerhalb der durchgeführten Messungen erfolgen kann, wurden diese anschließend ebenfalls mithilfe des jeweiligen *n*-Pentan Einlassmolenbruchs normiert, um aus Unterschieden der Profile ausschließlich interaktive Effekte zu erhalten. Für Acetaldehyd kann festgestellt werden, dass eine 25 %ige Addition beider oxygenierter Komponenten keinen Einfluss hat, während eine 50 %ige Addition für beide Fälle zu einer signifikanten Reduktion des Molenbruchs führt. Die Ergebnisse der kinetischen Modellierung sagen für die DME-Addition jedoch keinen und für die Ethanoladdition nur einen kleinen Effekt voraus. In diesem Fall ist es besonders interessant, auf welchen Wegen Acetaldehyd für die jeweiligen Brennstoffe und Brennstoffgemische vorrangig gebildet wird. Laut dem Modell wird Acetaldehyd im Oxidationsprozess von *n*-Pentan bevorzugt aus dem Ketohydroperoxid 2-Hydroxy-4-pentanon ($C_5H_{10}O_3$) gebildet, welches aber, wie bereits beschrieben, laut Rodriguez *et al.* [117] das am wenigsten gebildete Ketohydroperoxid ist. Auch für die Mischungen von *n*-Pentan und DME ist dies

der vorrangige Bildungsweg von Acetaldehyd, weshalb das Modell keine Unterschiede im Molenbruch vorhersagt. Möglicherweise fehlen im Modell entsprechende Reaktionen zur Beschreibung der Mischungen, da üblicherweise der Abbau der Ketohydroperoxide über eine O-O-Spaltung und anschließende β-Spaltung direkt Acetaldehyd produziert. Laut Ranzi *et al.* [116] ist jedoch auch ein Abbauweg über eine H-Abstraktion und anschließende β-Spaltung zu Pentadion und Keten möglich. Durch die Addition des reaktiven DME wird der Beitrag dieser Reaktion möglicherweise erhöht, wodurch für PD50 weniger Acetaldehyd gebildet werden würde. Da dieser Reaktionsweg jedoch nicht im Modell enthalten ist, kann in der Simulation kein Effekt beobachtet werden. Aufgrund der experimentellen Ergebnisse können an dieser Stelle also Verbesserungen im Modell vorgenommen werden. Die Effekte der Ethanoladdition auf den Molenbruch von Acetaldehyd können über die bevorzugte Bildung von Acetaldehyd aus dem sekundären Ethanolradikal, welches zu 70 % aus Ethanol gebildet wird, erklärt werden. Durch die Anwesenheit von *n*-Pentan und zur Verfügung stehende OH-Radikale wird die Reaktivität von Ethanol erhöht, es können mehr Brennstoffradikale gebildet werden, weshalb ebenfalls zusätzlich Acetaldehyd gebildet wird.

Im Gegensatz zum Acetaldehyd wird für Formaldehyd ein gegenläufiger Trend für die Addition von DME (Abb. 5.4c) und Ethanol (Abb. 5.4d) erhalten. Bei der DME-Addition kommt es zu einem Anstieg des Molenbruchs, der jedoch für PD75 und PD50 etwa gleich groß ist. Da Formaldehyd ein typisches Oxidationsintermediat ist, welches bei der Oxidation aller drei untersuchten Brennstoffe in vielen Reaktionen gebildet wird, wurden mithilfe des kinetischen Modells die wichtigsten Reaktionen zur Bildung von Formaldehyd für die Brennstoffe und die Mischungen mithilfe einer *Rate of Production Analysis* (s. Abb. 13 in Ref. [5]) analysiert. Bei der Oxidation von *n*-Pentan sind hauptsächlich Reaktionen von entstehenden Methylradikalen für die Bildung von Formaldehyd verantwortlich. Wird nun DME zugegeben, kommen die Bildungswege aus $CH_3OCH_2O_2$ (ROO von DME) und $CH_2OCH_2O_2H$ (QOOH von DME) hinzu. Da wie bereits gezeigt, die Mischung beider Brennstoffe den Umsatz beider Komponenten verstärkt und insgesamt mehr OH-Radikale zur Verfügung stehen, werden auch diese Bildungswege mehr hervorgehoben und somit mehr Formaldehyd gebildet.
Wird hingegen Ethanol zu *n*-Pentan addiert, kann für PE75 zunächst kein Effekt festgestellt werden, mit 50 % Ethanol wird jedoch eine Reduktion von Formaldehyd beobachtet. Durch die zuvor analysierte Verringerung der Reaktivität des Gesamtsystems würde jedoch für beide Mischungen insgesamt eine stärkere Reduktion erwartet werden. Die Bildung von Formaldehyd erfolgt bei der Oxidation von Ethanol vorrangig über Methoxyradikale und ebenfalls aus dem ROO-Radikal von Ethanol (hier $O_2C_2H_4OH$). Aufgrund des Verbrauchs von OH-Radikalen durch Ethanol gewinnt jedoch ein anderer Weg zur Bildung von Formaldehyd aus *n*-Pentan an Bedeutung. Das Ketohydroperoxid von *n*-Pentan wird nun zunehmend über einen unimolekularen Zerfall abgebaut. Daraus entsteht 2-Pentanoxid-4-on ($C_5H_9O_2$), welches durch eine β-Spaltung in Acetaldehyd und Acetonyl zerfällt. Durch eine O-Addition an das Acetonylradikal und anschließende β-Spaltung entstehen Formaldehyd und ein Acylradikal, wodurch die Formaldehydbildung gesteigert wird. Diese Erklärung ist nur ein möglicher Vorschlag und basiert zunächst vorrangig auf der Analyse des Modells. Es ist jedoch bekannt, dass gerade die Acetonreaktionen, und damit auch die Acetonylreaktionen, in dem verwendeten Mechanismus noch nicht vollständig sind und aktuell überarbeitet werden.

Zusammenfassung

Im Rahmen dieser Arbeit wurde die Niedertemperaturoxidation von Mischungen aus *n*-Pentan und den oxygenierten Isomeren Dimethylether oder Ethanol bei einer Stöchiometrie von 0.7 und einem Druck von 970 mbar im Temperaturbereich von 450-930 K in einem laminaren Strömungsreaktor mittels Molekularstrahl-Massenspektrometrie unter Verwendung von Elektronenstoßionisation untersucht. Für eine Vielzahl von Spezies wurden quantitative Molenbruchprofile in Abhängigkeit von der Temperatur erhalten. Spezies für die eine Quantifizierung aufgrund fehlender Referenzdaten nicht erfolgen konnte wurden mithilfe einer Normierung vergleichbar gemacht, um relative Trends und Effekte zwischen den Mischungen visualisieren zu können.

Durch die Analyse der Reaktivität der drei unterschiedlichen Brennstoffe und ihrer Mischungen wurde festgestellt, dass Ethanol aufgrund seiner Struktur keine für die Niedertemperaturoxidation wichtigen OH-Radikale produziert, sondern selbige aktiv verbraucht und damit die Reaktivität des Gesamtsystems mit *n*-Pentan reduziert. Für Dimethylether, der als sehr reaktiver Brennstoff im Niedertemperaturbereich bekannt ist, konnten hingegen starke synergistische Effekte mit dem Oxidationsverhalten des ebenfalls aktiven *n*-Pentans gefunden werden. Mithilfe der temperaturabhängigen Brennstoffumsätze und der Betrachtung der Hauptreaktionszyklen für die Niedertemperaturoxidation konnten diese Beobachtungen erklärt werden. Ein zur Unterstützung der Ergebnisse herangezogenes kinetisches Modell konnte diese Trends ebenfalls gut wiedergeben. Bei der Betrachtung einiger relevanter Intermediatspezies konnten die experimentellen Befunde ebenfalls gut über die Reaktivität und Interaktion der Brennstoffe erklärt werden, hier ließen die Ergebnisse der kinetischen Modellierung aber oft noch Raum für Verbesserungen. Insbesondere einige relevante fehlende Reaktionswege müssen für die Weiterentwicklung des Modells in Betracht gezogen werden.

KAPITEL 6

Untersuchung der Hochtemperaturoxidation von 2-Pentanon

Kleine Methylketone sind als Vertreter der sogenannten Biokraftstoffe der zweiten Generation interessant, da sie eine hohe Oktanzahl und somit eine sehr hohe Klopffestigkeit aufweisen. Für Brennstoffe wie Aceton (RON=110-117 [118, 119]) und 2-Butanon (RON=117 [46]) wurden bereits niedrige Emissionen von Ruß, NO_x und unverbrannten Kohlenwasserstoffen im Vergleich zu anderen Biokraftstoffkandidaten wie Ethanol und 2-Methylfuran gemessen [46]. In einer vorgemischten laminaren Niederdruckflamme wurde für 2-Butanon sogar bereits gezeigt, dass vergleichsweise wenig Rußvorläuferspezies und toxische oxygenierte Spezies gebildet werden [61]. Pentanon weist aufgrund seiner größeren Atomanzahl eine höhere Energiedichte auf, weshalb es interessant ist, ob ein ähnlich positives Emissionsverhalten vorliegt. Bisher wurden jedoch vorrangig Untersuchungen zum symmetrischen 3-Pentanon durchgeführt [120–122], wohingegen das asymmetrische 2-Pentanon bisher kaum Aufmerksamkeit erhielt. Die lineare, dreiatomige Kohlenstoffkette kann jedoch zu Veränderungen in der Kinetik beitragen, was sich zum einen in Form eines verringerten Effekts der Carbonylgruppe äußern könnte, zum anderen aber auch eine erhöhte Bildung von Rußvorläuferspezies wie C_3H_3 bedingen kann. Bisher wurden für 2-Pentanon vorrangig Zündverzugszeiten im Temperaturbereich von 1000-1500 K und für Drücke von 2.65, 20 und 40 bar gemessen [123, 124]. Eine vollständige Analyse der Kinetik mithilfe von Speziesprofilen liegt bisher nicht vor. Daher wurden im Rahmen dieser Arbeit Messungen in einer brennstoffreichen laminaren vorgemischten 2-Pentanon-Niederdruckflamme durchgeführt und 47 Spezies mithilfe von EI- und PI-MBMS quantifiziert. Darüber hinaus wurden die experimentell erhaltenen Daten durch die Modellierung mit einem kinetischen Modell aus der Arbeitsgruppe *Physical Chemical Fundamentals of Combustion* der *RWTH Aachen* zur Beschreibung der Hochtemperaturkinetik unterstützt, welches aus einem bereits existierenden Basismechanismus und neuen Berechnungen für den Submechanismus von 2-Pentanon besteht. Die erhaltenen Ergebnisse wurden in Form des Manuskripts [6] zur Veröffentlichung in *Proceedings of the Combustion Institute* eingereicht und sind bereits positiv begutachtet worden.

Flammenmessungen und kinetische Modellierung

Eine laminare vorgemischte Niederdruckflamme ($p = 40$ mbar) des Brennstoffes 2-Pentanon ($C_5H_{10}O/O_2$/Ar: 0.093/0.407/0.500) mit einer Stöchiometrie von $\phi = 1.6$ und einer Kaltgasgeschwindigkeit von 73.85 cm/s (bei den Einlassbedingungen von 333 K und 40 mbar; 2.574 cm/s bei 298 K und 1 atm) wurde mithilfe von EI-MBMS in Bielefeld und PI-MBMS an der *Advanced Light Source* in Berkeley, USA untersucht. Für die Ergebnisse beider Apparaturen wurden gute Übereinstimmungen gefunden; diese Kreuzvalidierung reduziert die Ungenauigkeiten in der Quantifizierung der Molenbruchprofile erheblich. Mithilfe der

schmalen Energieverteilung der Photoionisation wurden Messungen bei unterschiedlichen Photonenenergien durchgeführt, um spezifische Isomerengruppen voneinander trennen zu können. Außerdem wurden Photoionisationseffizienzkurven (PIE-Kurven) aufgenommen, um die entsprechend auftretenden Isomere identifizieren zu können. Im Folgenden werden daher nur die Ergebnisse der PI-MBMS-Messungen vorgestellt.

Zum Vergleich der experimentell erhaltenen Daten und zur Analyse der Kinetik in der Verbrennung von 2-Pentanon wurde darüber hinaus ein kinetisches Modell verwendet. Dazu wurde der aktuelle AramcoMech 2.0 [125] zusammen mit einem Submechanismus für 2-Butanon von Hemken *et al.* [62] und einem Submechanismus für kleine aromatische Spezies von Zhang *et al.* [126] als Basismechanismus verwendet und um einen neuen Submechanismus für die Hochtemperaturkinetik von 2-Pentanon ergänzt. Dieser wurde in Analogie zu den Reaktionen von 2-Butanon [63] und *n*-Pentan [87] von Kooperationspartnern des Instituts für *Physical Chemical Fundamentals of Combustion* der *RWTH Aachen* entwickelt. Außerdem wurden dort die Thermochemie sowie die Transporteigenschaften für 2-Pentanon und die entsprechenden Brennstoffradikale berechnet und in den Mechanismus integriert. Das Modell wurde zusätzlich zu den hier vorgestellten Flammendaten auch gegen Zündverzugszeiten aus der Literatur [123, 124] validiert. Das für die Simulation benötigte Temperaturprofil der Flamme wurde nach der in Kap. 2.5 vorgestellten Methode von Isabelle Graf in Bielefeld gemessen.

Brennstoffabbau und primäre Intermediate

Der primäre Brennstoffabbau über die im Hochtemperaturbereich typische H-Abstraktion gefolgt von einer β-Spaltung (vgl. Kap. 2.1) ist für 2-Pentanon in Abb. 6.1 dargestellt. Die prozentualen Anteile der Reaktionswege wurden im Bereich von einer Höhe über der Brenneroberfläche $h = 0 - 3.3$ mm (korrespondierend zu einem Brennstoffumsatz bis 20 %) aus dem Modell erhalten. Die zuerst erfolgende H-Abstraktion liefert vier Brennstoffradikale (C_5H_9O). Das 2-Pentanon-1-ylradikal wird in etwa zu gleichen Teilen über eine C-C-β-Spaltung zu Keten und Propyl (42 %) und über eine Isomerisierung zum 2-Pentanon-3-ylradikal (45 %) umgesetzt. Letzteres wird ausschließlich über C-C-β-Spaltungen zum Methylradikal und C_4H_6O abgebaut, wobei die Spaltung zwischen dem C4 und C5, aus der Methylvinylketon entsteht, mit 99.9 % deutlich gegenüber der Spaltung zwischen dem C1 und C2 zu Ethylketen (0.01 %) überwiegt. Dieses Ergebnis liegt darin begründet, dass der Reaktionsgeschwindigkeitskoeffizient für die Spaltung auf der Alkylseite im Modell aufgrund der höheren Aktivierungsenergie mehr als zwei Größenordnungen über dem für die Carbonylseite liegt. Aus dem 2-Pentanon-4-ylradikal werden größtenteils Propen und Acetyl über die C-C-β-Spaltung gebildet (91.5 %), während die C-H-β-Spaltung zu 3-Penten-2-on nur mit 8.5 % vorhergesagt wird. Diese Reaktion fällt für das 2-Pentanon-5-ylradikal mit nur 0.5 % zu 4-Penten-2-on sogar noch geringer aus. Hier überwiegt die C-C-β-Spaltung zu Ethen und Acetonyl mit 97 % stark.

Da die direkt gebildeten Brennstoffradikale mit dem verwendeten PI-MBMS-Experiment nicht getrennt und quantifiziert werden können, wurden deren primäre Abbauprodukte im Experiment untersucht. In Abb. 6.2 sind die Molenbruchprofile der stabilen Spaltungsprodukte der 2-Pentanon-1-yl-, -4-yl- und -5-ylradikale, nämlich Keten (a), Propen (b) und Ethen (c) dargestellt. Die grauen Schattierungen geben dabei einen Fehlerbereich von

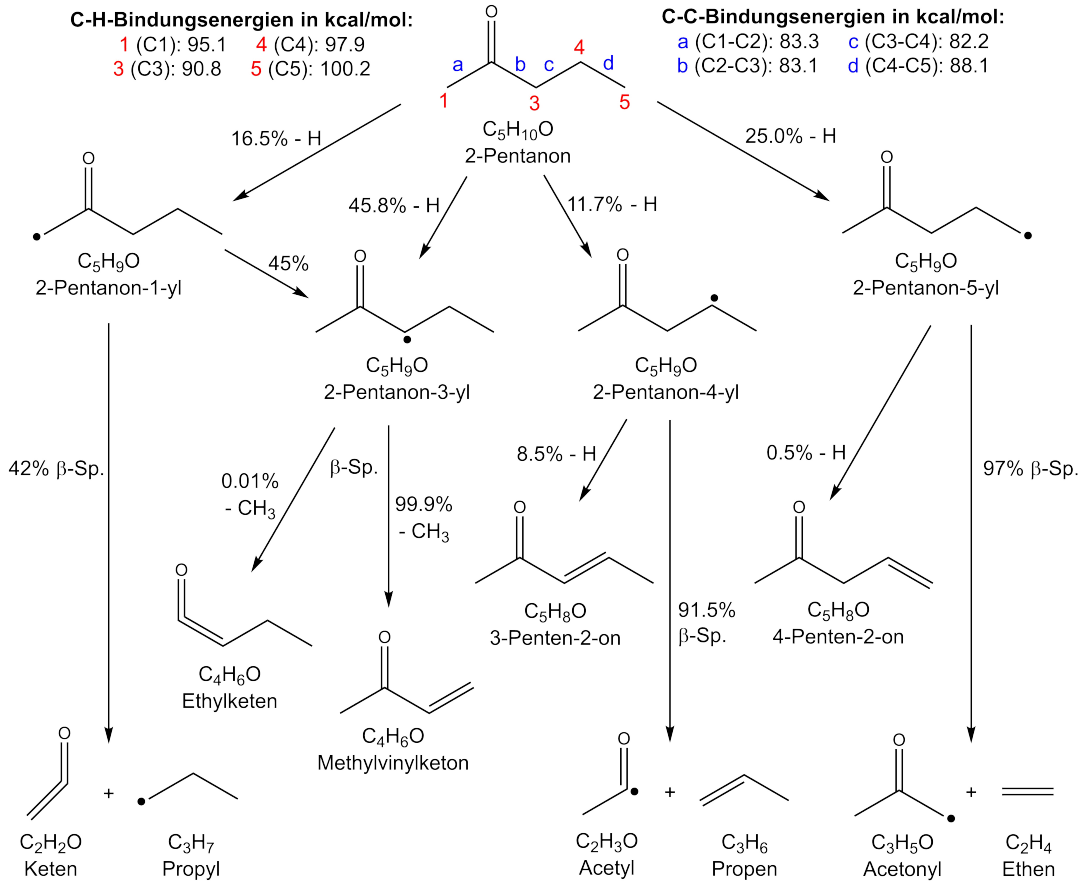

Abbildung 6.1: Reaktionsschema für 2-Pentanon aus der Reaktionsflussanalyse für die untersuchten Flammenbedingungen im Bereich von einer Höhe über der Brenneroberfläche $h = 0-3.3$ mm (korrespondierend zu einem Brennstoffumsatz bis 20 %) mit den entsprechenden prozentualen Angaben zur Wahrscheinlichkeit der Reaktionswege neben den Pfeilen. Die für das Brennstoffmolekül 2-Pentanon angegebenen C-H- und C-C-Bindungsenergien wurden aus den thermochemischen Daten des kinetischen Modells bestimmt. Adaptiert von [6].

einem Faktor 2 wieder, um einen übersichtlichen Vergleich mit dem Modell zu schaffen. Keten und Propen weisen maximale Molenbrüche im Bereich von $2-3 \cdot 10^{-3}$ auf, während der von Ethen mit $2.4 \cdot 10^{-2}$ etwa eine Größenordnung darüber liegt. Die Ergebnisse der kinetischen Modellierung stimmen für Propen und Ethen exzellent mit den experimentellen Ergebnissen überein, während Keten mit etwas mehr als einem Faktor 2 überschätzt wird. Dieses Phänomen wurde bereits in einer vorherigen Flammenuntersuchung für 2-Butanon von Hemken *et al.* [61] beobachtet und konnte bereits dort und auch in einer weiteren Arbeit von Minwegen *et al.* [123] auf die Unvollständigkeit des Aceton-Submechanismus im verwendeten Basismechanismus zurückgeführt werden, da Keten dort vorrangig aus dem Acetonylradikal gebildet wird. Insgesamt deutet die gute Übereinstimmung des Modells für die primären Spezies bereits auf einen relativ gut funktionierenden Submechanismus für 2-Pentanon hin.

Die weiteren primären Spezies, die aus dem 2-Pentanon-3-yl Radikal gebildet werden, sind neben CH_3 stabile Isomere der Summenformel C_4H_6O. Im zuerst durchgeführten

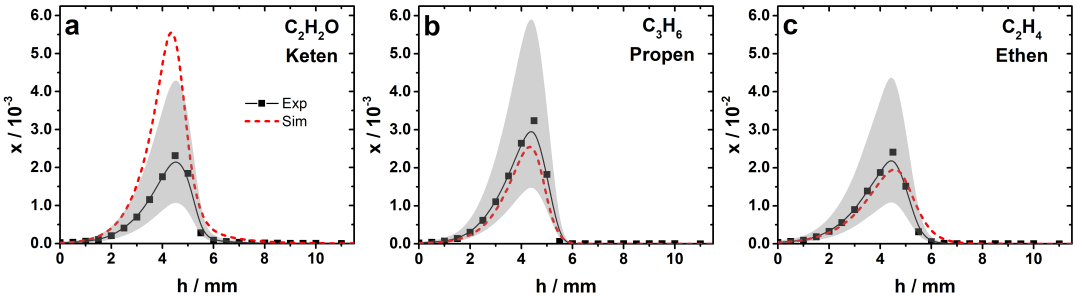

Abbildung 6.2: Molenbruchprofile ausgewählter primärer Intermediate nach initialer H-Abstraktion und anschließender β-Spaltung. Symbole: Experimentelle Ergebnisse mit einem grau schattierten experimentellen Fehler von einem Faktor 2, durchgezogene Linien: Verbindung der experimentellen Datenpunkte mit einer *Spline*-Funktion zur besseren Übersicht, unterbrochene Linien: Ergebnisse der kinetischen Modellierung. Adaptiert von [6].

EI-MBMS-Experiment konnten Methylvinylketon und Ethylketen nicht unterschieden werden. Aufgrund der stark unterschiedlichen Vorhersagen für beide Isomere ist es jedoch von besonderem Interesse, die Ergebnisse der kinetischen Modellierung mithilfe experimenteller Daten zu überprüfen. Mithilfe des PI-MBMS-Experiments konnten Messungen unterschiedlicher Photonenenergien durchgeführt und so die beiden Isomere getrennt werden. Für die Quantifizierung wird jedoch, wie bereits in Kap. 2.4 erläutert, für jede Spezies ein Photoionisationsquerschnitt benötigt. Für Ethylketen ist jedoch bisher kein solcher Wert tabelliert. Um dennoch eine erste Quantifizierung vornehmen zu können, wurde der Photoionisationsquerschnitt für Ethylketen daher mithilfe eines gemessenen Photoelektronenspektrums (PES) von Bock *et al.* [127] abgeschätzt. Dazu wurde das PES integriert und in Analogie zum Photoionisationsquerschnitt von Keten von Yang *et al.* [88] mit einem Wert von 24 Mb bei 10.35 eV skaliert. Für die Quantifizierung von Ethylketen ergibt sich damit eine erhöhte Unsicherheit, die hier mit einem Faktor 5-10 abgeschätzt wurde. Dadurch kann jedoch ein Vergleich der C_4H_6O Isomere erfolgen. In Abb. 6.3a sind die quantifizierten Molenbruchprofile für Methylvinylketon und Ethylketen dargestellt. Durch den verwendeten Faktor von 25 für die Darstellung des Molenbruchs von Ethylketen ist bereits die stark unterschiedliche Bildung beider Spezies ersichtlich. Methylvinylketon wird mit einem maximalen Molenbruch von $2.4 \cdot 10^{-3}$ mehr als hundert Mal so viel gebildet wie Ethylketen ($1.6 \cdot 10^{-5}$). Damit liegt der höhere Fehler aus der abgeschätzten Quantifizierung deutlich unterhalb des Molenbruchunterschieds und ist daher gut vertretbar. Zur eindeutigen Zuordnung der Isomere und einer weiteren Kreuzvalidierung des erhaltenen Verhältnisses wurde zudem eine PIE-Kurve aufgenommen. Diese ist in Abb. 6.3b einmal direkt (schwarze Quadrate) und einmal multipliziert mit einem Faktor von 25 (blaue Kreise) dargestellt, um auch den Anstieg bei ca. 8.8 eV zu visualisieren. Zudem sind sowohl der abgeschätzte Photoionisationsquerschnitt für Ethylketen als auch der für Methylvinylketon von Yang *et al.* [88] sowie die entsprechenden Ionisationsenergien beider Spezies [88, 127] eingezeichnet. Da die Anstiege im Photoionisationseffizienzsignal ausgezeichnet mit den Querschnitten und Ionisationsenergien von Ethylketen und Methylvinylketon übereinstimmen, kann die Existenz beider Spezies verifiziert werden. Durch die Skalierung der Querschnitte wird ein Verhältnis von 99.4 % Methylvinylketon und 0.6 % Ethylketen erhalten, welches sich perfekt mit dem Ergebnis der Molenbruchprofile in Abb. 6.3a (99.3 % Methylvinylketon, 0.7 % Ethylketen) deckt. Mit diesen experimentellen Ergebnissen konnte

zudem die stark unterschiedliche Vorhersage des kinetischen Modells für die beiden Isomere bestätigt werden.

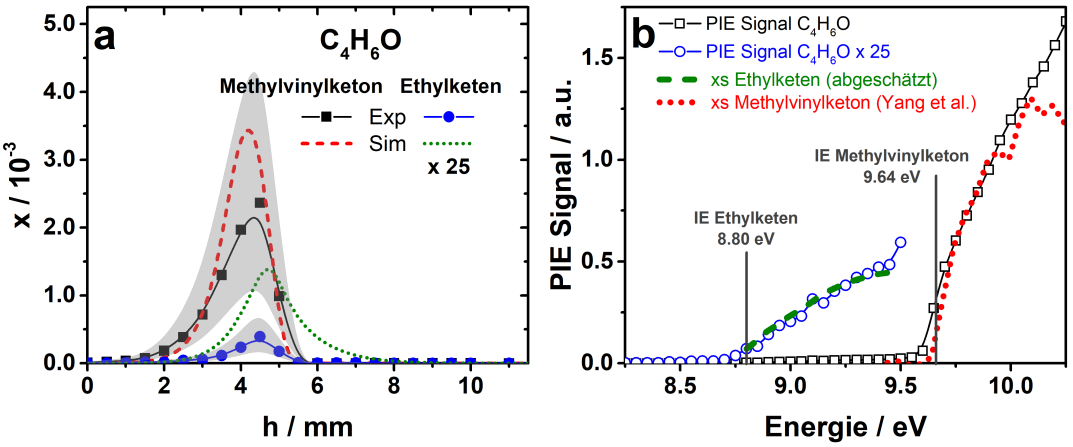

Abbildung 6.3: (a) Molenbruchprofile der detektierten C_4H_6O Isomere. Symbole: Experimentelle Ergebnisse mit einem grau schattierten experimentellen Fehler von einem Faktor 2, durchgezogene Linien: Verbindung der experimentellen Datenpunkte mit einer *Spline*-Funktion zur besseren Übersicht, unterbrochene Linien: Ergebnisse der kinetischen Modellierung. Für Ethylketen wurden sowohl experimentelle als auch modellierte Ergebnisse mit einem Faktor von 25 multipliziert. (b) Signal der Photoionisationseffizienz (PIE) für C_4H_6O (Quadrate) und erneut dargestellt und mit einem Faktor von 25 multipliziert (Kreise), um den frühen Anstieg sichtbar zu machen. Die Photoionisationsquerschnitte (xs) von Ethylketen (abgeschätzt, s. Text) und Methylvinylketon [88] wurden skaliert und zum Vergleich eingezeichnet. Die Ionisationsenergien (IE) von Ethylketen [127] und Methylvinylketon [88] sind in Form von horizontalen Linien dargestellt. Adaptiert von [6].

Niedertemperaturspezies

In der untersuchten Flamme konnten auch einige Spezies detektiert werden, die üblicherweise als Indiz für das Vorliegen einer Niedertemperaturkinetik gewertet werden. Die Bildung solcher Spezies in der Hochtemperaturumgebung der Flamme ist besonders interessant und konnte auch bereits in bisherigen Flammenuntersuchungen beobachtet werden [37, 61]. In Abb. 6.4 sind das Molenbruchprofil für Formaldehyd (a) und die korrigierten Signalintensitäten für C_5H_8O (b) und $C_5H_8O_2$ (c) dargestellt. Für Formaldehyd und C_5H_8O kann ein Versatz des Maximums von 1-2 mm zwischen den experimentellen Daten und der kinetischen Modellierung festgestellt werden. $C_5H_8O_2$ ist nicht im Speziespool des Modells enthalten. In diesem Zusammenhang sei daran erinnert, dass es sich bei dem verwendeten Modell und dem neu entwickelten Submechanismus für 2-Pentanon um eine reine Beschreibung der Hochtemperaturkinetik handelt. Typische Reaktionsklassen der Niedertemperaturkinetik (vgl. Kap. 2.1 und Abb. 2.1b) sind nicht im kinetischen Modell enthalten, wodurch eine Bildung der hier vorgestellten Spezies nicht korrekt modelliert werden kann. Die experimentellen Ergebnisse zeigen, dass Niedertemperaturreaktionen in Form von Sauerstoffadditionen in der Vorheizzone der Flamme stattfinden und für ein vollständiges Modell der Kinetik von 2-Pentanon berücksichtigt werden müssen.

Formaldehyd (Abb. 6.4a) wird vorrangig über die Reaktion von CH_3 mit O gebildet. CH_3

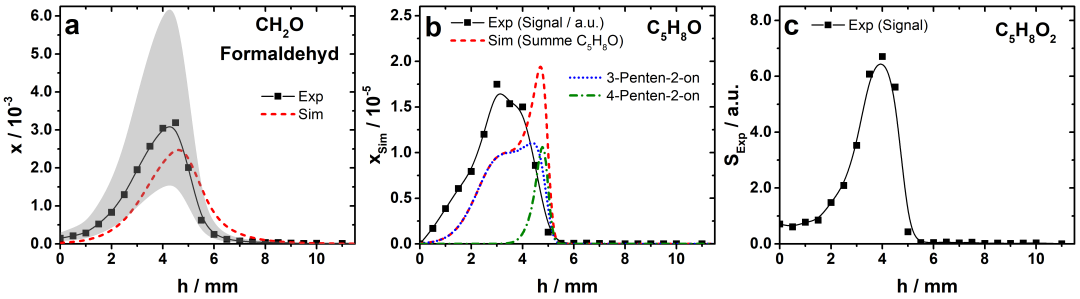

Abbildung 6.4: Profile ausgewählter oxygenierter Spezies zur Analyse der Niedertemperaturchemie. Für Formaldehyd (a) ist das Molenbruchprofil mit einem grau schattierten experimentellen Fehler von einem Faktor 2 gezeigt, während für C_5H_8O (b) und $C_5H_8O_2$ (c) aufgrund mangelnder Photoionisationsquerschnitte nur die korrigierten Signale dargestellt sind. Symbole: Experimentelle Ergebnisse, durchgezogene Linien: Verbindung der experimentellen Datenpunkte mit einer *Spline*-Funktion zur besseren Übersicht, unterbrochene Linien: Ergebnisse der kinetischen Modellierung. Adaptiert von [6].

kann auf vielen Wegen gebildet werden, unter anderem auch durch die C-C-β-Spaltung des 2-Pentanon-3-ylradikals (vgl. Abb. 6.1) relativ zu Beginn des Brennstoffabbaus, aber auch aus dem Abbau von Propyl-, Ethyl- und Acetonylradikalen. Spezies mit der Summenformel C_5H_8O (Abb. 6.4b) können den Pentenonen zugeordnet werden. Diese können wie in Abb. 6.1 dargestellt über eine C-H-β-Spaltung aus den Brennstoffradikalen, aber auch über eine O_2-Addition an das Brennstoffmolekül und eine anschließende HO_2-Eliminierung gebildet werden. Für letztere werden deutlich niedrigere Temperaturen benötigt. Die breite Form des Profils von C_5H_8O spricht für eine Kombination aus beiden Prozessen, abhängig von der Temperatur der Flamme in den jeweiligen Zonen. Ein ebenfalls früher Anstieg des Profils wird für $C_5H_8O_2$ beobachtet, das Maximum des Signals liegt jedoch ca. 1 mm weiter entfernt von der Brenneroberfläche als für C_5H_8O. Mögliche Strukturen korrespondierend zu $C_5H_8O_2$ entsprechen dem 2,4-Pentadion oder mehreren möglichen zyklischen Ethern. 2,4-Pentadion müsste über einer Radikalrekombination eines Acetyl- (C_2H_3O) und eines Acetonylradikals (C_3H_5O) gebildet werden, welche aus kinetischer Sicht relativ unwahrscheinlich ist, da das Acetonylradikal mesomeriestabilisiert ist, während Acylradikale in der Regel über eine α-Spaltung in das thermisch extrem stabile CO und ein Alkylradikal zerfallen. Zyklische Ether werden insbesondere im Bereich der Niedertemperaturkinetik durch eine O_2-Addition an das Brennstoffmolekül und eine anschließende Isomerisierung zum QOOH gebildet (vgl. Abb. 2.1b). Die Position des Profils spricht aber eher für eine bereits höher liegende Temperatur zur Bildung von $C_5H_8O_2$. Für die infrage kommenden Spezies sind keine Ionisationsenergien oder Photoionisationsquerschnitte tabelliert, sodass ein beobachteter Anstieg bei 9.1-9.3 eV in der PIE-Kurve von $C_5H_8O_2$ keiner Spezies direkt zugeordnet werden kann. Durch Einbeziehung typischer Reaktionsklassen der Niedertemperaturkinetik von 2-Pentanon in das verwendete Modell könnten daher mögliche Reaktionswege und Spezies aufgeklärt werden.

Zusammenfassung

In dieser Arbeit wurde eine brennstoffreiche laminare Niederdruckflamme des Brennstoffes 2-Pentanon mithilfe von EI- und PI-MBMS untersucht. Dabei wurden die Molenbruchprofile einer Vielzahl bei der Verbrennung von 2-Pentanon auftretender Spezies aufgenommen und

einige Spezies auch isomerenselektiv quantifiziert. Darüber hinaus wurde ein kinetisches Modell zur Beschreibung der Hochtemperaturkinetik von 2-Pentanon in Kooperation mit der *RWTH Aachen* entwickelt und zum Vergleich der experimentell erhaltenen Daten herangezogen. Mithilfe einer aus dem Modell erhaltenen Reaktionsflussanalyse der untersuchten Flammenbedingungen wurde die Bildung erster intermediärer Spezies analysiert. Dabei konnte für Keten, Propen, und Ethen eine gute Übereinstimmung zwischen Experiment und Modell gefunden werden, was die Funktionalität des neu entwickelten 2-Pentanon Submechanismus unterstreicht. Auch das Verhältnis der primär gebildeten Isomere Methylvinylketon und Ethylketen konnte mithilfe der isomerenselektiven PI-MBMS-Messungen eindeutig bestätigt werden. Darüber hinaus wurden Spezies und Reaktionswege beobachtet, die auf Reaktionen der Niedertemperaturkinetik hinweisen. Diese Erkenntnisse sprechen eindeutig für die Notwendigkeit, Reaktionen der Niedertemperaturkinetik von 2-Pentanon in das bestehende kinetische Modell zu integrieren.
Im Vergleich zum kleineren Methylketon 2-Butanon ist 2-Pentanon zwar aufgrund der höheren Energiedichte zu bevorzugen, jedoch ergab sich bezüglich der Bildung von toxischen Spezies in der Verbrennung von 2-Pentanon eine vergleichbare Konzentration von Formaldehyd und eine um etwa einen Faktor fünf höhere Konzentration des toxischen Methylvinylketon. Die vorliegenden experimentellen Ergebnisse können nun in erster Linie zur weiteren Untersuchung und Entwicklung kinetischer Modelle für Methylketone und eine Erweiterung des Modells um die Niedertemperaturkinetik verwendet werden.

KAPITEL 7

Zusammenfassung und Ausblick

In dieser Arbeit wurde die Oxidationschemie verschiedener konventioneller und alternativer Brennstoffe und deren Gemische unter verschiedenen Bedingungen ausführlich untersucht. Dazu wurden mit der laminaren vorgemischten Niederdruckflamme und dem laminaren Strömungsreaktor zwei ideale Modellexperimente genutzt, die sowohl im Druck- als auch Temperaturbereich ein großes Parameterfeld der Verbrennung abdecken. Zur Analytik der bei der Verbrennung entstehenden Spezies wurde die Molekularstrahl-Massenspektrometrie als bewährtes Instrument eingesetzt, da mit ihr eine Vielzahl stabiler und reaktiver Spezies gleichzeitig identifiziert und quantifiziert werden kann. Zur optimalen Strukturaufklärung wurde eine Kombination verschiedener Ionisationstechniken genutzt, da jede ihre individuellen Stärken und Grenzen aufweist.

In dieser Arbeit konnte gezeigt werden, dass eine Kombination mehrerer experimenteller Methoden mit einer zusätzlichen Unterstützung durch spezifische Referenzmessungen, theoretische Berechnungen und kinetische Modellierungen zu einem umfassenden Verständnis der Oxidationschemie komplexer Brennstoffmoleküle beitragen kann. Dazu wurden Messungen mit zum Teil hohem apparativen Aufwand und Messzeit an Großanlagen benötigt. So konnten in dieser Arbeit die Photoelektronenspektren von 18 in der Verbrennungschemie wichtigen Intermediatspezies aufgenommen und zur Identifizierung dieser Spezies genutzt werden. Dies ist ein besonders wichtiger Aspekt, da im Bereich der Analytik von Oxidationsintermediaten oft wesentliche Literaturdaten fehlen, die zur Identifizierung und Quantifizierung der auftretenden Spezies erforderlich sind. Selbstverständlich können solche Daten auch mithilfe von theoretischen Berechnungen bestimmt werden, was im Rahmen der hier vorgestellten Arbeiten auch zusätzlich genutzt wurde, jedoch sind solche Berechnungen auch mit hohem Zeit- und Kostenaufwand verbunden. Um Vergleichbarkeit mit experimentellen Daten sicherzustellen, müssen diese zudem idealerweise für die exakten experimentellen Randbedingungen bereitgestellt werden. In dieser Arbeit wurde daher gezeigt, dass die Messung von Referenzdaten am identischen Experiment von großem Nutzen ist.

Die Bildung von Verbrennungsintermediaten wurde für die verschiedenen durchgeführten Experimente zusätzlich auch mithilfe kinetischer Modellierungen simuliert, die auf die Messung von experimentellen Daten zur Weiterentwicklung und Validierung angewiesen sind. Mithilfe der Ergebnisse dieser Arbeit konnten wesentliche Erkenntnisse in die weitere Modellentwicklung verschiedener kinetischer Modelle einfließen. Zum Beispiel wurde in der Verbrennung von *iso*-Pentan eindeutig die Existenz einiger Spezies nachgewisen, die zuvor nicht im Modell enthalten waren. Auch für die Verbrennung von Diethylether konnte das vermutete Intermediat Ethylvinylether, welches erst kürzlich in ein entsprechendes Modell

aufgenommen wurde, eindeutig identifiziert werden und so die quantitative Vorhersage der Spezies optimiert werden. Darüber hinaus wurde jedoch auch gezeigt, dass die Entwicklung kinetischer Modelle an einigen Stellen noch Potential zur Optimierung aufweist. Insbesondere die experimentellen Ergebnisse zu Brennstoffgemischen und der Interaktion der Reaktionswege zweier Brennstoffmoleküle zeigten eindeutig, dass die verwendeten Modelle noch nicht vollständig in der Lage sind, solche Gemische zu modellieren.

Insgesamt wurde in dieser Arbeit an mehreren Beispielen festgestellt, dass die Brennstoffstruktur signifikant für den Verlauf der möglichen Reaktionswege und somit die Bildung von möglichen Schadstoffen verantwortlich ist. Dieses Kriterium wurde auch für die Addition unterschiedlicher Komponenten festgestellt. So wurden für die Addition von potentiellen Biokraftstoffen der gleichen Summenformel, aber unterschiedlicher Struktur (Alkohol und Ether), sowohl im Hoch- als auch im Niedertemperaturbereich unterschiedliche Einflüsse auf die Schadstoffbildung erhalten. Während im Hochtemperaturbereich vorrangig die Bildung von höhermolekularen Spezies beeinflusst wurde, wurde im Niedertemperaturbereich eine signifikante Auswirkung des Additivs auf die Reaktivität des Brennstoffgemisches beobachtet.

Ausblick

Für den Hochtemperaturbereich können die ersten stabilen Zerfallsprodukte, die im Experiment sehr zuverlässig bestimmt werden können, schon relativ gut von kinetischen Modellen vorhergesagt werden. Es sind jedoch die ersten radikalischen Zerfallsprodukte, die im Verbrennungsprozess besonders wichtig sind, da sie maßgeblich den weiteren Reaktionsverlauf bestimmen. Diese Spezies können jedoch nur mit sehr hohem experimentellem und theoretischem Aufwand quantifiziert werden [40, 42, 128, 129]. Gerade für Mischungen und insbesondere im Niedertemperaturbereich führen Interaktionen dieser ersten gebildeten radikalischen Spezies zu in Verbrennungsmodellen noch nicht enthaltenen Intermediaten und einer veränderten Reaktivität des Mischungssystems, weshalb hier noch ein erhöhtes Potential sowohl im experimentellen Bereich als auch in der Modellentwicklung liegt. Jedoch ist dies nicht nur für Brennstoffgemische eine große Herausforderung. Auch ein einzelnes Brennstoffmolekül, für das eine kinetische Modellierung über den Hochtemperaturbereich bereits gut möglich ist, stellt Modellierer im Niedertemperaturbereich bereits vor größere Schwierigkeiten, da in dieser Oxidationsumgebung sehr viele komplexe Reaktionen ablaufen. Dabei können mehrere aufeinanderfolgende Sauerstoffadditionen zur Bildung von hochoxidierten Spezies bis hin zu sogenannten sekundären organischen Aerosolen (SOAs) führen [130, 131]. Zum Verständnis der Bildungswege solcher Spezies sind umfassende Experimente mit hohem apparativem Aufwand, hoher Sensitivität und hoher Auflösung notwendig, wie kürzlich von Wang *et al.* [132, 133] gezeigt wurde. Erste Ergebnisse dieser Untersuchungen von Wang *et al.* zeigten auch, dass die Speziesverteilung unter motorischen Bedingungen, d.h. unter erhöhtem Druck, näherungsweise der unter Normaldruck im Modellexperiment entspricht. Modellexperimente wie die hier verwendeten können also durchaus hilfreiche Ergebnisse für den Anwendungsbereich der motorischen Verbrennung liefern. Eine detailliertere Aufklärung der Interaktion von Reaktionswegen in Brennstoffgemischen mithilfe solcher Methoden ist daher in Zukunft notwendig, um die Modellentwicklung für die Vorhersage der Schadstoffbildung möglicher zukünftiger Kraftstoffadditive zu optimieren.

Literaturverzeichnis

[1] J. Pieper, S. Schmitt, C. Hemken, E. Davies, J. Wullenkord, A. Brockhinke, J. Krüger, G.A. Gustavo, L. Nahon, A. Lucassen, W. Eisfeld und K. Kohse-Höinghaus, Isomer Identification in Flames with Double-Imaging Photoelectron/Photoion Coincidence Spectroscopy (i^{2}PEPICO) using Measured and Calculated Reference Photoelectron Spectra, *Z. Phys. Chem.*, **232**(2), 153–187, 2018.

[2] D. Felsmann, A. Lucassen, J. Krüger, C. Hemken, L.S. Tran, J. Pieper, G.A. Garcia, A. Brockhinke, L. Nahon und K. Kohse-Höinghaus, Progress in Fixed-Photon-Energy Time-Efficient Double Imaging Photoelectron/Photoion Coincidence Measurements in Quantitative Flame Analysis, *Z. Phys. Chem.*, **230**(8), 1067–1097, 2016.

[3] L.S. Tran, J. Pieper, H.-H. Carstensen, H. Zhao, I. Graf, Y. Ju, F. Qi und K. Kohse-Höinghaus, Experimental and kinetic modeling study of diethyl ether flames, *Proc. Combust. Inst.*, **36**, 1165–1173, 2017.

[4] L.S. Tran, J. Pieper, M. Zeng, Y. Li, X. Zhang, W. Li, I. Graf, F. Qi und K. Kohse-Höinghaus, Influence of the biofuel isomers diethyl ether and n-butanol on flame structure and pollutant formation in premixed n-butane flames, *Combust. Flame*, **175**, 47–59, 2017.

[5] H. Jin, J. Pieper, C. Hemken, E. Bräuer, L. Ruwe und K. Kohse-Höinghaus, Chemical interaction of dual-fuel mixtures in low-temperature oxidation, comparing n-pentane/dimethyl ether and n-pentane/ethanol, *Combust. Flame, zur Veröffentlichung akzeptiert*, 2018.

[6] J. Pieper, C. Hemken, R. Büttgen, I. Graf, N. Hansen, K.A. Heufer und K. Kohse-Höinghaus, A high-temperature study of 2-pentanone oxidation: experiment and kinetic modeling, *Proc. Combust. Inst., eingereicht, positiv begutachtet, in Überarbeitung*, 2018.

[7] World Energy Outlook Special Report, http://www.iea.org/publications/freepublications, 2017.

[8] The International Council on Clean Transportation (ICCT), http://www.theicct.org, 2012.

[9] Global Carbon Project, http://www.globalcarbonatlas.org.

[10] T.C. Bond et al., Bounding the role of black carbon in the climate system: A scientific assessment, *J. Geophys. Res. Atmos.*, **118**(11), 5380–5552, 2013.

[11] S.S. Lim et al., A comparative risk assessment of burden of disease and injury attributable to 67 risk factors and risk factor clusters in 21 regions, 1990–2010:

a systematic analysis for the Global Burden of Disease Study 2010, *The Lancet*, **380**(9859), 2224–2260, 2012.

[12] Institute for Health, Metrics and Evaluation (IHME), https://vizhub.healthdata.org/gbd-compare, 2016.

[13] S.C. Anenberg, J. Schwartz, D.T. Shindell, M. Amann, G. Faluvegi, Z. Klimont, G. Janssens-Maenhout, L. Pozzoli, R. Van Dingenen, E. Vignati, L. Emberson, N.Z. Muller, J.J. West, M. Williams, V. Demkine, W.K. Hicks, J. Kuylenstierna, F. Raes und V. Ramanathan, Global Air Quality and Health Co-benefits of Mitigating Near-Term Climate Change through Methane and Black Carbon Emission Controls, *Environ. Health Perspect.*, **120**(6), 831–839, 2012.

[14] R.A. Silva et al., Global premature mortality due to anthropogenic outdoor air pollution and the contribution of past climate change, *Environ. Res. Lett.*, **8**(3), 034005, 2013.

[15] A. Sydbom, A. Blomberg, S. Parnia, N. Stenfors, T. Sandström und S.E. Dahlén, Health effects of diesel exhaust emissions, *Eur. Respir. J.*, **17**(4), 733–746, 2001.

[16] J.F. Mejía, S.L. Choy, K. Mengersen und L. Morawska, Methodology for assessing exposure and impacts of air pollutants in school children: Data collection, analysis and health effects – A literature review, *Atmos. Environ.*, **45**(4), 813–823, 2011.

[17] A.A. Mehus, R.J. Reed, V.S.T. Lee, S.R. Littau, C. Hu, E.A. Lutz und J.L. Burgess, Comparison of Acute Health Effects From Exposures to Diesel and Biodiesel Fuel Emissions., *J. Occup. Environ. Med.*, **57**(7), 705–712, 2015.

[18] D. Larcher und J.-M. Tarascon, Towards greener and more sustainable batteries for electrical energy storage, *Nat. Chem.*, **7**(1), 19–29, 2015.

[19] BP Energy Outlook, https://www.bp.com/en/global/corporate/media/reports-and-publications.html, 2018.

[20] M.A. Delucchi und M.Z. Jacobson, Providing all global energy with wind, water, and solar power, Part II: Reliability, system and transmission costs, and policies, *Energy Policy*, **39**(3), 1170–1190, 2011.

[21] J. Blunden und D.S. Arndt, https://www.ametsoc.org/ams/index.cfm/publications/bulletin-of-the-american-meteorological-society-bams/state-of-the-climate, 2016.

[22] K. Kohse-Höinghaus, Clean combustion: Chemistry and diagnostics for a systems approach in transportation and energy conversion, *Prog. Energy Combust. Sci.*, **65**, 1–5, 2018.

[23] K. Kohse-Höinghaus, P. Oßwald, T.A. Cool, T. Kasper, N. Hansen, F. Qi, C.K. Westbrook und P.R. Westmoreland, Biofuel Combustion Chemistry: From Ethanol to Biodiesel, *Angew. Chem. Int. Ed.*, **49**(21), 3572–3597, 2010.

[24] C.-W. Zhou, Y. Li, E. O'Connor, K.P. Somers, S. Thion, C. Keesee, O. Mathieu, E.L. Petersen, T.A. DeVerter, M.A. Oehlschlaeger, G. Kukkadapu, C.-J. Sung, M. Alrefae,

F. Khaled, A. Farooq, P. Dirrenberger, P.-A. Glaude, F. Battin-Leclerc, J. Santner, Y. Ju, T. Held, F.M. Haas, F.L. Dryer und H.J. Curran, A comprehensive experimental and modeling study of isobutene oxidation, *Combust. Flame*, **167**, 353–379, 2016.

[25] S.M. Sarathy, P. Oßwald, N. Hansen und K. Kohse-Höinghaus, Alcohol combustion chemistry, *Prog. Energy Combust. Sci.*, **44**, 40–102, 2014.

[26] N. Hansen, T.A. Cool, P.R. Westmoreland und K. Kohse-Höinghaus, Recent contributions of flame-sampling molecular-beam mass spectrometry to a fundamental understanding of combustion chemistry, *Prog. Energy Combust. Sci.*, **35**(2), 168–191, 2009.

[27] F. Qi, Combustion chemistry probed by synchrotron VUV photoionization mass spectrometry, *Proc. Combust. Inst.*, **34**, 33–63, 2013.

[28] K. Kohse-Höinghaus, Combustion Chemistry Diagnostics for Cleaner Processes, *Chem. Eur. J.*, **22**(38), 13390–13401, 2016.

[29] J. Zádor, H. Huang, O. Welz, J. Zetterberg, D.L. Osborn und C.A. Taatjes, Directly measuring reaction kinetics of QOOH – a crucial but elusive intermediate in hydrocarbon autoignition, *Phys. Chem. Chem. Phys.*, **15**(26), 10753–10760, 2013.

[30] Z. Wang, L. Zhang, K. Moshammer, D.M. Popolan-Vaida, V.S.B. Shankar, A. Lucassen, C. Hemken, C.A. Taatjes, S.R. Leone, K. Kohse-Höinghaus, N. Hansen, P. Dagaut und S.M. Sarathy, Additional chain-branching pathways in the low-temperature oxidation of branched alkanes, *Combust. Flame*, **164**, 386–396, 2016.

[31] F. Battin-Leclerc, O. Herbinet, P.-A. Glaude, R. Fournet, Z. Zhou, L. Deng, H. Guo, M. Xie und F. Qi, Experimental confirmation of the low-temperature oxidation scheme of alkanes, *Angew. Chem. Int. Ed.*, **49**(18), 3169–3172, 2010.

[32] P.T. Lynch, T.P. Troy, M. Ahmed und R.S. Tranter, Probing combustion chemistry in a miniature shock tube with synchrotron VUV photo ionization mass spectrometry, *Anal. Chem.*, **87**(4), 2345–2352, 2015.

[33] Y. Li und F. Qi, Recent Applications of Synchrotron VUV Photoionization Mass Spectrometry: Insight into Combustion Chemistry, *Acc. Chem. Res.*, **43**(1), 68–78, 2010.

[34] N. Hansen, M. Schenk, K. Moshammer und K. Kohse-Höinghaus, Investigating repetitive reaction pathways for the formation of polycyclic aromatic hydrocarbons in combustion processes, *Combust. Flame*, **180**, 250–261, 2017.

[35] L.S. Tran, B. Sirjean, P.A. Glaude, R. Fournet und F. Battin-Leclerc, Progress in detailed kinetic modeling of the combustion of oxygenated components of biofuels, *Energy*, **43**(1), 4–18, 2012.

[36] S.S. Merchant, C.F. Goldsmith, A.G. Vandeputte, M.P. Burke, S.J. Klippenstein und W.H. Green, Understanding low-temperature first-stage ignition delay: Propane, *Combust. Flame*, **162**(10), 3658–3673, 2015.

[37] L. Seidel, K. Moshammer, X. Wang, T. Zeuch, K. Kohse-Höinghaus und F. Mauss, Comprehensive kinetic modeling and experimental study of a fuel-rich, premixed n-heptane flame, *Combust. Flame*, **162**(5), 2045–2058, 2015.

[38] M. Schenk, L. Leon, K. Moshammer, P. Oßwald, T. Zeuch, L. Seidel, F. Mauss und K. Kohse-Höinghaus, Detailed mass spectrometric and modeling study of isomeric butene flames, *Combust. Flame*, **160**(3), 487–503, 2013.

[39] N. Hansen, T. Kasper, S.J. Klippenstein, P.R. Westmoreland, M.E. Law, C.A. Taatjes, K. Kohse-Höinghaus, J. Wang und T.A. Cool, Initial steps of aromatic ring formation in a laminar premixed fuel-rich cyclopentene flame, *J. Phys. Chem. A*, **111**(19), 4081–4092, 2007.

[40] T. Baer und R.P. Tuckett, Advances in threshold photoelectron spectroscopy (TPES) and threshold photoelectron photoion coincidence (TPEPICO), *Phys. Chem. Chem. Phys.*, **19**, 9698–9723, 2017.

[41] A. Bodi, P. Hemberger, D.L. Osborn und B. Sztáray, Mass-Resolved Isomer Selective Chemical Analysis with Imaging Photoelectron Photoion Coincidence Spectroscopy, *J. Phys. Chem. Lett.*, **4**, 2948–2952, 2013.

[42] P. Oßwald, P. Hemberger, T. Bierkandt, E. Akyildiz, M. Köhler, A. Bodi, T. Gerber und T. Kasper, In situ flame chemistry tracing by imaging photoelectron photoion coincidence spectroscopy, *Rev. Sci. Instrum.*, **85**(2), 025101, 2014.

[43] J. Krüger, G.A. Garcia, D. Felsmann, K. Moshammer, A. Lackner, A. Brockhinke, L. Nahon und K. Kohse-Höinghaus, Photoelectron-photoion coincidence spectroscopy for multiplexed detection of intermediate species in a flame., *Phys. Chem. Chem. Phys.*, **16**(41), 22791–22804, 2014.

[44] A.K. Agarwal, Biofuels (alcohols and biodiesel) applications as fuels for internal combustion engines, *Prog. Energy Combust. Sci.*, **33**(3), 233–271, 2007.

[45] C.K. Westbrook, W.J. Pitz und H.J. Curran, Chemical kinetic modeling study of the effects of oxygenated hydrocarbons on soot emissions from diesel engines, *J. Phys. Chem. A*, **110**(21), 6912–6922, 2006.

[46] F. Hoppe, U. Burke, M. Thewes, K.A. Heufer, F. Kremer und S. Pischinger, Tailor-Made Fuels from Biomass: Potentials of 2-butanone and 2-methylfuran in direct injection spark ignition engines, *Fuel*, **167**, 106–117, 2016.

[47] H.L. MacLean und L.B. Lave, Evaluating automobile fuel/propulsion system technologies, *Prog. Energy Combust. Sci.*, **29**(1), 1–69, 2003.

[48] M.S. Graboski und R.L. McCormick, Combustion of fat and vegetable oil derived fuels in diesel engines, *Prog. Energy Combust. Sci.*, **24**(2), 125–164, 1998.

[49] G. Fontaras, G. Karavalakis, M. Kousoulidou, L. Ntziachristos, E. Bakeas, S. Stournas und Z. Samaras, Effects of low concentration biodiesel blends application on modern passenger cars. Part 2: Impact on carbonyl compound emissions, *Environ. Pollut.*, **158**(7), 2496–2503, 2010.

[50] R. Ballesteros, J.J. Hernández und J. Guillén-Flores, Carbonyls speciation in a typical European automotive diesel engine using bioethanol/butanol–diesel blends, *Fuel*, **95**, 136–145, 2012.

[51] L.G. Anderson, Ethanol fuel use in Brazil: air quality impacts, *Energy Environ. Sci.*, **2**(10), 1015–1037, 2009.

[52] X. Lu, D. Han und Z. Huang, Fuel design and management for the control of advanced compression-ignition combustion modes, *Prog. Energy Combust. Sci.*, **37**(6), 741–783, 2011.

[53] S. Saxena und I.D. Bedoya, Fundamental phenomena affecting low temperature combustion and HCCI engines, high load limits and strategies for extending these limits, *Prog. Energy Combust. Sci.*, **39**(5), 457–488, 2013.

[54] T.J. Jacobs und D.N. Assanis, The attainment of premixed compression ignition low-temperature combustion in a compression ignition direct injection engine, *Proc. Combust. Inst.*, **31**(2), 2913–2920, 2007.

[55] S. Kimura, O. Aoki, Y. Kitahara und E. Aiyoshizawa, Ultra-Clean Combustion Technology Combining a Low-Temperature and Premixed Combustion Concept for Meeting Future Emission Standards, *SAE Technical Paper*, (2001-01-0200), 2001.

[56] J. Warnatz, U. Maas und R.W. Dibble, *Combustion*, 3. Auflage, Springer, Berlin, 2001.

[57] T. Zeuch, G. Moréac, S.S. Ahmed und F. Mauss, A comprehensive skeletal mechanism for the oxidation of n-heptane generated by chemistry-guided reduction, *Combust. Flame*, **155**(4), 651–674, 2008.

[58] H.J. Curran, S.L. Fischer und F.L. Dryer, The reaction kinetics of dimethyl ether. II: Low-temperature oxidation in flow reactors, *Int. J. Chem. Kinet.*, **32**(12), 741–759, 2000.

[59] A. Multer, N. McGraw, K. Hohn und P. Vadlani, Production of Methyl Ethyl Ketone from Biomass Using a Hybrid Biochemical/Catalytic Approach, *Ind. Eng. Chem. Res.*, **52**(1), 56–60, 2012.

[60] H. Yoneda, D.J. Tantillo und S. Atsumi, Biological Production of 2-Butanone in Escherichia coli, *ChemSusChem*, **7**(1), 92–95, 2014.

[61] C. Hemken, U. Burke, I. Graf, L. Ruwe, S. Park, S.M. Sarathy, K.A. Heufer und K. Kohse-Höinghaus, A laminar flame investigation of 2-butanone, and the combustion-related intermediates formed through its oxidation, *Proc. Combust. Inst.*, **36**, 1175–1183, 2017.

[62] C. Hemken, U. Burke, K.-F. Lam, D.F. Davidson, R.K. Hanson, K.A. Heufer und K. Kohse-Höinghaus, Toward a better understanding of 2-butanone oxidation: Detailed species measurements and kinetic modeling, *Combust. Flame*, **184**, 195–207, 2017.

[63] S. Thion, P. Diévart, P. Van Cauwenberghe, G. Dayma, Z. Serinyel und P. Dagaut, An experimental study in a jet-stirred reactor and a comprehensive kinetic mechanism for the oxidation of methyl ethyl ketone, *Proc. Combust. Inst.*, **36**, 459–467, 2017.

[64] A.G. Gaydon, *The Spectroscopy of Flames*, 2. Auflage, Chapman and Hall Ltd., London, 1974.

[65] H.J. Curran, P. Gaffuri, W.J. Pitz und C.K. Westbrook, A Comprehensive Modeling Study of n-Heptane Oxidation, *Combust. Flame*, **114**(1-2), 149–177, 1998.

[66] J. Bugler, K.P. Somers, E.J. Silke und H.J. Curran, Revisiting the Kinetics and Thermodynamics of the Low-Temperature Oxidation Pathways of Alkanes: A Case Study of the Three Pentane Isomers, *J. Phys. Chem. A*, **119**(28), 7510–7527, 2015.

[67] R. van Basshuysen und F. Schäfer, *Handbuch Verbrennungsmotor*, 7. Auflage, Springer Vieweg, Wiesbaden, 2015.

[68] Z. Wang, X. Zhang, L. Xing, L. Zhang, F. Herrmann, K. Moshammer, F. Qi und K. Kohse-Höinghaus, Experimental and kinetic modeling study of the low- and intermediate-temperature oxidation of dimethyl ether, *Combust. Flame*, **162**(4), 1113–1125, 2015.

[69] T.A. Cool, A. McIlroy, F. Qi, P.R. Westmoreland, L. Poisson, D.S. Peterka und M. Ahmed, Photoionization mass spectrometer for studies of flame chemistry with a synchrotron light source, *Rev. Sci. Instrum.*, **76**(9), 094102, 2005.

[70] F. Qi, R. Yang, B. Yang, C. Huang, L. Wei, J. Wang, L. Sheng und Y. Zhang, Isomeric identification of polycyclic aromatic hydrocarbons formed in combustion with tunable vacuum ultraviolet photoionization, *Rev. Sci. Instrum.*, **77**(8), 084101, 2006.

[71] Y. Li, L. Zhang, Z. Tian, T. Yuan, J. Wang, B. Yang und F. Qi, Experimental Study of a Fuel-Rich Premixed Toluene Flame at Low Pressure, *Energy Fuels*, **23**(3), 1473–1485, 2009.

[72] Z. Zhou, X. Du, J. Yang, Y. Wang, C. Li, S. Wei, L. Du, Y. Li, F. Qi und Q. Wang, The vacuum ultraviolet beamline/endstations at NSRL dedicated to combustion research, *J. Synchrotron Radiat.*, **23**(4), 1035–1045, 2016.

[73] L. Nahon, N. de Oliveira, G.A. Garcia, J.-F. Gil, B. Pilette, O. Marcouillé, B. Lagarde und F. Polack, DESIRS: a state-of-the-art VUV beamline featuring high resolution and variable polarization for spectroscopy and dichroism at SOLEIL, *J. Synchrotron Radiat.*, **19**(4), 508–520, 2012.

[74] G.A. Garcia, H. Soldi-Lose und L. Nahon, A versatile electron-ion coincidence spectrometer for photoelectron momentum imaging and threshold spectroscopy on mass selected ions using synchrotron radiation, *Rev. Sci. Instrum.*, **80**(2), 023102, 2009.

[75] G.A. Garcia, B.K. Cunha de Miranda, M. Tia, S. Daly und L. Nahon, DELICIOUS III: A multipurpose double imaging particle coincidence spectrometer for gas phase vacuum ultraviolet photodynamics studies, *Rev. Sci. Instrum.*, **84**(5), 053112, 2013.

[76] K.M. Weitzel, J. Mähnert und M. Penno, ZEKE-PEPICO investigations of dissociation energies in ionic reactions, *Chem. Phys. Lett.*, **224**(3-4), 371–380, 1994.

[77] G.A. Garcia, L. Nahon und I. Powis, Two-dimensional charged particle image inversion using a polar basis function expansion, *Rev. Sci. Instrum.*, **75**(11), 4989, 2004.

[78] LOGEsoft, http://loge.se/Products/LOGE_Products.html, 2017.

[79] CHEMKIN-PRO, *Reaction Design*, 2009.

[80] A. Cuoci, A. Frassoldati, T. Faravelli und E. Ranzi, OpenSMOKE++: An object-oriented framework for the numerical modeling of reactive systems with detailed kinetic mechanisms, *Comput. Phys. Commun.*, **192**, 237–264, 2015.

[81] U. Struckmeier, P. Oßwald, T. Kasper, L. Böhling, M. Heusing, M. Köhler, A. Brockhinke und K. Kohse-Höinghaus, Sampling Probe Influences on Temperature and Species Concentrations in Molecular Beam Mass Spectroscopic Investigations of Flat Premixed Low-pressure Flames, *Z. Phys. Chem.*, **223**(4-5), 503–537, 2009.

[82] X. Yang, D. Felsmann, N. Kurimoto, J. Krüger, T. Wada, T. Tan, E.A. Carter, K. Kohse-Höinghaus und Y. Ju, Kinetic studies of methyl acetate pyrolysis and oxidation in a flow reactor and a low-pressure flat flame using molecular-beam mass spectrometry, *Proc. Combust. Inst.*, **35**, 491–498, 2015.

[83] H. Wang und D.A. Sheen, Combustion kinetic model uncertainty quantification, propagation and minimization, *Prog. Energy Combust. Sci.*, **47**, 1–31, 2015.

[84] G. Bieri, F. Burger, E. Heilbronner und J.P. Maier, Valence Ionization Energies of Hydrocarbons, *Helv. Chim. Acta*, **60**(7), 2213–2233, 1977.

[85] J.C. Traeger, Heat of formation for the 1-methylallyl cation by photoionization mass spectrometry, *J. Phys. Chem.*, **90**(17), 4114–4118, 1986.

[86] P. Masclet, G. Mouvier und J.F. Bocquet, Effets électroniques et effets stériques dus à la substitution alcoyle dans les dièns conjugués, *J. Chim. Phys.*, **78**, 99–106, 1981.

[87] J. Bugler, B. Marks, O. Mathieu, R. Archuleta, A. Camou, C. Grégoire, K.A. Heufer, E.L. Petersen und H.J. Curran, An ignition delay time and chemical kinetic modeling study of the pentane isomers, *Combust. Flame*, **163**, 138–156, 2016.

[88] B. Yang, J. Wang, T.A. Cool, N. Hansen, S. Skeen und D.L. Osborn, Absolute photoionization cross-sections of some combustion intermediates, *Int. J. Mass Spectrom.*, **309**, 118–128, 2012.

[89] T.A. Cool, J. Wang, K. Nakajima, C.A. Taatjes und A. Mcllroy, Photoionization cross sections for reaction intermediates in hydrocarbon combustion, *Int. J. Mass Spectrom.*, **247**(1–3), 18–27, 2005.

[90] J. Wang, B. Yang, T.A. Cool, N. Hansen und T. Kasper, Near-threshold absolute photoionization cross-sections of some reaction intermediates in combustion, *Int. J. Mass Spectrom.*, **269**(3), 210–220, 2008.

[91] J-P. Morizur, J. Mercier und M. Sarraf, 2-substituted-2,3-dihydro-4H-pyrans: Competition between 'retro Diels-Alder' fragmentation and substituent loss, *Org. Mass Spectrom.*, **17**(7), 327–330, 1982.

[92] M.J.S. Dewar und S.D. Worley, Photoelectron Spectra of Molecules. I. Ionization Potentials of Some Organic Molecules and Their Interpretation, *J. Chem. Phys.*, **50**(2), 654–667, 1969.

[93] N. Miyamoto, H. Ogawa, N. Nurun, K. Obata und T. Arima, Smokeless, low NOx, high thermal efficiency, and low noise diesel combustion with oxygenated agents as main fuel, *SAE Technical Paper*, (980506), 1998.

[94] T. Litzinger, M. Stoner, H. Hess und A. Boehman, Effects of oxygenated blending compounds on emissions from a turbocharged direct injection diesel engine, *Int. J. Engine Res.*, **1**(1), 57–70, 2000.

[95] D.T. Jones und D.R. Woods, Acetone-butanol fermentation revisited, *Microbiol. Rev.*, **50**(4), 484–524, 1986.

[96] N. Qureshi, B.C. Saha, R.E. Hector, B. Dien, S. Hughes, S. Liu, L. Iten, M.J. Bowman, G. Sarath und M.A. Cotta, Production of butanol (a biofuel) from agricultural residues: Part II – Use of corn stover and switchgrass hydrolysates, *Biomass Bioenergy*, **34**(4), 566–571, 2010.

[97] P. Dürre, Biobutanol: An attractive biofuel, *Biotechnol J.*, **2**(12), 1525–1534, 2007.

[98] D.C. Rakopoulos, C.D. Rakopoulos, E.G. Giakoumis und A.M. Dimaratos, Characteristics of performance and emissions in high-speed direct injection diesel engine fueled with diethyl ether/diesel fuel blends, *Energy*, **43**(1), 214–224, 2012.

[99] A. Paul, P.K. Bose, R. Panua und D. Debroy, Study of performance and emission characteristics of a single cylinder CI engine using diethyl ether and ethanol blends, *J. Energy Inst.*, **88**(1), 1–10, 2015.

[100] S. Imtenan, H.H. Masjuki, M. Varman, I.M. Rizwanul Fattah, H. Sajjad und M.I. Arbab, Effect of n-butanol and diethyl ether as oxygenated additives on combustion–emission-performance characteristics of a multiple cylinder diesel engine fuelled with diesel–jatropha biodiesel blend, *Energy Convers. Manag.*, **94**, 84–94, 2015.

[101] J. Pieper, Verbrennungschemie prototypischer Gemische konventioneller und oxygenierter Brennstoffe: Massenspektrometrische Untersuchungen zur Addition der Isomere Diethylether und n-Butanol zu n-Butan, *Masterarbeit*, (Universität Bielefeld), 2015.

[102] K. Yasunaga, F. Gillespie, J.M. Simmie, H.J. Curran, Y. Kuraguchi, H. Hoshikawa, T. Yamane und Y. Hidaka, A Multiple Shock Tube and Chemical Kinetic Modeling Study of Diethyl Ether Pyrolysis and Oxidation, *J. Phys. Chem. A*, **114**(34), 9098–9109, 2010.

[103] S.M. Burke, W. Metcalfe, O. Herbinet, F. Battin-Leclerc, F.M. Haas, J. Santner, F.L. Dryer und H.J. Curran, An experimental and modeling study of propene oxidation. Part 1: Speciation measurements in jet-stirred and flow reactors, *Combust. Flame*, **161**(11), 2765–2784, 2014.

[104] S.M. Burke, U. Burke, R. Mc Donagh, O. Mathieu, I. Osorio, C. Keesee, A. Morones, E.L. Petersen, W. Wang, T.A. DeVerter, M.A. Oehlschlaeger, B. Rhodes, R.K. Hanson, D.F. Davidson, B.W. Weber, C.-J. Sung, J. Santner, Y. Ju, F.M. Haas, F.L. Dryer, E.N. Volkov, E.J.K. Nilsson, A.A. Konnov, M. Alrefae, F. Khaled, A. Farooq, P. Dirrenberger, P.-A. Glaude, F. Battin-Leclerc und H.J. Curran, An experimental and modeling study of propene oxidation. Part 2: Ignition delay time and flame speed measurements, *Combust. Flame*, **162**(2), 296–314, 2015.

[105] W.K. Metcalfe, S.M. Burke, S.S. Ahmed und H.J. Curran, A Hierarchical and Comparative Kinetic Modeling Study of C1 - C2 Hydrocarbon and Oxygenated Fuels, *Int. J. Chem. Kinet.*, **45**(10), 638–675, 2013.

[106] K.P. Somers, J.M. Simmie, W.K. Metcalfe und H.J. Curran, The pyrolysis of 2-methylfuran: a quantum chemical, statistical rate theory and kinetic modelling study, *Phys. Chem. Chem. Phys.*, **16**(11), 5349–5367, 2014.

[107] S.M. Sarathy, S. Vranckx, K. Yasunaga, M. Mehl, P. Oßwald, W.K. Metcalfe, C.K. Westbrook, W.J. Pitz, K. Kohse-Höinghaus, R.X. Fernandes und H.J. Curran, A comprehensive chemical kinetic combustion model for the four butanol isomers, *Combust. Flame*, **159**(6), 2028–2055, 2012.

[108] S. Kokjohn, R. Hanson, D. Splitter, J. Kaddatz und R. Reitz, Fuel reactivity controlled compression ignition (RCCI) combustion in light- and heavy-duty engines, *SAE Int. J. Fuels Lubr.*, **4**(1), 2011–01–0357, 2011.

[109] J. Bugler, A. Rodriguez, O. Herbinet, F. Battin-Leclerc, C. Togbé, G. Dayma, P. Dagaut und H.J. Curran, An experimental and modelling study of n-pentane oxidation in two jet-stirred reactors: The importance of pressure-dependent kinetics and new reaction pathways, *Proc. Combust. Inst.*, **36**, 441–448, 2017.

[110] U. Burke, K.P. Somers, P. O'Toole, C.M. Zinner, N. Marquet, G. Bourque, E.L. Petersen, W.K. Metcalfe, Z. Serinyel und H.J. Curran, An ignition delay and kinetic modeling study of methane, dimethyl ether, and their mixtures at high pressures, *Combust. Flame*, **162**(2), 315–330, 2015.

[111] F. Herrmann, B. Jochim, P. Oßwald, L. Cai, H. Pitsch und K. Kohse-Höinghaus, Experimental and numerical low-temperature oxidation study of ethanol and dimethyl ether, *Combust. Flame*, **161**(2), 384–397, 2014.

[112] K. Moshammer, A.W. Jasper, D.M. Popolan-Vaida, A. Lucassen, P. Diévart, H. Selim, A.J. Eskola, C.A. Taatjes, S.R. Leone, S.M. Sarathy, Y. Ju, P. Dagaut, K. Kohse-Höinghaus und N. Hansen, Detection and identification of the keto-hydroperoxide ($HOOCH_2OCHO$) and other intermediates during low-temperature oxidation of dimethyl ether, *J. Phys. Chem. A*, **119**(28), 7361–7374, 2015.

[113] K. Moshammer, A.W. Jasper, D.M. Popolan-Vaida, Z. Wang, V.S.B. Shankar, L. Ruwe, C.A. Taatjes, P. Dagaut und N. Hansen, Quantification of the Keto-Hydroperoxide ($HOOCH_2OCHO$) and Other Elusive Intermediates during Low-Temperature Oxidation of Dimethyl Ether, *J. Phys. Chem. A*, **120**(40), 7890–7901, 2016.

[114] A. Rodriguez, O. Frottier, O. Herbinet, R. Fournet, R. Bounaceur, C. Fittschen und F. Battin-Leclerc, Experimental and modeling investigation of the low-temperature oxidation of dimethyl ether, *J. Phys. Chem. A*, **119**(28), 7905–7923, 2015.

[115] F.M. Haas, M. Chaos und F.L. Dryer, Low and intermediate temperature oxidation of ethanol and ethanol-PRF blends: An experimental and modeling study, *Combust. Flame*, **156**(12), 2346–2350, 2009.

[116] E. Ranzi, A. Cuoci, A. Frassoldati, M. Pelucchi und T. Faravelli, New reaction classes in the kinetic modeling of low temperature oxidation of n-alkanes, *Combust. Flame*, **162**(5), 1679–1691, 2015.

[117] A. Rodriguez, O. Herbinet, Z. Wang, F. Qi, C. Fittschen, P.R. Westmoreland und F. Battin-Leclerc, Measuring hydroperoxide chain-branching agents during n-pentane low-temperature oxidation, *Proc. Combust. Inst.*, **36**, 333–342, 2017.

[118] A. Elfasakhany, Performance and emissions analysis on using acetone–gasoline fuel blends in spark-ignition engine, *Eng. Sci. Technol. Int. J.*, **19**(3), 1224–1232, 2016.

[119] Y. Li, L. Meng, K. Nithyanandan, T.H. Lee, Y. Lin, C.-F. Lee und S. Liao, Experimental investigation of a spark ignition engine fueled with acetone-butanol-ethanol and gasoline blends, *Energy*, **121**, 43–54, 2017.

[120] A.M. Scheer, A.J. Eskola, D.L. Osborn, L. Sheps und C.A. Taatjes, Resonance Stabilization Effects on Ketone Autoxidation: Isomer-Specific Cyclic Ether and Ketohydroperoxide Formation in the Low-Temperature (400–625 K) Oxidation of Diethyl Ketone, *J. Phys. Chem. A*, **120**(43), 8625–8636, 2016.

[121] E.E. Dames, K.-Y. Lam, D.F. Davidson und R.K. Hanson, An improved kinetic mechanism for 3-pentanone pyrolysis and oxidation developed using multispecies time histories in shock-tubes, *Combust. Flame*, **161**(5), 1135–1145, 2014.

[122] Z. Serinyel, N. Chaumeix, G. Black, J.M. Simmie und H.J. Curran, Experimental and Chemical Kinetic Modeling Study of 3-Pentanone Oxidation, *J. Phys. Chem. A*, **114**, 12176–12186, 2010.

[123] H. Minwegen, U. Burke und K.A. Heufer, An experimental and theoretical comparison of C3-C5 linear ketones, *Proc. Combust. Inst.*, **36**, 561–568, 2017.

[124] K.-Y. Lam, W. Ren, Z. Hong, D.F. Davidson und R.K. Hanson, Shock tube measurements of 3-pentanone pyrolysis and oxidation, *Combust. Flame*, **159**(11), 3251–3263, 2012.

[125] Y. Li, C.W. Zhou, K.P. Somers, K. Zhang und H.J. Curran, The oxidation of 2-butene: A high pressure ignition delay, kinetic modeling study and reactivity comparison with isobutene and 1-butene, *Proc. Combust. Inst.*, **36**, 403–411, 2017.

[126] Y. Zhang, K.P. Somers, M. Mehl, W.J. Pitz, R.F. Cracknell und H.J. Curran, Probing the antagonistic effect of toluene as a component in surrogate fuel models at low temperatures and high pressures. A case study of toluene/dimethyl ether mixtures, *Proc. Combust. Inst.*, **36**, 413–421, 2017.

[127] H. Bock, T. Hirabayashi und S. Mohmand, Thermische Erzeugung von Alkyl- und Halogenketenen, *Chem. Ber.*, **114**, 2595–2608, 1981.

[128] F. Holzmeier, M.-P. Herbert, I. Fischer, M. Steglich, A. Bodi und P. Hemberger, A photoionization study of 2-propyl and t-butyl radicals, *J. Anal. Appl. Pyrolysis*, **124**, 454–460, 2017.

[129] F. Holzmeier, M. Lang, K. Hader, P. Hemberger und I. Fischer, H_2CN^+ and H_2CNH^+: New insight into the structure and dynamics from mass-selected threshold photoelectron spectra, *J. Chem. Phys.*, **138**(21), 214310, 2013.

[130] Y.B. Lim und P.J. Ziemann, Products and Mechanism of Secondary Organic Aerosol Formation from Reactions of n-Alkanes with OH Radicals in the Presence of NOx, *Environ. Sci. Technol.*, **39**(23), 9229–9236, 2005.

[131] M. Claeys, B. Graham, G. Vas, W. Wang, R. Vermeylen, V. Pashynska, J. Cafmeyer, P. Guyon, M.O. Andreae, P. Artaxo und W. Maenhaut, Formation of secondary organic aerosols through photooxidation of isoprene, *Science*, **303**(5661), 1173–1176, 2004.

[132] Z. Wang, B. Chen, K. Moshammer, D.M. Popolan-Vaida, S. Sioud, V.S.B. Shankar, D. Vuilleumier, T. Tao, L. Ruwe, E. Bräuer, N. Hansen, P. Dagaut, K. Kohse-Höinghaus, M.A. Raji und S.M. Sarathy, n-Heptane cool flame chemistry: Unraveling intermediate species measured in a stirred reactor and motored engine, *Combust. Flame*, **187**, 199–216, 2018.

[133] Z. Wang, D.M. Popolan-Vaida, B. Chen, K. Moshammer, S.Y. Mohamed, H. Wang, S. Sioud, M.A. Raji, K. Kohse-Höinghaus, N. Hansen, P. Dagaut, S.R. Leone und S.M. Sarathy, Unraveling the structure and chemical mechanisms of highly oxygenated intermediates in oxidation of organic compounds, *Proc. Natl. Acad. Sci.*, **114**(50), 13102–13107, 2017.

ANHANG A

Publikation 1

J. Pieper, S. Schmitt, C. Hemken, E. Davies, J. Wullenkord, A. Brockhinke, J. Krüger, G.A. Garcia, L. Nahon, A. Lucassen, W. Eisfeld, K. Kohse-Höinghaus

Isomer Identification in Flames with Double-Imaging Photoelectron/Photoion Coincidence Spectroscopy (i^{2}PEPICO) using Measured and Calculated Reference Photoelectron Spectra

Zeitschrift für Physikalische Chemie **232**(2), 153-187, 2018
DOI: 10.1515/zpch-2017-1009[1]

Abstract

Double-imaging photoelectron/photoion coincidence (i^{2}PEPICO) spectroscopy using a multiplexing, time-efficient, fixed-photon-energy approach offers important opportunities of gas-phase analysis. Building on successful applications in combustion systems that have demonstrated the discriminative power of this technique, we attempt here to push the limits of its application further to more chemically complex combustion examples. The present investigation is devoted to identifying and potentially quantifying compounds featuring five heavy atoms in laminar, premixed low-pressure flames of hydrocarbon and oxygenated fuels and their mixtures. In these combustion examples from flames of cyclopentene, *iso*-pentane, *iso*-pentane blended with dimethyl ether (DME), and diethyl ether (DEE), we focus on the unambiguous assignment and quantitative detection of species with the sum formulae C_5H_6, C_5H_7, C_5H_8, C_5H_{10}, and C_4H_8O in the respective isomer mixtures, attempting to provide answers to specific chemical questions for each of these examples.
To analyze the obtained i^{2}PEPICO results from these combustion situations, photoelectron spectra (PES) from pure reference compounds, including several examples previously unavailable in the literature, were recorded with the same experimental setup as used in the flame measurements. In addition, PES of two species where reference spectra have not been obtained, namely 2-methyl-1-butene (C_5H_{10}) and the 2-cyclopentenyl radical (C_5H_7), were calculated on the basis of high level *ab initio* calculations and Franck Condon (FC) simulations. These reference measurements and quantum chemical calculations support the early fuel decomposition scheme in the cyclopentene flame towards 2-cyclopentenyl

1 Zu dieser Publikation ist Supplemental Material online unter https://doi.org/10.1515/zpch-2017-1009 verfügbar.

as the dominant fuel radical as well as the prevalence of branched intermediates in the early fuel destruction reactions in the *iso*-pentane flame, with only minor influences from DME addition. Furthermore, the presence of ethyl vinyl ether (EVE) in DEE flames that was predicted by a recent DEE combustion mechanism could be confirmed unambiguously. While combustion measurements using i^{2}PEPICO can be readily obtained in isomer-rich situations, we wish to highlight the crucial need for high-quality reference information to assign and evaluate the obtained spectra.

Julia Pieper*, Steffen Schmitt, Christian Hemken, Emma Davies, Julia Wullenkord, Andreas Brockhinke, Julia Krüger, Gustavo A. Garcia, Laurent Nahon, Arnas Lucassen, Wolfgang Eisfeld and Katharina Kohse-Höinghaus*

Isomer Identification in Flames with Double-Imaging Photoelectron/Photoion Coincidence Spectroscopy (i^{2}PEPICO) using Measured and Calculated Reference Photoelectron Spectra

https://doi.org/10.1515/zpch-2017-1009
Received July 11, 2017; accepted August 31, 2017

Abstract: Double-imaging photoelectron/photoion coincidence (i^{2}PEPICO) spectroscopy using a multiplexing, time-efficient, fixed-photon-energy approach offers important opportunities of gas-phase analysis. Building on successful applications in combustion systems that have demonstrated the discriminative power of this technique, we attempt here to push the limits of its application further to more chemically complex combustion examples. The present investigation is devoted to identifying and potentially quantifying compounds featuring five heavy atoms in laminar, premixed low-pressure flames of hydrocarbon and oxygenated fuels and their mixtures. In these combustion

***Corresponding authors: Julia Pieper and Katharina Kohse-Höinghaus,** Physical Chemistry I, Bielefeld University, Universitätsstraße 25, 33615 Bielefeld, Germany,
Phone: +49 521 106 6308 (J. Pieper); +49 521 106 2052 (K. Kohse-Höinghaus),
Fax: +49 521 106 15 6887, e-mail: julia.pieper@uni-bielefeld.de (J. Pieper);
kkh@uni-bielefeld.de (K. Kohse-Höinghaus)
Steffen Schmitt, Emma Davies, Julia Wullenkord and Andreas Brockhinke: Physical Chemistry I, Bielefeld University, Universitätsstraße 25, 33615 Bielefeld, Germany
Christian Hemken: Physical Chemistry I, Bielefeld University, Universitätsstraße 25, 33615 Bielefeld, Germany; and Physico Chemical Fundamentals of Combustion (PCFC), RWTH Aachen University, Schinkelstraße 8, 52062 Aachen, Germany
Julia Krüger: Synchrotron SOLEIL, L'Orme des Merisiers, St. Aubin, B.P. 48, 91192 Gif-sur-Yvette, France; and Continental AG, Vahrenwalder Straße 9, 30165 Hannover, Germany
Gustavo A. Garcia and Laurent Nahon: Synchrotron SOLEIL, L'Orme des Merisiers, St. Aubin, B.P. 48, 91192 Gif-sur-Yvette, France
Arnas Lucassen: Physikalisch-Technische Bundesanstalt, Bundesallee 100, 38116 Braunschweig, Germany
Wolfgang Eisfeld: Theoretical Chemistry, Bielefeld University, Universitätsstraße 25, 33615 Bielefeld, Germany

examples from flames of cyclopentene, *iso*-pentane, *iso*-pentane blended with dimethyl ether (DME), and diethyl ether (DEE), we focus on the unambiguous assignment and quantitative detection of species with the sum formulae C_5H_6, C_5H_7, C_5H_8, C_5H_{10}, and C_4H_8O in the respective isomer mixtures, attempting to provide answers to specific chemical questions for each of these examples. To analyze the obtained i²PEPICO results from these combustion situations, photoelectron spectra (PES) from pure reference compounds, including several examples previously unavailable in the literature, were recorded with the same experimental setup as used in the flame measurements. In addition, PES of two species where reference spectra have not been obtained, namely 2-methyl-1-butene (C_5H_{10}) and the 2-cyclopentenyl radical (C_5H_7), were calculated on the basis of high-level *ab initio* calculations and Franck-Condon (FC) simulations. These reference measurements and quantum chemical calculations support the early fuel decomposition scheme in the cyclopentene flame towards 2-cyclopentenyl as the dominant fuel radical as well as the prevalence of branched intermediates in the early fuel destruction reactions in the *iso*-pentane flame, with only minor influences from DME addition. Furthermore, the presence of ethyl vinyl ether (EVE) in DEE flames that was predicted by a recent DEE combustion mechanism could be confirmed unambiguously. While combustion measurements using i²PEPICO can be readily obtained in isomer-rich situations, we wish to highlight the crucial need for high-quality reference information to assign and evaluate the obtained spectra.

Keywords: 3-buten-1-ol; 3-buten-2-ol; combustion chemistry; cyclopentadiene; cyclopentene; 2-cyclopentenyl radical; ethyl vinyl ether; *iso*-butanal; *iso*-butenol; laminar flames; 2-methoxypropene; 2-methyl-1-buten-3-yne; 2-methyl-1-butene; 2-methyl-2-butene; 3-methyl-1-butene; methyl ethyl ketone; *n*-butanal; 1,3-pentadiene; 1,4-pentadiene; 1-pentene; 2-pentene; PEPICO; photoelectron spectra; tetrahydrofuran.

1 Introduction

Gas-phase diagnostics in reactive systems can rely on a number of established techniques for the characterization of species distributions in atmospheric chemistry [1], photochemistry [2–4], catalysis [5], pyrolysis [6, 7], and combustion systems [7–10]. Especially when near-complete information on reactants, numerous intermediates, and products is desired in situations that may present hundreds of reactive compounds [11], universal techniques such as mass spectrometry are highly advantageous.

A large number of studies has applied variants of molecular-beam mass spectrometry (MBMS) using electron impact ionization (EI) or synchrotron-based photoionization (PI) for quantitative species analysis in pyrolysis, photolysis, and oxidation reactors [7, 12–15], shock tubes [16], and laboratory flame experiments [8, 17–20]. In combustion chemistry research, MBMS techniques may have advanced to be potentially the most often applied diagnostics for the characterization of the chemical reaction pathways, since an overview can be provided of basically all stable and short-lived transient species, such as radicals, occurring in the process. Such information is a prerequisite for the development and improvement of kinetic reaction mechanisms and thus extremely valuable especially for alternative fuels [21] and novel operation conditions [10, 22]. Currently, it is assumed that the combustion reactions for hydrocarbon fuels with up to four carbon atoms ("C_1–C_4 chemistry") as well as for selected types of biofuels including some alcohols, esters, and ethers can be quite reliably represented by chemical-kinetic reaction models [23–25]. In a large fraction of these mechanistic developments, validation with experiments using PI-MBMS with tunable vacuum ultraviolet (VUV) radiation from synchrotrons has played a crucial role because of its capability of isomer identification, making use of the improved energy resolution with respect to electron impact sources and separation of different molecular structures from photoionization efficiency (PIE) curves [7, 8, 26]. While immensely useful, PI-MBMS techniques are not without limitations, especially in situations where distinction is needed of isomers that show close-lying ionization energies and where vibronic structure is needed for enhanced differentiation.

Single- (iPEPICO) and double-imaging (i²PEPICO) photoelectron/photoion coincidence spectroscopy provides additional distinctive capability by mass-resolved photoelectron spectra (PES) that show an individual electronic and vibrational fingerprint structure for each species and isomer. The advances of PEPICO and threshold photoelectron/photoion spectroscopy (TPEPICO) in isomer-selective gas-phase diagnostics [27], including developments such as the multi-start multi-stop configuration [28], velocity map imaging (VMI) [29] of threshold electrons [30], and evaluation of the full VMI for fast [31–33] and slow electrons [34, 35], as well as numerous applications have very recently been described in a seminal perspective article by Baer and Tuckett [36]. Combustion-related applications are comparatively recent with isomer-selective analysis of combustion-related gas samples by Bodi et al. [37], the first demonstration of TPES in a flame by Oßwald et al. [38], and a very recent attempt to identify polycyclic aromatic hydrocarbons in a flame by Mercier et al. [39]. Highly multiplexed fixed-photon-energy measurements in flames from the complete VMI were shown to reduce precious measurement time at synchrotrons considerably [40]. Felsmann et al. [41] recently presented a full double-imaging diagnostic by i²PEPICO where

they considered the separation of isomers and obtained quantified mole fraction profiles for several combustion-relevant species. However, the lack of reference PES with a resolution suitable for the identification and reliable quantification of (isomeric) species is one of the factors that limit the application of this technique to more challenging situations in combustion chemistry.

In the present study, we follow up on the strategy demonstrated in [41] with application to chemical targets beyond C_4-fuel combustion. Our work aims at the unambiguous identification and the determination of quantitative amounts of species with 5 heavy atoms (C_5H_6, C_5H_7, C_5H_8, C_5H_{10}, C_4H_8O) in laminar, premixed low-pressure flames. To provide such information, the flame measurements were complemented with those of well-resolved reference PES of expected mixture components in the energy range of interest, using the same apparatus and instrument parameters in both experiments as recommended by Baer and Tuckett [36]. Specifically, the photoelectron spectra of 18 species with the sum formulae C_5H_6, C_5H_8, C_5H_{10}, and C_4H_8O were recorded in this way. Furthermore, photoelectron spectra of the 2-cyclopentenyl radical (C_5H_7) and of 2-methyl-1-butene (C_5H_{10}) were computed based on high-level *ab initio* calculations and Franck-Condon (FC) simulations. The relevant PES were then used to identify contributions of different isomers in the combustion of pure cyclopentene, of *iso*-pentane and its blend with dimethyl ether (DME), as well as of pure diethyl ether (DEE).

Cyclopentene flames offer interesting pathways of aromatic ring and – eventually – soot formation [26]. Generally, in combustion reactions the identity and relative fractions of the initial fuel radicals play an important role for the development of reaction mechanisms, since they are at the origin of all further reactions. However, they are often not detected in the experiment because of low concentrations, high reactivity, and low binding energies. Oßwald et al. [38] have been the first to identify the distribution of the fuel radicals in an *iso*-butane flame. Felsmann et al. [41] have detected fuel radical signals in previous i^{2}PEPICO experiments in a cyclopentene flame, but the presence of specific structures could not be proven because of the lack of reference PES of the relevant species. For this reason, we have now performed FC simulations on the base of high-level quantum calculations to obtain the PES of the predominantly expected 2-cyclopentenyl radical with the aim of confirming that H-abstraction from the fuel molecule preferentially forms this species.

iso-Pentane as a branched hydrocarbon fuel has been chosen to investigate the first steps of fuel decomposition in more detail, since C_4- and C_5-fuels are being considered as smaller representatives of larger branched alkanes such as *iso*-octane as a primary reference fuel [42–44], and precise knowledge about their combustion reactions can thus assist in improving the prediction quality of kinetic models for realistic fuels. Moreover, fuel blends of conventional

hydrocarbons with biofuel candidates are interesting to reduce soot precursor formation [45], but they may increase the formation of other toxic species, including carbonyl compounds [46, 47]. The distribution of the first stable fuel decomposition species has therefore been analyzed for pure *iso*-pentane combustion as well as for a mixture (80:20) of *iso*-pentane with dimethyl ether (DME) as a prototypical biofuel, the oxidation reactions of which had already been analyzed in depth [12, 14, 48, 49]. Specifically, we have determined isomeric distributions from mass-resolved PES at mass-to-charge ratios (m/z) of 70 (C_5H_{10}) and 68 (C_5H_8), respectively, and predominant reaction pathways *via* branched intermediates could be identified and compared to simulations of the respective flames with a kinetic model from the literature [50].

Diethyl ether combustion has only recently been studied, considering DEE as a highly promising, rather clean-burning potential biofuel [51–53]. Recent full speciation measurements in flames [51] have supported the development of initial reaction-kinetic models for this fuel [51, 52]. These previous analyses suggested the presence of ethyl vinyl ether (EVE) as a primary decomposition product in the combustion of DEE, a hypothesis for which unambiguous evidence could now be obtained in the present work.

These results underline the highly useful capability of i²PEPICO spectroscopy to elucidate species distributions in complex gas-phase systems such as laminar, premixed low-pressure flames of conventional and alternative fuels with their significant number of reactive intermediate species. Furthermore, our study demonstrates the need of reference spectra for these conditions that should be measured with the same experimental setup or calculated with an appropriate level of accuracy.

2 Methods

2.1 Experiment

All experiments were performed at the undulator-based DESIRS beamline of the synchrotron SOLEIL using the SAPHIRS endstation [54], equipped with the double-imaging spectrometer DELICIOUS III, to which the combustion system was adapted. Setup, technique, and evaluation procedure have been described previously [33, 40, 41, 55–57] and only a short summary is therefore presented here.

Flames were stabilized at 40 mbar on a water-cooled (333 K) home-built porous-plug burner of 65 mm diameter. This burner is mounted on a translational stage to permit sampling from different flame positions. Fuel-rich flame

conditions were established from mixtures of fuel, oxygen, and diluent argon as summarized in Table 1. Gas flows were regulated by calibrated mass flow controllers (Advanced Energy AERA series, MKS Instruments), while liquid fuels were metered by syringe pumps (ISCO Systems D1000 and D500, 1.5 L total volume), evaporated by a home-built evaporation system and mixed into the gas flow using preheated argon as carrier gas.

Samples were extracted from the burner chamber by a quartz nozzle (opening diameter: 350 μm, opening angle: 25°) and expanded (~10^{-4} mbar) *via* differential pumping to preserve the initial gas composition of the sample. The center of the resulting molecular beam was then separated by a copper skimmer, expanded further (~10^{-6} mbar) and guided into the ionization chamber where it was crossed with the ionizing VUV beam. The beamline DESIRS [57] at the synchrotron SOLEIL delivers tunable VUV radiation between 5 and 40 eV with high spectral resolution, high photon flux, and adjustable polarization. A gas filter, filled here with argon or xenon, is used to block high harmonic energies from the undulator spectrum. After dispersion *via* a 6.65 m normal-incidence monochromator used here with the low-dispersion grating (200 grooves/mm), the VUV beam exhibits a typical bandwidth of 2–20 meV and a flux of 10^{12}–10^{13} photons/s. It is then focused into the ionization chamber and intersects the molecular beam with a diameter of 100–200 μm.

The DELICIOUS III [33] spectrometer records photons and electrons resulting from the ionization process in coincidence with a multi-start/multi-stop technique. Electrons are analyzed by a velocity map imaging (VMI) spectrometer and the coincident ions are analyzed by a modified Wiley-McLaren time-of-flight imaging analyzer (WM-TOF) that has a typical mass resolving power of $m/\Delta m$ <1700 (full width at half maximum, FWHM), although due to the geometrical constraints of the coupling of the combustion chamber to the spectrometer, the resolving power is degraded here down to $m/\Delta m$ (FWHM) ~300. The electron

Tab. 1: Conditions for the investigated fuel-oxygen-argon flames with equivalence ratio ϕ, featuring identical inlet gas velocity (75 cm/s), argon dilution (25%), and pressure in the burner chamber (40 mbar).

Fuel	Sum formula	x_{Fuel}	x_{O_2}	x_{Ar}	ϕ
Cyclopentene	C_5H_8	0.15	0.60	0.25	1.70 ± 0.05
iso-Pentane	C_5H_{12}	0.13	0.62	0.25	1.70 ± 0.05
iso-Pentane/dimethyl ether (80:20)	C_5H_{12}/C_2H_6O	0.12/0.03	0.60	0.25	1.70 ± 0.05
Diethyl ether	$C_4H_{10}O$	0.17	0.58	0.25	1.81 ± 0.05

The mixture composition of *iso*-pentane and dimethyl ether is given in mol-%.

kinetic energy resolution of the VMI is not constant, but ranges from around 30% at the center of the detector (slow electrons) to about 3–4% on the detectors edge (fast electrons), resulting in a kinetic energy (KE) resolution for the corresponding PES in the range of 30–140 meV for photoelectron energies of 0–3.6 eV [54]. The acquired composite mass-multiplexed raw photoelectron image is then filtered for a given cation mass and Abel inversed *via* the pBasex algorithm [55] in order to retrieve the PES by angle integration.

In addition, preparatory speciation measurements were also performed for these flames under the same conditions, using the same burner chamber and EI-MBMS detection with a mass resolution of ~4000 in Bielefeld and procedures that have been described before [18, 51]. Although these measurements were not intended to provide full species datasets, given the different focus of this work, they will be used to provide complementary, supporting information wherever necessary, since they rely on a different physical process for species detection.

Moreover, reference photoelectron spectra were measured at the DESIRS beamline with the DELICIOUS III spectrometer for the following pure compounds: C_5H_6: 2-methyl-1-buten-3-yne and cyclopentadiene, C_5H_8: 1,4-pentadiene, cyclopentene, and a mixture of *cis*- and *trans*-1,3-pentadiene, C_5H_{10}: 3-methyl-1-butene, 1-pentene, a mixture of *cis*- and *trans*-2-pentene, and 2-methyl-2-butene, C_4H_8O: *n*-butanal, *iso*-butanal, 3-buten-2-ol, 3-buten-1-ol, methyl ethyl ketone, tetrahydrofuran, *iso*-butenol, ethyl vinyl ether, and 2-methoxypropene.

All substances were used with a purity of >98% without further purification. Liquid flows were metered by a syringe pump (Protea PM-1000, 10 mL syringe, Hamilton #1010), evaporated by a home-built evaporation system and transported by a preheated argon carrier flow. The reference gases were introduced through the burner into the ionization chamber in order to obtain reference PES that are comparable to the spectra obtained in the flame experiment. All reference PES were measured at a fixed photon energy of 10.1 eV and evaluated in the KE range of 8.3–10.1 eV; in addition, spectra for *n*-butanal and *iso*-butanal were also recorded at 12.5 eV and evaluated in the KE range of 9.0–12.5 eV.

2.2 Theoretical PES calculations

For two species of relevance for the present work, photoelectron spectra were not experimentally obtained, namely the spectrum of the 2-cyclopentenyl radical (2CP) and that of the 2-methyl-1-butene molecule (2M1B). Therefore, these spectra were simulated by *ab initio* calculations.

The first step in simulating PES is to describe the initial and final state of the ionization process. In this study, the vibrational and electronic ground state

of the neutral molecule was used as initial state, whereas the final state, i.e. the electronic ground state of the cation, may be vibrationally excited. For both, ground and final states, the equilibrium geometries are determined first in order to compute the adiabatic ionization energy (IE). The accuracy of the computed IE depends strongly on the electron correlation treatment used. Generally, coupled-cluster (CC) methods are considered to provide the required accuracy [58]. In this work, the coupled cluster method CCSD(T)-F12a was chosen for the geometry optimizations due to the improved basis set convergence compared to conventional CCSD(T) methods [59].

To calculate the adiabatic IE, the energy difference between cation and neutral molecule must be corrected for the respective zero-point vibrational energies. These were determined from harmonic oscillator calculations with an in-house program, using symmetry to its full capacity yielding normal coordinates and harmonic frequencies. The transition probabilities from the ground state to the different vibrational states of the cation were calculated by FC simulations using the algorithm of Sharp and Rosenstock [60]. The resulting stick spectra were convoluted with Gaussian functions with FWHM corresponding to the experimental resolution of 30–70 meV in the respective photoelectron energy range [54] in order to achieve an easier comparison between experiment and simulation. All *ab initio* calculations in this work were carried out using the Molpro suite of programs [61].

2.3 Flame modeling

Experimentally obtained results from this work were compared to simulations of the analyzed low-pressure premixed *iso*-pentane flame using the kinetic model (including thermodynamic and transport data) from Bugler et al. [50]. The simulations were carried out using the current version of the LOGEsoft software package [62] for burner-stabilized premixed flames considering thermal diffusion and multi-component transport properties. As an input parameter, a “perturbed” temperature profile was determined which inherently considers the influence of the sampling nozzle that perturbs the gas flow; it was determined from the first-stage pressure profile according to a previously described procedure [18, 63, 64]. The resulting relative temperature profile was calibrated with an exhaust gas temperature of (2247 ± 100) K, measured in the *iso*-pentane flame at a height above the burner *h* of 20 mm by OH planar laser-induced fluorescence as described in [65]. The full temperature profile for the simulation is available in Table S1 and Figure S1 in Supplemental Material 1.

3 Results and discussion

3.1 Reference photoelectron spectra

For the identification of intermediate species from flame measurements with the i²PEPICO technique, reference photoelectron spectra are essential. VMI-PES for 18 compounds were obtained experimentally, and PES for two further species, namely the 2-cyclopentenyl radical and 2-methyl-1-butene, were obtained from high-level quantum calculations.

3.1.1 Measured reference spectra

Internal consistency between the PES measured in the flames and from the pure compounds was ascertained by using the same setup with identical gas delivery and molecular-beam sampling. Thus all spectra possess the same spectral resolution and no shifts or corrections are needed, a significant advantage as also proposed by Baer and Tuckett [36]. Figure 1 presents the experimental results, with structures of sum formula C_5H_6 (2-methyl-1-buten-3-yne and cyclopentadiene) in Figure 1a, C_5H_8 (1,4-pentadiene, cyclopentene, and a mixture of *cis*- and *trans*-1,3-pentadiene) in Figure 1b, C_5H_{10} (3-methyl-1-butene, 1-pentene, a mixture of *cis*- and *trans*-2-pentene, and 2-methyl-2-butene) in Figure 1c, and C_4H_8O (*n*-butanal,

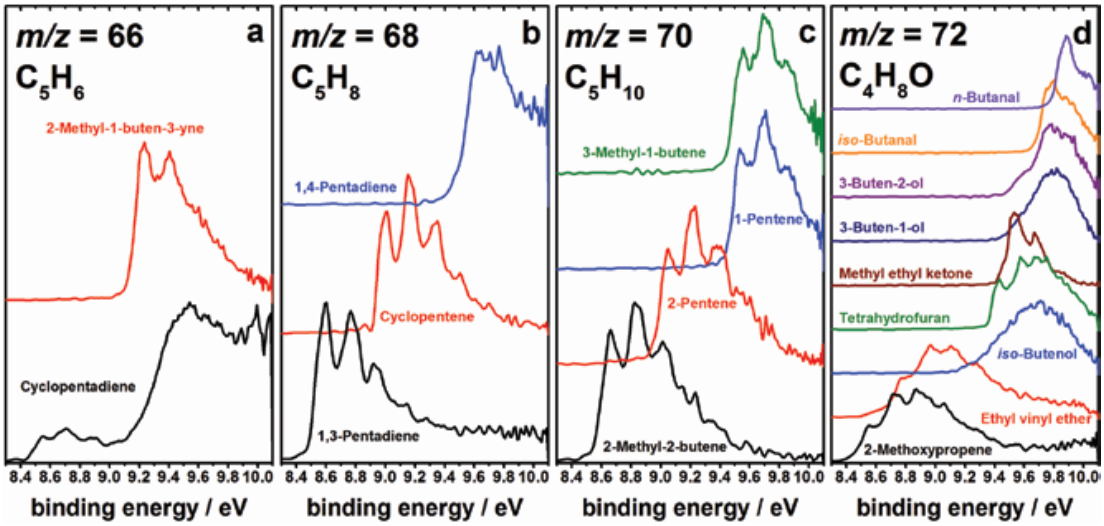

Fig. 1: Measured reference VMI-PES for different molecular structures of sum formulae (a) C_5H_6, (b) C_5H_8, (c) C_5H_{10}, and (d) C_4H_8O. All spectra were taken at fixed photon energy of 10.1 eV. For clarity, they are normalized (with highest intensity set to 1) and displayed with vertical displacement (along the y-axis) as solid lines without error bars.

iso-butanal, 3-buten-2-ol, 3-buten-1-ol, methyl ethyl ketone, tetrahydrofuran, *iso*-butenol, ethyl vinyl ether, and 2-methoxypropene) in Figure 1d.

Very distinct structural features are seen in the PES of the C_5H_6 and C_5H_8 compounds in Figure 1a and b. On the other hand, among the C_5H_{10} isomers in Figure 1c, 3-methyl-1-butene and 1-pentene show nearly identical spectra which makes them difficult to distinguish in a mixture. For the oxygenated C_4H_8O species (Figure 1d), the spectra of *n*-butanal, *iso*-butanal, 3-buten-2-ol, and 3-buten-1-ol are again quite similar, while only the PES of methyl ethyl ketone and tetrahydrofuran show a clear vibrational structure. The tabulated data of all measured PES including uncertainties is available in Supplemental Material 2. For those compounds where PES are available in the literature these are listed in Table S2 in Supplemental Material 1 and a graphical comparison with the PES obtained in this work is given in Figure S2 in Supplemental Material 1.

3.1.2 Calculated reference spectra

3.1.2.1 2-Cyclopentenyl radical (2CP)

The 2CP system consists of an allylic C_3H_3 part and an aliphatic C_2H_4 group forming a 5-membered ring (see left panel of Figure 2). The well-known resonance stabilization effect within the allyl part implies a C_{2v} symmetry of the equilibrium

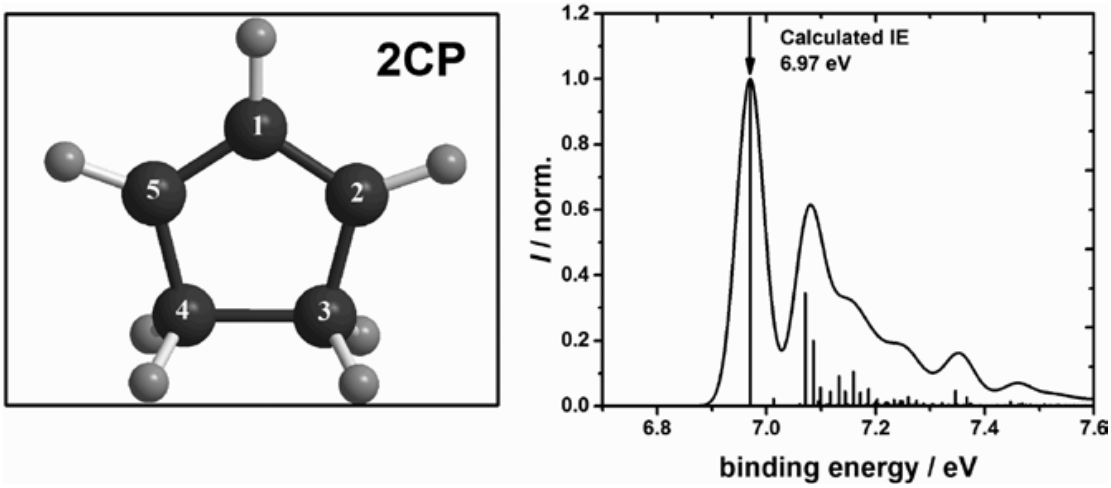

Fig. 2: Left: Optimized geometry for the 2-cyclopentenyl radical at CASSCF/MRCI-F12a/aug-cc-pVTZ level of theory. The allylic part comprises C^2–C^1–C^5. Right: FC simulation at CCSD(T)-F12a/aug-cc-pVTZ (cation) and CASSCF/MRCI-F12a/aug-cc-pVTZ (radical) level of theory for the 2-cyclopentenyl radical (2CP). The calculated IE is indicated and the stick spectrum has been convoluted (solid line) with the experimental FWHM considering its energy-dependence given in [54].

geometries of both neutral radical as well as cation. Both geometries have been optimized at CCSD(T)-F12a/aug-cc-pVTZ level of theory, but only the cation turns out to have a stable C_{2v} minimum at this level of theory. The equilibrium geometry of the neutral radical shows a very slight in-plane distortion of the allyl system lowering the symmetry to C_s. We also observed unusual instabilities during the numerical force constant calculations, which pointed to an artifact. Such problems are easily overlooked but not uncommon in open-shell systems with symmetry and a complicated electronic structure. The reason for the artificial distortion is usually referred to as "doublet instability" or "artificial symmetry-breaking" of the electronic wave function [66–69]. One possibility to overcome this issue is to use multi-reference electronic structure methods. Therefore, the radical has been recomputed using CASSCF/MRCI-F12a/aug-cc-pVTZ [70, 71] and paying attention to the wave function symmetry. A stable electronic structure has been achieved by choosing an active space of 13 electrons in 14 active orbitals for a CASSCF calculation to generate the 1-electron basis (molecular orbitals). This is followed by a MRCI-F12a calculation with an active space of 7 electrons in 7 active orbitals and including all electrons in the correlation treatment except the 10 core electrons. This approach yields a stable C_{2v} equilibrium geometry as expected and robust force constants for the harmonic frequency calculation. Final equilibrium geometries and harmonic frequencies are summarized in Tables S3–S6 in Supplemental Material 1.

The adiabatic IE, i.e. the 0–0 ionization including zero-point energy, needs to be calculated before the PES can be simulated. Unfortunately, all truncated CI methods including MRCI-F12a are not size-extensive and thus not suitable to compute ionization energies. Therefore, the CCSD(T)-F12a energies are used to determine the IE. The energy difference between the CCSD(T)-F12a and MRCI-F12a geometry of the radical is only 4 μeV and thus not relevant. The predicted adiabatic IE is IE(2CP) = 6.97 eV, which is in very good agreement with the only experimental value reported in the literature at 7.00 eV using energy-selected electron impact [72]. This IE together with the harmonic frequencies and normal modes of the two sets of MRCI-F12a and CCSD(T)-F12a calculations is used for the FC simulation.

The resulting spectrum shows the highest intensity for the 0–0-transition due to the relatively small change in geometry upon ionization (see right panel of Figure 2). The second peak at 7.09 eV is mainly caused by single excitations into mode 9 and 10, both a_1 ring deformation modes. Mode 9 corresponds to C^1, C^2 and C^5 moving to the ring center whereas mode 10 corresponds mainly to an increase of the angle C^2–C^1–C^5. After these two main peaks the intensity falls rapidly with only a small shoulder at 7.36 eV. This corresponds mainly to a single excitation into mode 3, a totally symmetric C–H stretching mode basically located at C^3–H_2

and C^4–H_2, respectively. The tabulated data of the simulated PES can be found in Supplemental Material 3.

3.1.2.2 2-Methyl-1-butene (2M1B)

In contrast to the cyclic 2CP that has a completely rigid molecular structure, 2M1B can show internal rotations around several single bonds. These have been investigated with different methods (HF, MP2, KS-B3LYP, CCSD(T)-F12a) using the cc-pVDZ basis set. Three rotamers were found (see Figure 3), of which two (2M1B-B and 2M1B-C) are essentially equivalent with an energy difference of <0.01 meV, which can be attributed to numerical errors. However, there is an energy difference of about 10 meV between 2M1B-A and 2M1B-B/C. The equilibrium geometries have no symmetry. Together with the larger number of electrons, this situation limits the range of methods and basis sets that can be used due to the higher numerical effort compared to 2CP. Therefore, the geometry optimizations were carried out at CCSD(T)-F12a/aug-cc-pVDZ level and frequency calculations at MP2/cc-pVDZ level only. The accuracy of MP2 frequencies and normal coordinates are fully sufficient for the aim of the present study. The optimized geometries and calculated frequencies are presented in Tables S7–S11 in Supplemental Material 1, and the tabulated data of the simulated PES are given in Supplemental Material 3.

Considering the high temperature of our flames (before the quartz nozzle) leading to high Boltzmann internal energy as compared to the low energy difference of only about 10 meV between 2M1B-A and 2M1B-B/C which are connected by low barriers, the total spectrum for 2M1B was approximated as superposition of two partial spectra for 2M1B-A and 2M1B-B. Every single transition is weighed equally, and since 2M1B-B and 2M1B-C are equivalent, the final spectrum is a 1:2 superposition of the two partial spectra of 2M1B-A and 2M1B-B. The resulting total spectrum and the spectra for single transitions due to the two rotamers

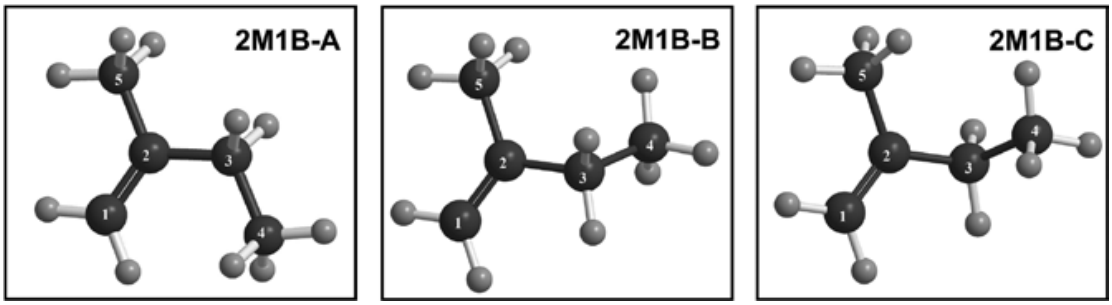

Fig. 3: Optimized geometries for different rotamers of 2-methyl-1-butene (2M1B) at CCSD(T)-F12a/aug-cc-pVDZ level of theory.

are shown in Figure 4. For all rotamers, the 0–0-transition is quite weak resulting from the large change in geometry upon ionization. Hence, the first peak at 9.15 eV has its maximum above the adiabatic IEs of IE(2M1B-A) = 9.11 eV and IE(2M1B-B/C) = 9.09 eV and is caused by transitions into low-frequency torsional modes for both rotamers (mainly modes 33, 35, and 38 for 2M1B-A$^+$ and modes 35, 37, and 38 for 2M1B-B$^+$). 2M1B-B has its main contribution to the following peak at 9.24 eV, generated by multi-mode excitations into mode 31, a torsional mode predominantly located at C^1H_2 and C^3H_2, and the above-mentioned low-frequency torsional modes. By contrast, the third peak at 9.32 eV results from transitions of 2M1B-A, namely excitations into the C^1–C^2 stretching mode 11 combined with some low-frequency torsional modes, particularly modes 33, 35, and 38. The fourth peak at 9.52 eV has contributions from both rotamers and corresponds mostly to simultaneous excitations into one C–H stretching mode (C^5–H_3 stretching mode 9 for 2M1B-A$^+$ and C^3–H_2 stretching mode 8 for 2M1B-B$^+$) and different low-frequency torsional modes. In summary, many transitions have an influence on the total spectrum as a consequence of the floppy molecular structure in a hot environment such as our flames.

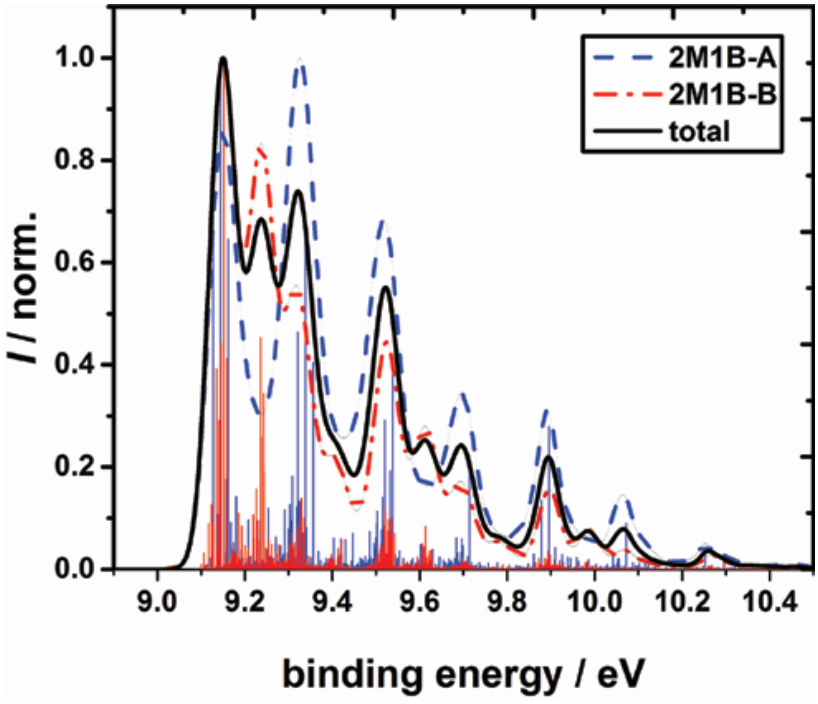

Fig. 4: FC simulations for the rotamers 2M1B-A and 2M1B-B of 2-methyl-1-butene using geometries optimized at CCSD(T)-F12a/aug-cc-pVDZ and frequency calculations at MP2/cc-pVDZ level of theory. The stick spectra have been convoluted (dashed blue and dot-dashed red line) with the experimental FWHM considering its energy-dependence given in [54]. The solid black line shows the total spectrum weighting each rotamer equally.

3.2 Combustion measurements

The measured and calculated reference photoelectron spectra have been applied in the analysis of selected combustion examples to identify and quantify important combustion intermediates, focusing on species with five heavy atoms. Specific chemical questions are addressed sequentially for measured signals for the set of compounds with the elemental composition of $C_xH_yO_z$ (x = 4, 5; y = 6–8, 10; z = 0, 1) using the reference spectra determined in this work. The first example will be devoted to $m/z = 67$ (C_5H_7), reporting the occurrence of the 2-cyclopentenyl radical in the combustion of cyclopentene. Next, we discuss the isomeric composition for $m/z = 70$ (C_5H_{10}) and $m/z = 68$ (C_5H_8) in flames fueled by pure *iso*-pentane and by a mixture of this fuel with dimethyl ether. Finally, the species assignment will be presented for $m/z = 72$ (C_4H_8O) in the fuel decomposition reactions of diethyl ether.

3.2.1 Fuel radicals: C_5H_7 ($m/z = 67$)

Radicals are of essential importance in the combustion mechanism since they drive the chain reactions from the fuel to the products. The initial decomposition products of the fuel in the high-temperature environment of a laminar premixed flame, i.e. fuel radicals that may be formed by hydrogen abstraction reactions of the fuel itself, are at the origin of the subsequent further reaction pathways, and therefore their identification and quantification is highly desirable for the development and critical inspection of predictive kinetic mechanisms. Higher complexity of the molecular fuel structure, such as in branched or saturated and unsaturated cyclic compounds with and without side chains, increases the number of fuel radicals that may be formed in the first reaction steps. With this increasing number of potential structures, the development of mechanisms for realistic fuels for the range of temperature and pressure in modern engines can profit from techniques that enable unambiguous detection of such decisive intermediates [14]. Beyond the more established C_1–C_4 mechanisms, the combustion chemistry of C_5-fuels has received attention because of specific pathways leading to aromatic compounds that are important as soot precursors [17, 26, 73]. In cyclopentene flames, pathways to first aromatic ring formation may efficiently proceed through the resonantly stabilized cyclopentadienyl radical [26], and a number of important isomeric structures in these flames have been detected before.

Unambiguous identification of the structure of the initial fuel radical C_5H_7 ($m/z = 67$) in a fuel-rich cyclopentene flame has, however, not yet been achieved, despite the interest in the initial branching pathways of the fuel decomposition.

Problematic aspects in the detection include low signal because of low concentration, probable fragmentation of the parent cyclopentene (fuel) molecule ($m/z=68$), and potential interference from the ^{13}C-isotope of the prominent C_5H_6 signal ($m/z=66$). Also, fuel radicals exhibit very low ionization energies, making it difficult to separate their signals from species with higher concentrations when ionizing at high photon energies for multiplexing purposes. The PES of $m/z=67$ in a fuel-rich cyclopentene flame has been recently detected [41], selectively using a low photon energy of 7.7 eV. However, due to a lack of reference spectra, the identity of the detected species could only be assumed from tabulated ionization energies. Here, with the newly calculated PES of the 2-cyclopentenyl radical, a more rigorous identification at this mass is possible.

Figure 5 shows the measured PES of $m/z=67$ from the fuel-rich cyclopentene flame (left) together with possible structures of C_5H_7 radicals (right) that could contribute to the measured signal; indicated IEs are taken from the literature [72, 74, 75]. The preferred H-abstraction reaction at flame temperatures is expected to favor the formation of cyclopentenyl radicals as the first step [26]. However, linear or branched isomers of C_5H_7 should not be completely ruled out, as they can be produced from ring-opening reactions or from combination reactions of fuel decomposition products. To discriminate from build-up reactions later in

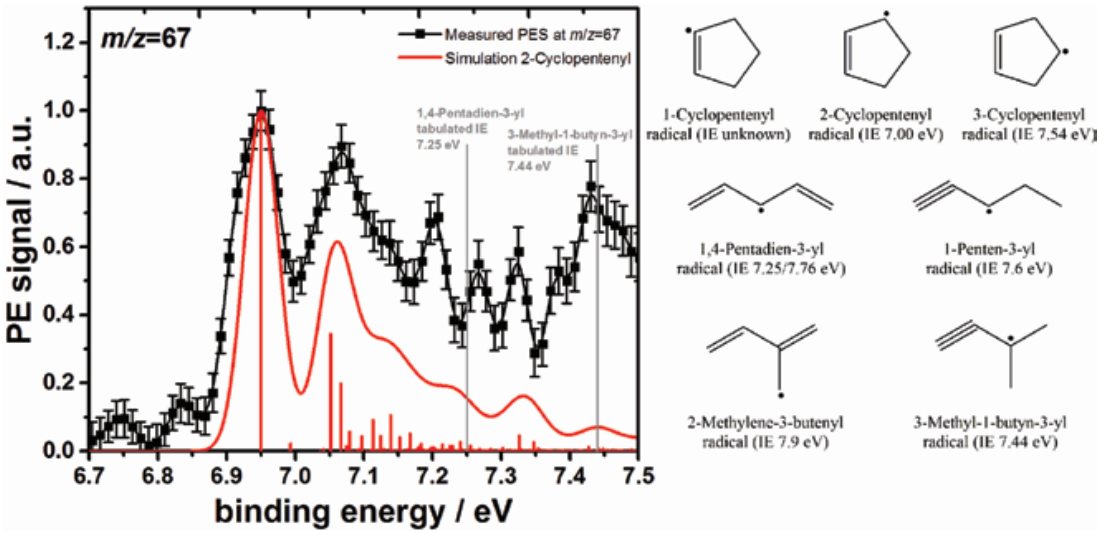

Fig. 5: Left: Measured PES at $m/z=67$ and 1.0 mm distance from the burner surface in the fuel-rich cyclopentene flame (black line and symbols including error bars from the evaluation with the pBasex algorithm [55]) and the FC simulation for the 2-cyclopentenyl radical at CASSCF/MRCI-F12a/aug-cc-pVTZ (radical) and CCSD(T)-F12a/aug-cc-pVTZ level of theory (red stick spectrum and envelope from convolution). The simulated spectrum has been shifted by 20 meV towards the maximum of the experimental spectrum for comparison. Right: Structures and ionization energies (IEs) [72, 74, 75] of selected isomers with $m/z=67$.

the flame and ascertain that only initial H-abstraction products are observed, the measurement was performed at a distance from the burner surface of $h = 1$ mm early in the reaction progress. Furthermore, the low, fixed photon energy of 7.7 eV was chosen to ionize only radicals and to obtain signals only from these species without contributions from fragments of higher-mass species.

The first peak in the measured PES in Figure 5 at 6.95 eV lies within 0.05 eV of the tabulated IE of the 2-cyclopentenyl radical obtained by energy-selected electron impact (7.00 eV [72]), indicating the presence of this isomer, whereas all other isomers in Figure 5 show higher ionization energies. More information is available from the complete PES that is compared to the calculated spectrum of the 2-cyclopentenyl radical, convoluted with the experimental energy resolution following [54].

The calculated ionization energy of 6.97 eV matches the position of the first measured peak at 6.95 eV remarkably well within a range of 20 meV, and the calculated PES thus further supports the presence of the 2-cyclopentenyl radical. The intensity of the second peak does not fit the measured spectrum equally well and might suggest contributions of a further molecule to this signal, although there are no tabulated IEs of further isomers fitting this peak. The three following peaks also suggest that they correspond to a different species whose spectrum is superimposed with the long structureless tail of the 2CP PES. A further explanation could be temperature-dependent contributions of vibrational modes of the 2-cyclopentenyl radical, with temperature differences between the experiment and the calculation. In a previous study, the temperature in the molecular beam was estimated to be 280 K [40], while for the calculations, no excited initial vibrational states have been considered, corresponding to a temperature of 0 K. It may seem trivial to include the temperature dependence in the FC simulations, however, the used program which is non-commercial does not yet include this option.

Further possible isomers with IEs in the measured range could be the 1,4-pentadien-3-yl radical for which widely different IEs of 7.25 eV [74] and 7.76 eV [75] are given in the literature, and the 3-methyl-1-butyn-3-yl radical with an IE of 7.44 eV [74]. The latter species can be ruled out since it cannot be formed directly from early fuel decomposition reaction because of its branched structure. The 1,4-pentadien-3-yl radical might be produced from the 2-cyclopentenyl radical *via* ring opening and subsequent stabilization. Slight contributions of 1,4-pentadien-3-yl in the range of 7.25–7.4 eV to the measured PES might thus be possible but cannot be verified without a reference PES. A measurement for this radical would require a clean, direct production process and thus presents a considerable challenge, but a high-level quantum calculation is similarly challenging and time demanding. In summary, the calculated reference spectrum underlines the presence of

2-cyclopentenyl as a dominant initial fuel radical, providing useful information for further mechanism development.

3.2.2 First products of fuel consumption reactions: C_5H_{10} ($m/z=70$)

The first steps in the fuel consumption mechanism are addressed here for *iso*-pentane (C_5H_{12}, $m/z=72$) as a branched C_5-fuel as well as for an 80:20 mixture of *iso*-pentane with DME. Following upon the formation of the first fuel radicals (C_5H_{11}), which were not detected, the initial stable products can help to identify reaction sequences and branching ratios that are at the start of the overall fuel oxidation. The number of possible isomers leads to rather complex photoelectron spectra, and one of the aims here is to examine the capability to identify, separate, and potentially quantify their contributions from such measured spectra to support chemical insight into the reaction processes. The isomeric distribution from mass-resolved PES at $m/z=70$ was inspected first with an attempt to identify species that correspond to products of composition C_5H_{10} after H-abstraction and a subsequent C–H-β-scission from the fuel molecule. A scheme of these first decomposition steps is given in Figure 6. Since the fuel molecule itself has

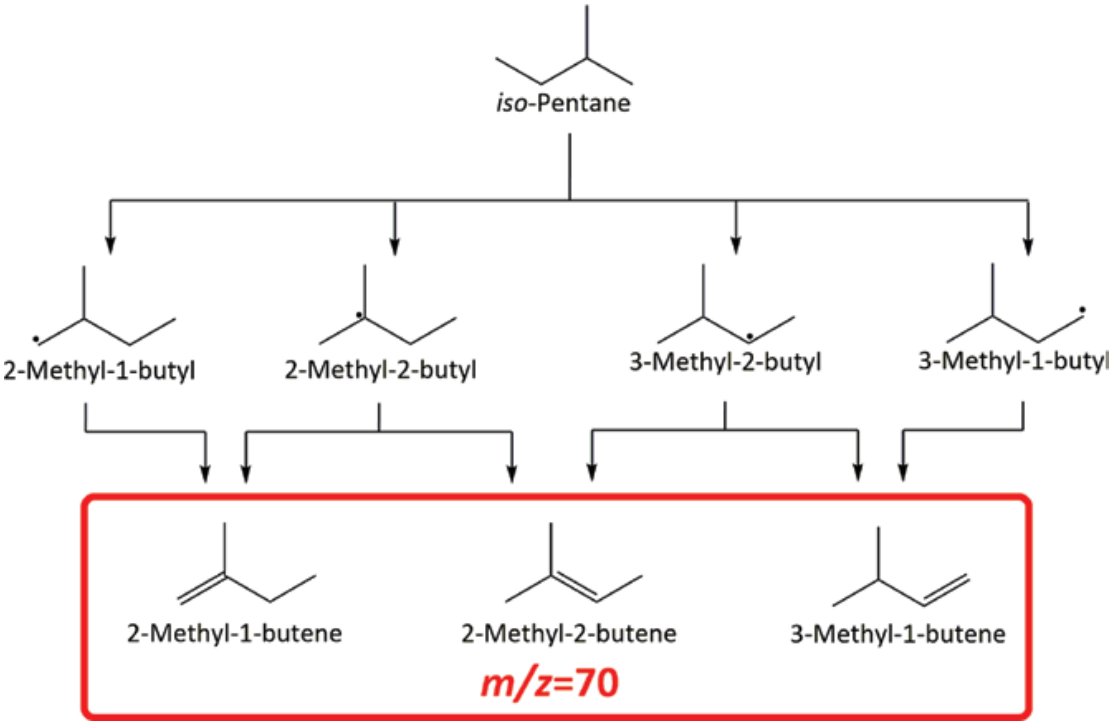

Fig. 6: Initial decomposition reactions of *iso*-pentane by H-abstraction and C–H-β-scission. Other reactions (such as the more prominent C–C-β-scissions of the fuel radicals) are not shown here, as they are not discussed in this work.

a branched structure, methylbutenes, namely 2-methyl-1-butene, 2-methyl-2-butene, and 3-methyl-1-butene, are most likely to be formed.

Nonetheless, linear isomers such as 1-pentene and 2-pentene (*cis*- and *trans*-conformation) should not be ruled out completely, as they can be formed by build-up reactions from linear fuel destruction products. However, their contribution is expected to be small compared to the branched structures. The most plausible isomers that could contribute to the signals of C_5H_{10} are shown in Figure 7 together with their ionization energies. Cyclopentane (IE: 10.3 eV [76]) cannot be detected at the fixed photon energy of 10.1 eV used in the measurements.

Regarding the comparably low mass resolution of the WM-TOF, C_4H_6O species (also at $m/z = 70$) could, in principle, also contribute to this signal. Separation of hydrocarbon and oxygenated species with the same m/z ratio was, however, possible with the complementary measurements in the *iso*-pentane flame under identical conditions with EI-MBMS and a mass resolution of ~4000. These experiments reveal a mole fraction of $2.0 \cdot 10^{-5}$ for the sum of C_4H_6O isomers (calibrated as 2-butenal), while the sum of C_5H_{10} isomers has been evaluated to be $7.8 \cdot 10^{-4}$ (calibrated as 2-methyl-2-butene), which is about a factor of 40 above the C_4H_6O contributions. The performed simulation with the mechanism of Bugler et al. [50] (see Section 2.3) also predicts the mole fraction sum of C_5H_{10} isomers to be more than a magnitude higher than that of C_4H_6O isomers. A significant contribution of C_4H_6O species to the PES of $m/z = 70$ can therefore be ruled out here.

Only small contributions are again expected for the linear C_5H_{10} isomers 1-pentene and *cis*- and *trans*-2-pentene. They were predicted in the simulation to be about 4.3% of the sum of all C_5H_{10} isomers, including 3.8% of 2-pentene and 0.5% of 1-pentene. Complementary information has also been obtained from gas chromatography (GC) measurements under identical flame conditions (see Section S.5 in Supplemental Material 1), which showed the presence of all three methylbutenes and also of 2-pentene, but no observable signal for 1-pentene (see Figure S3 in Supplemental Material 1). The PES of 1-pentene will thus not be considered in the evaluation procedure.

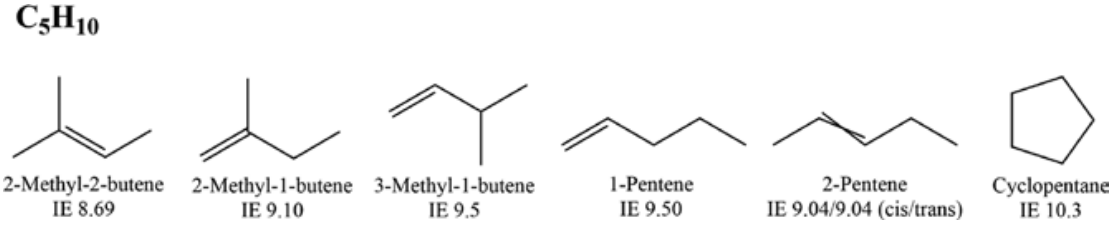

Fig. 7: Structures and ionization energies (IEs) [76–78] of expected isomers of the sum formula C_5H_{10} ($m/z = 70$) in the combustion of *iso*-pentane.

The contribution of 2-pentene could be determined, however, even though the PES of 2-methyl-1-butene and 2-pentene occur in the same energy range. Figure 8 shows the results for $m/z=70$ measured at $h=3.2$ mm in the *iso*-pentane flame with a fixed photon energy of 10.1 eV. Figure 8a presents the inverted 2D image of the electrons that coincide with the ions of $m/z=70$. The angular integration of such an image yields the photoelectron spectrum for $m/z=70$ in Figure 8b. To obtain the relative contributions of each isomer, measured and calculated reference PES of 2-methyl-2-butene, 3-methyl-1-butene, 2-pentene, and 2-methyl-1-butene, respectively, were considered in the evaluation; for the sake of clarity, they are normalized to their respective intensity maxima and are presented in Figure 8c. The contributions from these spectra versus the measured

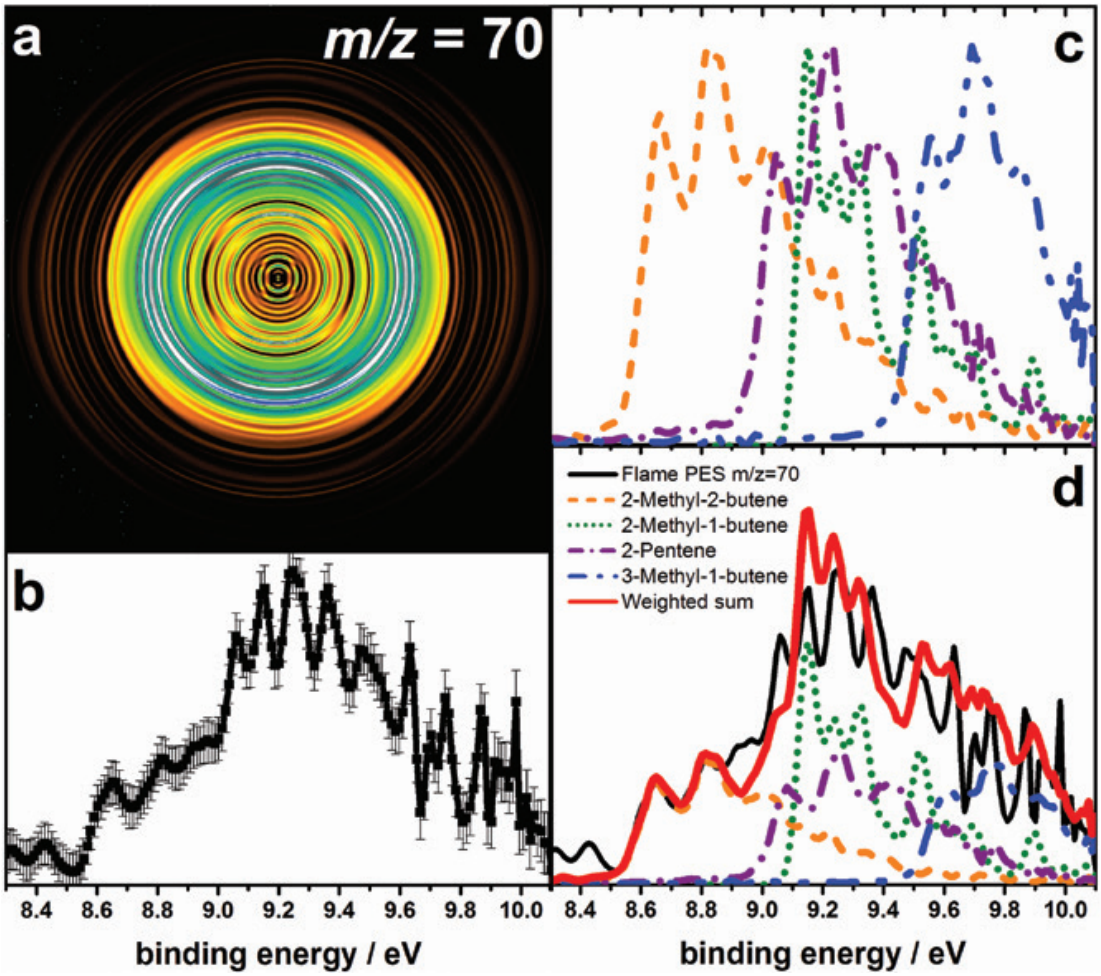

Fig. 8: (a) Inverted 2D electron image corresponding to ions with $m/z=70$. (b) PES of $m/z=70$ measured in the fuel-rich *iso*-pentane flame at $h=3.2$ mm and a fixed photon energy of 10.1 eV. (c) Normalized reference spectra with $m/z=70$ and sum formula C_5H_{10}. (d) Comparison of the measured PES to the weighted sum of all reference spectra following the subtraction procedure of Felsmann et al. [41].

PES as obtained from a subtraction procedure described in [41], is evident from the weighted sum shown in Figure 8d together with the scaled reference spectra. The full step-by-step subtraction analysis is provided in Figure S4 in Supplemental Material 1.

The overall structure of the measured PES of $m/z = 70$ can be reproduced satisfactorily from the weighted contributions of the different isomers. However, some peaks are not captured well by the reference spectra, especially in the range of 9.8–10.1 eV. It should be noted that the signal in this range must be interpreted with care, due to the noise level of the raw image which is inherently amplified by the Abel transformation especially close to the chosen fixed photon energy, i.e. for slow electrons. Temperature differences occurring between the flame and reference samples might also contribute to some of the observed deviations. Especially for the two signatures below 8.6 eV, no stable C_5H_{10} isomer is known with such low ionization energy. Hot bands corresponding to transitions from excited vibrational states could be one possible explanation, resulting in peaks at a lower binding energy. Such bands should be found at a distance corresponding to reasonable vibrational wavenumbers (i.e. ~1600 cm^{-1} ≈0.2 eV for a C=C stretch vibrational mode), as indeed observed in the spectrum in Figure 8. Further investigation of reference samples at elevated temperatures might assist in the clarification.

Remaining differences are observed near 9.05 and 9.4 eV. The evaluation faces some challenges here since the PES of 2-methyl-1-butene and 2-pentene overlap in this energy region (compare also Figures 1c and 4). As stated above, the simulation with the mechanism of Bugler et al. [50] predicts only a small contribution of linear isomers, supporting the chemically reasonable assumption that branched 2-methyl-1-butene is more likely to be formed directly from the branched fuel structure of *iso*-pentane (compare also Figure 6). In the subtraction procedure, the PES of 2-methyl-1-butene has thus been subtracted before that of 2-pentene, which results in a smaller contribution of 2-pentene (see Figure S4 in Supplemental Material 1), in accord with the chemical-kinetic model. Baer and Tuckett [36] have commented on the subtraction routine of Felsmann et al. [41] and noted that it may lead to a higher global error. We have thus also used a minimization procedure based on a Levenberg-Marquardt algorithm [79]. More detailed information is given in Section S.7 of Supplemental Material 1. It should be noted here that the measured spectrum could be analyzed with a slightly improved overall fit, but with the result of an unreasonably high contribution of 2-pentene. Small changes in the spectral structure may have important leverage in such automatic evaluation procedures, and the results should be considered carefully.

For a quantitative evaluation of the measured spectrum in Figure 8, the contribution of each of the four isomers was calculated by considering the area of

each scaled reference PES and the photoionization cross section (PICS) of the respective species at the fixed photon energy of 10.1 eV. From the sum mole fraction of C_5H_{10} of $7.8 \cdot 10^{-4}$ (calibrated directly as 2-methyl-2-butene with about 30% uncertainty) determined in the EI-MBMS measurements, the mole fraction of each isomer was obtained. The results are presented in Table 2 together with the predicted mole fractions from the simulations (left panel); also, the values for the DME-doped flame are included for comparison (right panel).

As the most prominent isomer, 2-methyl-1-butene is produced in the *iso*-pentane flame at $h = 3.2$ mm. Concerning the respective contributions of 38.8% vs. 34.4%, experiment and simulation show reasonable agreement. Similarly, measured and predicted contributions of 3-methyl-1-butene agree satisfactorily, with somewhat larger deviations observed for 2-methyl-2-butene. Both the latter isomers attain contributions of ~18–24% in the experiment and ~28–33% in the simulations. The experiment also confirms the contribution of 2-pentene, but also with a higher deviation. Overall, the sum of C_5H_{10} isomers is predicted to be $9.9 \cdot 10^{-4}$, which is in quite good agreement with the result of $7.8 \cdot 10^{-4}$ from the experiment.

The results for the DME-doped *iso*-pentane flame in Table 2 and Figure S7 in Supplemental Material 1 show that neither the structure of the PES nor the occurrence of the various isomers is significantly altered by the addition of DME. Within the experimental uncertainty, observed trends are also consistent with the simulation. The overall C_5H_{10} mole fraction is reduced slightly, corresponding to the replacement of the C_5-fuel by DME that cannot produce C_5H_{10} intermediates

Tab. 2: Contributions C (in %) of isomers of $m/z = 70$ and their mole fractions x at $h = 3.2$ mm in the fuel-rich flames of pure *iso*-pentane and of *iso*-pentane doped with 20% DME from experiment and simulation.

	***iso*-Pentane**				***iso*-Pentane/DME (80:20)**			
	Experiment		**Simulation**		**Experiment**		**Simulation**	
	C	***x***	***C***	***x***	***C***	***x***	***C***	***x***
2-Methyl-2-butene [80]	18.6	$1.5 \cdot 10^{-4}$	32.8	$3.3 \cdot 10^{-4}$	23.1	$1.0 \cdot 10^{-4}$	32.9	$3.0 \cdot 10^{-4}$
2-Methyl-1-butene [80]	38.8	$3.0 \cdot 10^{-4}$	34.4	$3.4 \cdot 10^{-4}$	42.0	$1.8 \cdot 10^{-4}$	34.3	$3.1 \cdot 10^{-4}$
3-Methyl-1-butene [80]	24.1	$1.9 \cdot 10^{-4}$	28.5	$2.8 \cdot 10^{-4}$	19.0	$8.4 \cdot 10^{-5}$	28.5	$2.6 \cdot 10^{-4}$
2-Pentene [81][a]	18.5	$1.4 \cdot 10^{-4}$	3.8	$3.8 \cdot 10^{-5}$	15.9	$7.0 \cdot 10^{-5}$	3.9	$3.5 \cdot 10^{-5}$
1-Pentene [82]	n.q.	–	0.5	$4.5 \cdot 10^{-6}$	n.q.	–	0.4	$3.8 \cdot 10^{-6}$
Sum C_5H_{10}	100	$7.8 \cdot 10^{-4}$	100	$9.9 \cdot 10^{-4}$	100	$4.4 \cdot 10^{-4}$	100	$9.1 \cdot 10^{-4}$

Photoionization cross sections were taken from the literature (references are given behind the species names). n.q., not quantifiable in the experiment. [a]Mean value of *cis*- and *trans*-isomer.

easily. These results are not unexpected since the nature of the initial *iso*-pentane destruction reactions towards the observed C_5H_{10} isomers (compare Figure 6) should be similar with and without the presence of dimethyl ether in the system. Despite the complexity of the isomer mixture, leading to overlapping photoelectron spectra in a narrow energy range, the prevalence of branched intermediates could be unambiguously established.

3.2.3 Stable products from initial fuel consumption reactions: C_5H_8 ($m/z = 68$)

Following the reaction pathways towards the formation of stable products from the abovementioned C_5H_{10} intermediates, species with $m/z = 68$ of sum formula C_5H_8 will be analyzed. Special attention will be given to isoprene (2-methyl-1,3-butadiene), which is expected to be the most abundant isomer in the early *iso*-pentane fuel consumption reactions because of its branched structure. Isoprene is known to participate in atmospheric reactions, as it decomposes *via* reactions with OH radicals and ozone and thus can lead to toxic aldehydes and peroxides that are involved in particle formation in the upper troposphere [83]. Together with isoprene, Figure 9 shows further isomers of $m/z = 68$ that are likely to occur in the *iso*-pentane flame, including 3-methyl-1,2-butadiene, *cis*- and *trans*-1,3-pentadiene, 1,4-pentadiene, and cyclopentene.

Branched isomers of C_5H_8 will be formed primarily because of the branched fuel structure, of which 3-methyl-1,2-butadiene with its two vicinal C=C double bonds is structurally unfavorable and might undergo internal rearrangements. The simulation predicts isoprene to be formed almost exclusively. Because of the limited mass resolution of the WM-TOF (see Section 2.1), oxygenated species with $m/z = 68$ and sum formula C_4H_4O cannot be separated from the hydrocarbon signal. They can, in principle, be unambiguously detected in the complementary EI-MBMS measurements that did, however, not even show a quantifiable signal for these species. Also the simulation predicts a mole fraction of only $2.5 \cdot 10^{-7}$ for

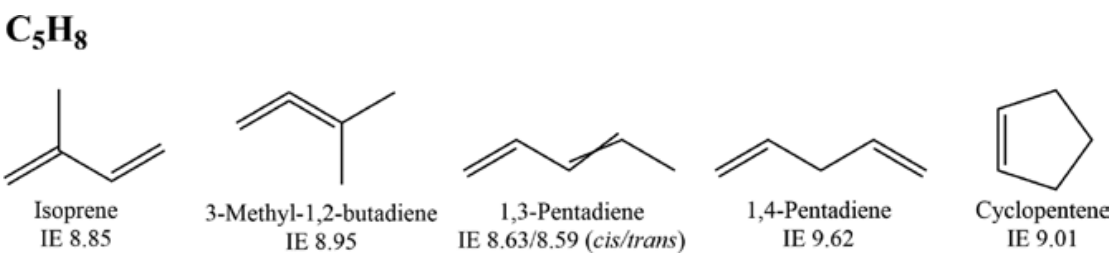

Fig. 9: Structures and ionization energies (IEs) [76–78] of the expected isomers of the sum formula C_5H_8 ($m/z = 68$) in the combustion of *iso*-pentane.

the sum of oxygenated compounds with $m/z = 68$, more than two orders of magnitude smaller than that for the sum of the C_5H_8 hydrocarbon species ($9.8 \cdot 10^{-5}$).

To determine the contributions of the different C_5H_8 isomers, the same procedure has been applied as discussed for the C_5H_{10} spectra above (see Section 3.2.2). Figure 10 presents the results for $m/z = 68$ measured at $h = 3.2$ mm at a fixed photon energy of 10.1 eV. Figure 10a shows the inverted 2D image for the electrons coincident with the ions of $m/z = 68$ and Figure 10b the resulting PES. The measured reference PES of 1,3-pentadiene (mixture of *cis*- and *trans*-isomers), cyclopentene, and 1,4-pentadiene are given in Figure 10c together with that of isoprene that was taken from the literature [84]; all PES have been normalized to their respective intensity maxima for better comparison. The resulting weighted sum

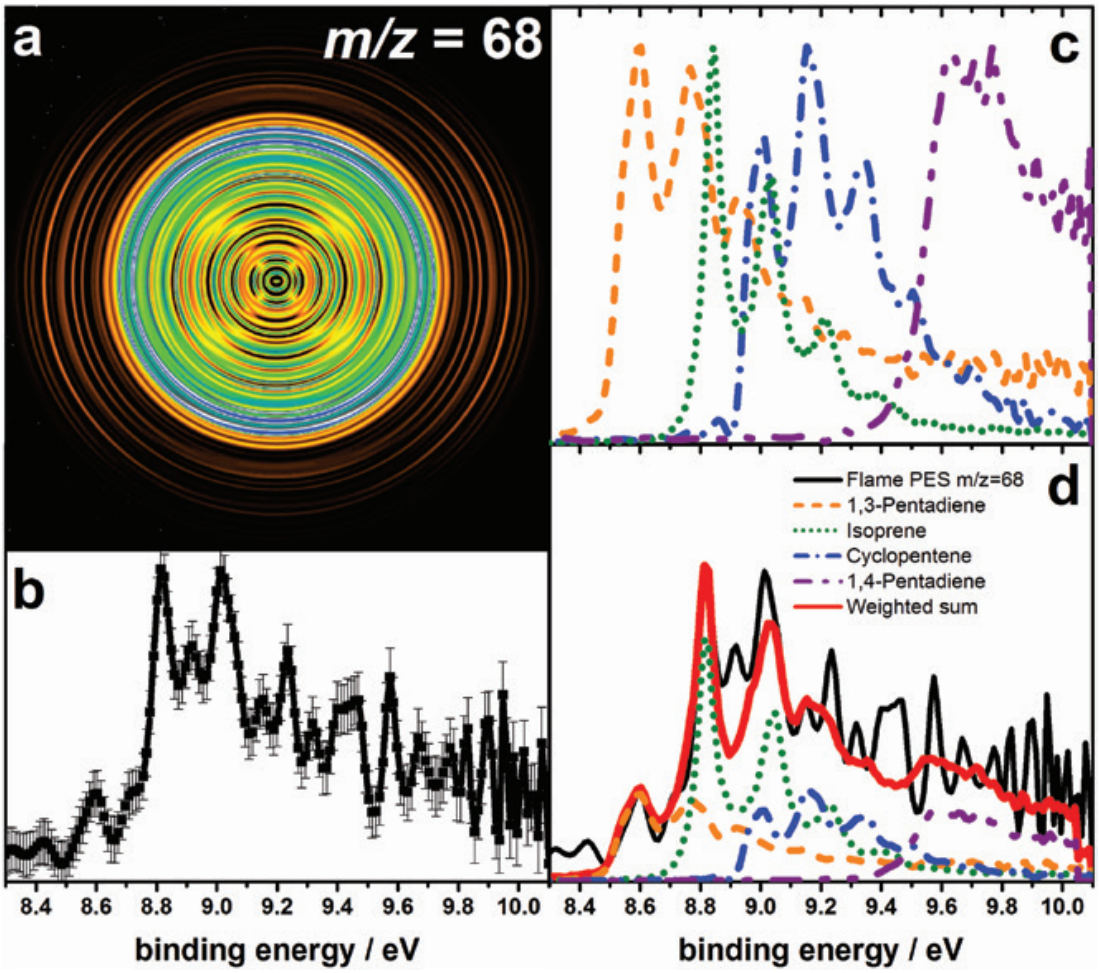

Fig. 10: (a) Inverted 2D electron image corresponding to ions with $m/z = 68$. (b) PES of $m/z = 68$ measured in the fuel-rich *iso*-pentane flame at $h = 3.2$ mm and a fixed photon energy of 10.1 eV. (c) Normalized reference spectra with $m/z = 68$ and sum formula C_5H_8. (d) Comparison of the measured PES to the weighted sum of all reference spectra following the subtraction procedure of Felsmann et al. [41].

from the subtraction procedure is given in Figure 10d together with the scaled reference spectra; the full subtraction analysis is provided in Figure S5 in Supplemental Material 1.

Satisfactory agreement between the measured PES and the weighted sum of the reference spectra is observed. The peaks near 8.6, 8.8, and 9.0 eV are well matched by the respective structures of 1,3-pentadiene and isoprene, with contributions also from cyclopentene. Further observed peaks in this region, especially at 8.9, 9.2, and 9.4 eV cannot be reproduced completely with the considered reference PES; also, the peak intensity near 9.0 eV is somewhat low. However, as previously mentioned, intensities could be different as a function of temperature between the hot flame and the cold-gas reference spectra. As for the C_5H_{10} isomers discussed before, it is more challenging to assign clear reference spectra to the measured spectrum above ~9.5 eV due to the noise level of the raw image which is inherently amplified by the Abel transformation in this region. The PES of 1,4-pentadiene may thus appear a bit more speculative, since the structure cannot be clearly identified. A full TPES energy scan would have been required to provide unambiguity, but time limitations prevented such an attempt. Other possible C_5H_8 isomers near this range could include 2-pentyne with a calculated IE of 9.44 eV according to Hansen et al. [73]; however, it seems unlikely that this species would be formed from *iso*-pentane as a fuel decomposition product. No clear identification was given for this species in flames of allene, propyne, cyclopentene, and benzene in Ref. [73], and 2-pentyne was also not observed in the cyclopentene flame studied by Hansen et al. [26] where the observed C_5H_8 signal was predominantly due to the fuel itself. We have not considered 2-pentyne here for these reasons, but we would like to mention that reference PES for this species are also lacking in the literature. Finally, similar to the discussion for $m/z = 70$, structures at 8.3–8.4 eV were noted that cannot be assigned to further species and that might be hot bands.

The contribution of each of the four analyzed isomers was calculated considering the respective photoionization cross sections at the fixed photon energy of 10.1 eV. The resulting mole fractions for each isomer, obtained from these percentages and the sum mole fraction of $9.8 \cdot 10^{-5}$ for C_5H_8 from the EI-MBMS measurements are reported in Table 3 together with the results of the simulations (left panel); for comparison, the respective information is also included for the DME-doped flame (right panel).

It is not easy to compare experiment and simulation quantitatively in this case since the mechanism of Bugler et al. [50] does not include cyclopentene and 1,4-pentadiene. The presence of cyclopentene has been demonstrated by the present i^{2}PEPICO measurement and this species should thus be included in

Tab. 3: Contributions *C* (in %) of isomers of $m/z = 68$ and their mole fractions *x* at $h = 3.2$ mm in the fuel-rich flames of pure *iso*-pentane and of *iso*-pentane doped with 20% DME from experiment and simulation.

	***iso*-Pentane**				***iso*-Pentane/DME (80:20)**			
	Experiment		**Simulation**		**Experiment**		**Simulation**	
	C	***x***	***C***	***x***	***C***	***x***	***C***	***x***
1,3-Pentadiene [80]	21.7	$2.1 \cdot 10^{-5}$	3.6	$1.8 \cdot 10^{-5}$	20.4	$1.5 \cdot 10^{-5}$	3.7	$1.6 \cdot 10^{-5}$
Isoprene [85]	37.4	$3.7 \cdot 10^{-5}$	94.8	$4.8 \cdot 10^{-4}$	30.9	$2.2 \cdot 10^{-5}$	94.8	$4.3 \cdot 10^{-4}$
Cyclopentene [81]	25.2	$2.5 \cdot 10^{-5}$	n.a.	–	30.6	$2.2 \cdot 10^{-5}$	n.a.	–
1,4-Pentadiene [80]	15.7	$1.5 \cdot 10^{-5}$	n.a.	–	18.1	$1.3 \cdot 10^{-5}$	n.a.	–
3-Methyl-1,2-butadiene [80]	n.q.	–	1.6	$7.8 \cdot 10^{-6}$	n.q.	–	1.5	$7.0 \cdot 10^{-6}$
Sum C_5H_8	100	$9.8 \cdot 10^{-5}$	100	$5.1 \cdot 10^{-4}$	100	$7.2 \cdot 10^{-5}$	100	$4.5 \cdot 10^{-4}$

Photoionization cross sections were taken from the literature (references are given behind the species names). n.q., Not quantifiable in the experiment; n.a., not available in the kinetic model.

kinetic reaction mechanisms for *iso*-pentane combustion. Also, the measurements suggest consideration of 1,4-pentadiene in the mechanism to examine pathways for its formation. From their analysis of PIE curves for flame-sampled C_5H_8 species in fuel-rich flames of several fuels, Hansen et al. [73] also discussed the presence of 1,4-pentadiene. Both experiment and model agree in that isoprene is the most abundant isomer. Isoprene contributes to $m/z = 68$ with ~37% in the experiment, while 1,3-pentadiene, cyclopentene and 1,4-pentadiene show a similar content of ~15–20% each. In the simulations, isoprene contributes with 94.8% and only small contributions of 1,3-pentadiene of 3.6% and 3-methyl-1,2-butadiene of 1.6% are predicted. Isoprene's mole fraction is with $3.7 \cdot 10^{-5}$ comparatively small, about an order of magnitude lower than predicted by the model with $4.8 \cdot 10^{-4}$. Given the still sparse information on fuel-specific C_5-reactions, results such as those presented here, with the detection of several isomers from their photoelectron spectra, may provide clues for the further development of kinetic reaction mechanisms.

As already shown for the distribution of the C_5H_{10} isomers (see Section 3.2.2), the PES of $m/z = 68$ was also determined for the DME-doped *iso*-pentane flame and evaluated as for the pure *iso*-pentane flame. Results are shown in Figure S8 in Supplemental Material 1 and included in Table 3 (right panel). Again, the *iso*-pentane/DME mixture leads to lower mole fractions of C_5-species, as expected, with consistent trends in experiment and simulation, but only moderate changes in the isomer composition. These results also support the previous conclusion that the presence of DME in the *iso*-pentane flame does not affect the C_5-fuel destruction steps significantly under the investigated conditions. Again, the measured

photoelectron spectra demonstrate the prominent formation of branched isomers in the fuel-specific reaction pathways.

3.2.4 Oxygenated intermediates: C_4H_8O ($m/z=72$)

Flames of biomass-derived fuels feature numerous intermediates that contain heteroatoms such as oxygen or nitrogen [12, 86, 87], rendering the analysis at a given m/z ratio more challenging. The i²PEPICO technique presents useful opportunities to identify the isomeric distribution and structures of such combustion intermediates due to their individual fingerprint photoelectron spectra. Here we will place special emphasis on the separation of intermediates with elemental composition C_4H_8O at $m/z=72$ in a fuel-rich diethyl ether flame that has been previously investigated with EI- and VUV-PI-MBMS [51]. In the previous study, Tran et al. [51] reported the detection of ethyl vinyl ether (EVE, $m/z=72$) for the first time as intermediate in their DEE flame and suggested that this species should be included in the respective kinetic mechanism where it had not yet been considered [52]. Figure 11 illustrates the first two steps in the DEE fuel consumption pathway including EVE formation *via* H-abstraction and C–H-β-scission.

Relying on the high mass resolution of their EI-MBMS instrument, Tran et al. [51] could separate the species of interest with sum formula C_4H_8O ($m/z=72$)

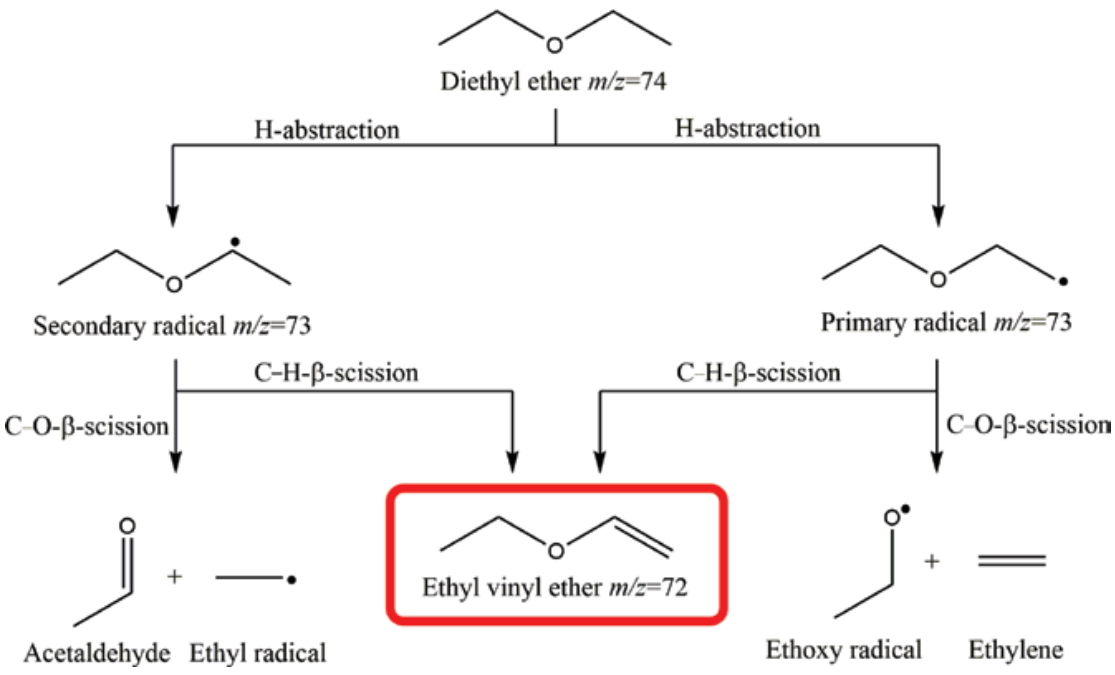

Fig. 11: First decomposition steps of diethyl ether by H-abstraction and C–H- and C–O-β-scission reactions forming ethyl vinyl ether and other products.

clearly from hydrocarbon species with the same nominal mass (C_5H_{12}, also $m/z=72$). They had assigned their C_4H_8O signal as EVE and determined a mole fraction of ~$1.0 \cdot 10^{-5}$ from direct calibration. The photoionization efficiency spectrum at $m/z=72$ from their complementary VUV-PI-MBMS experiment [51] exhibits a noticeable onset near the tabulated IE of EVE of 8.98 eV [88].

As a prerequisite to analyze the isomer composition in the DEE flame for species with the elemental composition C_4H_8O further, fixed-photon-energy measurements at 10.1 eV were performed with the i²PEPICO technique to record the PES of nine reference compounds with the sum formula C_4H_8O; these reference spectra are given in Figure 12.

Measurements in the DEE flame were performed at $h=2.3$ mm, the distance from the burner where the previous study [51] showed the maximum concentration of C_4H_8O species. The energy was scanned in the flame experiment to record the threshold photoelectron spectrum (TPES) with a higher resolution of 10 meV, because according to the reference spectra in Figure 12, several species with very similar PES might contribute to this signal. Results are given in Figure 13a together with the measured TPES (black lines and symbols) and the three reference PES in the scanned energy range of 8.35–9.35 eV, i.e. those of 2-methoxypropene (blue dotted line), ethyl vinyl ether (red line), and *iso*-butenol (green dashed line). Please remember for the comparison that the reference spectra were

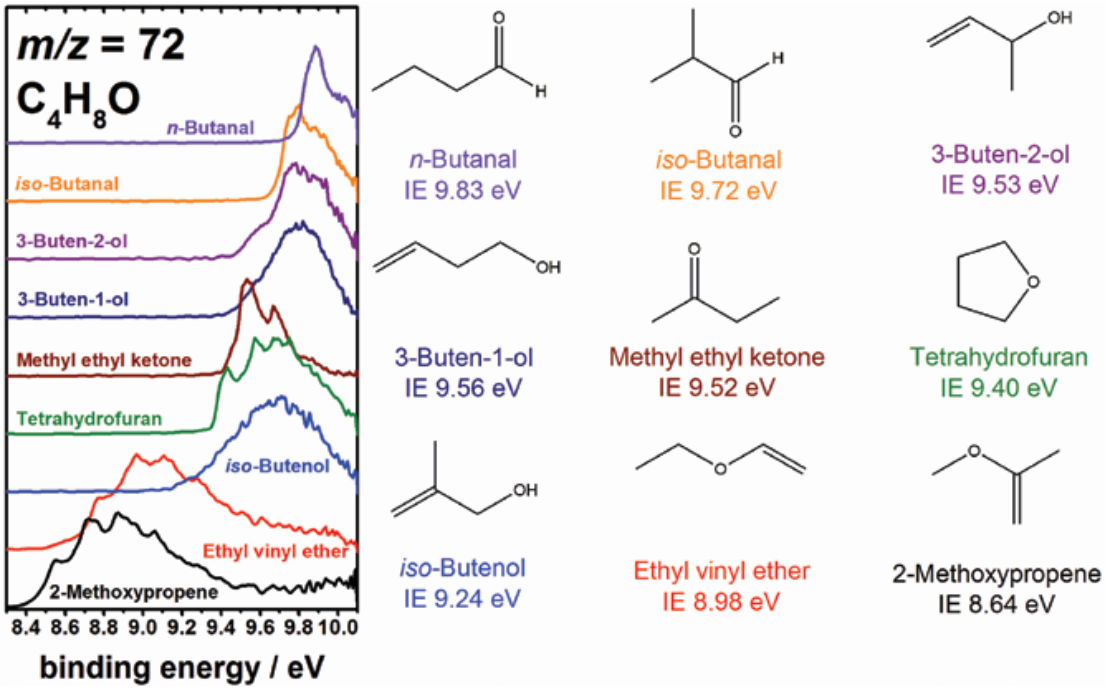

Fig. 12: Left: Measured reference PES at 10.1 eV of selected oxygenated species with the sum formula C_4H_8O. Right: Corresponding structures and tabulated IEs [88–93] of these compounds.

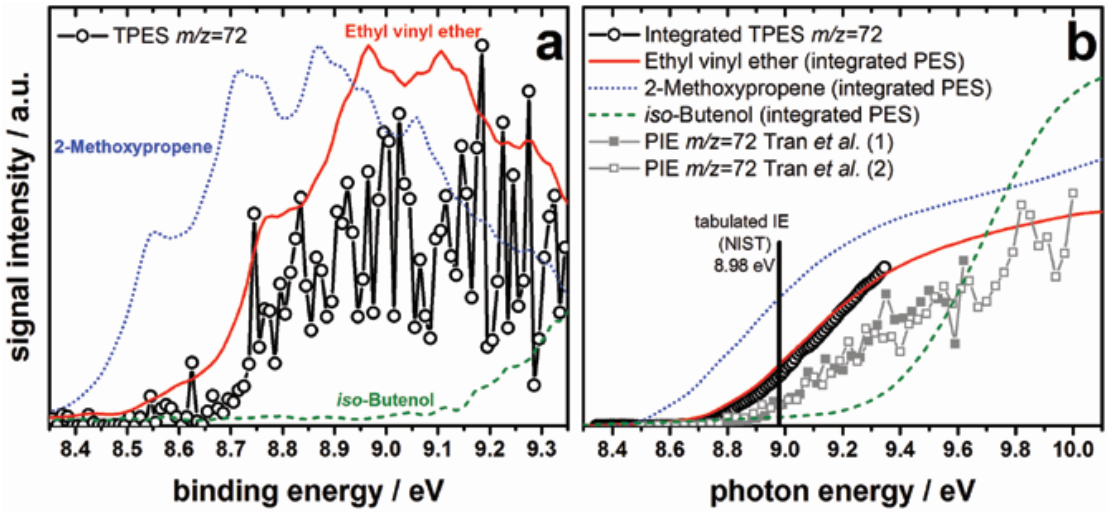

Fig. 13: (a) TPES of $m/z = 72$ measured in the fuel-rich DEE flame at $h = 2.3$ mm in the energy range of 8.35–9.35 eV ($\Delta E = 10$ meV; black lines and open circles), together with the PES of 2-methoxypropene (blue dotted line), ethyl vinyl ether (red line), and *iso*-butenol (green dashed line) measured at a fixed photon energy of 10.1 eV (the latter are presented as lines without error bars for clarity). (b) Integrated TPES and reference PES based on the data of (a): flame TPES for $m/z = 72$ (black open circles), PES of 2-methoxypropene (blue dotted line), ethyl vinyl ether (red line), and *iso*-butenol (green dashed line). For comparison, the PIE curves from two identical measurements obtained by Tran et al. [51] are included (gray lines and symbols, with permission of Elsevier/The Combustion Institute). The tabulated IE for ethyl vinyl ether is taken from [88].

recorded at fixed photon energy with lower energy resolution (about 30–70 meV in the respective KE range) as that for the flame scan.

The observed signal from the flame in Figure 13a starts to rise near 8.55 eV and shows a more substantial increase at 8.70 eV, corresponding well to the onset of the photoelectron signal in the reference PES of EVE at 8.55 eV. The TPES can be used to evaluate the ionization onset, potentially with higher precision than currently available in the literature. However, here, the low density of the DEE flame and the limited synchrotron beamtime lead to the low signal-to-noise observed in the recorded TPES. For this reason, the TPES measured in the DEE flame and the three presented reference spectra of 2-methoxypropene, ethyl vinyl ether, and *iso*-butenol have been integrated to yield the PIE curves. These are presented in Figure 13b together with the PIE curves measured by PI-MBMS from Ref. [51]. Excellent agreement between the integrated TPES measured in the flame and the integrated reference PES of ethyl vinyl ether is seen, with a resulting onset near 8.75 eV. A shift between the PEPICO and PI-MBMS measurements of ~0.1 eV is noted, with very good reproducibility for each technique, however. This shift again shows the necessity of measuring reference spectra with the same apparatus. Please also note the quite high quality of the PIE curve (open circles

in Figure 13b) as the integration result of the noisy TPES (black lines and open circles in Figure 13a), demonstrating the advantages of the PEPICO technique even at low signal levels. As a recommendation from both the present measurements as well as those with PI-MBMS from Tran et al. [51], the IE for ethyl vinyl ether should be ~8.75 eV rather than the tabulated value of 8.98 eV [88].

The presence of EVE in the combustion of DEE can be clearly confirmed from the comparison of position and shape of the measured TPES and the reference PES of EVE. The six further reference compounds are not ionized below 9.35 eV (compare Figure 12) and can thus not contribute to the flame signal. Also, an increase of the signal for 2-methoxypropene at 8.40 eV is not observed in the flame TPES. Contributions of *iso*-butenol in this energy range seem possible but hard to quantify.

Measurements to identify or exclude isomers with higher IEs, e.g. to determine the contribution of *n*-butanal, would be interesting for a comparison of experiment and simulation with a kinetic model. They are hard to perform, however, since the C_4H_8O signal is quite low and therefore noisy (see Figure 13a); ionization with higher photon energy would also lead to contributions from the fuel DEE itself (IE = 9.51 eV [94]) that is present in high concentrations, making it challenging to separate with the available experimental mass resolution. From the fuel decomposition analysis as well as the experimental and simulation results in Ref. [51], it seems, however, quite unlikely that further C_4H_8O isomers can contribute substantially in the fuel consumption reactions of diethyl ether, because they would have to be formed by combination from smaller molecular building blocks.

4 Summary and conclusions

With the analysis of combustion intermediates featuring five heavy atoms in flames of different fuels, the discriminative capacity of double-imaging photoelectron/photoion coincidence spectroscopy has been examined under isomer-rich, chemically complex conditions. The i²PEPICO approach that profits from the unambiguous fingerprint PES of each species was applied to flames of cyclopentene, pure *iso*-pentane and its blend with dimethyl ether, and diethyl ether to provide specific information about the chemical composition at a given mass. The technique had already been proven advantageous over more widely used photoionization MBMS measurements that can only identify the contribution of several isomers if their ionization energies are not too close and the corresponding slopes of the photoionization efficiency curves can each be assigned to a single species. The multiplexing capability of fixed-photon-energy measurements was

applied since it offers a much superior acquisition efficiency and requires only the photoionization cross section at a single fixed energy for a quantitative interpretation of the i²PEPICO experiments.

To analyze the flame-sampled spectra, reference photoelectron spectra of 18 C_4- and C_5-species with the sum formulae of C_5H_6, C_5H_8, C_5H_{10}, and C_4H_8O were determined, including several compounds for which such spectra are reported for the first time. Measurements of these reference spectra were performed since these species were expected to be produced in the combustion reactions of the investigated fuels. Reference spectra were recorded in the range of 8–12 eV with the same experimental setup as for the flame measurements. In addition, the photoelectron spectra of the 2-cyclopentenyl radical and the 2-methyl-1-butene molecule were obtained from Franck-Condon simulations on the basis of high-level quantum chemistry calculations.

At low photon energies, the detection of the initial radicals produced in a cyclopentene flame was possible and the 2-cyclopentenyl radical could be unambiguously identified with the aid of the calculated reference spectrum. Information on such species immediately involved in the fuel destruction reactions is of significant importance for mechanism development since they are at the origin of subsequent fuel conversion reactions.

In the combustion of *iso*-pentane ($m/z=72$), the isomers of C_5H_{10} ($m/z=70$) and of C_5H_8 ($m/z=68$) were identified and quantified based on the measured and calculated reference spectra and complementary EI-MBMS measurements. The results show a preference to form branched methylbutenes and only a small contribution of the linear isomer 2-pentene that is unlikely to be formed in the fuel decomposition. The experiment shows the dominant isomer to be 2-methyl-1-butene and to a lesser extent the presence of 2-methyl-2-butene and 3-methyl-1-butene, while a simulation with a recent kinetic model from the literature [50], developed specifically to describe the combustion of the pentane isomers, predicts the three methylbutenes in similar amounts. The present experiments thus provide interesting information for a deeper analysis of the early fuel consumption reactions. For C_5H_8 species with $m/z=68$, the experiments revealed significant contributions of cyclopentene and pentadienes, while the simulations with the model of Bugler et al. [50] predict almost exclusively isoprene. It should be noted that cyclopentene and 1,4-pentadiene have not yet been included in their kinetic model, and the present results can thus support further development to improve the prediction capability of the model.

The same i²PEPICO approach has been successfully applied to a fuel mixture of the previously analyzed fuel-rich *iso*-pentane flame, doped with 20% DME. The results confirm the expectations that DME does not affect the first fuel-specific reactions significantly under the present pressure and temperature conditions – a

result that should, however be put to further examination in the low-temperature auto-ignition regime where the peroxide-forming early oxidation chemistry of both fuels could lead to interactive effects.

Furthermore, the present measurements have been successful to unambiguously identify ethyl vinyl ether as an intermediate in a DEE flame, relying on the scanned photoelectron spectrum in the flame and the obtained reference spectra for several C_4H_8O isomers taken at fixed photon energy. In spite of the small and quite noisy signal, the present TPES result offers superior spectral information over recent PI-MBMS measurements that reported the PIE curve of this species in a DEE flame at similar conditions [51]. From these measurements, the IE for EVE can be recommended as ~8.75 eV. Again, the present results may serve for the improvement of the very recent, newly developed kinetic model for the alternative fuel diethyl ether [51].

It may be concluded that photoelectron spectra measured in flames with fixed-photon-energy i²PEPICO spectroscopy can support isomer identification in combustion systems featuring chemically complex mixtures beyond the reasonably well understood C_1–C_4 reactions. Several aspects have been instrumental for successful results. Reference spectra of the pure compounds recorded with the same setup under identical conditions as recommended by Baer and Tuckett [36] have proven a valuable prerequisite to remove any ambiguities such as potential resolution effects or shifts in the assignment of isomer contributions in the flame spectra. For species such as the fuel radicals in the combustion of C_4 and C_5 fuels for which reference measurements for the different isomer structures would be extremely challenging or impossible, high-level quantum calculations seem inevitable to provide the necessary reference spectra. Similarly, theoretical calculations can be a useful complement to measured reference PES for molecular structures in complex isomer mixtures. It should be noted that to obtain reliable results, these may need examination of different conformers and calculations on different levels so that they can be quite time-consuming. In further developments it may be useful to compare measured and calculated PES for several cases to assess the quality of both. Problems in resolving all contributions from flame spectra may arise from vibronic contributions and potentially hot bands, which would possibly be remedied by providing reference spectra at different temperatures. In any case, the flames can serve as moderately elevated temperature reactors to access PES of interesting radicals. In situations where several isomers contribute to the combustion reactions, a stand-alone analysis with i²PEPICO measurements is, in principle, possible as demonstrated in previous work [38, 40, 41], but the value of supporting, complementary and independent measurements using PI-MBMS or gas chromatography whenever useful has been demonstrated here to exclude certain isomers or to compare PIE curves and PES. Furthermore,

assignment of quantitative concentrations from the analysis of the same combustion situation with electron-ionization molecular-beam mass spectrometry was of significant value since oxygenated and hydrocarbon isomers could be separated by their exact mass and since sum concentrations at a given mass signal were available from an independent physical process. While photoelectron/photoion coincidence techniques have meanwhile proven themselves as invaluable diagnostic tools for gas-phase combustion analysis, we recommend to see them as one building block in a full analysis of specific combustion problems that should rely on the combination of cutting-edge experiments, theory, and kinetic analysis with the potential to further improve dedicated reaction mechanisms developed for this purpose.

Acknowledgments: The experiments at the SOLEIL synchrotron were performed under proposal 20150205. We would like to thank the SOLEIL staff for smoothly running the facility and for ongoing support during our measurements. In particular, we appreciate the technical help provided by Jean-François Gil. We wish to thank Dr. Michael Letzgus for programming support with the numerical minimization procedure.

References

1. O. Welz, J. D. Savee, D. L. Osborn, S. S. Vasu, C. J. Percival, D. E. Shallcross, C. A. Taatjes, Science **335** (2012) 204.
2. S. R. Leone, M. Ahmed, K. R. Wilson, Phys. Chem. Chem. Phys. **12** (2010) 6564.
3. P. Hemberger, M. Steinbauer, M. Schneider, I. Fischer, M. Johnson, A. Bodi, T. Gerber, J. Phys. Chem. A **114** (2010) 4698.
4. M. Steinbauer, J. Giegerich, K. H. Fischer, I. Fischer, J. Chem. Phys. **137** (2012) 014303.
5. F. Jiao, J. Li, X. Pan, J. Xiao, H. Li, H. Ma, M. Wei, Y. Pan, Z. Zhou, M. Li, S. Miao, J. Li, Y. Zhu, D. Xiao, T. He, J. Yang, F. Qi, Q. Fu, X. Bao, Science **351** (2016) 1065.
6. F. Holzmeier, M.-P. Herbert, I. Fischer, M. Steglich, A. Bodi, P. Hemberger, J. Anal. Appl. Pyrolysis **124** (2017) 454.
7. F. Qi, Proc. Combust. Inst. **34** (2013) 33.
8. N. Hansen, T. A. Cool, P. R. Westmoreland, K. Kohse-Höinghaus, Prog. Energy Combust. Sci. **35** (2009) 168.
9. Z. S. Li, B. Li, Z. W. Sun, X. S. Bai, M. Aldén, Combust. Flame **157** (2010) 1087.
10. K. Kohse-Höinghaus, Chem. Eur. J. **22** (2016) 13390.
11. T. Lu, C. K. Law, Prog. Energy Combust. Sci. **35** (2009) 192.
12. K. Moshammer, A. W. Jasper, D. M. Popolan-Vaida, Z. Wang, V. S. Bhavani Shankar, L. Ruwe, C. A. Taatjes, P. Dagaut, N. Hansen, J. Phys. Chem. A **120** (2016) 7890.
13. J. Zádor, H. Huang, O. Welz, J. Zetterberg, D. L. Osborn, C. A. Taatjes, Phys. Chem. Chem. Phys. **15** (2013) 10753.

14. Z. Wang, L. Zhang, K. Moshammer, D. M. Popolan-Vaida, V. S. Bhavani Shankar, A. Lucassen, C. Hemken, C. A. Taatjes, S. R. Leone, K. Kohse-Höinghaus, N. Hansen, P. Dagaut, S. M. Sarathy, Combust. Flame **164** (2016) 386.
15. F. Battin-Leclerc, O. Herbinet, P.-A. Glaude, R. Fournet, Z. Zhou, L. Deng, H. Guo, M. Xie, F. Qi, Angew. Chem. Int. Ed. **49** (2010) 3169.
16. P. T. Lynch, T. P. Troy, M. Ahmed, R. S. Tranter, Anal. Chem. **87** (2015) 2345.
17. L. Ruwe, K. Moshammer, N. Hansen, K. Kohse-Höinghaus, Combust. Flame **175** (2017) 34.
18. L. Seidel, K. Moshammer, X. Wang, T. Zeuch, K. Kohse-Höinghaus, F. Mauss, Combust. Flame **162** (2015) 2045.
19. Y. Li, F. Qi, Acc. Chem. Res. **43** (2010) 68.
20. N. Hansen, M. Schenk, K. Moshammer, K. Kohse-Höinghaus, Combust. Flame **180** (2017) 250.
21. L. S. Tran, B. Sirjean, P. A. Glaude, R. Fournet, F. Battin-Leclerc, Energy **43** (2012) 4.
22. S. S. Merchant, C. F. Goldsmith, A. G. Vandeputte, M. P. Burke, S. J. Klippenstein, W. H. Green, Combust. Flame **162** (2015) 3658.
23. C.-W. Zhou, Y. Li, E. O'Connor, K. P. Somers, S. Thion, C. Keesee, O. Mathieu, E. L. Petersen, T. A. DeVerter, M. A. Oehlschlaeger, G. Kukkadapu, C.-J. Sung, M. Alrefae, F. Khaled, A. Farooq, P. Dirrenberger, P.-A. Glaude, F. Battin-Leclerc, J. Santner, Y. Ju, T. Held, F. M. Haas, F. L. Dryer, H. J. Curran, Combust. Flame **167** (2016) 353.
24. S. M. Sarathy, P. Oßwald, N. Hansen, K. Kohse-Höinghaus, Prog. Energy Combust. Sci. **44** (2014) 40.
25. K. Kohse-Höinghaus, P. Oßwald, T. A. Cool, T. Kasper, N. Hansen, F. Qi, C. K. Westbrook, P. R. Westmoreland, Angew. Chem. Int. Ed. **49** (2010) 3572.
26. N. Hansen, T. Kasper, S. J. Klippenstein, P. R. Westmoreland, M. E. Law, C. A. Taatjes, K. Kohse-Höinghaus, J. Wang, T. A. Cool, J. Phys. Chem. A **111** (2007) 4081.
27. B. Brehm, E. von Puttkamer, Z. Naturforsch. A **22** (1967) 8.
28. A. Bodi, B. Sztáray, T. Baer, M. Johnson, T. Gerber, Rev. Sci. Instrum. **78** (2007) 084102.
29. A. T. J. B. Eppink, D. H. Parker, Rev. Sci. Instrum. **68** (1997) 3477.
30. B. Sztáray, T. Baer, Rev. Sci. Instrum. **74** (2003) 3763.
31. X. Tang, X. Zhou, M. Niu, S. Liu, J. Sun, X. Shan, F. Liu, L. Sheng, Rev. Sci. Instrum. **80** (2009) 113101.
32. A. Bodi, P. Hemberger, T. Gerber, B. Sztáray, Rev. Sci. Instrum. **83** (2012) 083105.
33. G. A. Garcia, B. K. Cunha de Miranda, M. Tia, S. Daly, L. Nahon, Rev. Sci. Instrum. **84** (2013) 053112.
34. J. C. Poully, J. P. Schermann, N. Nieuwjaer, F. Lecomte, G. Grégoire, C. Desfrançois, G. A. Garcia, L. Nahon, D. Nandi, L. Poisson, M. Hochlaf, Phys. Chem. Chem. Phys. **12** (2010) 3566.
35. P. Bréchignac, G. A. Garcia, C. Falvo, C. Joblin, D. Kokkin, A. Bonnamy, P. Parneix, T. Pino, O. Pirali, G. Mulas, L. Nahon, J. Chem. Phys. **141** (2014) 164325.
36. T. Baer, R. P. Tuckett, Phys. Chem. Chem. Phys. **19** (2017) 9698.
37. A. Bodi, P. Hemberger, D. L. Osborn, B. Sztáray, J. Phys. Chem. Lett. **4** (2013) 2948.
38. P. Oßwald, P. Hemberger, T. Bierkandt, E. Akyildiz, M. Köhler, A. Bodi, T. Gerber, T. Kasper, Rev. Sci. Instrum. **85** (2014) 025101.
39. X. Mercier, S. Batut, A. Faccinetto, G. Vanhove, A. El Bakali, P. Desgroux, D. Bozanic, G. Garcia, L. Nahon, Proc. 8th Eur. Combust. Meet. (2017) 529.
40. J. Krüger, G. A. Garcia, D. Felsmann, K. Moshammer, A. Lackner, A. Brockhinke, L. Nahon, K. Kohse-Höinghaus, Phys. Chem. Chem. Phys. **16** (2014) 22791.

41. D. Felsmann, A. Lucassen, J. Krüger, C. Hemken, L.-S. Tran, J. Pieper, G. A. Garcia, A. Brockhinke, L. Nahon, K. Kohse-Höinghaus, Z. Phys. Chem. **230** (2016) 1067.
42. X. C. Lu, D. Han, Z. Huang, Prog. Energy Combust. Sci. **37** (2011) 741.
43. J.-B. Masurier, F. Foucher, G. Dayma, P. Dagaut, Proc. Combust. Inst. **35** (2015) 3125.
44. M. Jia, M. Xie, Fuel **85** (2006) 2593.
45. C. K. Westbrook, W. J. Pitz, H. J. Curran, J. Phys. Chem. A **110** (2006) 6912.
46. B.-Q. He, S.-J. Shuai, J.-X. Wang, H. He, Atmos. Environ. **37** (2003) 4965.
47. G. Fontaras, G. Karavalakis, M. Kousoulidou, L. Ntziachristos, E. Bakeas, S. Stournas, Z. Samaras, Environ. Pollut. **158** (2010) 2496.
48. K. Zhang, K. Moshammer, P. Oßwald, K. Kohse-Höinghaus, Proc. Combust. Inst. **34** (2013) 763.
49. F. Herrmann, P. Oßwald, K. Kohse-Höinghaus, Proc. Combust. Inst. **34** (2013) 771.
50. J. Bugler, B. Marks, O. Mathieu, R. Archuleta, A. Camou, C. Grégoire, K. A. Heufer, E. L. Petersen, H. J. Curran, Combust. Flame **163** (2016) 138.
51. L.-S. Tran, J. Pieper, H.-H. Carstensen, H. Zhao, I. Graf, Y. Ju, F. Qi, K. Kohse-Höinghaus, Proc. Combust. Inst. **36** (2017) 1165.
52. K. Yasunaga, F. Gillespie, J. M. Simmie, H. J. Curran, Y. Kuraguchi, H. Hoshikawa, M. Yamane, Y. Hidaka, J. Phys. Chem. A **114** (2010) 9098.
53. J. Hashimoto, K. Tanoue, N. Taide, Y. Nouno, Proc. Combust. Inst. **35** (2015) 973.
54. X. Tang, G. A. Garcia, J.-F. Gil, L. Nahon, Rev. Sci. Instrum. **86** (2015) 123108.
55. G. A. Garcia, L. Nahon, I. Powis, Rev. Sci. Instrum. **75** (2004) 4989.
56. G. A. Garcia, H. Soldi-Lose, L. Nahon, Rev. Sci. Instrum. **80** (2009) 023102.
57. L. Nahon, N. de Oliveira, G. A. Garcia, J.-F. Gil, B. Pilette, O. Marcouillé, B. Lagarde, F. Polack, J. Synchrotron Rad. **19** (2012) 508.
58. R. J. Bartlett, M. Musiał, Rev. Mod. Phys. **79** (2007) 291.
59. G. Knizia, T. B. Adler, H.-J. Werner, J. Chem. Phys. **130** (2009) 054104.
60. T. E. Sharp, H. M. Rosenstock, J. Chem. Phys. **41** (1964) 3453.
61. H.-J. Werner, P. J. Knowles, G. Knizia, M. Manby, M. Schütz, MOLPRO Version 2009 (2009).
62. LOGE Lund Combustion Engineering, LOGEsoft v1.08 (2016).
63. U. Struckmeier, P. Oßwald, T. Kasper, L. Böhling, M. Heusing, M. Köhler, A. Brockhinke, K. Kohse-Höinghaus, Z. Phys. Chem. **223** (2009) 503.
64. L.-S. Tran, J. Pieper, M. Zeng, Y. Li, X. Zhang, W. Li, I. Graf, F. Qi, K. Kohse-Höinghaus, Combust. Flame **175** (2017) 47.
65. X. Yang, D. Felsmann, N. Kurimoto, J. Krüger, T. Wada, T. Tan, E. A. Carter, K. Kohse-Höinghaus, Y. Ju, Proc. Combust. Inst. **35** (2015) 491.
66. P.-O. Löwdin, Rev. Mod. Phys. **35** (1963) 496.
67. J. Paldus, A. Veillard, Mol. Phys. **35** (1978) 445.
68. E. R. Davidson, W. T. Borden, J. Phys. Chem. **87** (1983) 4783.
69. W. Eisfeld, K. Morokuma, J. Chem. Phys. **113** (2000) 5587.
70. T. Shiozaki, G. Knizia, H.-J. Werner, J. Chem. Phys. **134** (2011) 034113.
71. T. Shiozaki, H.-J. Werner, J. Chem. Phys. **134** (2011) 184104.
72. F. P. Lossing, J. C. Traeger, J. Am. Chem. Soc. **97** (1975) 1579.
73. N. Hansen, S. J. Klippenstein, J. A. Miller, J. Wang, T. A. Cool, M. E. Law, P. R. Westmoreland, T. Kasper, K. Kohse-Höinghaus, J. Phys. Chem. A **110** (2006) 4376.
74. F. P. Lossing, J. C. Traeger, Int. J. Mass Spectrom. Ion Phys. **19** (1976) 9.
75. S. Pignataro, A. Cassuto, F. P. Lossing, J. Am. Chem. Soc. **89** (1967) 3693.
76. G. Bieri, F. Burger, E. Heilbronner, J. P. Maier, Helv. Chim. Acta **60** (1977) 2213.

77. J. C. Traeger, J. Phys. Chem. **90** (1986) 4114.
78. P. Masclet, G. Mouvier, J. F. Bocquet, J. Chim. Phys. **78** (1981) 99.
79. M. Newville, T. Stensitzki, D. B. Allen, A. Ingargiola, LMFIT: Non-Linear Least-Square Minimization and Curve-Fitting for Python, http://dx.doi.org/10.5281/zenodo.11813 (2014).
80. B. Yang, J. Wang, T. A. Cool, N. Hansen, S. Skeen, D. L. Osborn, Int. J. Mass Spectrom. **309** (2012) 118.
81. T. A. Cool, J. Wang, K. Nakajima, C. A. Taatjes, A. Mcllroy, Int. J. Mass Spectrom. **247** (2005) 18.
82. J. Wang, B. Yang, T. A. Cool, N. Hansen, T. Kasper, Int. J. Mass Spectrom. **269** (2008) 210.
83. F. Paulot, J. D. Crounse, H. G. Kjaergaard, J. H. Kroll, J. H. Seinfeld, P. O. Wennberg, Atmos. Chem. Phys. **9** (2009) 1479.
84. G. Martins, A. M. Ferreira-Rodrigues, F. N. Rodrigues, G. G. B. de Souza, N. J. Mason, S. Eden, D. Duflot, J.-P. Flament, S. V. Hoffmann, J. Delwiche, M.-J. Hubin-Franskin, P. Limão-Vieira, Phys. Chem. Chem. Phys. **11** (2009) 11219.
85. T. Adam, R. Zimmermann, Anal. Bioanal. Chem. **389** (2007) 1941.
86. A. Lucassen, K. Zhang, J. Warkentin, K. Moshammer, P. Glarborg, P. Marshall, K. Kohse-Höinghaus, Combust. Flame **159** (2012) 2254.
87. A. Lucassen, P. Oßwald, U. Struckmeier, K. Kohse-Höinghaus, T. Kasper, N. Hansen, T. A. Cool, P. R. Westmoreland, Proc. Combust. Inst. **32** (2009) 1269.
88. J.-P. Morizur, J. Mercier, M. Sarraf, Org. Mass Spectrom. **17** (1982) 327.
89. J. L. Holmes, F. P. Lossing, Can. J. Chem. **60** (1982) 2365.
90. J. M. Behan, F. M. Dean, R. A. W. Johnstone, Tetrahedron **32** (1976) 167.
91. J. L. Holmes, F. P. Lossing, P. C. Burgers, Int. J. Mass Spectrom. Ion Phys. **47** (1983) 133.
92. J. C. Traeger, D. J. McAdoo, Int. J. Mass Spectrom. Ion Process. **68** (1986) 35.
93. J. C. Traeger, Org. Mass Spectrom. **20** (1985) 223.
94. M. J. S. Dewar, S. D. Worley, J. Chem. Phys. **50** (1969) 654.

Supplemental Material: The online version of this article offers supplementary material (https://doi.org/10.1515/zpch-2017-1009).

ANHANG B

Publikation 2

D. Felsmann, A. Lucassen, J. Krüger, C. Hemken, L.S. Tran, J. Pieper, G.A. Garcia, A. Brockhinke, L. Nahon, K. Kohse-Höinghaus

Progress in Fixed-Photon-Energy Time-Efficient Double Imaging Photoelectron/Photoion Coincidence Measurements in Quantitative Flame Analysis

Zeitschrift für Physikalische Chemie **230**(8), 1067-1097, 2016
DOI: 10.1515/zpch-2016-0760

Abstract

Photoelectron photoion coincidence (PEPICO) spectroscopy as an attractive new technique for combustion analysis was used in a fixed-photon-energy configuration to provide quantitative species profiles in laminar premixed flames. While such measurements are conventionally performed with molecular-beam mass spectrometry (MBMS) using electron ionization (EI) or vacuum ultraviolet (VUV) photoionization (PI) with synchrotron radiation, these techniques have some limitations. The possibility to record photoelectron spectra (PES) simultaneously with photoionization data, providing fingerprint information for reliable species identification, presents a significant advantage of PEPICO spectroscopy especially in complex reactive mixtures. The multiplex approach presented here, enhanced by the imaging capabilities of the electron and ion detection in the so-called double-imaging PEPICO scheme (i^{2}PEPICO), provides, in different experimental situations, an unprecedentedly detailed combustion analysis regarding both species identification and quantification. Problems and perspectives of the present fixed-photon-energy PEPICO approach will be discussed.

Daniel Felsmann, Arnas Lucassen, Julia Krüger,
Christian Hemken, Luc-Sy Tran, Julia Pieper, Gustavo A. Garcia,
Andreas Brockhinke, Laurent Nahon, and
Katharina Kohse-Höinghaus*

Progress in Fixed-Photon-Energy Time-Efficient Double Imaging Photoelectron/Photoion Coincidence Measurements in Quantitative Flame Analysis

DOI 10.1515/zpch-2016-0760
Received January 25, 2016; accepted March 1, 2016

Abstract: Photoelectron photoion coincidence (PEPICO) spectroscopy as an attractive new technique for combustion analysis was used in a fixed-photon-energy configuration to provide quantitative species profiles in laminar premixed flames. While such measurements are conventionally performed with molecular-beam mass spectrometry (MBMS) using electron ionization (EI) or vacuum ultraviolet (VUV) photoionization (PI) with synchrotron radiation, these techniques have some limitations. The possibility to record photoelectron spectra (PES) simultaneously with photoionization data, providing fingerprint information for reliable species identification, presents a significant advantage of PEPICO spectroscopy especially in complex reactive mixtures. The multiplex approach presented here, enhanced by the imaging capabilities of the electron and ion detection in the so-called double-imaging PEPICO scheme (i^2PEPICO), provides, in different experimental situations, an unprecedentedly detailed combustion analysis regarding both species identification and quantification. Problems and perspectives of the present fixed-photon-energy PEPICO approach will be discussed.

***Corresponding author: Katharina Kohse-Höinghaus,** Department of Chemistry, Bielefeld University, Universitätsstraße 25, 33615 Bielefeld, Germany, e-mail: kkh@uni-bielefeld.de
Daniel Felsmann, Christian Hemken, Luc-Sy Tran, Julia Pieper, Andreas Brockhinke: Department of Chemistry, Bielefeld University, Universitätsstraße 25, 33615 Bielefeld, Germany
Arnas Lucassen: Physikalisch-Technische Bundesanstalt, Bundesallee 100, 38116 Braunschweig, Germany
Julia Krüger, Gustavo A. Garcia, Laurent Nahon: Synchrotron SOLEIL, L'Orme des Merisiers, St. Aubin, B.P. 48, 91192 Gif-sur-Yvette, France

Keywords: Photoelectron Photoion Coincidence (PEPICO) Spectroscopy, Molecular-Beam Mass Spectrometry (MBMS), Combustion, Multiplex Analysis, Intermediate Species.

1 Introduction

Complex diagnostic problems in the gas phase, concerning chemical dynamics and reaction kinetics, species identification, and quantification have been increasingly addressed in recent years using advanced mass spectrometric techniques [1–5]. Such applications are reported within fields as diverse as atmospheric chemistry [3], organometallic catalysis [2], interstellar chemistry [6–10], aerosol formation [1], photochemistry [1, 11], biomass pyrolysis [12], and combustion chemistry [5, 12–14]. These reactive systems may involve dozens to hundreds of species, some of unknown structure [15–17], in amounts that may reach from the sub-ppm to the percent level. Reliable detection and identification of components in the reacting mixture, including isomers, is a prerequisite for the development of detailed reaction mechanisms. Molecular-beam mass spectrometry (MBMS) as a universal, yet invasive, technique [1, 4, 13, 18, 19] is being employed to study reactive processes in photolysis, pyrolysis, and oxidation reactors [12–14, 17, 20], shock tubes [21], and laboratory flames [4, 5, 12, 13].

While laboratory variants of MBMS usually rely on electron ionization (EI), the use of tunable vacuum ultraviolet (VUV) radiation from synchrotron sources for photoionization (PI) has become more common to identify species not only by their exact mass, but also by their ionization energy (IE). Such PI-MBMS studies have been widely used in combustion research to analyze chemically sensitive aspects such as low-temperature oxidation [17, 20] and high-molecular-weight soot precursor formation [22]. Especially the introduction of alternative fuels [23, 24] and novel combustion regimes [14, 17] demand detailed information to build reliable reaction mechanisms of predictive quality [15, 16]. In comparison to the less involved EI-MBMS technique that offers analysis of the reaction system by mass/charge (m/z) ratio and reaction time (or height above the burner h in a laminar flame), VUV-PI-MBMS at synchrotrons provides a third discriminative dimension in terms of the finely tunable photoionization energy. The high energy resolution of PI-MBMS is instrumental for species and structure identification. To obtain quantitative species profiles, PI-MBMS relies on photoionization cross sections for stable and radical species that are often measured at the same beamlines [25–29].

Even more information, however, can be gained with photoelectron photoion coincidence (PEPICO) spectroscopy, a technique that has been known and ap-

plied to the detailed study of photoionization processes for nearly five decades ([30, 31] and references therein), and that has recently found popularity for complex mixture analysis in synchrotron facilities [32–35], since it offers a fourth discriminative dimension originating from the detection of the associated electrons. Indeed, in addition to the detection of the ion, the information carried by the electron from the same ionization event can be analyzed in PEPICO combustion diagnostics via highly specific fingerprint photoelectron spectra (PES) of the reactive species. Quite recently, Oßwald et al. [33] have – for the first time in a burning flame – demonstrated detection of reactant, product, and intermediate species. In their study, performed at the Swiss Light Source (SLS), they could detect and partially quantify several chemical species in a $C_2H_4/O_2/Ar$ flame. Also they were able, for the example of an *iso*-butane flame, to distinguish between the first four isomeric fuel radicals formed by H-abstraction from the fuel molecule. In their threshold (T)-PEPICO approach, they have scanned the ionizing photon energy to generate threshold photoelectron spectra (TPES). Scanning the photon energy with appropriate resolution can be quite time-consuming, and Krüger et al. [35] have thus demonstrated more recently a highly multiplexed fixed-photon-energy PEPICO method. With this fixed-photon-energy technique, they have recorded PES to provide isomer separation for some carefully selected conditions in flames. Felsmann et al. [36] have performed a comparison of both the scanning TPEPICO [33] and fixed-photon-energy PEPICO [35] approaches. Their study has combined the results from four MBMS instruments to study almost identical premixed $C_2H_4/O_2/Ar$ flames, using synchrotron-based PI-MBMS at the Advanced Light Source (ALS) in Berkeley, TPEPICO at the SLS, PEPICO at SOLEIL as well as laboratory-based EI-MBMS in Bielefeld. The comparison clearly demonstrated the detailed information that can be obtained with significant time savings by using the fixed-photon-energy PES approach with the double-imaging PEPICO spectrometer at SOLEIL [37–39].

While results from all measurements in the chosen ethene flame were in good general agreement, the fixed-photon-energy PEPICO approach in [35, 36] can be considered as a first proof of principle, while a demonstration of a more general applicability of this technique to combustion analysis in more complex isomer-rich situations has not yet been reported. The present article will therefore discuss the potential of the fixed-photon-energy PEPICO method to obtain quantitative species profiles in flames and to distinguish the contributions of different chemical species to a given m/z signal. The analysis relies on intense post-treatment of signals obtained within typically 5–60 min, using the double-imaging capacity of the spectrometer and the pBasex image inversion algorithm [40]. Several fuels were chosen for these experiments, namely dimethyl ether (DME), cyclopentene (CP), and methyl propanoate (MP). DME is discussed as a promising alternative

fuel and fuel additive that can be produced from biomass, natural gas, and coal; it exhibits pronounced low-temperature chemistry and its combustion has been extensively studied both experimentally and with kinetic mechanisms [17, 21, 41–45]. Cyclopentene as a cyclic hydrocarbon fuel was chosen because of the established wealth of soot precursors produced in its combustion [46–48]. Methyl propanoate as a small-chain methyl ester gives insight into the combustion properties that arise from the ester function of a fuel, important for biodiesel combustion [49, 50]. For these fuels, detailed quantitative species analysis and kinetic models are largely available for comparison.

In these chemically quite different situations, we have further investigated the suitability of fixed-photon-energy PEPICO measurements to elucidate specific aspects of the flame structure, efficiently using allocated beam time to investigate these increasingly complex systems. From the electron signal, quantitative species profiles could be derived here for the first time using the fixed-photon-energy approach. The obtained results are discussed in terms of necessary post-treatment routines. Furthermore, suitable measurement procedures, necessary signal-to-noise (S/N) considerations, and strategies for data evaluation have been investigated to provide time-efficient isomer-selective flame measurements.

2 Experiments

For the PEPICO experiments, a transportable burner chamber was adapted to the SAPHIRS endstation, equipped with the DELICIOUS III [39] double-imaging spectrometer, located at the undulator-based DESIRS beamline [37] of the synchrotron SOLEIL. DESIRS delivers tunable VUV radiation between 5–40 eV with high spectral resolution, high flux, and adjustable polarization. For the present experiments, energies between 7–16 eV in linear horizontal polarization mode were chosen. A windowless gas filter [51] that was used to block higher harmonics from the undulator was filled with Ar for energies in the 8–15.76 eV range and with Xe for energies below 8 eV. After dispersion via a 6.65 m normal-incidence monochromator with a low dispersion grating (200 grooves/mm), the VUV beam exhibited a typical bandwidth of 2–20 meV and a flux of the order of 10^{12}–10^{13} photons/s and was focused into the ionization chamber. At the intersection with the molecular beam extracted from the flame experiment, the VUV spot had a diameter of about 100–200 μm, depending on the used monochromator exit slit size.

The analyzed flames were stabilized in a burner chamber at low pressure (33 and 40 mbar) on a water-cooled (333 K) home-built porous-plug burner of 65 mm

Table 1: Flame conditions for the low-pressure flames stabilized on a 65 mm burner. Flow rates are given in standard liter per minute (slm) along with their uncertainties; DME: dimethyl ether, CP: cyclopentene, MP: methyl propanoate.

	ϕ	Pressure/ mbar	Argon dilution/ %	Gas flow rate/slm		
				Fuel	Oxygen	Argon
DME	1.40 ± 0.05	33.3 ± 0.3	25	1.12 ± 0.02	2.39 ± 0.05	1.17 ± 0.02
CP	1.70 ± 0.06	40.0 ± 0.4	25	0.69 ± 0.01	2.82 ± 0.06	1.17 ± 0.02
MP	1.50 ± 0.05	40.0 ± 0.4	50	0.54 ± 0.01	1.81 ± 0.04	2.35 ± 0.05

diameter. The burner was mounted on a translation stage, allowing sampling at different positions above the burner to measure spatially resolved species profiles. The gas flows were regulated with calibrated mass flow controllers (MKS Instruments and Aera, ± 2%), and the liquid fuels were metered by two combined syringe pumps (ISCO Systems D1000 and D500) with a total volume of 1.5 L to minimize downtime of the system due to refilling. The liquid fuels were injected into a home-built evaporation system, evaporated and transported into the burner with Ar as the carrier gas. Flame conditions, gas flows, and evaporation temperatures are provided in Table 1. The DME and the MP flame conditions were chosen to be identical to those reported by Wang et al. [41] and Felsmann et al. [49], respectively. The CP flame conditions were somewhat different from those of Hansen et al. [46], who studied a $CP/O_2/Ar$ flame with PI-MBMS at 50 mbar and 25% Ar dilution for a stoichiometry of $\phi = 2.0$, but very similar to those reported in [47, 48] for earlier EI-MBMS studies.

Flame samples were extracted from the flame by a quartz cone (300 µm diameter at the tip, 25° angle) and expanded into the first-stage chamber at $\sim 10^{-4}$ mbar. This first-stage chamber was pumped by three turbo-molecular pumps (Edwards nEXT 300D) to maintain the low pressure even with high load from the flame chamber (at ~ 40 mbar). A copper skimmer with an orifice of 1.5 mm separated the center part of the molecular beam and guided it into the ionization chamber ($\sim 10^{-6}$ mbar) where it was crossed with the ionizing VUV beam.

The DELICIOUS III spectrometer recorded the electrons and ions generated from the ionization of the sampled molecules in coincidence, using a multi-start/multi-stop detection method. The electrons were detected via a velocity map imaging detector (VMI) and the cations were analyzed by a modified Wiley-McLaren time-of-flight imaging analyzer (WM-TOF) with a mass resolution of $m/\Delta m < 300$ (full width at half maximum, FWHM). The ultimate electron kinetic energy resolution is about 4% on the detector edge. The resulting energy resolution in the presented PES is of the order of 100–200 meV. The modes of operation, set-up, and data analysis procedures were presented and discussed

in the literature [38–40]. In particular, we used the filtering advantage of the i^{2}PEPICO, namely the region-of-interest (ROI) selection in the ion image to enhance the signal-to-noise ratio and selectivity, following the procedures described in [34, 35].

As a reference for these PEPICO measurements, the premixed low-pressure flames of cyclopentene and methyl propanoate have also been investigated in this work with the EI-MBMS instrument in Bielefeld described previously [52, 53]. The flames were stabilized at low pressures with the same conditions as documented in Table 1. Gas flows were regulated by calibrated mass flow controllers (<2% uncertainty); liquid fuels were metered by a syringe pump (ISCO Systems D1000), evaporated, and added to the gas stream. The EI-MBMS setup consists of a two-stage Wiley-McLaren time-of-flight spectrometer equipped with a reflectron detection unit with high mass resolution ($m/\Delta m$ = 4000), enabling determination of the elemental C/H/O composition of the measured species [52, 53]. Samples from the flame zone were extracted with a quartz cone (350 µm diameter at the tip, 25° angle) and ionized with five different ionization energies (between 10 and 18 eV) to analyze the flame and minimize fragmentation.

The evaluation of this EI-MBMS experiment followed routines previously reported in [52, 53]. Briefly, mole fractions of major species were determined based on the elemental balances of C, H, and O, using an internal calibration method. At the highest distance from the burner, only CO, CO_2, H_2, and H_2O were thus considered as products, and the determined CO/CO_2 ratio enabled their quantification. The uncertainty in major species mole fractions is ~ 15%, except for H_2 where it is estimated to be ~ 20% [53]. For intermediate species, a calibration factor k_i relative to Ar was used to determine the mole fraction. This calibration factor was either determined by direct calibration with cold-gas mixtures, or estimated using the relative-ionization-cross-section method (RICS) [54] or the convolution of the literature ionization cross sections with the known energy distribution of the ionizing electrons [55]. These methods are explained in more detail in [53]. The latter methods (RICS and convolution) lead to uncertainties of factors 2–4, depending on the nature of the species and the quality of the available cross section, while direct calibration leads to an uncertainty of ~ 30%. An in-depth discussion of experimental uncertainties associated with quantitative species measurements in flame experiments using MBMS is included in the recent review of Egolfopoulos et al. [56].

3 Results and discussion

In light of the focus of this study to demonstrate the time-efficient application of the i^{2}PEPICO technique with fixed photon energies for combustion analysis, we first address species quantification. Such information is of high importance for kinetic mechanism development in combustion, but it is often time-consuming to obtain with the established photoionization techniques because of the need to scan the photon energy. Additionally, information is typically lost due to the integration over all electron energies. Here, we demonstrate the use of the electron-related signal for the quantification of main species and some unambiguously identifiable intermediates. This approach was applied to well-studied flames of DME and CP, using comparatively short measurement times of 3.5–5 min. Subsequently, we demonstrate the application of the fixed-photon-energy PEPICO approach to more complex situations in the MP and CP flames, using measurement times of up to 1 h. We discuss separation of oxygenated and hydrocarbon isomeric structures and the use of fingerprint PES for this purpose, including application of such procedures to radical and higher-mass species.

3.1 Quantitative flame analysis with time-efficient fixed-photon-energy PEPICO measurements

In our earlier PEPICO measurements [35, 36], we reported a proof of principle without an attempt to provide quantitative species mole fractions. For the first time, we now determine absolute species concentrations in flames as a function of position (or reaction time) from fixed-photon-energy PEPICO experiments.

3.1.1 Major species profiles

In both EI-MBMS and PI-MBMS measurements [52, 53, 57, 58], quantitative species concentrations are derived from the ion signals, whereas in this study, the coincident electron signal is used for quantification. For the flames studied here, major species (fuel, O_2, Ar, H_2, CO, H_2O, CO_2) mole fraction profiles were measured as a function of height h above the burner. At each position, signals were acquired at fixed photon energy of 16 eV with 200 s integration time. At this energy, all neutral species can be ionized so that all m/z signals are recorded simultaneously in coincidence with all corresponding electrons, demonstrating the high multiplexing capacity of the experiment.

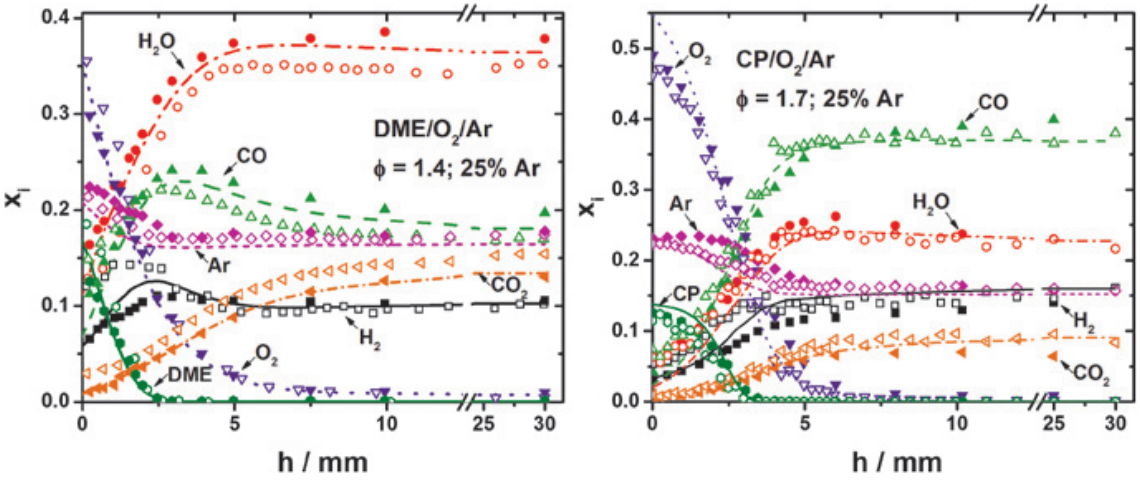

Figure 1: Major species mole fractions x_i as a function of height h above the burner. Left: DME flame, filled symbols: PEPICO experiment, open symbols: reference flame of Wang et al. [41], lines: simulation with Burke et al. [45] model. Right: CP flame, filled symbols: PEPICO experiment, open symbols: EI-MBMS, lines: simulation with Gueniche et al. [60] model.

The DME and CP flames were analyzed to examine the applicability of the present species quantification procedure, and results from the PEPICO experiment were then compared to reference PI-MBMS (DME) or EI-MBMS (DME, CP) measurements and simulations with flame models using the CHEMKIN II/PREMIX code [59]. Similarly to the EI-MBMS evaluation discussed before (Section 2), the mole fractions of major species were calculated here from the C/H/O element balance. A cold-gas calibration with a $CO/CO_2/Ar$ mixture served to determine the CO/CO_2 ratio in the exhaust region at $h = 30$ mm. The inlet conditions were calculated from the C and O element balance. To consider potential early reactions at the burner surface and back-diffusion, the mole fractions of CO, CO_2, H_2, and H_2O at $h = 0$ mm were taken into account.

Resulting major species profiles are presented in Figure 1, in the left panel for the DME flame and the right panel for the CP flame. DME results are compared to previous experimental values by Wang et al. [41], and to predictions of the model by Burke et al. [45], using the temperature profile reported in [41]. No fragmentation correction of the fuel was applied to the present dataset, since fragmentation from the fuel is not likely to contribute to any of the major species signals. Given the two independent experimental setups, the agreement between the results by Wang et al. [41] and the present PEPICO measurements is quite good. The model simulation represents the overall flame structure well, with the present dataset in slightly better agreement, especially for the initial rise of the H_2 mole fraction profile.

Major species profiles measured by fixed-photon-energy PEPICO for the CP flame are compared in the right panel of Figure 1 with the EI-MBMS results; also,

simulations performed with the model by Gueniche et al. [60] are included. The temperature profile used in the simulation was measured in the EI-MBMS setup using the first-stage pressure [18], calibrated with an exhaust-gas temperature of 2200 K, as also reported by Kamphus et al. [47] for a similar CP flame. Similar good agreement as for the DME flame is observed between the two datasets and the simulation, with the exception of slightly larger deviations at $h \sim 2–6$ mm between the model prediction and the PEPICO measurements for H_2 and Ar mole fractions.

The overall good agreement in Figure 1 thus demonstrates that quantitative major species mole fraction profiles can be obtained from the total electron yield (TEY) at a given mass. With longer measurement time intervals, the PEPICO approach would permit a potential advantage over PI-MBMS in that fragmentation contributions could become directly evident in the fingerprint PE spectra.

3.1.2 Intermediate species profiles

Intermediate species profiles are quantitatively evaluated with a formalism similar to that usually taken for the evaluation of PI-MBMS experiments [41, 46, 61, 62]. Equation (1) describes the total electron signal S_i corresponding to a given species i,

$$S_i = x_i(h) \cdot t_{int} \cdot D_i(M_i) \cdot FKT(T, \bar{M}) \cdot c(E) \cdot \sigma(E). \quad (1)$$

Here, x_i is the mole fraction at height h; t_{int} is the data acquisition time; M is the molar mass, D is the mass discrimination factor; FKT is a sampling function that depends on the temperature T and the mean molar mass $\bar{M}$; $c(E)$ is an instrument factor that includes the photon flux at a given energy and $\sigma(E)$ the photoionization cross section, also depending on the photon energy E. Here, D has been assumed to be equal to 1 for all masses; c must be determined for each specific scan, assuming a constant photon flux.

The fixed-photon-energy PEPICO approach offers the advantage that only one value of the cross section is needed for the evaluation. The electron signal in a PES is highly state-selective and Equation (1) would have to be evaluated for each energy if the measurements were performed in scanning mode. Here, the fixed photon energy with a distribution of ~ 5 meV (FWHM) permits to use Equation (1) at each given energy, and a single carefully selected energy is sufficient to determine a full species set using tabulated photoionization cross sections. An involved procedure is typically necessary in PI-MBMS to determine quantitative intermediate species concentrations in a cascading sequence, as explained by Cool et al. [61]. Since the fixed-photon-energy PEPICO technique reduces the experimental error

by avoiding this cascading procedure, it can present a significant advantage over regular PI-MBMS measurements. In contrast, scanned threshold PEPICO measurements, cannot, in principle, use normal tabulated absolute cross sections for a quantitative analysis for two reasons: first, the ionization cross sections depend on the electron kinetic energy and here only threshold electrons are used; second, the likely presence of resonant autoionization will distort the measured intensities. Therefore, a separate TPEPICO database would have to be built to determine accurate species concentrations. Oßwald et al. [33] discussed the necessity of state-selective cross sections for the data evaluation of their scanning *i*PEPICO experiment. In their data evaluation, they also had to take an energy-dependent factor α into account to consider the finite size of their electron detector [33]. Here, due to the larger energy span covered by the present VMI detector [39], such corrections are not necessary, reducing the uncertainty.

Figure 2 shows the mole fraction profiles of selected intermediates including CH_3, C_2H_4, and CH_2O for the DME flame (left panel) and C_3H_3, C_3H_5, and C_6H_6 for the CP flame (right panel). A data acquisition time of 300 s was used for each height h. For the DME flame, 10.9 eV was chosen as the fixed photon energy, because this value includes the ionization energy of CH_2O as an important intermediate in this flame. For the CP flame, 10.4 eV was chosen to include numerous C_3, C_4, and C_5 intermediates. The present results from the electron signal evaluation in the DME flame in Figure 2 are compared with those by Wang et al. [41], showing very good agreement of the different experimental datasets. Overall shapes and peak values differ slightly, potentially due to the different experimental setups, and maximum mole fractions deviate by less than 20%. For the CP flame, shown in the right panel of Figure 2, the fixed-photon-energy experiment is compared to our present EI-MBMS measurements, the PI-MBMS results from Hansen et al. [46], and to simulations with the Gueniche et al. model [60]. Very good agreement is seen between both independent measurements from the present study. Also, the earlier PI-MBMS [46] and the PEPICO results for C_3H_3 and C_6H_6 are in good quantitative agreement. The only exception is seen for C_3H_5, where the PI-MBMS experiment by Hansen et al. [46] results in a factor of five lower maximum mole fraction than derived by the two other methods. The reason for this discrepancy is unclear, especially since the same photoionization cross sections were used in the PI-MBMS and PEPICO evaluation. The simulation slightly underpredicts the mole fractions of C_3H_3 and C_3H_5 by about a factor of two. The mole fraction of C_6H_6, however, is severely under-predicted, but the good agreement of the experimental datasets suggests that an improvement of the model for this species is desirable.

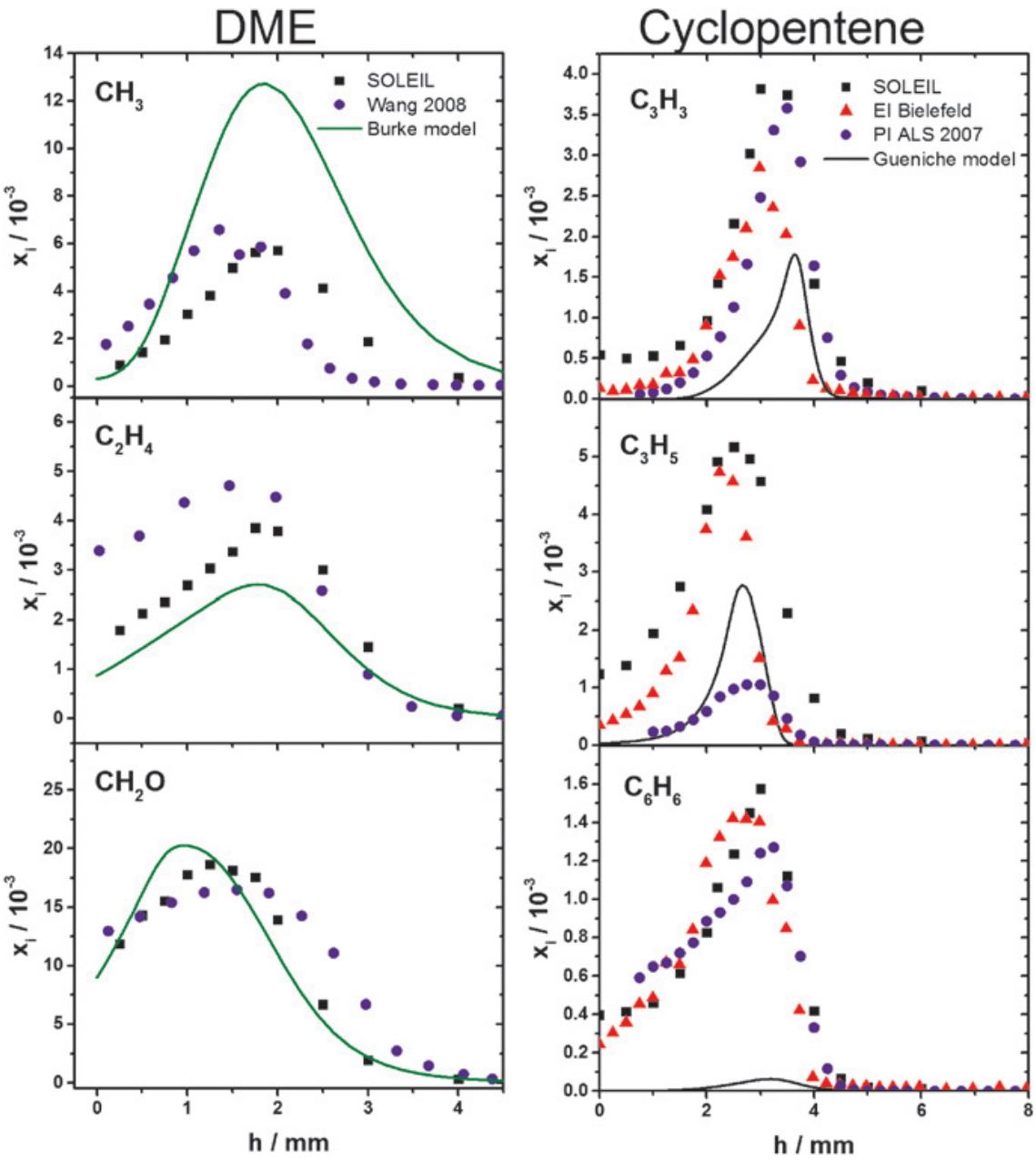

Figure 2: Selected intermediate species mole fractions x_i as a function of height h evaluated from PEPICO measurements at fixed photon energy E with an integration time of 300 s (black squares). Left: DME flame, $E = 10.9$ eV, blue circles: Wang et al. [41], lines: simulation with Burke et al. [45] model. Right: CP flame, $E = 10.4$ eV, red triangles: EI-MBMS, blue circles: PI-MBMS measurements of Hansen et al. [46], lines: simulation with Gueniche et al. [60] model.

3.1.3 Distinction of species at the same nominal mass

With the limited mass resolution of the WM-TOF in the double-imaging DELICIOUS III spectrometer [39], species separation must rely on ionization energies as well as photoelectron spectra. It is thus interesting to analyze how species at

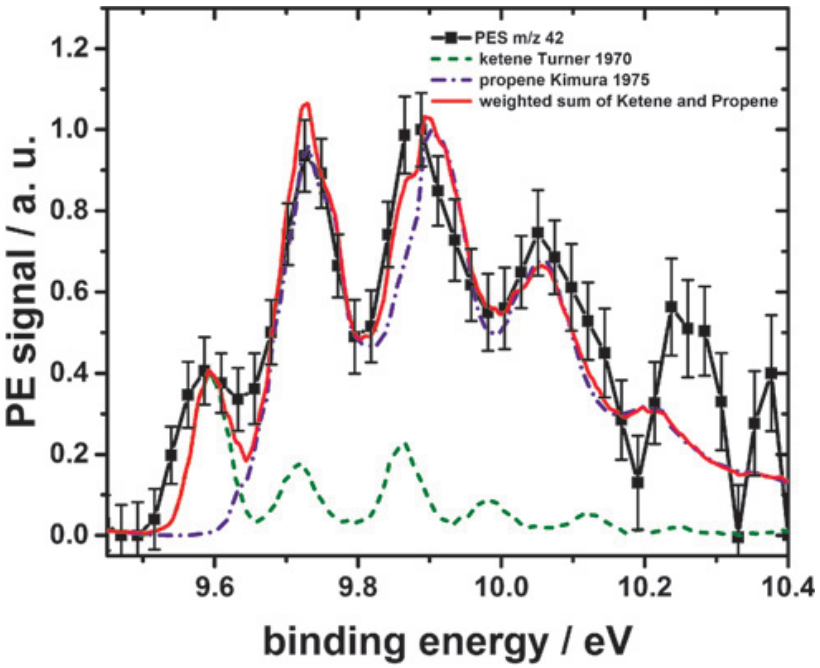

Figure 3: PES of $m/z = 42$ at $h = 2.5$ mm measured with an acquisition time of 300 s at 10.4 eV in the CP flame (black line and symbols) including error bars from the evaluation with the pBasex algorithm [40]; green dashed line: PES of ketene [63]; blue dash-dotted line: PES of propene [64]; red line: sum of weighted ketene and propene contributions.

the same nominal mass that exhibit similar ionization energies could potentially be resolved in the fixed-photon-energy PEPICO approach used here and to investigate whether such species separation could lead to quantitative mole fraction results. To this end we demonstrate species separation for the example of $m/z = 42$ from the same fixed-photon-energy measurement at 10.4 eV as before in the CP flame; this signal typically represents ketene (C_2H_2O) and propene (C_3H_6). Our earlier studies [35, 36] have shown that an identification of both species via threshold PES is possible, but no attempt of quantification was made. Figure 3 shows the PES of $m/z = 42$ measured here at $h = 2.5$ mm where most of the intermediate species are at their peak mole fractions. This PES was derived from the 2D electron image via the pBasex algorithm [40]. Five distinct peaks at 9.59, 9.73, 9.89, 10.05, and 10.22 eV are observed, corresponding to specific energy-dependent ionization processes.

The observed features in Figure 3 agree well with the literature spectra of ketene [63] and propene [64]. The first peak at 9.59 eV corresponds quite well to the literature IE of ketene of 9.617 eV [65] and the second, measured at 9.73 eV, excellently to that of propene of 9.73 eV [65], but it also includes contributions from the vibrational modes of ketene. The third and fourth peaks arise mostly from vibrational modes of propene. A third vibrational mode of propene may

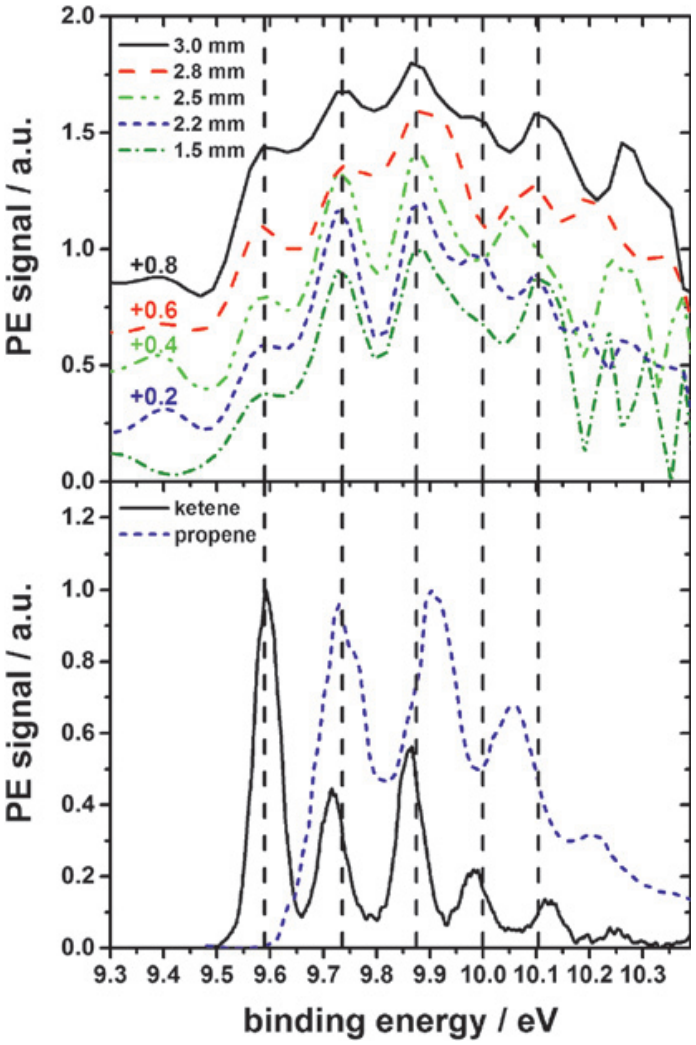

Figure 4: Top: PES of $m/z = 42$ measured with an acquisition time of 300 s at 10.4 eV in the CP flame at different heights h; the spectra have been vertically displaced for clarity. Bottom: literature PES of ketene [63] and propene [64].

contribute to the signal at 10.22 eV. A shift in position and intensity compared to the literature PES [64] is observed here that may result from the rather poor signal-to-noise ratio in this region. Indeed, for very low S/N at these high energies which are detected near the center of the VMI, the pBasex conversion may lead to somewhat distorted signals. It should be noted that a complete VMI image corresponds to only $\sim 10^4$ coincident electrons in the time-efficient measurements here, with a small fraction of these electrons detected at the center. This distortion effect above 10.2 eV becomes more pronounced with decreasing signals at heights above or below the concentration maximum, as evident from Figure 4, which shows selected PES as a function of height h in comparison to the literature PES of ketene [63] and propene [64].

All five peaks in the PES (marked by dashed lines in Figure 4) are observed at all heights above the burner. The ratio between the first and second peak is a good indicator for the change in mole fractions of ketene and propene. This ratio increases from 0.4 : 1 at $h = 1.5$ mm to 0.7 : 1 at $h = 3.0$ mm, corresponding to

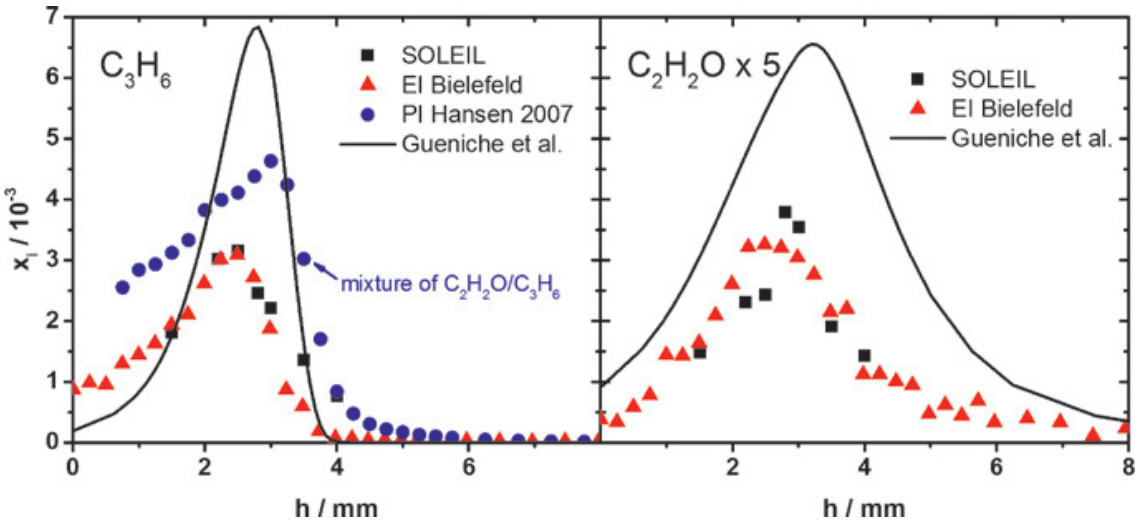

Figure 5: Mole fractions x_i as a function of height h for propene (left) and for ketene (right, multiplied by a factor of 5) evaluated from PEPICO measurements at fixed photon energy $E = 10.4\,\text{eV}$ with an integration time of 300 s in the CP flame (black squares); red triangles: EI-MBMS, blue circles: PI-MBMS measurements of Hansen et al. [46], lines: simulation with Gueniche et al. [60] model.

an increase in ketene contribution. It can thus be assumed that the ketene profile peaks later in the flame.

Mole fractions for both species at different heights were determined from the electron signal using Equation (1). First, the literature spectra were convoluted to fit the same nominal resolution as the measured PES and simulated point-by-point. These convoluted spectra were weighted with appropriate factors to fit the measured PES and integrated in the electron binding energy range of 0–10.4 eV. The measured TEY was then weighted by the ratio of areas from the convoluted spectra for each species. The quantification was performed using cross sections for 10.4 eV from Yang et al. [27] for ketene and Cool et al. [66] for propene. The instrument factor c was calculated from the fuel signal. Figure 5 shows the resulting mole fraction profiles.

The PEPICO and the EI-MBMS measurements of the present study are seen to be in remarkable agreement. The PI-MBMS measurements of Hansen et al. [46] show a deviation of ~25%. These authors did not separate the two species, however, and their profile represents the sum of ketene and propene, evaluated with an estimated cross section. They suggested ketene to be present in higher concentrations [46]. In contrast to this assumption, our measurements show propene to be the dominant species with a maximum mole fraction of 3.2×10^{-3}, approximately five times higher than the ketene mole fraction. The dominance of propene kinetically results from a combination of an H-atom with the allyl radical (C_3H_5), detected with very high mole fraction ($\sim 5.0 \times 10^{-3}$) in the CP

flame (see Figure 2). Allyl can result from a dominant consumption pathway of CP, initiated by H-addition on the double bond, ring opening, and β-scission ($CP + H \rightarrow cyC_5H_9 \rightarrow CH_2CHCH_2CH_2CH_2 \rightarrow C_3H_5 + C_2H_4$) [60].

The overall good agreement between the present experiment – performing quantitative species evaluation from the electron signal in the fixed-photoelectron PEPICO approach – and reference measurements by more established MBMS techniques in combustion analysis is encouraging, especially regarding the multiplex capacity of the present approach, the relatively straight-forward evaluation without additional correction factors or cascading procedures, and the capability to evaluate species with the same nominal mass and similar ionization energies. Note that the EI-MBMS approach uses the higher mass resolution to separate ketene and propene, which would not be possible for structural isomers where PEPICO techniques have a unique advantage.

3.2 Identification of intermediate species in chemically complex situations

With the preceding examples, we have shown species identification, separation, and quantification from fixed-photon-energy PEPICO in rather unambiguous analytical situations. Previous investigations [33, 35, 36] have provided examples for species identification mainly for pairs and triplets of isomers that exhibit significantly different IEs, typically by ≥ 0.5 eV. In that case, the different species-specific fingerprint PES are spread over considerable energy ranges with limited overlap and can thus be distinguished quite well. Such examples include allene (IE: 9.691 eV) and propyne (IE: 10.37 eV) at $m/z = 40$; 1,3-butadiene (IE: 9.072 eV), 2-butyne (IE: 9.58 eV), and 1-butyne (IE: 10.18 eV) at $m/z = 54$; and ethenol (IE: 9.33 eV) and acetaldehyde (IE: 10.22 eV) at $m/z = 44$ [33, 35, 36]. In the following section we will analyze some more complex situations, where very close IEs lead to overlapping vibrational features of the fingerprint PES. This analysis was performed from fixed-photon-energy PEPICO measurements with data acquisition times up to 1 h.

3.2.1 Separation of numerous species at $m/z = 56$ in the methyl propanoate flame

As a first example we demonstrate the identification of species in a methyl propanoate flame studied before [49]. Figure 6 shows the fixed-photon-energy PES of $m/z = 56$ measured in this MP flame at $h = 2.25$ mm with a data acqui-

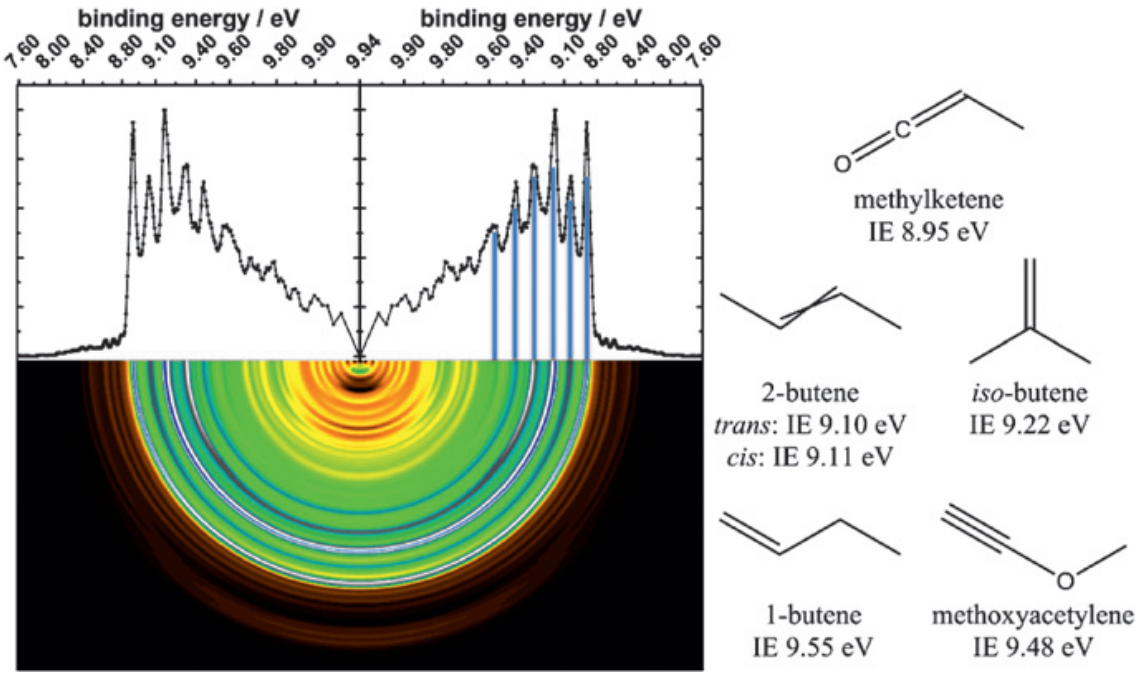

Figure 6: Left: fixed-photon-energy PES of $m/z = 56$ in the MP flame at $h = 2.25$ mm recorded at 9.94 eV photon energy (top), 2D image from the pBasex [40] inversion procedure (bottom). Right: structures and IEs of species potentially contributing to the signal at $m/z = 56$.

sition time of 3600 s (top) along with the result from the pBasex [40] inversion procedure (bottom). Here, a photon energy of 9.94 eV, lower than the IE of MP (IE: 10.15 eV), was chosen to avoid fragmentation processes from the fuel. The spectrum shows six distinguishable peaks between 8.90 and 9.58 eV. Contributions by several species are expected and some plausible structures are given in the right panel of Figure 6.

Because of the limited mass resolution, this measured spectrum can be due to a mixture of species with the sum formulae C_3H_4O or C_4H_8. In our recent study of this MP flame by EI-MBMS, the signatures of C_3H_4O (56.026 u) and C_4H_8 (56.063 u) were resolved clearly by mass. C_3H_4O was predominantly assigned to methylketene as the expected isomer with a peak mole fraction of 2.65×10^{-4}, and C_4H_8 isomers could not be resolved but their sum mole fraction was of the order of 5×10^{-5}. In a slightly different MP flame, Yang et al. [50], in a PI-MBMS experiment with limited mass resolution of $m/\Delta m = 400$, have not separated C_3H_4O and C_4H_8; they have identified methylketene by its IE, but did not rule out contributions from other C_4H_8 isomers. Their photoionization efficiency (PIE) curves were difficult to interpret, because individual contributions with small differences in IE could not clearly be identified by changes of the slopes in the PIE curve. It should be noted also that the separation procedure becomes more cumbersome when the species with the smallest IE contributes with the largest mole fraction.

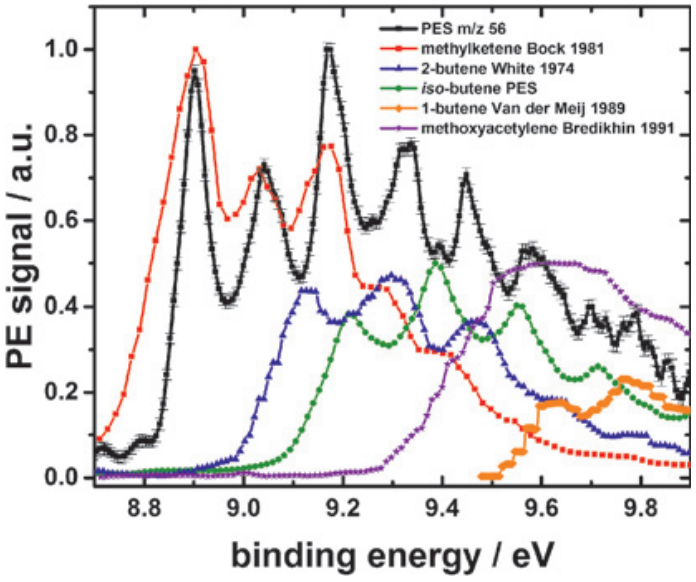

Figure 7: PES of $m/z = 56$ at $h = 2.25$ mm measured with an acquisition time of 3600 s at 9.94 eV in the MP flame (black line and symbols) including error bars from the evaluation with the pBasex algorithm [40]; compared to PES of methylketene (red squares) [67], 2-butene (blue triangles) [68], *iso*-butene (green circles, this work), methoxyacetylene (purple stars) [69], and 1-butene (orange diamonds) [70].

Realizing this complex situation, it will be attempted here to resolve the different contributions to the signal at $m/z = 56$ by a consecutive subtraction procedure. As a starting point, the PES in Figure 6 is shown in more detail in Figure 7 (black line) and compared with the respective literature PES for all possible isomers [67–70] (colored lines).

Methylketene (IE: 8.95 eV) is identified by the peak detected at 8.90 eV. This feature and the following two peaks can be assigned to methylketene as evident from the literature spectrum [67]. The signatures above ~ 9.3 eV are not pronounced in the methylketene literature spectrum, indicating that butenes (C_4H_8) might also contribute to the signal. The PES of the *cis*- and *trans*-2-butenes are found to be almost similar and exhibit three pronounced features at 9.11, 9.31, and 9.47 eV [68]; the two peaks in the measured PES near 9.33 eV and 9.45 eV should thus mostly correspond to the 2-butene isomers. Contributions of *iso*-butene, 1-butene, and methoxyacetylene cannot be ruled out at this point. The *iso*-butene PES shown in Figure 7 has been extracted here from an *iso*-butene flame measurement at $h = 1$ mm and a fixed photon energy of 11 eV. Unfortunately, the literature spectra given in Figure 7 of methoxyacetylene [69] and 1-butene [70] are only available in unsatisfactory resolution.

With the detailed background given in Figure 7, we can now start to identify the contributing species by subtraction. For this procedure, the measured and literature spectra were all compared with the same resolution, i. e. measured and more highly resolved spectra were convoluted to fit the literature spectra with the lowest resolution. Figure 8 shows the process in detailed steps.

The first step, shown in Figure 8a, presents the subtraction of the weighted literature spectrum of methylketene from the measured PES. The resulting resid-

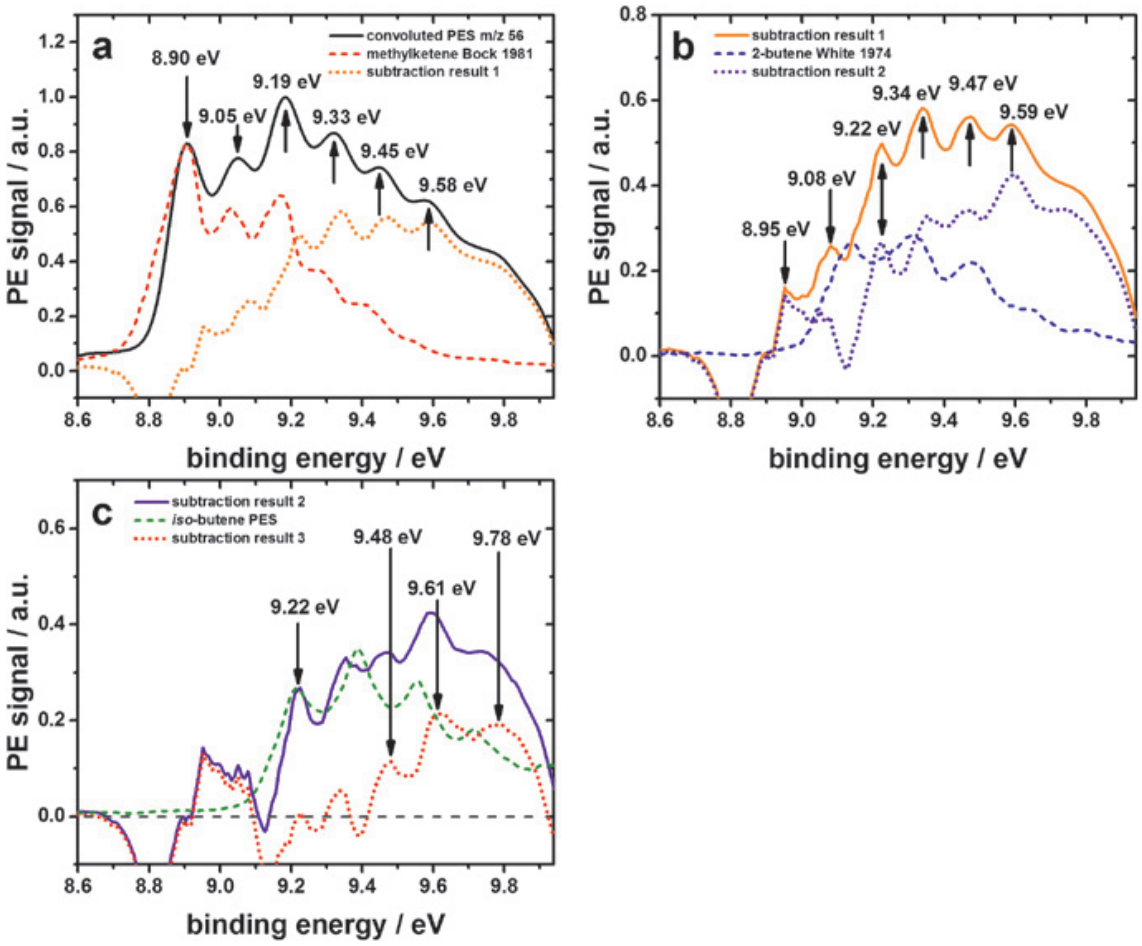

Figure 8: Measured PES for $m/z = 56$, convoluted to a resolution of ~0.12 eV (FWHM) to enable subtraction of literature spectra for the identification of contributing species. Sequential subtraction a) of the methylketene spectrum [67]; b) of the 2-butene spectrum [68]; c) of the *iso*-butene spectrum.

ual PES, here termed subtraction result 1 (orange), is also shown in Figure 8b and used for the subsequent subtraction procedure. It shows six features at 8.95, 9.08, 9.22, 9.34, 9.47, and 9.59 eV. The shoulder at 8.95 eV mainly results from the slight differences between literature and measured PES for methylketene and is therefore not discussed further. The peak at 9.08 eV may be due from a small amount of 2-butene isomers; the slight deviation to the IEs of the 2-butene isomers (IE(*trans*): 9.10 eV, IE(*cis*): 9.11 eV) [65] might arise from the convolution and subtraction procedure, as well as from the digitalization of the literature spectrum that exhibits limited resolution within our region of interest. Subtracting the weighted *cis*-2-butene spectrum (blue) provides subtraction result 2 (purple). For clarity this spectrum is also displayed in Figure 8c. The sharp peak at 9.22 eV in Figure 8c shows an excellent match with the spectrum of *iso*-butene. The remaining spectrum, *i. e.* subtraction result 3, exhibits three further some-

what poorly pronounced peaks at 9.48, 9.61, and 9.78 eV. These peaks could either be assigned to methoxyacetylene (IE: 9.48 eV) [69] and/or 1-butene (IE: 9.55 eV) [70]. While some residues from the species with lower ionization energies might also contribute; the subtraction routine has clearly supported identification of methylketene, 2-butene, and *iso*-butene.

The example shows that the PEPICO technique is in principle capable to separate species in situations where previous experiments have faced difficulties. This has been achieved here using ionization with fixed photon energy and comparatively short acquisition time. The approach can obviously be improved by extending the measurement time to enhance the signal-to-noise ratio. Furthermore, relevant literature PES spectra, mostly measured in the past with fixed photon energy from He(I) sources at 21.22 eV, are often available only with insufficient resolution. Therefore it is highly recommended to extend the database of photoelectron spectra of combustion-relevant intermediates that could be used as reference in species identification, if possible with a common constant resolution.

3.2.2 Interpretation of fingerprint PES in the cyclopentene flame

As a second example, we present the analysis of $m/z = 66$, measured at $h = 2.5$ mm in the CP flame with a fixed photon energy of 9.70 eV. Selected C_5H_6 isomers that have been discussed in previous flame studies [46–48, 71, 72] are shown in Scheme 1.

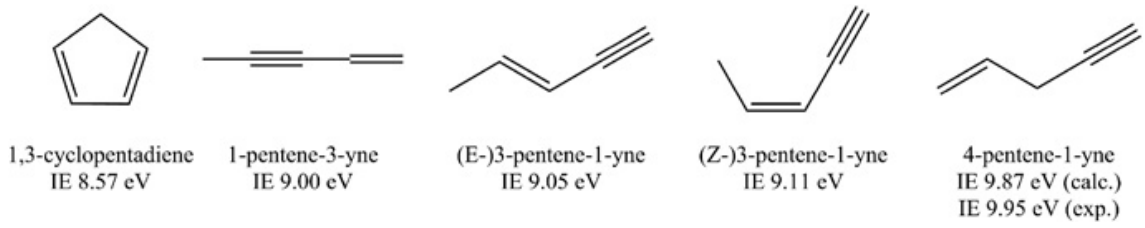

Scheme 1: Selected C_5H_6 isomers ($m/z = 66$).

From the CP fuel decomposition pathway, 1,3-cyclopentadiene (IE: 8.57 eV) [65] should predominantly be formed, as found in PI-MBMS studies of Hansen et al. [46, 71]. The signal detected at $m/z = 66$ in our EI-MBMS measurement in the CP flame was therefore calibrated as 1,3-cyclopentadiene and resulted in a maximum mole fraction of 3.6×10^{-3}, which is in very good agreement to that of 4.2×10^{-3} measured by EI-MBMS by Lamprecht et al. [48]. Hansen et al. [71] have attempted to investigate the C_5H_6 isomer composition

for a number of fuels including allene, propyne, and CP. In their allene and propyne flames, they found evidence of 1-pentene-3-yne (IE: 9.00 eV) [65] and 4-pentene-1-yne (IE: 9.87 eV (calculated), 9.95 eV (measured)) [71]; also they have suggested potential contributions by the E- and Z-isomers of 3-pentene-1-yne (IE(E): 9.05 eV, IE(Z): 9.11 eV) [73]. Their analysis was based on subtraction of the PIE for the CP flame, assumed to correspond to 1,3-cyclopentadiene, from the respective PIE curves in the allene and propyne flames, and subsequent comparison with Franck–Condon simulations for the possible isomers. Using estimated cross sections, they have provided approximate concentration ratios for these isomers. In a further study of allene and propyne flames, Hansen et al. [72] have used estimated cross sections (20 Mb at 10.25 eV) to determine the sum of the mole fractions of different isomers quantitatively. They obtained a value of $\sim 4 \times 10^{-5}$ for the linear isomers and a peak mole fraction of $\sim 1.5 \times 10^{-4}$ for 1,3-cyclopentadiene in both fuels. From this result it could thus be expected that linear isomers might also have to be considered for CP combustion. The complexity of the situation that impedes quantitative concentration measurements of all contributing isomers was noted in these publications [46, 71, 72].

In our fixed-photon-energy PEPICO experiment, we have now tried to investigate the contributions of cyclic and linear isomers to the $m/z = 66$ signal in more detail. The measured PES in our CP flame is shown in Figure 9. Following the discussion above, several isomers should potentially be considered, of which 1,3-cyclopentadiene is expected to be the dominant one. As seen in Figure 9a, the first two peaks at 8.55 and 8.71 eV correspond remarkably well to the literature spectra of 1,3-cyclopentadiene [74], whereas the signatures at 8.99, 9.16, and 9.27 eV may correspond to 1-pentene-3-yne [73]. The isomers of 3-pentene-1-yne might contribute to the small feature at 9.10 eV. Unfortunately, PES for these species are not available in the literature so that they could not be considered in the present evaluation. The fourth isomer, 4-pentene-1-yne, is not detected since its IE is above the used ionizing photon energy. Figure 9b shows the measured PES in comparison with literature spectra of 1,3-cyclopentadiene [74] and 1-pentene-3-yne [73] that were convoluted to the lesser resolution of the measured spectrum and weighted to fit the experimental result. The measured spectrum is very well reproduced by the sum of the two convoluted literature spectra (green line in Figure 9b). This good fit is illustrated by the subtraction result (grey line); however, small remaining peaks are seen at 9.10 eV and above 9.40 eV which might be attributed to some contribution of 3-pentene-1-yne.

To quantify the two reliably detected isomers, the total electron yield from $m/z = 66$ was weighted by the integrated areas of the convoluted 1,3-cyclopentadiene and 1-pentene-3-yne literature spectra between 0 and 9.7 eV and evaluated using Equation (1). The instrument factor c was determined directly

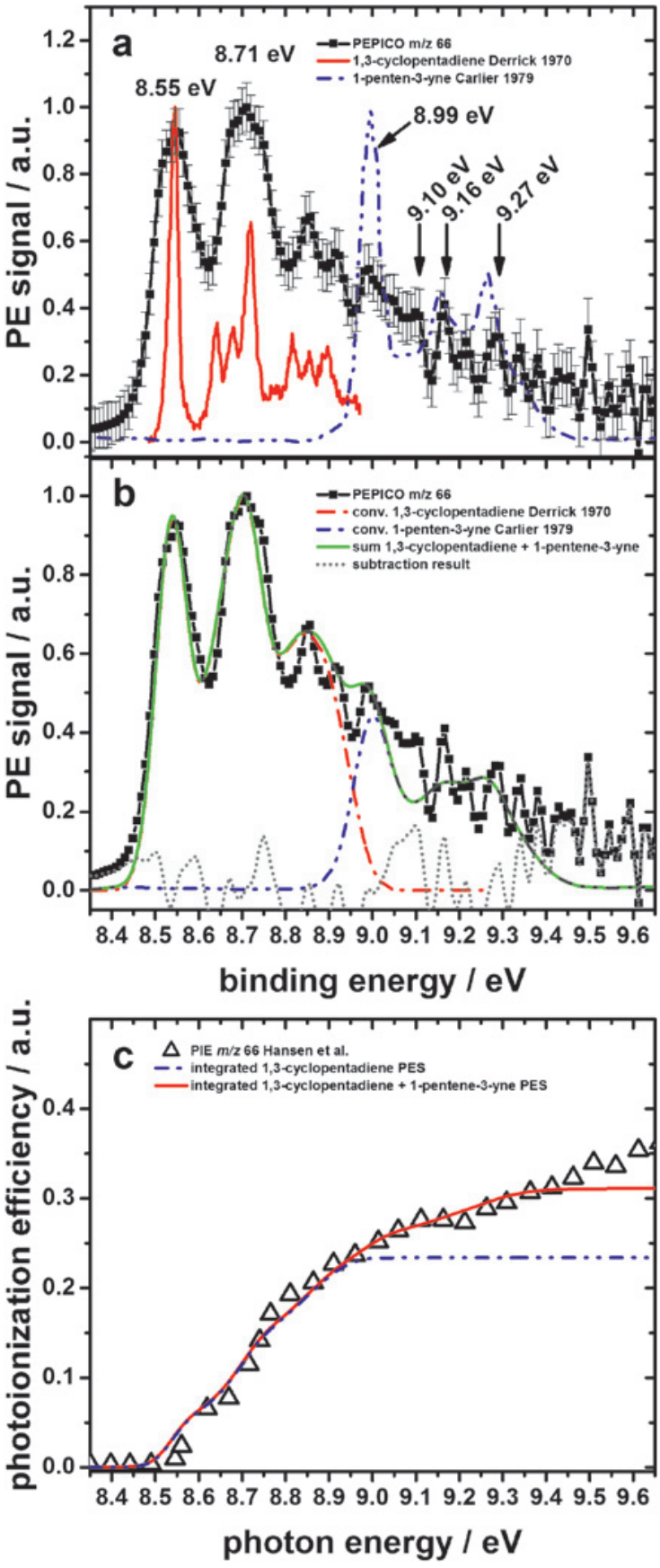

Figure 9: Panels a) and b) show the PES of $m/z = 66$ at $h = 2.5\,\mathrm{mm}$ measured with an acquisition time of $900\,\mathrm{s}$ at $9.70\,\mathrm{eV}$ in the CP flame (black line and symbols) including error bars from the evaluation with the pBasex algorithm [40] in comparison to: a) literature spectra of 1,3-cyclopentadiene [74] and 1-pentene-3-yne [73]; b) convoluted literature spectra and subtraction result. Panel c) shows the PIE curve from Hansen et al. [71] compared to weighted sum of integrated PES for 1,3-cyclopentadiene [74] and 1-pentene-3-yne [73].

from the cyclopentene (fuel) signal. With a recent cross section of 10.15 Mb for 1,3-cyclopentadiene [75], its maximum mole fraction was evaluated as 7.1×10^{-3}, while a mole fraction of 1.3×10^{-3} was determined for 1-pentene-3-yne using the same cross section of 18.19 Mb as in Hansen et al.'s work [71]. These results could now, for the first time, identify a quantitative contribution of a linear isomer to $m/z = 66$ in the CP flame, and its mole fraction is shown to be quite substantial, with a ratio of 1,3-cyclopentadiene to 1-pentene-3-yne at $h = 2.5$ mm of 5.5 : 1.

It is interesting upon the unambiguous identification of 1-pentene-3-yne in the present i^{2}PEPICO measurement to re-analyze the measured PIE curve of Hansen et al. [71], presented in Figure 9c. We have attempted to represent their result by a weighted sum of the PES for 1,3-cyclopentadiene and 1-pentene-3-yne that were integrated to yield PIE curves. The resulting PIE spectra are given in Figure 9c, and show a clear contribution of the linear isomer. It would have been very difficult to infer and even more to quantify the presence of 1-pentene-3-yne directly from the PIE curve since the differentiation of such a curve leads in general to a very noisy PES.

3.2.3 Detection of radicals at low photon energies

After providing some examples for the application of the fixed-photon-energy PEPICO approach to major and stable intermediate species, we now apply this technique to detect and identify radical species. Radicals are of essential importance in combustion since they drive the chain reactions from the fuel to the products. MBMS techniques allow radical detection in the flame environment in spite of difficulties arising from their high reactivity, fragmentation potential, limited mole fractions, and low ionization energies. Of particular interest are radicals that are formed directly from the fuel decomposition. Their detection needs low photoionization energies to avoid interference of species with high concentrations, as demonstrated in the TPEPICO measurements of [33]. For the CP flame studied here, we have used a fixed photon energy of 7.7 eV and a moderate sampling time of 1800 s. Indeed, it was possible to detect fuel radical species of the sum formula C_5H_7 at $m/z = 67$. Also, signals corresponding to C_4H_7 at $m/z = 55$ were detected for the first time in CP flames. Figure 10 shows the measured spectra in comparison with literature data [76–78].

The signal at $m/z = 67$ (Figure 10a) corresponds to isomers that are formed by H-abstraction of the fuel. The identification of these species is highly desirable, as they provide evidence for the initial branching pathways, one of the clues for the development of predictive mechanisms. The positions of the seven peaks observed in Figure 10a are given in Table 2.

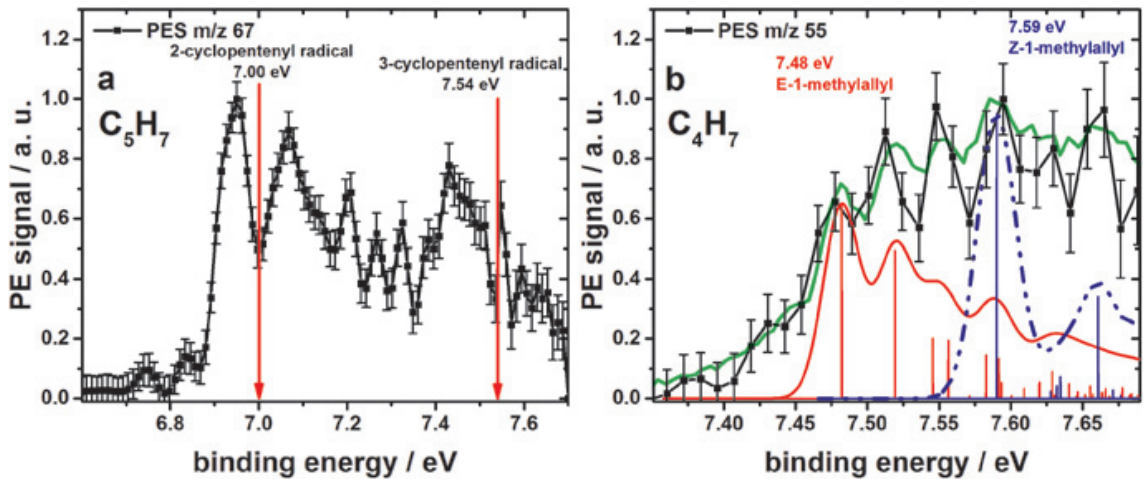

Figure 10: PES at $h = 1.0$ mm measured with an acquisition time of 1800 s at 7.70 eV in the CP flame (black line and symbols in a and b) including error bars from the evaluation with the pBasex algorithm [40]; a) $m/z = 67$ with literature IE of 2-cyclopentenyl [76] and 3-cyclopentenyl [77]; b) $m/z = 55$ with measured literature spectra (green line), Franck–Condon (FC) simulations (red and blue sticks), and convolution of FC simulations (red solid and blue dashed lines, FWHM = 25 meV) of (E)-1-methylallyl and (Z)-1-methylallyl by Lang et al. [78].

Table 2: Peak energies in the PES of $m/z = 67$, recorded at 7.7 eV.

Peak No.	1	2	3	4	5	6	7
Energy/ eV	6.95	7.07	7.21	7.27	7.33	7.43	7.55

The fuel radicals 2-cyclopentenyl and 3-cyclopentenyl are most likely to be present. Unfortunately their PES have not yet been reported, so that the identification of these two species must rely on their ionization energies, 7.00 eV for 2-cyclopentenyl [76] and 7.54 eV for 3-cyclopentenyl [77]. The measured PES shows the first peak at 6.95 eV, within 0.05 eV of the tabulated IE of 2-cyclopentenyl, providing evidence for the presence of this species. Peaks 2–5 originate most likely from the vibrational transitions of the 2-cyclopentenyl radical since they decrease in signal strength. The increased signal strength of the sixth peak at 7.43 eV indicates the presence of a second isomer, within 0.11 eV of the literature IE of 3-cyclopentenyl. The detection of the two cyclic C_5H_7 isomers may indicate the prevalence of the cyclic structure in the first radical attack (by H, OH, or O) at the fuel. However, linear isomers cannot be ruled out at this point, since the 7.55 eV peak could also indicate contributions of the mesomer-stabilized linear isomer pent-1-yn-3yl with a tabulated IE of 7.6 eV [65]. In this context, it must be noted that the determination of the ionization potentials of highly unstable radicals is not easy and literature data is scarce. Since the sample was taken at $h = 1$ mm dis-

tinctly upstream of the flame front, the detected radical species should predominantly be formed directly from the fuel. To enhance the reliability of the identification of such highly reactive species, a critical examination and renewed determination of the IE of possible isomers would be advisable. Also, information on PES and cross sections would permit to determine the mole fraction ratio between these isomers and thus give insight into the first branching ratio and subsequent reaction pathways in CP combustion.

The C_4H_7 radical has been detected in fuel-rich flames of several fuels [53, 62]. Possible isomers are the 1-methylallyl radical (IE(E): 7.48 eV, IE(Z): 7.59 eV) and 2-methylallyl radical (IE: 7.88 eV). Figure 10b shows the obtained fixed-photon-energy PES in comparison to the data measured (green line) and computed with Franck–Condon simulations (red and blue sticks and lines) by Lang et al [78]. Because of the low photon energy of 7.7 eV, only the two 1-methylallyl constitutional isomers may contribute to the recorded signal, since 2-methylallyl is not ionized at this energy. The excellent agreement between the two independent datasets confirms that both isomers participate in the combustion reactions of cyclopentene.

3.2.4 Detection of species with $m/z > 100$

Understanding the formation of polycyclic aromatic hydrocarbons (PAH) and soot is one of the remaining challenges in combustion. While details of the formation of the so-called "first aromatic ring" [13, 46, 79] seem quite well known, the reactions to higher-molecular intermediates are an active field of research [13, 16, 80]. We have thus, as a further example, examined the suitability of the fixed-photon-energy PEPICO approach for the detection of selected two-ring aromatics. By the EI-MBMS measurements in this work, indene, C_9H_8 ($m/z = 116$) and naphthalene, $C_{10}H_8$ ($m/z = 128$), were detected with peak mole fractions of the order of 1.0×10^{-5}–2.0×10^{-5}, compared to 4.2×10^{-6} and 9.5×10^{-6}, respectively, by Lamprecht et al. [48], while Kamphus et al. [47] detected only naphthalene (1.2×10^{-4}). Here, an attempt was made to detect and identify these species from their PES, in reasonable data acquisition time, although they are at the detection limit of our PEPICO setup. A photon energy of 8.75 eV was chosen to exclude species at higher IEs that might produce interfering signals due to substantial mole fractions. With a data acquisition time of 5800 s, relatively small signals of $\sim 10^4$ electrons that represent a complete PES were detected in coincidence with a given mass, corresponding to ~ 40 counts at the peak in the related mass spectrum. Figure 11 presents the measured PES along with literature spectra [81–83] for some possible species.

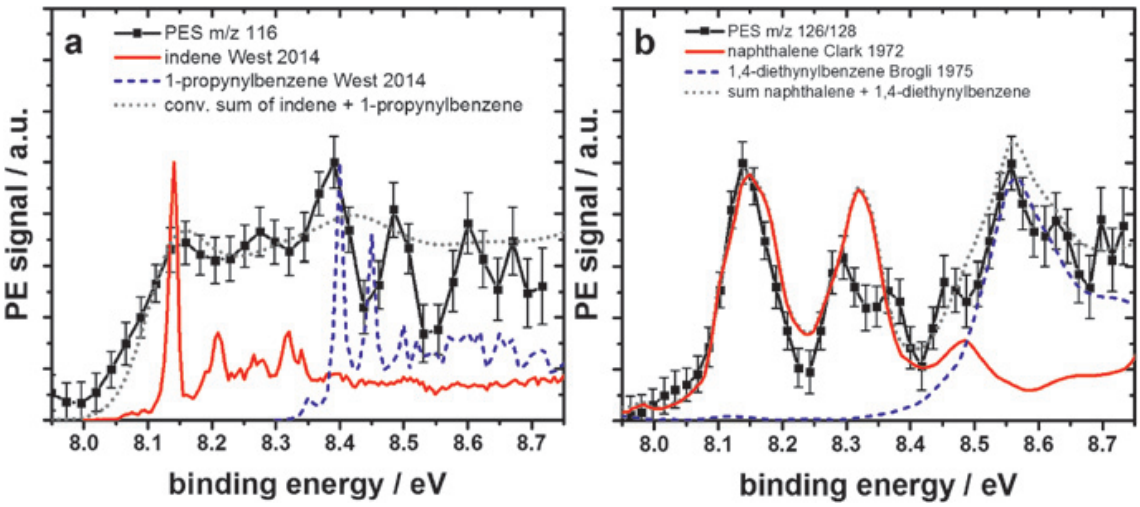

Figure 11: PES (black lines and symbols) of $m/z = 116$ (a) and $m/z = 126/128$ (b), taken in the fuel-rich CP flame at $h = 4$ mm, compared to the respective literature spectra by West et al. [81], Clark et al. [82], and Brogli et al. [83]; weighted sums of different species are indicated in light grey.

The PES at $m/z = 116$ (Figure 11a) shows an onset at 8.01 eV and a first peak at 8.16 eV, corresponding to the TPES of indene [81]. In spite of the relatively low resolution, a second species is seen to contribute to the signal above ~ 8.35 eV. The peak at 8.39 eV agrees well with the IE of 1-propynylbenzene of 8.40 eV, recently reported by West et al. [81]. The TPES from their study shows good agreement with our measurements. The first vibrational structure, assigned to a progression of a ring deformation [81] at 8.45 eV, was observed at a slightly different energy of 8.48 eV. This slight shift may result from the limited resolution in our measured PES. Evident from the sum spectrum in Figure 11a, the contributions of indene and 1-propynylbenzene approximate the measured PES in this energy range quite well.

Figure 11b shows the measured spectrum of the combined signals at $m/z = 126$ and $m/z = 128$, since these signals could not be separated due to their low intensities and limited mass resolution for $m/z \geq 120$. Nonetheless, a comparison with literature spectra of the most abundant respective isomers, 1,4-diethynylbenzene ($m/z = 126$), and naphthalene ($m/z = 128$) demonstrates the presence of both species. From the energy region between 8.0–8.50 eV, naphthalene is identified by its IE of 8.12 eV and two vibrational signatures that are in satisfactory agreement with the spectrum recorded by Clark et al. [82]. The present measurements show two features at 8.30 and 8.37 eV where the literature spectrum indicates only one broad peak at 8.32 eV. This may be a consequence of the slightly better resolution in the present experiment that reveals an additional vibrational mode. Besides naphthalene, 1,4-diethynylbenzene is iden-

tified by the signal at 8.56 eV that fits to the tabulated IE of 8.58 eV [65] and the PES recorded by Brogli et al. (blue dashed line) [83]. Again, the weighted sum of these two species (Figure 11b, grey line) agrees quite well with the measured spectrum. While indene and naphthalene have been determined in the cyclopentene flames by Lamprecht et al. [48] and Kamphus et al. [47], 1,4-propynylbenzene and 1,4-diethynylbenzene have been identified here for the first time. Their presence could underline the importance of aromatic species with side chains that may be involved in the PAH formation mechanism.

4 Summary and conclusions

The present study has shown examples for the application of a time-efficient multiplexing i^2PEPICO technique to combustion chemistry analysis, using carefully selected fixed photon energies. The aim was not to analyze a particular flame structure in detail, but to explore the present limits of the fixed-photon-energy PEPICO technique, a relatively new approach in combustion diagnostics. To this end, challenging analytic problems were chosen that might demonstrate some of the beneficial aspects of this experimentally involved but highly selective method to reveal interesting aspects in combustion chemistry. In addition to the most advanced photoionization mass spectrometric techniques that use VUV radiation from synchrotrons, the PEPICO technique exhibits even higher discriminative power by using the information of the coincident electron. The double-imaging DELICIOUS III spectrometer [39] provides, in combination with the pBasex inversion algorithm [40] for post-treatment, unique features that make fixed-photon-energy measurements in complex gas-phase diagnostics comparatively short in duration while still meaningful and carrying much more information than a simple PIE curve.

We have successfully demonstrated quantification of major and selected intermediate species from the electron signal for the first time using this approach. From a single measurement, multiple species were evaluated quantitatively in dimethyl ether and cyclopentene flames, and species profiles were obtained in very good agreement with EI-MBMS measurements or PI-MBMS experiments in previous work. Because of the fingerprint nature of the photoelectron spectra, often spread out over a large energy range, species with significantly different ionization energies can readily be quantified as long as PES and cross sections are available in sufficient resolution and precision. As a further advantage, fragmentation contributions might be resolved in situations with well-resolved PES. In comparison to scanned, TPEPICO, measurements it is beneficial that the narrow

energy distribution of only a few meV in fixed-photon-energy PEPICO permits the use of a single well-defined cross section at that given energy for quantification, in contrast to TPES which would need a specific database to account for autoionization resonances and the dependence of the partial cross sections on the electron kinetic energy to be used quantitatively. Furthermore, the large area of the VMI in the DELICIOUS III spectrometer [39] allows for the detection of a large kinetic energy range of electrons so that corrections for their imaging [33] are not necessary, again facilitating quantitative interpretation. Evidently, the same approach can be used to determine PES with high energy resolution for combustion-relevant species [32].

In further examples in this study, more complex fixed-photon-energy PEPICO spectra were analyzed in situations with multiple species contributing to the signal at a given mass and/or with very close-lying ionization energies. In a methyl propanoate flame, five species with highly overlapping PES and ionization energies in a 0.8 eV energy range were successfully separated at $m/z = 56$. For the first time, the contributions of linear isomers to $m/z = 66$ in a cyclopentene flame were analyzed, with unambiguous identification of 1-pentene-3-yne by its fingerprint PES in competition to a much larger signal of 1,3-cyclopentadiene, until now assumed to be the only contributing isomer in this flame. In comparison to the synchrotron-based photoionization MBMS technique that is being used as one of the most advanced approaches in combustion diagnostics, the fingerprint PES provides convincing advantages because several vibrational signatures are typically recorded that facilitate species identification.

Using low photon energies, fuel-derived radicals, formed upon the first radical attack on the fuel molecule, have been identified in the cyclopentene flame, hinting at the conservation of the ring structure in the early fuel decomposition. Such information is extremely helpful in guiding the development of detailed reaction mechanisms. Also, further radicals could be identified without interference from stronger signals of species with higher concentrations at such low photon energies. For example, at $m/z = 55$ the 1-methylallyl radical was detected, with clear identification of two different constitutional isomers.

At higher masses, the fixed-photon-energy PEPICO measurements, in spite of limited sensitivity, have proven valuable to identify aromatic species with side chains, namely 1,4-propynylbenzene at $m/z = 116$, next to indene, and 1,4-diethynylbenzene at $m/z = 126$, both detected for the first time in fuel-rich cyclopentene combustion. Their detection would provide useful information regarding the formation pathways of higher-molecular aromatics.

All examples demonstrated here have used limited and competitive amounts of valuable measurement time at large-scale facilities, suggesting that fixed-photon-energy multiplexing i^2PEPICO could become a more common addition

to the arsenal of combustion diagnostics, as well as for other gas-phase reaction systems showing significant complexity. This is even more relevant since the scheme presented here could also be used with fixed-photon-energy VUV laboratory sources, such as high-repetition-rate lasers or continuous discharge lamps, alleviating the need for large facility access and/or the need for fully tunable light sources. To prove even more valuable in the future, high-resolution PES and cross sections should be a target for the many intermediate species involved, either from theoretical or experimental studies.

Acknowledgement: The experiments in SOLEIL were performed under proposal number 20140050. We would like to thank the general SOLEIL staff for smoothly running the facility and for ongoing support during our measurements. In particular we appreciate the technical help provided by Jean-François Gil in mounting the burner chamber.

List of Abbreviations

Abbreviation	Translation
(T)PEPICO	(threshold) photoelectron/photoion coincidence spectroscopy
i^2PEPICO	(double) imaging PEPICO
EI/PI – MBMS	electron ionization/photoionization molecular-beam mass spectrometry
VUV	vacuum ultraviolet
(T)PES	(threshold) photoelectron spectrum
IE	ionization energy
DME/CP/MP	dimethyl ether/cyclopentene/methyl propanoate
VMI	velocity map imaging
WM-TOF	Wiley-McLaren time-of-flight
FWHM	full width at half maximum
PIE	photoionization efficiency

References

1. S. R. Leone, M. Ahmed, and K. R. Wilson, Phys. Chem. Chem. Phys. **12** (2010) 6564.
2. D. A. Plattner, Int. J. Mass Spectrom. **207** (2001) 125.

3. O. Welz, J. D. Savee, D. L. Osborn, S. S. Vasu, C. J. Percival, D. E. Shallcross, and C. A. Taatjes, Science **335** (2012) 204.
4. Y. Li and F. Qi, Acc. Chem. Res. **43** (2010) 68.
5. C. A. Taatjes, N. Hansen, D. L. Osborn, K. Kohse-Höinghaus, T. A. Cool, and P. R. Westmoreland, Phys. Chem. Chem. Phys. **10** (2008) 20.
6. D. S. N. Parker, F. Zhang, Y. S. Kim, R. I. Kaiser, A. Landera, V. V. Kislov, A. M. Mebel, and A. G. G. M. Tielens, P. Natl. Acad. Sci. USA **109** (2012) 53.
7. A. Bellili, M. Schwell, Y. Bénilan, N. Fray, M.-C. Gazeau, M. Mogre. Al-Mogren, J.-C. Guillemin, L. Poisson, and M. Hochlaf, J. Mol. Spectrosc. **315** (2015) 196.
8. H.-W. Jochims, M. Schwell, J.-L. Chotin, M. Clemino, F. Dulieu, H. Baumgärtel, and S. Leach, Chem. Phys. **298** (2004) 279.
9. S. Pilling, D. P. P. Andrade, R. B. de Castilho, R. L. Cavasso-Filho, A. F. Lago, L. H. Coutinho, G. G. B. d. Souza, H. M. Boechat-Roberty, and A. Naves de Brito, Proc. Int. Astron. Union **4** (2008) 371.
10. J. Zhen, P. Castellanos, D. M. Paardekooper, N. Ligterink, H. Linnartz, L. Nahon, C. Joblin, and A. G. G. M. Tielens, Astrophys. J. Lett. **804** (2015) L7.
11. P. Hemberger, M. Steinbauer, M. Schneider, I. Fischer, M. Johnson, A. Bodi, and T. Gerber, J. Phys. Chem. A **114** (2010) 4698.
12. F. Qi, Proc. Combust. Inst. **34** (2013) 33.
13. N. Hansen, T. A. Cool, P. R. Westmoreland, and K. Kohse-Höinghaus, Prog. Energ. Combust. **35** (2009) 168.
14. F. Battin-Leclerc, O. Herbinet, P.-A. Glaude, R. Fournet, Z. Zhou, L. Deng, H. Guo, M. Xie, and F. Qi, Angew. Chem. Int. Ed. **49** (2010) 3169.
15. T. Lu and C. K. Law, Prog. Energ. Combust. **35** (2009) 192.
16. H. Wang, Proc. Combust. Inst. **33** (2011) 41.
17. K. Moshammer, A. W. Jasper, D. M. Popolan-Vaida, A. Lucassen, P. Diévart, H. Selim, A. J. Eskola, C. A. Taatjes, S. R. Leone, S. M. Sarathy, Y. Ju, P. Dagaut, K. Kohse-Höinghaus, and N. Hansen, J. Phys. Chem. A **119** (2015) 7361.
18. U. Struckmeier, P. Oßwald, T. Kasper, L. Böhling, M. Heusing, M. Köhler, A. Brockhinke, and K. Kohse-Höinghaus, Z. Phys. Chem. **223** (2009) 503.
19. L. Deng, A. Kempf, O. Hasemann, O. P. Korobeinichev, and I. Wlokas, Combust. Flame **162** (2015) 1737.
20. J. Zádor, H. Huang, O. Welz, J. Zetterberg, D. L. Osborn, and C. A. Taatjes, Phys. Chem. Chem. Phys. **15** (2013) 10753.
21. P. T. Lynch, T. P. Troy, M. Ahmed, and R. S. Tranter, Anal. Chem. **87** (2015) 2345.
22. S. A. Skeen, H. A. Michelsen, K. R. Wilson, D. M. Popolan, A. Violi, and N. Hansen, J. Aerosol. Sci. **58** (2013) 86.
23. F. L. Dryer, Proc. Combust. Inst. **35** (2015) 117.
24. K. Kohse-Höinghaus, P. Oßwald, T. A. Cool, T. Kasper, N. Hansen, F. Qi, C. K. Westbrook, and P. R. Westmoreland, Angew. Chem. Int. Ed. **49** (2010) 3572.
25. C. A. Taatjes, D. L. Osborn, T. M. Selby, G. Meloni, H. Fan, and S. T. Pratt, J. Phys. Chem. A **112** (2008) 9336.
26. T. A. Cool, J. Wang, K. Nakajima, C. A. Taatjes, and A. McIlroy, Int. J. Mass Spectrom. **247** (2005) 18.
27. B. Yang, J. Wang, T. A. Cool, N. Hansen, S. Skeen, and D. L. Osborn, Int. J. Mas. Spectrom. **309** (2012) 118.

28. B. Gans, L. A. Vieir Mendes, S. Boyé-Péronne, S. Douin, G. Garcia, H. Soldi-Lose, B. K. Cunha de Miranda, C. Alcaraz, N. Carrasco, P. Pernot, and D. Gauyacq, J. Phys. Chem. A **114** (2010) 3237.
29. B. Gans, G. A. Garcia, S. Boyé-Péronne, J.-C. Loison, S. Douin, F. Gaie-Levrel, and D. Gauyacq, J. Phys. Chem. A **115** (2011) 5387.
30. T. Baer, Annu. Rev. Phys. Chem. **40** (1989) 637.
31. T. Arion and U. Hergenhahn, J. Electron Spectrosc. **200** (2015) 222.
32. A. Bodi, P. Hemberger, D. L. Osborn, and B. Sztáray, J. Phys. Chem. Lett. **4** (2013) 2948.
33. P. Oßwald, P. Hemberger, T. Bierkandt, E. Akyildiz, M. Köhler, A. Bodi, T. Gerber, and T. Kasper, Rev. Sci. Instrum. **85** (2014) 025101.
34. G. A. Garcia, X. Tang, J.-F. Gil, L. Nahon, M. Ward, S. Batut, C. Fittschen, C. A. Taatjes, D. L. Osborn, and J.-C. Loison, J. Chem. Phys. **142** (2015) 164201.
35. J. Krüger, G. A. Garcia, D. Felsmann, K. Moshammer, A. Lackner, A. Brockhinke, L. Nahon, and K. Kohse-Höinghaus, Phys. Chem. Chem. Phys. **16** (2014) 22791.
36. D. Felsmann, K. Moshammer, J. Krüger, A. Lackner, A. Brockhinke, T. Kasper, T. Bierkandt, E. Akyildiz, N. Hansen, A. Lucassen, P. Oßwald, M. Köhler, G. A. Garcia, L. Nahon, P. Hemberger, A. Bodi, T. Gerber, and K. Kohse-Höinghaus, Proc. Combust. Inst. **35** (2015) 779.
37. L. Nahon, N. de Oliveira, G. A. Garcia, J.-F. Gil, B. Pilette, O. Marcouillé, B. Lagarde, and F. Polack, J. Synchrotron Radiat. **19** (2012) 508.
38. G. A. Garcia, H. Soldi-Lose, and L. Nahon, Rev. Sci. Instrum. **80** (2009) 023102.
39. G. A. Garcia, B. K. Cunha de Miranda, M. Tia, S. Daly, and L. Nahon, Rev. Sci. Instrum. **84** (2013) 053112.
40. G. A. Garcia, L. Nahon, and I. Powis, Rev. Sci. Instrum. **75** (2004) 4989.
41. J. Wang, M. Chaos, B. Yang, T. A. Cool, F. L. Dryer, T. Kasper, N. Hansen, P. Oßwald, K. Kohse-Höinghaus, and P. R. Westmoreland, Phys. Chem. Chem. Phys. **11** (2009) 1328.
42. D. Liu, J. Santner, C. Togbé, D. Felsmann, J. Koppmann, A. Lackner, X. Yang, X. Shen, Y. Ju, and K. Kohse-Höinghaus, Combust. Flame **160** (2013) 2654.
43. F. Herrmann, B. Jochim, P. Oßwald, L. Cai, H. Pitsch, and K. Kohse-Höinghaus, Combust. Flame **161** (2014) 384.
44. H. Xu, C. Yao, T. Yuan, K. Zhang, and H. Guo, Combust. Flame **158** (2011) 1673.
45. U. Burke, K. P. Somers, P. O'Toole, C. M. Zinner, N. Marquet, G. Bourque, E. L. Petersen, W. K. Metcalfe, Z. Serinyel, and H. J. Curran, Combust. Flame **162** (2015) 315.
46. N. Hansen, T. Kasper, S. J. Klippenstein, P. R. Westmoreland, M. E. Law, C. A. Taatjes, K. Kohse-Höinghaus, J. Wang, and T. A. Cool, J. Phys. Chem. A **111** (2007) 4081.
47. M. Kamphus, M. Braun-Unkhoff, and K. Kohse-Höinghaus, Combust. Flame **152** (2008) 28.
48. A. Lamprecht, B. Atakan, and K. Kohse-Höinghaus, Proc. Combust. Inst. **28** (2000) 1817.
49. D. Felsmann, H. Zhao, Q. Wang, I. Graf, T. Tan, X. Yang, E. A. Carter, Y. Ju, and K. Kohse-Höinghaus, Proc. Combust. Inst., submitted for publication (2015).
50. B. Yang, C. K. Westbrook, T. A. Cool, N. Hansen, and K. Kohse-Höinghaus, Z. Phys. Chem. **225** (2011) 1293.
51. B. Mercier, M. Compin, C. Prevost, G. Bellec, R. Thissen, O. Dutuit, and L. Nahon, J. Vac. Sci. Technol. A **18** (2000) 2533.
52. P. Oßwald, H. Güldenberg, K. Kohse-Höinghaus, B. Yang, T. Yuan, and F. Qi, Combust. Flame **158** (2011) 2.
53. M. Schenk, L. Leon, K. Moshammer, P. Oßwald, T. Zeuch, L. Seidel, F. Mauss, and K. Kohse-Höinghaus, Combust. Flame **160** (2013) 487.
54. J. C. Biordi, Prog. Energ. Combust. **3** (1977) 151.

55. A. Lucassen, N. Labbe, P. R. Westmoreland, and K. Kohse-Höinghaus, Combust. Flame **158** (2011) 1647.
56. F. N. Egolfopoulos, N. Hansen, Y. Ju, K. Kohse-Höinghaus, C. K. Law, and F. Qi, Prog. Energ. Combust. **43** (2014) 36.
57. T. A. Cool, A. McIlroy, F. Qi, P. R. Westmoreland, L. Poisson, D. S. Peterka, and M. Ahmed, Rev. Sci. Instrum. **76** (2005) 094102.
58. Y. Li, L. Zhang, Z. Tian, T. Yuan, J. Wang, B. Yang, and F. Qi, Energ. Fuel. **23** (2009) 1473.
59. R. J. Kee, J. F. Grcar, M. D. Smooke, and J. A. Miller, Report No. SAND85-8240, Sandia National Laboratories (1985), Modification of PREMIX Version 2.5 (1991).
60. H. A. Gueniche, J. Biet, P. A. Glaude, R. Fournet, and F. Battin-Leclerc, Fuel **88** (2009) 1388.
61. T. A. Cool, J. Wang, N. Hansen, P. R. Westmoreland, F. L. Dryer, Z. Zhao, A. Kazakov, T. Kasper, and K. Kohse-Höinghaus, Proc. Combust. Inst. **31** (2007) 285.
62. K. Moshammer, S. Vranckx, H. K. Chakravarty, P. Parab, R. X. Fernandes, and K. Kohse-Höinghaus, Combust. Flame **160** (2013) 2729.
63. D. W. Turner, Philos. T. R. Soc. Lond. **268** (1970) 7.
64. K. Kimura, S. Katsumata, T. Yamazaki, and H. Wakabayashi, J. Electron Spectrosc. **6** (1975) 41.
65. Y.-K. Kim, K. K. Irikura, M. E. Rudd, M. A. Ali, P. M. Stone, J. Chang, J. S. Coursey, R. A. Dragoset, A. R. Kishore, K. J. Olsen, A. M. Sansonetti, G. G. Wiersma, D. S. Zucker, and M. A. Zucker, available from world wide web: http://physics.nist.gov/PhysRefData/Ionization (2006).
66. T. A. Cool, K. Nakajima, T. A. Mostefaoui, F. Qi, A. McIlroy, P. R. Westmoreland, M. E. Law, L. Poisson, D. S. Peterka, and M. Ahmed, J. Chem. Phys. **119** (2003) 8356.
67. H. Bock, T. Hirabayashi, and S. Mohmand, Chem. Ber. **114** (1981) 2595.
68. R. M. White, T. A. Carlson, and D. P. Spears, J. Electron Spectrosc. **3** (1974) 59.
69. A. A. Bredikhin, B. Acad. Sci. USSR Ch. **40** (1991) 1583.
70. C. E. van der Meij, J. van Eck, and A. Niehaus, Chem. Phys. **130** (1989) 325.
71. N. Hansen, S. J. Klippenstein, J. A. Miller, J. Wang, T. A. Cool, M. E. Law, P. R. Westmoreland, T. Kasper, and K. Kohse-Höinghaus, J. Phys. Chem. A **110** (2006) 4376.
72. N. Hansen, J. A. Miller, C. A. Taatjes, J. Wang, T. A. Cool, M. E. Law, and P. R. Westmoreland, Proc. Combust. Inst. **31** (2007) 1157.
73. P. Carlier, G. Mouvier, D. Mesnard, and L. Miginiac, J. Electron Spectrosc. **16** (1979) 147.
74. P. J. Derrick, L. Åsbrink, O. Edqvist, and E. Lindholm, Spectrochim. Acta Part A: Mol. Spectrosc. **27** (1971) 2525.
75. C. A. Taatjes, D. L. Osborn, T. M. Selby, G. Meloni, A. J. Trevitt, E. Epifanovsky, A. I. Krylov, B. Sirjean, E. Dames, and H. Wang, J. Phys. Chem. A **114** (2010) 3355.
76. F. P. Lossing and J. C. Traeger, J. Am. Chem. Soc. **97** (1975) 1579.
77. S. Pignataro, A. Cassuto, and F. P. Lossing, J. Am. Chem. Soc. **89** (1967) 3693.
78. M. Lang, F. Holzmeier, P. Hemberger, and I. Fischer, J. Phys. Chem. A **119** (2015) 3995.
79. C. S. McEnally, L. D. Pfefferle, B. Atakan, and K. Kohse-Höinghaus, Prog. Energ. Combust. **32** (2006) 247.
80. M. Schenk, N. Hansen, H. Vieker, A. Beyer, A. Gölzhäuser, and K. Kohse-Höinghaus, Proc. Combust. Inst. **35** (2015) 1761.
81. B. West, A. Sit, A. Bodi, P. Hemberger, and P. M. Mayer, J. Phys. Chem. A **118** (2014) 11226.
82. P. A. Clark, F. Brogli, and E. Heilbronner, Helv. Chim. Acta **55** (1972) 1415.
83. F. Brogli, E. Heilbronner, J. Wirz, E. Kloster-Jensen, R. G. Bergman, K. P. C. Vollhardt, and A. J. Ashe, Helv. Chim. Acta **58** (1975) 2620.

ANHANG C

Publikation 3

L.S. Tran, J. Pieper, H.-H. Carstensen, H. Zhao, I. Graf, Y. Ju, F. Qi, K. Kohse-Höinghaus

Experimental and kinetic modeling study of diethyl ether flames

Proceedings of the Combustion Institute **36**, 1165-1173, 2017
DOI: 10.1016/j.proci.2016.06.087[1]

Abstract

Diethyl ether (DEE, $C_4H_{10}O$) is being considered as a promising biofuel. However, its combustion chemistry has not been well studied. Particularly lacking are quantitative intermediate species profiles in flames that provide a stringent test for kinetic models, and flame speed data at elevated pressures. In the present paper, we obtain species distributions in low-pressure flames and measure flame speeds at elevated pressure to gain insights into high-temperature combustion chemistry of DEE. Specifically, a fuel-rich DEE flame (ϕ=1.8) with 25% argon dilution at 4 kPa was investigated by using a dedicated combination of electron ionization (EI) molecular-beam mass spectrometry (MBMS) with gas chromatography (GC) and tunable synchrotron vacuum ultraviolet (VUV) photoionization (PI) MBMS. High-pressure flame speeds of DEE were measured in a constant-volume cylindrical chamber at an initial temperature of 298 K at an equivalence ratio of ϕ=1.4 and pressures up to 507 kPa. Moreover, a new detailed kinetic model for DEE combustion was developed, with the most noticeable advances over the solely existing model by Yasunaga et al. [J. Phys. Chem. A 114 (2010) 9098–9109] being a more complete description of the reactions of DEE radicals and the use of accurate theoretical methods, *i.e.* CBS-QB3, to determine the rate constants for important primary reactions. In contrast to the previously published one, the present model includes reactions of DEE radicals that directly involve the formation of ethyl vinyl ether (EVE), an addition supported by identification and quantification of EVE by PI-MBMS in the flame experiment. Finally, the results showed that DEE flames yield low concentrations of aromatic species. However, high acetaldehyde emission was observed, originating from the dominant pathways of DEE consumption via H-abstractions from C-α positions followed by β-scissions.

1 Zu dieser Publikation ist Supplemental Material online unter http://doi.org/10.1016/j.proci.2016.06.087 verfügbar.

Available online at www.sciencedirect.com

ScienceDirect

Proceedings of the Combustion Institute 36 (2017) 1165–1173

Proceedings of the Combustion Institute

www.elsevier.com/locate/proci

Experimental and kinetic modeling study of diethyl ether flames

Luc-Sy Tran [a,*], Julia Pieper [a], Hans-Heinrich Carstensen [b], Hao Zhao [c], Isabelle Graf [a], Yiguang Ju [c], Fei Qi [d], Katharina Kohse-Höinghaus [a]

[a] *Department of Chemistry, Bielefeld University, Universitätsstraße 25, D-33615 Bielefeld, Germany*
[b] *Laboratory for Chemical Technology (LCT), Ghent University, Technologiepark 914, 9052 Ghent, Belgium*
[c] *Department of Mechanical and Aerospace Engineering, Princeton University, Princeton NJ 08544, USA*
[d] *Key Laboratory for Power Machinery and Engineering of MOE, Shanghai Jiao Tong University, Shanghai 200240, PR China*

Received 25 November 2015; accepted 10 June 2016
Available online 24 June 2016

Abstract

Diethyl ether (DEE, $C_4H_{10}O$) is being considered as a promising biofuel. However, its combustion chemistry has not been well studied. Particularly lacking are quantitative intermediate species profiles in flames that provide a stringent test for kinetic models, and flame speed data at elevated pressures. In the present paper, we obtain species distributions in low-pressure flames and measure flame speeds at elevated pressure to gain insights into high-temperature combustion chemistry of DEE. Specifically, a fuel-rich DEE flame ($\phi \sim 1.8$) with 25% argon dilution at 4 kPa was investigated by using a dedicated combination of electron ionization (EI) molecular-beam mass spectrometry (MBMS) with gas chromatography (GC) and tunable synchrotron vacuum ultraviolet (VUV) photoionization (PI) MBMS. High-pressure flame speeds of DEE were measured in a constant-volume cylindrical chamber at an initial temperature of 298 K at an equivalence ratio of $\phi = 1.4$ and pressure up to 507 kPa. Moreover, a new detailed kinetic model for DEE combustion was developed, with the most noticeable advances over the solely existing model by Yasunaga et al., 2010 being a more complete description of the reactions of DEE radicals and the use of accurate theoretical methods, *i.e.* CBS-QB3, to determine the rate constants for important primary reactions. In contrast to the previously published one, the present model includes reactions of DEE radicals that directly involve the formation of ethyl vinyl ether (EVE), an addition supported by identification and quantification of EVE by PI-MBMS in the flame experiment. Finally, the results showed that DEE flames yield low concentrations of aromatic species. However, high acetaldehyde emission was observed, originating from the dominant pathways of DEE consumption via H-abstractions from C_{α} positions followed by β-scissions.

Keywords: Biofuel; Diethyl ether; Laminar premixed flame; Molecular-beam mass spectrometry; Detailed kinetic model

1. Introduction

Increasing energy demand in the transport sector, coupled with the need to reduce greenhouse gas

* Corresponding author.
E-mail addresses: luc-sy.tran@uni-bielefeld.de, tran.luc.sy.iutdn@gmail.com (L.-S. Tran).

http://dx.doi.org/10.1016/j.proci.2016.06.087
1540-7489 © 2016 by The Combustion Institute. Published by Elsevier Inc.

emissions, continues to motivate research directed toward renewable fuels. Biofuels such as ethers, esters, and alcohols are discussed as additives or replacement fuels [1]. Diethyl ether (DEE), available via dehydration of ethanol over solid acid catalysts, is considered as a promising biofuel [2,3]. DEE has several favorable properties for diesel engine combustion including a high cetane number (>125) and energy density (33.9 MJ/kg), more favorable than that of dimethyl ether (28.6 MJ/kg), broad flammability limits, and high miscibility with diesel fuel [3]. Unfortunately, only limited investigations on the combustion chemistry of DEE have been performed, including measurements of ignition delay times [4,5], species profiles from pyrolysis and a non-premixed flame [5,6], and flame speeds [7–9]. Data are particularly scarce regarding species profiles in DEE combustion. Especially intermediate species profiles in laminar flames are known to provide a stringent test for kinetic models that may then be used for the prediction of pollutant emissions. To the best of our knowledge, quantitative sets of species profiles in premixed DEE flames are not yet available. We have thus studied the combustion chemistry of DEE in a fuel-rich low-pressure laminar premixed flame by investigating a full set of species profiles with a combination of advanced analytic techniques. To broaden the available parameter range, we also measured the laminar flame speeds of DEE in a constant-volume chamber at elevated pressure. A new detailed kinetic model relying on a systematic analysis of DEE radical reactions is proposed to describe the combustion of DEE, in particular with respect to intermediates and pollutant formation.

2. Experiments and Modeling

2.1. Flame experiments

A fuel-rich ($\phi \sim 1.8$, C/O ~ 0.52) premixed flame of DEE/oxygen/argon (17.3%/57.7%/25%) was stabilized on a home-made flat burner (McKenna type) of 64 mm diameter (Bielefeld) at 4 kPa, with a cold gas velocity (333 K, 4 kPa) of 73 cm/s and an overall mass flow rate of 4.35×10^{-3} g/(cm^2 s). Adapted conditions to provide the same mass flow rate were applied with a McKenna burner of 60 mm diameter at the Taiwan Light Source. An EI-MBMS-GC setup (Bielefeld) was used, complemented with a VUV-PI-MBMS system (Taiwan), to provide a detailed chemical analysis of stable and reactive species together with isomer identification.

2.2. EI-MBMS-GC experiment

A detailed description of the experimental setup is given elsewhere [10]. In brief, gas samples were extracted from the flame by a quartz cone (300 μm orifice, 25° opening angle) and transferred into a molecular beam, then directed through a copper skimmer to the ion source of the mass spectrometer. The two-stage Wiley-McLaren ion source with a reflectron time-of-flight (TOF) detection unit provides a mass resolution of $m/\Delta m \sim 4000$, enabling the determination of the exact elemental composition of C/H/O species. Soft ionization energies (10.0, 11.5, 13.0 eV for intermediates, 16 and 18 eV for main species) were used to minimize undesired fragmentation. Ions were detected using a multichannel plate (MCP) with a multichannel scaler for data recording. The mole fraction evaluation followed previously reported procedures [10]. Combined with a gas chromatograph equipped with an Alumina BOND/Na_2SO_4 column, the setup was able to distinguish stable hydrocarbon isomers to provide supplemental information for the evaluation of the EI-MBMS data, which was done using the cross section of the dominant isomer. The same MCP of the EI-MBMS setup was used to detect species of the GC effluent. Generally, in the EI-MBMS experiment the error is <30% for directly calibrated species, and below a factor of 2 for species calibrated with the convolution procedure [10]. For radicals for which the relative ionization cross section (RICS) procedure [11] was used, the error is estimated to be in the range of factors of 2–4. The flame temperature was derived from the pressure in the first pumping stage and calibrated at 20 mm above the burner by OH planar laser-induced fluorescence without the sampling nozzle present [12].

2.3. VUV-PI-MBMS experiment

Information regarding the identification of oxygenated isomers that could not be separated by the present GC setup was obtained using a VUV-PI-MBMS instrument. A detailed description can be found elsewhere [13]. In brief, this system includes modules devoted to sampling and ionization; ion transfer and storage; and ion detection, the latter housing the TOF-MS with a mass resolution of $m/\Delta m \sim 3500$ and a detection limit of <1 ppm. Samples were withdrawn from the flame by a quartz nozzle (400 μm orifice, 25° included angle) to form a molecular beam which was then intersected and ionized by the tunable VUV synchrotron radiation with energy resolution of $E/\Delta E \sim 1000$ and average photon flux of $\sim 10^{12}$ photons/s.

2.4. Flame speed experiments

Laminar flame speeds of DEE were measured in a heated high-pressure, constant-volume cylindrical chamber. Mixtures of DEE/oxygen/nitrogen (4.43%/18.99%/76.58%) at $\phi = 1.4$ were studied with an initial gas temperature of 298 K for pressures of 101, 203, 304, 405, and 507 kPa, respectively. Details of the apparatus and procedures

were described elsewhere [14]. In brief, the cylindrical chamber was housed in an oven and filled with a quiescent combustible mixture and then centrally ignited. The unsteady flame front time history was measured directly using high-speed Schlieren imaging. The time-dependent flame front location data were analyzed by using an automated flame-edge detection and circle-fitting program. The unstretched flame speed relative to the burned gas ($S_{b,0}$) was calculated using the extrapolation procedure described in [14], and this extrapolated flame velocity was converted to the unstretched propagation speed relative to the unburned gas ($S_{u,0}$) using the density ratio calculated by CHEMKIN [15]. The uncertainty of the measured flame speed is below 10%.

2.5. Model development and simulations

A preliminary analysis with the solely available model by Yasunaga et al. [5] showed that the decomposition of the DEE radicals is an essential part of its flame chemistry, hence good kinetic data for these reactions are needed. However, the Yasunaga model was largely constructed using estimated rate constants for the primary reactions. We have therefore used a more accurate quantum chemistry computation method, *i.e.* CBS-QB3, to determine rate constants for several important reaction classes and thermochemical data of related species. Note that while several low-temperature-chemistry studies were reported for the reaction schemes or reaction rate constants of DEE and its radicals [16–18], only very scarce kinetic data is available for the high-temperature oxidation of this fuel.

Thermochemical data for DEE, DEE radicals, and species in the oxidation pathways were obtained from quantum chemistry calculations in the present work or relied on recent results of [19]; these results are provided in Section S.I.1 in Supplemental Material 1. The formation enthalpies for DEE and the $C_2H_5OCHCH_3$ radical calculated in the present work are in good agreement (within 1 kcal/mol) with values in the literature [5,20,21]. A slightly higher discrepancy of 1.54 kcal/mol is noted between the formation enthalpy of the $C_2H_5OCH_2CH_2$ radical from Yasunaga et al. [5] and the value in the present work, which is, however, in good agreement with that in Burcat's database [20].

The new DEE sub-mechanism contains the following major classes of elementary reactions: (i) unimolecular decomposition, (ii) H-atom abstractions, (iii) fuel radical isomerization, (iv) fuel radical decomposition by C–O and C–H bond β-scissions, (v) fuel radical oxidation, (vi) fuel radical–radical disproportionation forming ethyl vinyl ether (EVE, C_4H_8O), and (vii) consumption reactions of primary products. These reaction classes have been thoroughly discussed for several fuels in previous studies [22,23]. Some of these classes, *i.e.* (iii), (vi), and C–H bond β-scissions yielding EVE were not included in the Yasunaga mechanism [5]. Important pathways of DEE combustion are summarized in Fig. 1. Rate constants for C–O and C–H bond β-scissions (channels Ia, Ic, IIa, and IIc in Fig. 1) and isomerization (channel "iso") were calculated here using the CBS-QB3 method; details of the used CBS-QB3 approach are given in [24]. The present model has used high-pressure limiting rate constants for the unimolecular decomposition reactions of the fuel radicals. This is justified by the very low decomposition barriers which are rapidly overcome at the high temperatures of the flame. More information is available in Section S.I. of Supplemental Material 1. The rate constant for C–O bond β-scission of $C_2H_5OCHCH_3$ calculated here is ~700 times slower at 1200 K than that in the Yasunaga model. The DEE radical oxidation by O_2 (Ib, IIb) can lead to the formation of EVE via ethoxyethylperoxy radicals. The role of this reaction class has recently been identified in the low- and high-temperature oxidation of alcohols [23,25]. Rate constants for reactions in these oxidation routes recently calculated by Sakai et al. [19] for the temperature range 500–2500 K are adopted in the present model.

Together with the reactions of the DEE radicals described above, H-abstractions from DEE by H and OH play an important role in DEE combustion. H-abstractions by H-atom have also been investigated here for both α and β positions (see definitions in Fig. 1) to obtain reliable rate constants and branching ratios, while those for H-abstractions by OH are based on theoretical work by Zhou et al. [26]. Note that the Yasunaga model [5] also used the kinetic data from [26], but with an erroneous sign for the activation energy of channel I (4040 cal/mol instead of –4040 cal/mol). Rate constants of H-abstractions by H-atom calculated here are about two times slower at 1200 K than those in the Yasunaga model [5]. Additional information on the thermochemical data and rate constants calculated in the present work is available in Supplemental Material 1.

Pressure-dependent rate constants for the unimolecular decompositions of DEE were taken from Yasunaga et al. [5]. Missing C–H bond scissions were added with estimated rate constants of 1×10^{14} cm^3/mol s for the recombination of H-atoms with the DEE radicals. The DEE sub-mechanism has been added to the recently updated NUIG database [27] without any changes to ensure internal consistency. Reactions of most of the primary products (ethylene, acetaldehyde, ethanol, formaldehyde, etc.) are already included in the reaction base and decomposition reactions of ethyl vinyl ether have been taken from [24]. Reactions of some products involved in low-temperature oxidation were newly added, and high-pressure limiting rate constants were used for unimolecular initiation

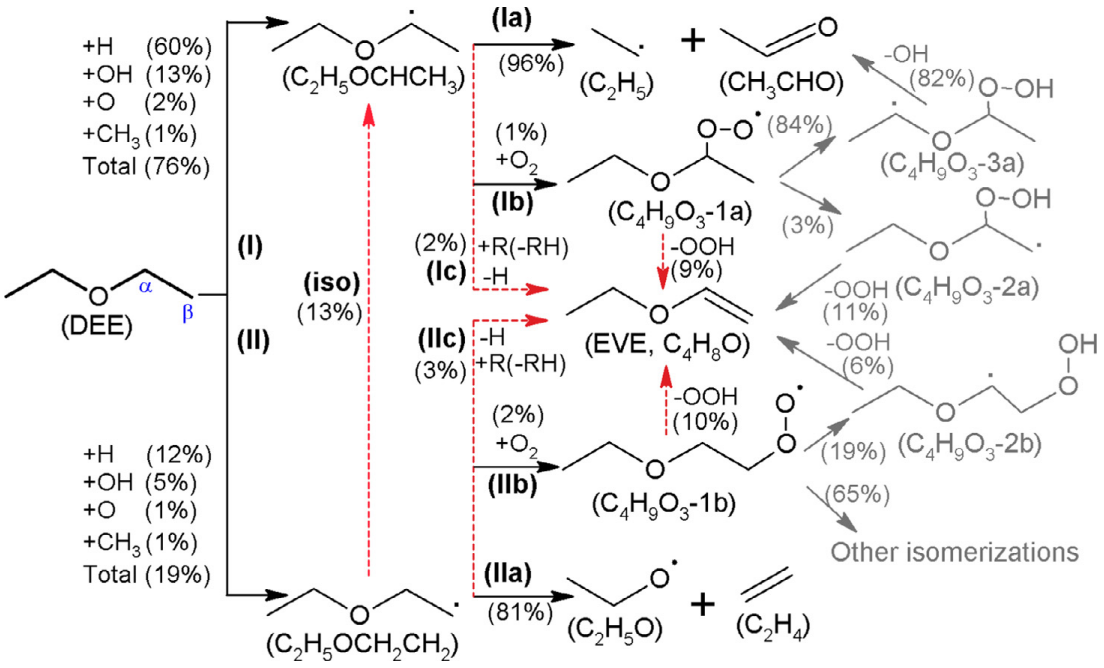

Fig. 1. Important DEE reaction pathways. Percentages given are relative rates of consumption of a species in the present low-pressure flame, analyzed in the region of 0–100% fuel conversion. Pathways indicated by dashed lines were not considered in the Yasunaga model [5].

reactions. However, previous work [24] demonstrated that the latter reaction class has minor importance under premixed flame conditions. Moreover, successions of H-abstractions/β-scissions of low-temperature oxidation products were written as irreversible since the reverse rate constants cannot be calculated from the global equilibrium constants. Transport properties of species for which no data is available in the literature were estimated based on the correlations proposed by Wang and Frenklach [28]. The complete reaction mechanism for DEE combustion includes 2385 elementary reactions among 380 chemical species and is available in CHEMKIN format together with thermodynamic and transport properties in Supplemental Material 2.

Prior to applying the newly developed kinetic model to simulate the current experimental data, it was tested against several datasets published in the literature, measured in non-premixed flames [6], pyrolysis experiments [5], and including ignition delay times [4,5] and flame speeds [7], with encouraging results (see Supplemental Material 1, Section S.I.2.). Simulations were performed using CHEMKIN [15] for premixed flames and OpenSMOKE++ [29] for other configurations.

3. Results and discussion

3.1. Species profiles in premixed low-pressure flame

In this study, more than 40 species, including reactants, products, stable intermediates, and radical species, were identified and quantified. Temperature and mole fraction profiles of the main species (DEE, O_2, Ar, CO, CO_2, H_2O, and H_2) as a function of the distance above the burner (h) as well as species mole fractions with the respective calibration method, electron energy, and literature ionization threshold for each intermediate are available in Supplemental Material 1, Fig. S12 and Table S4. Isomer identification is provided in Section S.II.2. Fig. S12 shows that DEE is fully consumed at $h > 3.5$ mm. The mole fractions of the main species at $h = 30$ mm are close to equilibrium values.

In the following, we discuss selected intermediate species, with a special focus on primary species, defined as those produced directly from the fuel or from its radicals. The discussion includes the comparison of experiments and predictions by the present kinetic model and that of Yasunaga et al. [5] and analyzes the degradation pathways of DEE together with the formation of intermediates. Figs. 2–4 display mole fraction profiles of selected labile and stable intermediates in the range of C_1–C_6. Overall, they show reasonable agreement, especially with respect to the peak locations and profile shapes, between experiment and predictions by both models. Note that the present model predicts also well the pyrolysis and ignition delay time data of Yasunaga et al. [5] as mentioned earlier.

The performance of the present model can be further analyzed regarding the degradation pathways of DEE. Fig. 1 includes a rate-of-production (ROP) analysis with this model for DEE consumption, globally performed in the region of 0–100% fuel conversion. Under these conditions, H-abstraction reactions are responsible for ~95% of

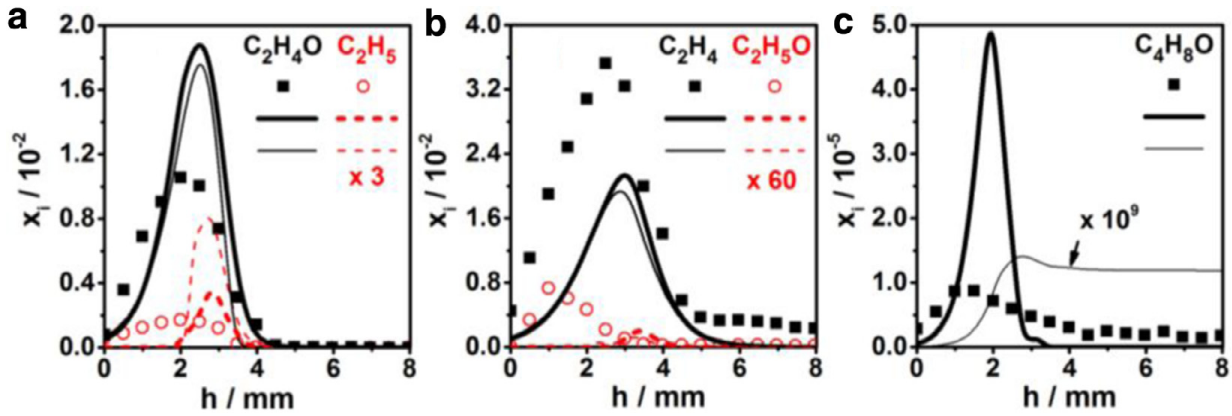

Fig. 2. Mole fraction profiles of "direct" primary species: C_2H_5, C_2H_4O, C_2H_4, C_2H_5O, C_4H_8O. Symbols: experiment, thick lines: present model, thin lines: Yasunaga model [5]. For clarity, the indicated multiplication factors have been used (for experiments and both models) for C_2H_5 and C_2H_5O.

total DEE consumption. H-abstractions by flame-propagating radicals mainly (~76%) occur at the $C_{-\alpha}$ position of DEE (see Fig. 1) because of its lowest C–H bond energy (96 kcal/mol), yielding the $C_2H_5OCHCH_3$ radical. H-abstractions from the $C_{-\beta}$ positions (C–H bond energy of 103 kcal/mol) producing the $C_2H_5OCH_2CH_2$ radical account for ~19% of total DEE consumption. Both fuel radicals, *i.e.* $C_2H_5OCHCH_3$ and $C_2H_5OCH_2CH_2$, react largely by C–O bond β-scission leading to the formation of acetaldehyde (CH_3CHO) + ethyl (C_2H_5) and ethylene (C_2H_4) + ethoxy (C_2H_5O), respectively. Another fraction of these two fuel radicals is consumed by oxidation, disproportionation, and C–H bond β-scissions producing EVE, which is consumed by H-abstraction and retro-ene reactions. Note that the four-centered elimination DEE(+M)→C_2H_5OH+C_2H_4(+M) (not shown in Fig. 1) plays only a minor role (<2%) in DEE consumption in the present low-pressure flame.

Species produced directly from the two DEE radicals via β-scissions (here called "direct" primary intermediates) are presented in Fig. 2. C_2H_4O and C_2H_4 were measured with very high mole fractions of 1.05×10^{-2} and 3.53×10^{-2}, respectively. By VUV-PI-MBMS, C_2H_4O was identified as acetaldehyde (~95%) and vinyl alcohol (~5%), see Fig. S14. C_4H_8O (Fig. 2c) was evaluated as EVE and is present at lower concentration than C_2H_4O and C_2H_4. It is important to note that the photoionization efficiency (PIE) spectra of $m/z = 72$ from VUV-PI-MBMS show a clear onset near the IP of EVE (8.98 eV [21], see Fig. S14). Although the formation of EVE accounts for only ~5% of the consumption of the fuel radicals, this intermediate species is important because it is a primary fuel destruction product that was unambiguously identified for the first time in DEE combustion. C_2H_5 and C_2H_5O were detected at much lower concentrations (see Fig. 2) because of their high reactivity. However, their subsequent reactions contribute significantly to the formation of further important intermediates. C_2H_5 reacts with H to produce CH_3 that in turn reacts with H or HCO, contributing with ~55% to the formation of CH_4. The latter species was measured with a high mole fraction of 1.9×10^{-2}. Other reactions of C_2H_5 partially contribute to the formation of C_2H_4 (by C–H bond β-scission, oxidation, or disproportionation), C_2H_6 (by recombining with H-atom), C_3H_8 (by recombining with CH_3), and C_4H_{10} (by self-recombination). These species, which are presented in Fig. 3, are overall reasonably predicted by the present model. C_4H_{10} was identified by GC to be exclusively *n*-butane. C_2H_5O in turn decomposes mainly into formaldehyde (CH_2O) and CH_3 by C–O bond β-scission. The C_2H_5O radical also recombines with an H-atom to produce ethanol (C_2H_6O). Under the present flame conditions, these two pathways contribute significantly to the formation of formaldehyde (~60%) and ethanol (20%), respectively. Formaldehyde was detected with a high mole fraction of 1.2×10^{-2} (see Fig. 3e).

The mole fractions of several other C_1–C_6 products including radical and stable species are presented in Fig. 4. These species are produced mainly by secondary reactions, as supported by the ROP analysis from the kinetic model. The corresponding reactions are part of the base mechanism and not the focus of this work. Since acetaldehyde is a dominant primary species of DEE combustion, its decomposition contributes to the formation of several species, detected in the present flame, as discussed hereafter. Methanol (CH_4O) with a measured mole fraction of 7.9×10^{-4} (Fig. 4a) is mainly produced by the disproportionation reaction of two CH_3O, and by H-abstractions from acetaldehyde by CH_3O. The profile of C_3H_6O is also shown in Fig. 4a as a sum of propanal and acetone; both isomers were identified by VUV-PI-MBMS.

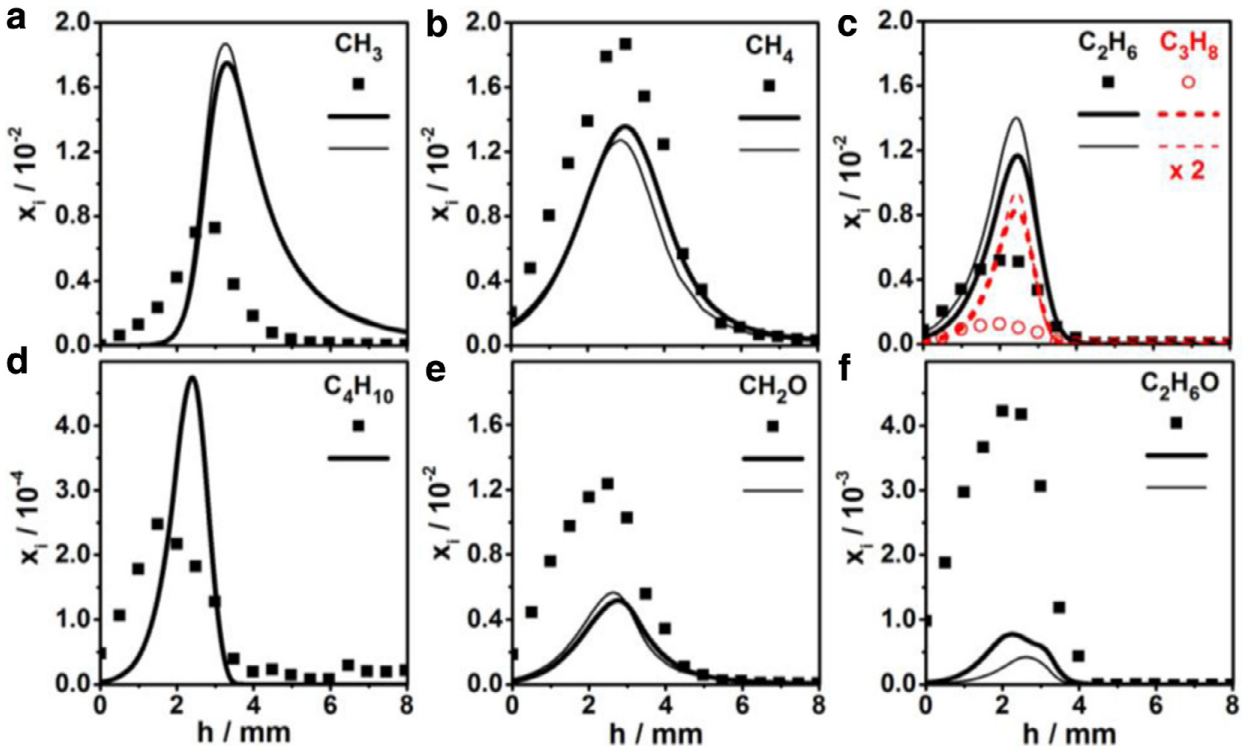

Fig. 3. Mole fraction profiles of further important species: CH_3, CH_4, C_2H_6, C_3H_8, C_4H_{10}, CH_2O, C_2H_6O. Symbols: experiment, thick lines: present model, thin lines: Yasunaga model [5]. For clarity, a multiplication factor of 2 has been used (for experiments and both models) for C_3H_8.

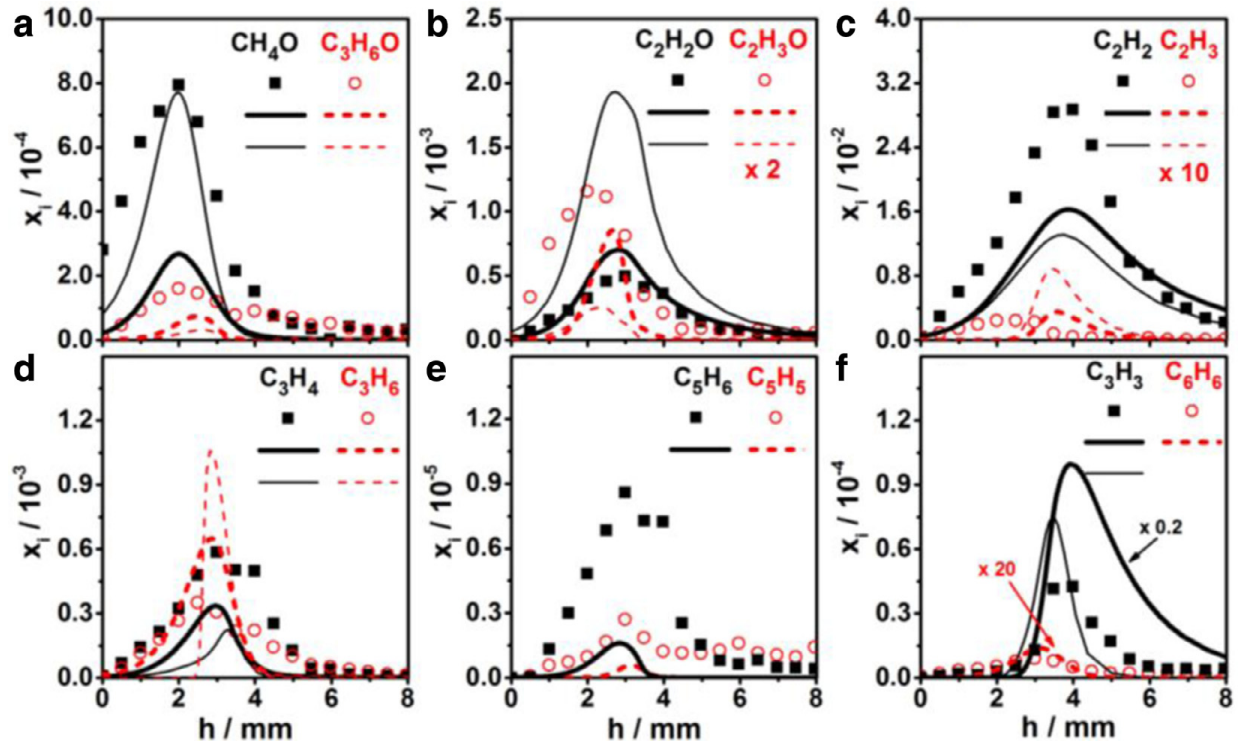

Fig. 4. Mole fraction profiles of other labile and stable intermediates in the C_1–C_6 range. Symbols: experiment, thick lines: present model, thin lines: Yasunaga model [5]. For clarity, the indicated multiplication factors have been used (for experiments and both models) for some species, with the exception of C_3H_3 and C_6H_6 for which only the simulation with the present model was multiplied by 0.2 and 20 respectively.

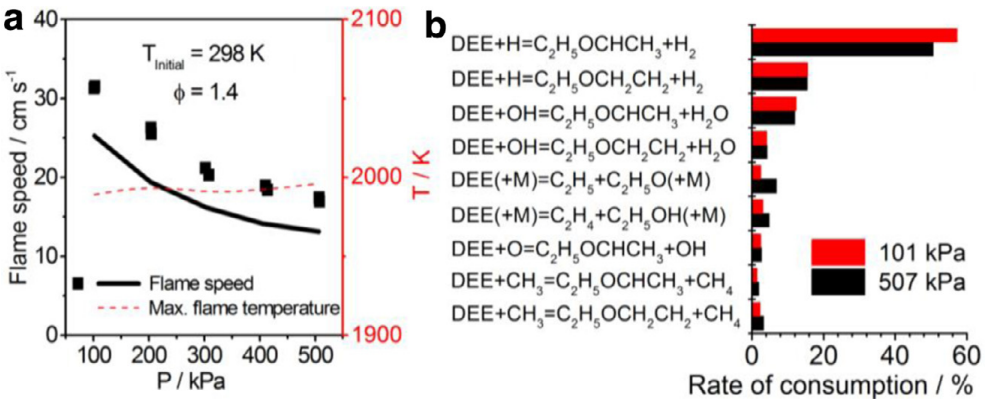

Fig. 5. (a) Flame speeds of DEE and related maximum flame temperature. Symbols: experiment, lines: present model. (b) Relative consumption rates of DEE at 101 and 507 kPa.

According to the model, the formation of propanal and acetone mainly results from combination of CH_3 with the acetaldehyde radicals CH_2CHO and CH_3CO (*i.e.* $CH_3+CH_2CHO \leftrightarrows C_2H_5CHO$, $CH_3+CH_3CO \leftrightarrows C_2H_6CO$). The profile for the sum of these acetaldehyde radicals (C_2H_3O) is presented in Fig. 4b, together with that for ketene (C_2H_2O) which is produced mainly from $CH_3CO+CH_3 \leftrightarrows C_2H_2O+CH_4$. The prediction for ketene is clearly better in the present model. Small C_2–C_6 soot precursors are also presented in Fig. 4. C_5H_6 (1,3-cylopentadiene), C_5H_5 (cylopentadienyl radical), and C_6H_6 (benzene), known as important cyclic soot precursors, were detected at low mole fractions ($<10^{-5}$), while smaller species including C_2H_2 (Fig. 4c), C_3H_4, and C_3H_6 (Fig. 4d) are present in the 10^{-2}–10^{-4} range. According to the GC analysis, allene and propyne are identified for C_3H_4 isomers with propyne as the most abundant one. C_4H_6 is for a large part 1,3-butadiene, and C_4H_8 is predominantly 1-butene. The present model also predicts these trends (see Table S5), while the Yasunaga model [5] does not include reactions for the formation of hydrocarbon species from C_4. Fig. 4f shows the peak location of C_6H_6 to be closer to the burner than that of C_3H_3 (propargyl). Although an under-prediction is noted for benzene, the model represents this trend in peak locations, indicating that the main route of benzene formation is likely not propargyl recombination. Benzene is predicted to be largely produced by the recombination of an H-atom and the C_6H_5 radical or C_3H_3 and C_3H_5 radicals. Because of its very low mole fraction ($<10^{-5}$), benzene was difficult to be well predicted by the present model (under-prediction by a factor of ~20), however, with higher concentrations, *e.g.* in sooting flames, its prediction could be expected to be improved.

3.2. Flame speeds at elevated pressure

To study the DEE high-temperature reaction chemistry at elevated pressures, flame speeds of DEE were measured at an initial temperature of 298 K for $\phi \sim 1.4$ at pressures of 101, 203, 304, 405, and 507 kPa. The results are presented in Fig. 5a along with predictions by the present kinetic model. The flame speed decreases with increasing pressure, a trend well captured by the present model which, however, under-predicts the absolute flame speeds by ~16%. The predicted flame temperature rises only slightly with increasing pressure. Sensitivity analyses (not shown) indicate that the kinetics of small species control the flame speed at all studied conditions. The chain-branching reaction of O_2 with H, producing OH and O ($O_2+H \leftrightarrows OH+O$) promotes the reactivity significantly, while the three-body termination reaction $H+CH_3(+M) \leftrightarrows CH_4(+M)$ has the largest effect on the reduction of flame propagation, especially at high pressures, since this reaction reduces the H-atom concentration and competes with the former. No large sensitivity was seen for the primary reactions involving DEE decomposition and oxidation. Hence, the observed deviations between model and experiment could result from uncertainties in the small-species kinetics in the base mechanism and/or in the experiment. Note that the present model well predicts the flame speed data by Gillespie et al. [7] (Fig. S11). Different uncertainties of the two setups and different sensitivities of the model under the two different inlet conditions could contribute to the noted discrepancies.

The ROP analysis in Fig. 5b indicates that a large part of DEE is consumed by H-abstractions by flame-propagating radicals, especially with H and OH. This trend is similar to that observed in the low-pressure flame described earlier. Note that the contribution of the four-centered elimination $DEE(+M) \rightarrow C_2H_4+C_2H_5OH(+M)$ and the C–O bond scission $DEE(+M) \rightarrow C_2H_5+C_2H_5O(+M)$ to the DEE consumption increases with increasing pressure, suggesting that the distribution of ethanol and acetaldehyde will change with pressure.

4. Summary

The high-temperature combustion chemistry of DEE was investigated experimentally with a focus on obtaining quantitative species profiles at flame conditions. More than 40 species were identified and quantified in a low-pressure fuel-rich ($\phi \sim 1.8$) premixed flame using EI-MBMS-GC, complemented with VUV-PI-MBMS. The data provides a good basis for model development and examination. Furthermore, high-pressure flame speeds of DEE were determined at an initial gas temperature of 298 K, at $\phi = 1.4$, from 101 to 507 kPa. The obtained experimental results were compared to predictions with a newly developed detailed kinetic model that contains systematically updated thermochemical and kinetic data from dedicated CBS-QB3 calculations. Reasonable agreement between experiment and predictions by the proposed mechanism was observed. Acetaldehyde, known as carcinogen for humans, was detected at high amounts, in agreement with the model prediction. It is seen to be largely produced from the dominant pathway of DEE consumption via H-abstractions followed by β-scissions. However, cyclopentadiene and benzene, known as important soot precursors, were measured at low mole fractions ($<10^{-5}$). The DEE flame speed was observed to decrease with increasing pressure, and it is affected strongly by the kinetic of small species. The present study demonstrates that at all pressures investigated, DEE consumption is mainly controlled by H-abstractions by H and OH and subsequent decomposition of the fuel radicals. Theoretical calculations were used in particular to determine reliable rate constants and branching ratios for these reactions. Among the unimolecular pathways, only the four-centered elimination and the C–O bond scission contributed to a minor degree to DEE consumption, and this contribution increases with pressure.

Acknowledgments

L.S.T. thanks the Alexander von Humboldt Foundation for a research fellowship. The authors thank their colleagues Y. Li, B. Yang, and their students for discussions and for their help and contribution to some PIE spectra using the PI-MBMS setup at National Synchrotron Radiation Research Center. Also we thank M. Zeng for participation in some of the simulations. Y.J. would like to thank the grant support of NSF CBET-1507358.

Supplementary materials

Supplementary material associated with this article can be found, in the online version, at doi:10.1016/j.proci.2016.06.087.

References

[1] K. Kohse-Höinghaus, P. Oßwald, T.A. Cool, T. Kasper, N. Hansen, F. Qi, C.K. Westbrook, P.R. Westmoreland, Angew. Chem. Int. Ed. 49 (21) (2010) 3572–3597.
[2] A. Paul, P.K. Bose, R. Panua, D. Debroy, J. Energy Inst. 88 (1) (2015) 1–10.
[3] D.C. Rakopoulos, C.D. Rakopoulos, E.G. Giakoumis, A.M. Dimaratos, *Energy* 43 (1) (2012) 214–224.
[4] M. Werler, L.R. Cancino, R. Schiessl, U. Maas, C. Schulz, M. Fikri, *Proc. Combust. Inst.* 35 (2015) 259–266.
[5] K. Yasunaga, F. Gillespie, J.M. Simmie, H.J. Curran, Y. Kuraguchi, H. Hoshikawa, M. Yamane, Y. Hidaka, *J. Phys. Chem. A* 114 (34) (2010) 9098–9109.
[6] J. Hashimoto, K. Tanoue, N. Taide, Y. Nouno, *Proc. Combust. Inst.* 35 (2015) 973–980.
[7] F. Gillespie, W.K. Metcalfe, P. Dirrenberger, O. Herbinet, P.-A. Glaude, F. Battin-Leclerc, H.J. Curran, *Energy* 43 (1) (2012) 140–145.
[8] Y. Di, Z. Huang, N. Zhang, B. Zheng, X. Wu, Z. Zhang, *Energy Fuels* 23 (5) (2009) 2490–2497.
[9] N. Zhang, Y. Di, Z. Huang, B. Zheng, Z. Zhang, *Energy Fuels* 23 (12) (2009) 5798–5805.
[10] M. Schenk, L. Leon, K. Moshammer, P. Oßwald, T. Zeuch, L. Seidel, F. Mauss, K. Kohse-Höinghaus, *Combust. Flame* 160 (3) (2013) 487–503.
[11] J.C. Biordi, *Prog. Energy Combust. Sci.* 3 (3) (1977) 151–173.
[12] X. Yang, D. Felsmann, N. Kurimoto, J. Krüger, T. Wada, T. Tan, E.A. Carter, K. Kohse-Höinghaus, Y. Ju, *Proc. Combust. Inst.* 35 (2015) 491–498.
[13] Z.Y. Zhou, Y. Wang, X.F. Tang, W.H. Wu, F. Qi, *Rev. Sci. Instrum.* 84 (1) (2013) 014101.
[14] D. Liu, J. Santner, C. Togbe, D. Felsmann, J. Koppmann, A. Lackner, X. Yang, X. Shen, Y. Ju, K. Kohse-Höinghaus, *Combust. Flame* 160 (12) (2013) 2654–2668.
[15] CHEMKIN-PRO 15092, *Reaction Design* (2009).
[16] R.S. Tranter, R.W. Walker, *Phys. Chem. Chem. Phys.* 3 (21) (2001) 4722–4732.
[17] S. Di Tommaso, P. Rotureau, O. Crescenzi, C. Adamo, *Phys. Chem. Chem. Phys.* 13 (32) (2011) 14636–14645.
[18] J. Zádor, C.A. Taatjes, R.X. Fernandes, *Prog. Energy Combust. Sci.* 37 (4) (2011) 371–421.
[19] Y. Sakai, H. Ando, H.K. Chakravarty, H. Pitsch, R.X. Fernandes, *Proc. Combust. Inst.* 35 (2015) 161–169.
[20] E. Goos, A. Burcat, B. Ruscic, available at <http://burcat.technion.ac.il/dir/>.
[21] NIST Chemistry WebBook, available at < http://webbook.nist.gov/chemistry/>.
[22] H.J. Curran, P. Gaffuri, W.J. Pitz, C.K. Westbrook, *Combust. Flame* 114 (1–2) (1998) 149–177.
[23] S.M. Sarathy, S. Vranckx, K. Yasunaga, M. Mehl, P. Oßwald, W.K. Metcalfe, C.K. Westbrook, W.J. Pitz, K. Kohse-Höinghaus, R.X. Fernandes, H.J. Curran, *Combust. Flame* 159 (6) (2012) 2028–2055.
[24] L.-S. Tran, R. De Bruycker, H.-H. Carstensen, P.-A. Glaude, F. Monge, M.U. Alzueta, R.C. Martin, F. Battin-Leclerc, K.M. Van Geem, G.B. Marin, *Combust. Flame* 162 (11) (2015) 4283–4303.

[25] G. da Silva, J.W. Bozzelli, L. Liang, J.T. Farrell, *J. Phys. Chem. A* 113 (31) (2009) 8923–8933.
[26] C.-W. Zhou, J.M. Simmie, H.J. Curran, *Phys. Chem. Chem. Phys.* 12 (26) (2010) 7221–7233.
[27] S.M. Burke, W. Metcalfe, O. Herbinet, F. Battin-Leclerc, F.M. Haas, J. Santner, F.L. Dryer, H.J. Curran, *Combust. Flame* 161 (11) (2014) 2765–2784.
[28] H. Wang, M. Frenklach, *Combust. Flame* 96 (1-2) (1994) 163–170.
[29] A. Cuoci, A. Frassoldati, T. Faravelli, E. Ranzi, *Comput. Phys. Commun.* 192 (2015) 237–264.

ANHANG D

Publikation 4

L.S. Tran, J. Pieper, M. Zeng, Y. Li, X. Zhang, W. Li, I. Graf, F. Qi, K. Kohse-Höinghaus

Influence of the biofuel isomers diethyl ether and *n*-butanol on flame structure and pollutant formation in premixed *n*-butane flames

Combustion and Flame **175**, 47-59, 2017
DOI: 10.1016/j.combustflame.2016.06.031[1]

Abstract

Diethyl ether (DEE) and its isomer *n*-butanol are both considered as promising fuel additives or neat biofuels. While some effects of their addition to hydrocarbon fuels under engine conditions have been reported, fundamental studies that aim at understanding the joint reaction pathways of such fuel mixtures remain quite scarce. Here, we have chosen *n*-butane as a well-studied hydrocarbon base fuel, and we have added these oxygenated isomers individually under identical conditions in premixed low-pressure flames. Different combustion behavior of the respective alkane-biofuel mixtures must then be related to the fuel structure. Analyses were performed in five fuel-rich flames including flames of *n*-butane, DEE, and *n*-butanol as well as two flames of *n*-butane doped with 50% DEE or 50% *n*-butanol. In this series, the carbon-to-oxygen ratio, argon dilution, pressure, and gas velocity were kept constant. More than 40 species in the range of C_0-C_8 were identified and quantified in each flame by electron ionization (EI) molecular-beam mass spectrometry (MBMS) coupled with gas chromatography (GC). The experiments were partially complemented by tunable synchrotron vacuum ultraviolet (SVUV) photoionization (PI)-MBMS. To assist in the interpretation of the data, a kinetic model was established by combining different sub-mechanisms for these fuels available in the literature. As expected, the formation of toxic carbonyls, such as formaldehyde and acetaldehyde, increased significantly upon addition of both oxygenated fuels to *n*-butane. Blending *n*-butane with DEE noticeably reduces the formation of soot precursors, because primary reactions of DEE mainly release C_1-C_2 hydrocarbon species to the system. *n*-Butanol addition, however, shows no significant reduction effects or even higher formation of soot precursors. These trends were observed both in the experiments and model predictions, and the higher ability of *n*-butanol to form

1 Zu dieser Publikation ist Supplemental Material online unter http://doi.org/10.1016/j.combustflame.2016.06.031 verfügbar.

soot precursors compared to DEE indeed results mainly from the differences in the fuel structure.

Combustion and Flame 175 (2017) 47–59

Contents lists available at ScienceDirect

Combustion and Flame

journal homepage: www.elsevier.com/locate/combustflame

Influence of the biofuel isomers diethyl ether and *n*-butanol on flame structure and pollutant formation in premixed *n*-butane flames

Luc-Sy Tran[a], Julia Pieper[a], Meirong Zeng[a,c], Yuyang Li[b], Xiaoyuan Zhang[b], Wei Li[c], Isabelle Graf[a], Fei Qi[b,*], Katharina Kohse-Höinghaus[a,**]

[a] Department of Chemistry, Bielefeld University, Universitätsstraße 25, D-33615 Bielefeld, Germany
[b] Key Laboratory for Power Machinery and Engineering of MOE, Shanghai Jiao Tong University, Shanghai 200240, PR China
[c] National Synchrotron Radiation Laboratory, University of Science and Technology of China, Hefei, Anhui 230029, PR China

ARTICLE INFO

Article history:
Received 25 February 2016
Revised 31 May 2016
Accepted 1 June 2016
Available online 27 July 2016

Keywords:
Biofuel
DEE
n-butanol
n-butane
Molecular-beam mass spectrometry
Kinetic model

ABSTRACT

Diethyl ether (DEE) and its isomer *n*-butanol are both considered as promising fuel additives or neat biofuels. While some effects of their addition to hydrocarbon fuels under engine conditions have been reported, fundamental studies that aim at understanding the joint reaction pathways of such fuel mixtures remain quite scarce. Here, we have chosen *n*-butane as a well-studied hydrocarbon base fuel, and we have added these oxygenated isomers individually under identical conditions in premixed low-pressure flames. Different combustion behavior of the respective alkane-biofuel mixtures must then be related to the fuel structure. Analyses were performed in five fuel-rich flames including flames of *n*-butane, DEE, and *n*-butanol as well as two flames of *n*-butane doped with 50% DEE or 50% *n*-butanol. In this series, the carbon-to-oxygen ratio, argon dilution, pressure, and gas velocity were kept constant. More than 40 species in the range of C_0–C_8 were identified and quantified in each flame by electron ionization (EI) molecular-beam mass spectrometry (MBMS) coupled with gas chromatography (GC). The experiments were partially complemented by tunable synchrotron vacuum ultraviolet (SVUV) photoionization (PI)-MBMS. To assist in the interpretation of the data, a kinetic model was established by combining different sub-mechanisms for these fuels available in the literature. As expected, the formation of toxic carbonyls, such as formaldehyde and acetaldehyde, increased significantly upon addition of both oxygenated fuels to *n*-butane. Blending *n*-butane with DEE noticeably reduces the formation of soot precursors, because primary reactions of DEE mainly release C_1–C_2 hydrocarbon species to the system. *n*-Butanol addition, however, shows no significant reduction effects or even higher formation of soot precursors. These trends were observed both in the experiments and model predictions, and the higher ability of *n*-butanol to form soot precursors compared to DEE indeed results mainly from the differences in the fuel structure.

1. Introduction

More than 90% of fuels consumed world-wide today are petroleum-based. The demand for transportation energy is rising, and most of this increase comes from heavy-duty-diesel vehicles [1]. As is well known, soot emissions are an important problem of diesel engines. Soot from fuel combustion has been demonstrated to contribute to respiratory dysfunction, heart diseases, and lung cancer [2–4]. Efforts are made to understand the formation process of soot and its precursors and to develop new combustion technologies to reduce soot emissions. At the same time, the need to reduce greenhouse gas emissions continues to motivate research towards renewable fuels such as alcohols, esters, and ethers [5–7]. It has been shown that the addition of oxygenated compounds represented in biofuels to petroleum fuels is also a promising way to reduce soot emissions [8–10].

Diethyl ether (DEE, $C_4H_{10}O$) can be produced via dehydration of ethanol over solid acid catalysts and is being proposed as a promising biofuel [11–13]. Because of several favorable properties for diesel engines, including a high cetane number (~125), a more favorable lower heating value (LHV) of 33.9 MJ kg^{-1} than that of dimethyl ether (28.6 MJ kg^{-1}), broad flammability limits, and high miscibility with diesel fuel, DEE has recently been examined as an additive to diesel fuel [11–13]. Moreover, DEE is being considered as an excellent ignition improver for homogeneous charge compression ignition (HCCI) engines operated with biogas or liquefied petroleum gas (LPG) [14,15]. In view of these interesting properties,

* Corresponding author.
** Corresponding author. Fax: +49 521 106 6027.
E-mail addresses: fqi@sjtu.edu.cn (F. Qi), kkh@uni-bielefeld.de (K. Kohse-Höinghaus).

http://dx.doi.org/10.1016/j.combustflame.2016.06.031
0010-2180/

the combustion chemistry of DEE in fundamental experimental setups has been increasingly investigated, including analysis of ignition delay times [16,17], flames [18,19], and flame speeds [19,20].

n-Butanol, an alcohol and isomer of DEE, can be produced via fermentation processes [21,22] and has been proposed as an alternative to conventional fuels [23], with a high LHV (~33.1 MJ kg^{-1}) and research octane number (~96) [7]. *n*-Butanol was studied as a fuel or as a blending agent for use in spark ignition engines [24,25] as well as in diesel and HCCI engines [26–29]. A large number of fundamental studies on the combustion chemistry of *n*-butanol have reported ignition delay times [30–32], species profiles in premixed [33,34] and non-premixed flames [18,35], and flame speeds [35,36], to name only some. A very detailed compilation of previous studies on this fuel can be found in the review article on alcohol combustion chemistry by Sarathy et al. [37].

Only a few comparative studies have recently become available that evaluated the influence of DEE and *n*-butanol addition on the performance and combustion characteristics of engines [13,38,39]. Rakopoulos [39] pointed out that with increasing percentage (up to 24 vol%) of DEE and *n*-butanol in blends with diesel, smoke opacity, NO_x, and CO were reduced, whereas unburned hydrocarbon emissions increased. Trends regarding DEE and *n*-butanol addition were quite similar, with *n*-butanol showing a slightly better smoke reduction. Opposite effects were noted under the conditions of [38] where DEE showed a more efficient smoke reduction, similar to the results by Imtenan et al. [13] for diesel and jatropha biodiesel upon DEE or *n*-butanol addition, with a reduction of smoke opacity of up to 27% by 10% addition of *n*-butanol and up to 38.5% when adding the same amount of DEE.

To the best of our knowledge, fundamental studies that aim to understand the cooperative combustion pathways in hydrocarbon fuel mixtures blended with these two isomeric oxygenated fuels are not yet available in the literature. We have thus studied the influence of the addition of DEE and *n*-butanol to *n*-butane on the reaction pathways and species pool under premixed low-pressure flame conditions to enhance the understanding of such systems.

2. Experiments

The experiments were performed in laminar premixed flat low-pressure flames using a combination of electron ionization molecular-beam mass spectrometry coupled with a gas chromatograph (EI-MBMS-GC) in Bielefeld as described in [40–42], complemented with synchrotron vacuum ultraviolet photoionization molecular-beam mass spectrometry (SVUV-PI-MBMS) measurements in Hefei following the procedures in [43–46], to provide a detailed chemical analysis of stable and reactive species together with isomer identification. The use of two different analysis techniques is particularly useful since it allows an independent confirmation of the species concentrations quantified in both studies.

2.1. Flame conditions

Five fuel-rich flames, *i.e.* *n*-butane/oxygen/argon (ϕ = 1.7), *n*-butane/DEE/oxygen/argon (ϕ = 1.75), *n*-butane/*n*-butanol/oxygen/argon (ϕ = 1.75), DEE/oxygen/argon (ϕ = 1.8), and *n*-butanol/oxygen/argon (ϕ = 1.8) were investigated. Fuel-rich conditions were chosen to obtain quantifiable amounts of higher-mass soot precursor species to analyze potential interaction effects from the species pools generated by the two different fuel classes in flames of fuel mixtures. These flames were stabilized on a home-made flat burner of 64 mm diameter (Bielefeld) at identical pressure (4 kPa), argon dilution (25%), cold gas velocity (73 cm s^{-1} at 333 K and 4 kPa), and C/O ratio (0.52), resulting in slightly different equivalence ratios ϕ. Note that data obtained in the DEE/oxygen/argon flame was partially included in our previous study to test a newly-developed DEE model [19]. Because experimental data for flames containing DEE is still scarce, the DEE/oxygen/argon and *n*-butane/DEE/oxygen/argon flames were also analyzed under similar conditions at the National Synchrotron Radiation Laboratory in Hefei using SVUV-PI-MBMS to enhance the reliability of the data. There, flames were stabilized on a commercial stainless steel McKenna burner of 60 mm diameter. In both experiments, calibrated mass-flow controllers established the gas flows; liquid fuels were metered by a syringe pump, evaporated at 343–433 K, and added to the gas stream. Flow rates were adapted to obtain near-identical mass flux. Both burners were cooled with water at a constant temperature of 333 K. Table 1 summarizes all flame conditions, and it also introduces abbreviated names for all flames that will be used in the following sections. Centerline species profiles were measured as a function of height above the burner *h* using the two MBMS setups described in the following section.

2.2. Measurement procedures

2.2.1. EI-MBMS-GC experiment

A detailed description of the EI-MBMS-GC system can be found elsewhere [40–42]. In brief, gas samples were extracted from the flame by a quartz cone (0.3 mm orifice, 25° included angle) which leads to an immediate quenching of the reaction due to the expansion of the sample into the first pumping stage chamber (10^{-5} kPa). This preserves the gas composition of the sample and enables the detection of reactive species such as radicals. The so-formed molecular beam is then skimmed by a home-made copper skimmer and passed into the ionization chamber (10^{-7} kPa). Here the sample is crossed with a pulsed electron beam (10^9 electrons/pulse) emitted by a tungsten filament of a two-stage Wiley-McLaren ion source. The generated ions were extracted into a time-of-flight mass analyzer, energetically focused by a reflectron, then detected with a multichannel plate and counted with a multichannel scaler. This setup (Kaesdorf) enables high mass resolution of $m/\Delta m$ ~4000 so that the exact elemental composition of C/H/O can be determined for each species. Soft ionization energies (10.0, 11.5, 13.0 eV for intermediates, 16.0 and 18.0 eV for major species) were used to minimize undesired fragmentation. Measured ion signals were integrated by fitting Gaussian-shaped curves to the signal peaks. Integrated signals were corrected for fragment ions originating from the fuel itself and from intermediate species for which a fragmentation pattern was obtained from cold-gas measurements. Isotope corrections of ^{13}C and ^{18}O contributions were also performed when necessary.

The coupled gas chromatograph enabled the identification of stable isomers. To ensure direct compatibility of pure MBMS measurements and GC-MBMS measurements, sampling was performed directly from the flame environment. A low-pressure sampling interface allowed transfer of a gas sample from the first pumping stage into the high-pressure environment of the GC (130 kPa). Here a temporal separation was performed with an Alumina BOND/Na_2SO_4 column (Restek GmbH) and an appropriate temperature program (323 K hold for 2.5 min, heating rate 293 K min^{-1} to 473 K, hold for 10 min), leading to a reasonable separation of hydrocarbons in the C_1–C_6 range. The outlet of the column was connected to the ionization chamber so that full mass spectra could be recorded as a function of the retention time. This simplifies the assignment of occurring signals as chromatograms can be obtained for each specific nominal mass. This procedure therefore presents a significant advantage here over classical FID detection. Spectra were averaged for 3.2 s (0.05 min) to improve the signal-to-noise ratio but keep a maximum of time resolution. A resolving power of 1.00 was achieved for *trans*-2-butene and 1-butene, which corresponds to a FWHM (full width at half maximum) of 0.05 min

Table 1
Flame conditions. SLM: standard liter per minute, ṁ: inlet mass flux.

Flame (abbreviated name)	Gas flow rate (SLM)					ṁ (g cm^{-2} s^{-1})	Ratio		ϕ
	Ar	O_2	DEE	*n*-Butanol	*n*-Butane		C/H	C/O	
n-Butane (Bu)	1.14	2.71	0.00	0.00	0.71	0.004013	0.40	0.52	1.70
n-Butane/DEE (Bu/DEE)[a]	1.14	2.67	0.37	0.00	0.37	0.004174	0.40	0.52	1.75
	1.00	2.35	0.33	0.00	0.33	0.004174	0.40	0.52	1.75
DEE (DEE)[a]	1.14	2.63	0.79	0.00	0.00	0.004355	0.40	0.52	1.80
	1.00	2.31	0.70	0.00	0.00	0.004355	0.40	0.52	1.80
n-Butane/*n*-Butanol (Bu/BuOH)	1.14	2.67	0.00	0.37	0.37	0.004174	0.40	0.52	1.75
n-Butanol (BuOH)	1.14	2.63	0.00	0.79	0.00	0.004355	0.40	0.52	1.80

[a] Slightly different conditions with an Ar flow of 1.00 SLM were used in the PI-MBMS experiment.

for both signals. Retention times were measured with a precision of ± 0.10 min. The GC data evaluation followed routines previously described in [42]. Stable species were identified based on their individual retention times. Peak areas were integrated and normalized by the individual ionization cross sections of the isomers to obtain quantitative ratios.

2.2.2. SVUV-PI-MBMS experiment

Detailed descriptions of the apparatus can be found elsewhere [43–46]. In brief, this MBMS system includes modules devoted to sampling, ionization, ion transfer and detection. Flame species were sampled from the flame by a quartz nozzle (0.4 mm orifice, 30° included angle) to form a molecular beam. The molecular beam was then intersected and ionized by the tunable VUV synchrotron radiation with an energy-resolving power ($E/\Delta E$) of ~4000 and an average photon flux of $\sim 1.5 \times 10^{13}$ photons s^{-1}. The ions were transferred by an ion guide to a home-made reflectron time-of-flight mass spectrometer with a mass-resolving power ($m/\Delta m$) of ~2500. Ion detection and spectra recording system are similar to those in the EI-MBMS setup. Since all species of a nominal mass occur as a single peak, signals are integrated numerically. Corrections for contributions of ^{13}C and ^{18}O isotopes from other species are applied afterwards when necessary.

The methodology of species identification was previously reported in [44–46]. Structural isomers were distinguished by measuring photoionization efficiency (PIE) spectra, with uncertainties in the determination of ionization energies of ± 0.05 and ± 0.10 eV for strong and poor signal-to-noise ratio, respectively.

Isomer identification by SVUV-PI-MBMS together with that by GC described above have provided useful information for the evaluation of the EI-MBMS data, which was done using the cross section of the most dominant isomer.

2.2.3. EI- and PI-MBMS data evaluation

The evaluation of the molecular-beam experiment follows routines previously reported in [41–46]. For both experiments, ion signals were recorded as a function of their flight time and assigned to their exact mass by a second-order polynomial mass calibration. The integrated ion signal S_i of a species i is directly proportional to its mole fraction x_i, as described by Eq. (1).

$$S_i = x_i \cdot c \cdot SW \cdot D_i \cdot \varphi \cdot FKT(h) \cdot \int \sigma_i(E) \cdot f(E-\tau)\mathrm{d}\tau \qquad (1)$$

Here c is an instrument factor, SW is the number of summarized spectra (sweeps), D_i is the mass discrimination factor of species i, φ is the number of ionizing particles (electrons or photons), FKT is a temperature- and thus position-dependent sampling function, $\sigma_i(E)$ is the electron ionization or photoionization cross section of species i at the energy E, and $f(E\text{-}\tau)$ is the energy distribution of the ionizing particles with τ being the integration variable. Note that for the photoionization approach, due to a narrow energy distribution, the integral simplifies to $\sigma_i(E)$.

Eq. (1) can be simplified if the signal can be referenced to another species R (usually argon) of known mole fraction in the same measurement:

$$\frac{S_i}{S_R} = \frac{x_i}{x_R} \cdot \frac{D_i}{D_R} \cdot \frac{\int \sigma_i(E) \cdot f(E-\tau)\mathrm{d}\tau}{\int \sigma_i(E) \cdot f(E-\tau)\mathrm{d}\tau} = \frac{x_i}{x_R} \cdot k_{i/R}(E) \qquad (2)$$

Here the species-related terms can be condensed into a calibration factor k. For major species (namely, fuels, O_2, Ar, H_2, H_2O, CO, and CO_2), their mole fractions were determined in both experiments based on the elemental C, H, and O balances derived from the exhaust gas, also considering early reactant consumption at the burner surface from the inlet conditions. Associated errors in mole fractions of these major species are typically < 30%.

For intermediate species, as a consequence of the characteristics of the two ionization methods, different approaches were used for quantification of these species as described below.

The broad energy distribution of the electrons in the EI-MBMS experiment allows the detection of argon even at very low nominal ionization energies. Thus Eq. (2) can be used once the calibration factor for the specific, nominal electron energy is known. Calibration factors for intermediate species with argon as the reference ($k_{i/Ar}$) were obtained by direct cold-gas calibration measurements whenever stable gaseous cold-gas mixtures are feasible. In all other cases, calibration factors were estimated using either the relative ionization cross section method (RICS) [47], assuming the similarity of the shape of the electron ionization cross sections of structurally similar species, or the convolution of the literature ionization cross sections with the known energy distribution of the ionizing electrons [42]. Generally, the error is < 30% for directly calibrated species, and below a factor of 2 for species calibrated with the convolution procedure. For radicals for which the RICS method was used, the error is estimated to be in the range of factors of 2–4. Each species is associated with an individual absolute uncertainty. However, this uncertainty for a given species is identical for all measured flames and therefore, relative comparison of trends between the flames can be performed with significantly higher precision. Indeed, from four-fold repetition of flame measurements, the relative error between raw signal profiles was determined to be < 5%; however, when fuels are different, fragmentation correction processes could increase this value.

In the PI-MBMS experiment, SVUV-PI provides a very narrow and accurate ionization energy distribution. However, the reference species argon has a very high threshold (15.759 eV), its signal is not present in every scan, and thus a different quantification approach must be applied. Therefore, mole fractions were calculated from Eq. (1). For this calculation, the species-specific variables including cross section and mass discrimination factor as well as the sampling function, photon flux, and instrument factor must be known. Mass discrimination factors were determined experimentally. The product c·FKT(h) was obtained from the argon signal (measured at 16.64 eV) and mole fraction profiles from the major species calculation. When all necessary parameters of

Eq. (1) are known, the relationship is used to calculate the intermediate species mole fraction based on literature photoionization cross sections. The lowest available photon energy above the ionization threshold is used to determine the mole fraction profile to minimize undesired fragmentation. If more than one species is measured at a nominal mass, Eq. (1) is used in reverse to calculate and subtract signal contributions from species with lower ionization threshold. Typically the uncertainties are within 10% for major species, within 25% for intermediates with known photoionization cross sections (PICSs), many of which are available in the online database [48], and a factor of 2 for those with estimated PICSs.

The respective calibration method, electron/photon energy, ionization threshold, and references for the electron ionization and/or photoionization cross section for each intermediate species are summarized in Tables S1 and S2 (EI-MBMS experiment) and Table S3 (PI-MBMS experiment, compared to EI-MBMS) of Supplemental material 1. All experimentally obtained data is also presented in Supplemental material 3.

2.2.4. Flame temperature measurement

The temperature profiles of the flames in Bielefeld were determined based on the temperature dependence of the sampling rate through the probe orifice accounting for the distortion caused by the sampling cone. Assuming a constant pumping speed, the gas flow rate through the sampling orifice can be expressed by the pressure of the first-stage chamber (p_{1st}) [49]. This dependence is given by

$$p_{1st} = C \cdot \sqrt{\frac{\gamma}{\bar{M}T}} \cdot \left(\frac{2}{\gamma+1}\right)^{Z} \tag{3}$$

with $Z=(\gamma+1)/2(\gamma-1)$. $\overline{M}$ is the mean molar mass, γ is the adiabaticity coefficient (C_p/C_v), close to unity and therefore set equal to 1, and C is a temperature-independent device-specific constant. The latter parameter was determined by solving Eq. (3) using the exhaust gas temperature measured without the sampling cone by OH planar laser-induced fluorescence described previously [50].

The method used for flame temperature measurement in Hefei was previously described in [51]. Briefly, the temperature profiles were measured by a Pt-6%Rh/Pt-30%Rh thermocouple of 0.1 mm in diameter, coated with Y_2O_3–BeO anti-catalytic ceramic, and were corrected for the radiative heat loss and the cooling effects of sampling nozzle.

The uncertainty of the measured temperature is estimated to be ± 5%. The temperature profiles are used as input parameters in the flame model simulations without any shift between measurement and computation. Temperature profiles are available together with the experimental data sets in Supplemental material 3.

3. Kinetic model

To facilitate interpretation of the obtained experimental results and to elucidate potential interaction between the species pools from the different fuels in the mixtures, a kinetic model has been established by combining different sub-mechanisms available in the literature. The complete version of the model includes 2385 elementary reactions among 380 chemical species; it is available in CHEMKIN format together with thermodynamic and transport properties in Supplemental material 2.

The reaction database of the NUI-Galway group, recently given in [52,53], was used as a *core model*. This database has been generated in a hierarchical way, based on AramcoMech1.3 [54], and contains already reactions of C_0–C_6 species, including also the butane isomers. For those it has been validated against a lot of references [55–58]. Reactions of toluene and ethylbenzene [59] were additionally taken from the same group to keep consistency with the core model. To represent the combustion reactions of *n*-butanol and DEE, the sub-mechanism (136 reactions) of *n*-butanol proposed by Sarathy *et al.* [60], and that (142 reactions) for DEE recently developed by Tran et al. [19] were combined with the core model as such sub-mechanisms have not been included in the core model before. Rate constants as well as thermodynamic and transport properties in the original sub-mechanisms were used without any change to ensure internal consistency. Decomposition reactions of the fuel radicals of *n*-butane, DEE, and *n*-butanol produce some common primary species, such as CH_3, C_2H_4, C_2H_5 (for all three fuels), C_3H_6, and C_4H_8 (for *n*-butane and *n*-butanol), and their thermodynamic properties from the core model were used, noting that they are fortunately consistent between the three databases; primary species are defined here as those produced directly from the fuel or from fuel radicals. While it may already be challenging to assess uncertainties for a given simulation for one fuel with a well-described and validated model from the literature, we would like to point out here that different sources of the sub-mechanisms and the core model make it harder to quantify the uncertainty of the combined model.

The *n*-butanol [60] and DEE [19] mechanisms have been previously examined against several experimental results such as ignition delay times [16,17,30–32], data from premixed [33,34] and non-premixed flames [18,35], and flame speeds [20,36]. Note that before adding the sub-mechanisms of DEE and *n*-butanol, the core model described above has been tested against species profiles obtained in the present premixed *n*-butane flame with good agreement between simulations and experiments. As – to the best of our knowledge – there are no experimental data on the mixtures of *n*-butane with either DEE or *n*-butanol available in the literature, it was not possible to validate the combined model against other experimental data. In order to check influences of individual sub-mechanisms on each other, simulations were performed for the pure *n*-butane, DEE, and *n*-butanol flames using both the combined model and the respective individual model. In general, both simulations provided similar results (not shown in the paper). An exception is the formation of ethanol and its related radicals in the *n*-butanol simulations, for which increases of a factor of 3 and 30%, respectively, were noted when the DEE sub-mechanism was added. *n*-Butanal produced from *n*-butanol radicals isomerizes partially at high temperature to ethyl vinyl ether which decomposes into ethanol and acetylene by retro-ene reactions. The latter reaction was not included in the original *n*-butanol sub-mechanism, but it is present in the DEE sub-mechanism. Therefore, the addition of the DEE sub-mechanism affects the formation of ethanol in *n*-butanol simulations by the combined model. However, according to the model, ethanol is present with low mole fractions ($<3\times10^{-5}$) in flames containing *n*-butanol, and does not occur as primary species in the rate of production analysis of fuel decomposition; therefore it does not significantly affect the overall performance of the model.

It is important to note that this work does not attempt to propose a new comprehensive model, but it uses rather a single model version (in the following called the *present model*) to analyze the combustion of the studied C_4 fuels, including mixtures, in the present flame situation. Simulated results presented in following sections are obtained from this model. Simulations were performed using the PREMIX module of the CHEMKIN package [61] supplied with the inlet mass flux and composition, combustion-chamber pressure, and the measured temperature profile.

4. Results and discussion

In the following, flame temperatures and mole fraction profiles of major species will be presented (Section 4.1). Then, reaction

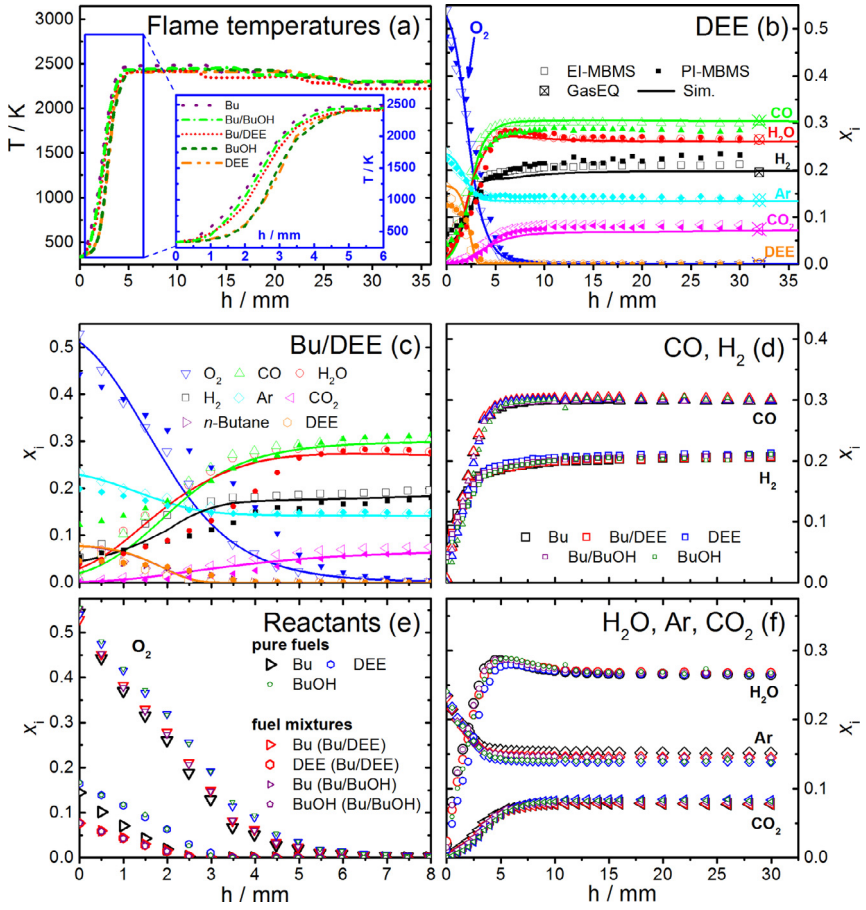

Fig. 1. (a) Flame temperatures (Bielefeld), (b) mole fraction x_i profiles of major species as a function of height above burner h in the DEE flame, (c) major species in the early stage (h = 0–8 mm) of the n-butane/DEE flame, (d–f) comparison of CO, H_2, reactants, H_2O, CO_2, and Ar profiles in the five flames. Open symbols in (b-f): EI-MBMS experiment, close symbols in (b,c): PI-MBMS experiment, lines in (b,c): present model simulation (using the temperature profiles measured in Bielefeld); open symbols with crosses indicated at h = 32 mm in (b) are equilibrium values.

pathways involved in flames of fuel mixtures and selected intermediates species profiles will be analyzed (Section 4.2). Finally, the influence of DEE and n-butanol addition on the formation of pollutants will be discussed in detail (Section 4.3).

4.1. Temperatures and major species

Figure 1 displays the temperature profiles measured in Bielefeld for the EI-MBMS experiment for the five flames as well as the mole fraction profiles of major species including reactants (n-butane, DEE, n-butanol, and O_2), diluent (Ar), and main products (CO, CO_2, H_2O, and H_2) as a function of height h. As seen in Fig. 1a, the stand-off distance of the flames increases in the order n-butane < mixtures < oxygenated fuels, reflecting the differences in flame speed. The maximum flame temperature slightly decreases in the order n-butane (2485 K) > mixtures (2420–2460 K) > oxygenated fuels (2420–2440 K). This trend is in good agreement with the sequence of their adiabatic temperatures (2600 K for the n-butane flame, 2566–2571 K for the mixture flames, and 2528–2540 K for the flames of the oxygenated fuels).

Synchrotron-based PI-MBMS measurements were performed in Hefei for some conditions to support the EI-MBMS analysis. Both experimental setups were completely independent, presenting slight differences in the flame stabilization and stand-off distances. The maximum temperatures measured in Bielefeld for the DEE and n-butane/DEE flames were found to be ~180 K higher than those measured in Hefei (available in Supplemental material 3). This deviation is a result mainly from the difference of the two flame setups and includes the experimental uncertainties of the two temperature measurement methods. Data from PI-MBMS experiments for DEE and n-butane/DEE flames are therefore added for comparison in Fig. 1 b,c (filled symbols). It can be noted that the flames are established at a slightly larger distance from the burner in the PI-MBMS experiment, as a result from the above-mentioned differences of the two setups, especially regarding the sizes of the burners and sampling probes.

Good agreement within experimental uncertainties is found between PI-MBMS and EI-MBMS data and the simulation for the major species. It should be noted in addition that simulations for the PI-MBMS experiment using the respective Hefei temperature profile (see Supplemental material 4) present similarly good agreement to the Hefei experimental data, both with regard to the profile position and mole fraction value. This behavior indicates that the quality of the agreement between experiments and simulations does not vary with the differences of the two used setups, showing that the effects of the different probes and burners are mainly thermal and that catalytic effects, wall reactions, or residual reactions in the probe should be of minor importance.

The mole fractions of major species at h = 30 mm shown in Fig. 1b are very close to equilibrium values (open symbols with cross) calculated using Gaseq [62] for the respective flame temperature. A comparison of the structure of all five flames is given in Fig. 1 d–f, demonstrating that the trends of these major species profiles are generally similar as a result of using an identical C/O ratio for all flames. Differences in mole fraction profiles of reactants (fuels and O_2) in Fig. 1e reflect respective differences in

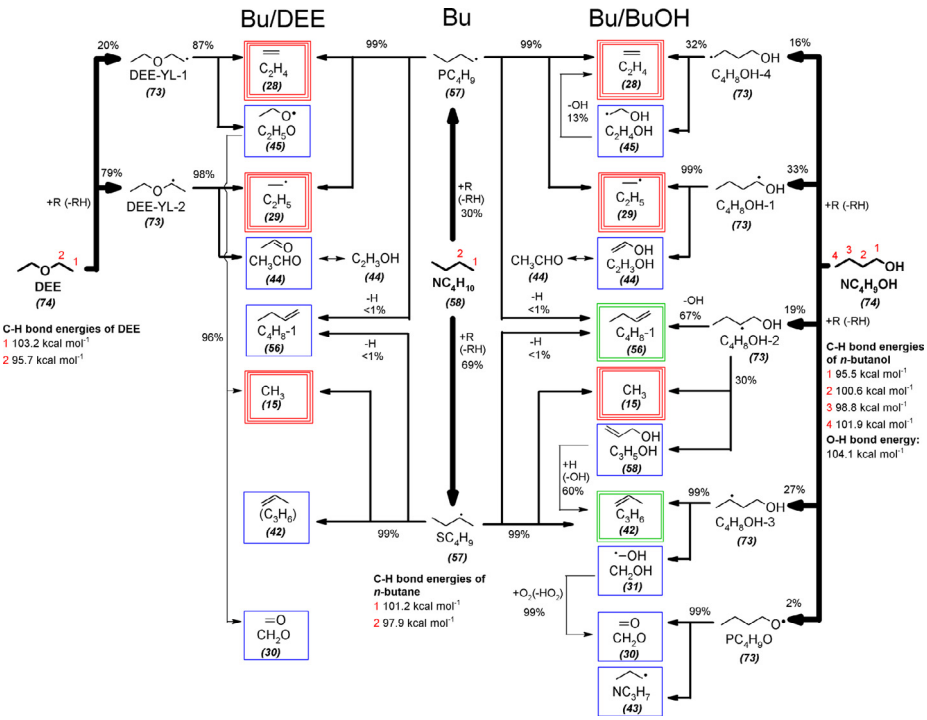

Fig. 2. Rate of production analysis for the consumption of *n*-butane (NC_4H_{10}), DEE, and *n*-butanol (NC_4H_9OH) in the mixture flames ($\phi = 1.75$) for a distance h~2.1–2.2 mm corresponding to a temperature of ~1100 K and ~78% of fuel conversion. Percentages are relative rates of consumption of a given species. Species bordered by triple, double, or single lines are primary species of all three fuels, of two fuels (*n*-butane and either oxygenated fuel), or of one fuel, respectively. Line thicknesses indicate specific reaction steps (thick: H-abstractions from fuels, intermediate: β-scissions from fuel radicals, thin: further reactions from primary species). While isomerization reactions of fuel radicals occur, these are not indicated for clarity. Respective bond energies are shown for DEE [19], *n*-butane (calculated from the thermodynamic data used in the present model), and *n*-butanol [60].

initial inlet composition, necessary to match the identical C/O ratio (compare Table 1).

4.2. Composition of the intermediate species pools

More than 40 intermediates, including stable and radical species as well as different isomers, were identified and quantified in each flame. The peak mole fractions for important intermediate species are summarized in Tables S1–S3 of Supplemental material 1. The full datasets are available in Supplemental material 3. In the following, we concentrate on reporting important examples of species involved during the combustion/co-combustion of *n*-butane, DEE, and *n*-butanol in the present flame situation.

4.2.1. Fuel destruction and primary species

To gain insight into the decomposition pathways of the studied C_4 fuels in the mixture flames and to elucidate differences and similarities in the composition of primary species when adding the different oxygenated isomers to *n*-butane, rate of production analyses (ROP) are presented in Fig. 2. These analyses were performed using the present model to simulate the *n*-butane/DEE and *n*-butane/*n*-butanol flames at h~2.1–2.2 mm, corresponding to a temperature of ~1100 K and ~78% of fuel conversion.

To emphasize common features as well as differences between the mixture components and their decomposition products, Fig. 2 uses differently coded boxes to highlight primary species shared by all three fuels (triple line), by the base fuel and one oxygenated additive (double line), and those highlighted with a single line are not shared between the base fuel and either oxygenated additive.

As can be seen, H-abstractions by flame-propagating radicals (R) are responsible for approximately 99% of the total consumption of *n*-butane, DEE, and *n*-butanol under these flame conditions. Unimolecular initiation reactions including the dehydration of *n*-butanol (i.e. four-center elimination of water) play only minor roles (<1%) at the ROP analysis conditions and are therefore not shown in Fig. 2. However, at locations further from the burner where temperatures are higher, the dehydration of *n*-butanol becomes important and contributes partly to the formation of 1-butene as discussed below. In the case of *n*-butane and DEE, H-abstraction reactions mainly occur at C2 positions followed by those from C1 positions (Fig. 2), which is consistent with the difference in the dissociation energies of C–H bonds between C2 (95.7–97.9 kcal mol^{-1}) and C1 (101.2–103.2 kcal mol^{-1}) positions (see Fig. 2). In the case of *n*-butanol, given its asymmetry, H-abstractions can produce five different fuel radicals (C_4H_8OH-1, C_4H_8OH-2, C_4H_8OH-3, C_4H_8OH-4, PC_4H_9O), with the most important H-abstraction occurring at C1 position because of its lowest C-H bond energy (95.5 kcal mol^{-1} [60]). Subsequent decomposition of butyl radicals (PC_4H_9, SC_4H_9) releases only hydrocarbon species, i.e. predominantly C_1–C_3 species including methyl (CH_3), ethylene (C_2H_4), ethyl (C_2H_5), and propene (C_3H_6). C_4 hydrocarbon species including 1-butene (C_4H_8-1) and 2-butene (not shown in Fig. 2) are also primary species but are formed by very minor channels (<1%) of the *n*-butane radical consumption. When adding DEE to *n*-butane, the composition of primary species will be modified because the decomposition of the DEE radicals (DEE-YL-1, DEE-YL-2) leads to the simultaneous formation of both hydrocarbon and oxygenated species. Specifically, C-C β-scission of the DEE-YL-1 radical yields C_2H_4 and the ethoxy radical (C_2H_5O) which in turn decomposes into formaldehyde (CH_2O) and CH_3, while decomposition of the DEE-YL-2 radical produces C_2H_5 and acetaldehyde (CH_3CHO). DEE reactions mainly yield species smaller than C_3, while C_3 hydrocarbons are dominant primary species of *n*-butane decomposition. Therefore, DEE addition will decrease hydrocarbon species with three and more carbon atoms but increase C_1 and C_2 carbonyl components.

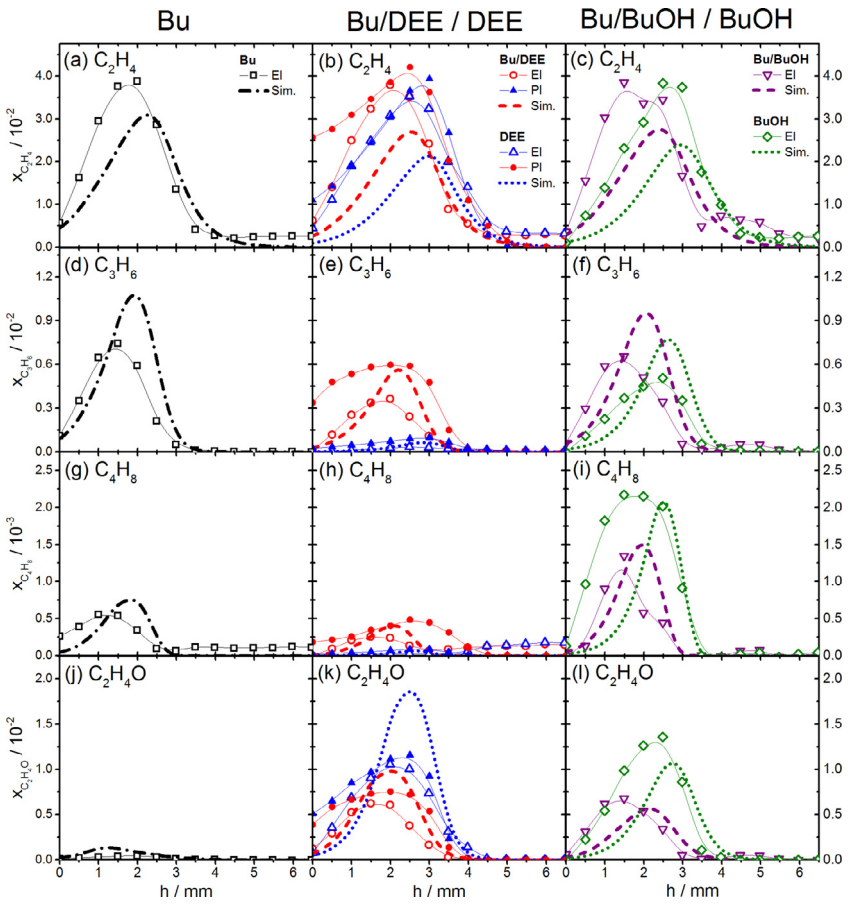

Fig. 3. Mole fraction profiles of selected primary species. Left: *n*-butane, middle: *n*-butane/DEE and DEE flames, right: *n*-butane/*n*-butanol and *n*-butanol flames. Open symbols: EI-MBMS experiment, closed symbols: PI-MBMS experiment (only DEE and *n*-butane/DEE flames), thick lines: present model (using the temperature profiles measured in Bielefeld). Note that experimental results have been connected by a spline function (thin lines) to guide the eye.

In the case of *n*-butanol addition, the fuel radicals again decompose simultaneously into hydrocarbon and oxygenated primary species. However, in contrast to DEE, *n*-butanol reactions release not only small hydrocarbon species in the C_1–C_2 range (CH_3, C_2H_4, C_2H_5), but also C_3 and C_4 species (C_3H_6, C_3H_7, C_4H_8-1). Furthermore, the nature of oxygenated species is different (Fig. 2). The pool of primary hydrocarbon species from *n*-butanol decomposition seems to be analogous to that of *n*-butane, but *n*-butanol additionally contributes numerous oxygenated intermediates such as unsaturated alcohols (e.g., vinyl alcohol C_2H_3OH and propenol C_3H_5OH) and radicals of saturated alcohols (e.g., hydroxyethyl radicals C_2H_4OH and hydroxymethyl radicals CH_2OH).

All species given in the boxes in Fig. 2 were detected in the present experiments. Some important examples will be presented below; further species mole fractions are available in Supplemental materials 1 and 3. Figure 3 shows mole fraction profiles of C_2H_4 (a primary species produced by all three fuels), C_3H_6 and C_4H_8 (two shared primary species in the *n*-butane/*n*-butanol flame that result only from *n*-butane in the *n*-butane/DEE flame, however), and C_2H_4O (the different isomers of which are formed as primary species only by the respective oxygenated fuels and not from *n*-butane). Examples for isomer identification by GC and PI-MBMS are given in Table 2 and Fig. 4.

C_2H_4 can be produced in several ways from both primary and secondary reactions, and therefore its experimentally determined peak mole fraction seems to be only slightly affected by the fuel change (Fig. 3a–c). Similar observations can also be made for several other small hydrocarbons given in Tables S1 and S2. A very good agreement between EI- and PI-MBMS data is found for the DEE and *n*-butane/DEE flames where both experiments were compared. C_3H_6 and C_4H_8 mole fractions are affected differently when *n*-butane is replaced by *n*-butanol, with a decrease of C_3H_6 and an increase of C_4H_8. These trends are well predicted by the model (Fig. 3). The rate of production analysis in Fig. 2 shows that a large part of *n*-butane is consumed leading to the formation of C_3H_6, while this species can be formed from *n*-butanol only by a channel of lesser importance. Therefore, the formation of C_3H_6 should be correlated with the amount of *n*-butane in the flame. Since C_4H_8 formation is promoted from *n*-butanol, an opposite trend is noted.

Both GC and PI-MBMS analyses show that 1-butene is the most abundant C_4H_8 isomer in all five flames; this was also confirmed by the present model predictions (Table 2). The EI-MBMS signal of C_4H_8 was thus calibrated as 1-butene. A similar trend favoring 1-butene was also noted for a fuel-rich *n*-butanol flame studied previously [34], but in a similar *n*-butane flame, 2-butene (sum of *cis*/*trans* isomers) was found to be slightly more abundant [63]. In the present PI-MBMS experiment, *cis* and *trans* isomers of 2-butene also cannot be separated because of their close ionization thresholds. These two isomers are also not distinguished in the present model. In the *n*-butane/DEE flame, both C_3H_6 and C_4H_8 cannot be produced by the primary reactions of DEE. Therefore, mole fractions of both species decrease significantly when DEE is used as additive or as neat fuel, compared to neat *n*-butane and *n*-butanol where C_3H_6 and C_4H_8 are primary products. These trends were observed by both MBMS experiments and model predictions (Fig. 3). According to the PI-MBMS analysis, the two isomers of C_2H_4O, acetaldehyde (CH_3CHO) and vinyl alcohol (C_2H_3OH), are formed in the DEE and *n*-butane/DEE flames, with acetaldehyde as the

Table 2
C_4H_8 isomer identification by EI-MBMS-GC ("GC") and PI-MBMS ("PI"), compared to present model predictions ("Sim.") using the flame temperatures measured in Bielefeld. Simulations with the flame temperatures obtained in Hefei are added for the DEE and *n*-Butane/DEE flames for comparison (right column). Numbers given are fractions (in %) of the peak mole fraction of detected species, and those in bold font correspond to the most abundant isomers.

Detected species	Flame													
	Bu		DEE				Bu/DEE				BuOH		Bu/BuOH	
	GC	Sim.	GC	PI	Sim.		GC	PI	Sim.		GC	Sim.	GC	Sim.
1-Butene	**61**	**76**	**72**	**57**	**69**	**90**	**59**	**55**	**77**	**87**	**75**	**95**	**89**	**90**
trans-2-Butene	27	21	28	42	6	2	21	45	19	11	14	4	6	8
cis-2-Butene	7		–				15				11		3	
iso-Butene	5	3	–	–	25	8	5	–	4	2	–	1	2	1

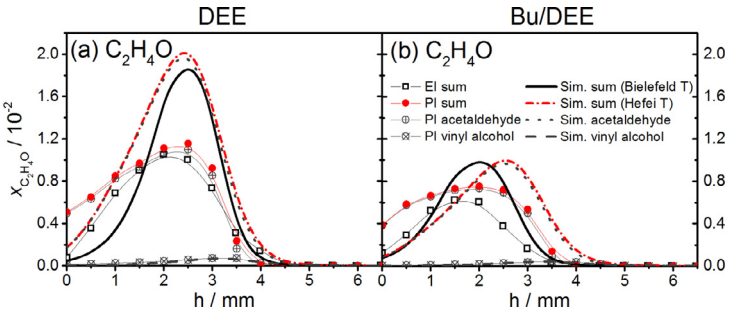

Fig. 4. C_2H_4O isomers (acetaldehyde and vinyl alcohol) in the DEE (left) and *n*-butane/DEE (right) flames; comparison of mole fraction profiles obtained in the EI- and PI-MBMS experiment (symbols). The model predictions (thick lines) using the flame temperatures measured in Bielefeld (for EI data) and in Hefei (for PI data) are presented for comparison. Note that experimental results have been connected by a spline function (thin lines) to guide the eye.

most abundant one in both flames (Fig. 4). This trend is well predicted by the present model. A similar dominance of acetaldehyde was also noted for a fuel-rich *n*-butanol flame studied previously [34] even though vinyl alcohol is a primary species of *n*-butanol reactions (Fig. 2), since vinyl alcohol can tautomerize quickly to acetaldehyde. In the EI-MBMS measurements, C_2H_4O (Fig. 3) was thus calibrated as acetaldehyde for all five flames. The resulting acetaldehyde mole fractions by EI-MBMS are in good agreement with the isomer sums measured by PI-MBMS for the flames containing DEE (Fig. 4). It can be noted that C_2H_4O (predominantly acetaldehyde) was observed to increase significantly in flames containing the oxygenated fuels (Fig. 3). This trend is also well predicted by the present model.

4.2.2. Soot precursors

One of the advantages of the use of oxygenated fuels as additives is their potential to reduce soot emissions [8–10]. In the present section we focus on describing soot precursors detected in the five flames with EI-MBMS. Among approximately 30 detected hydrocarbon intermediates with masses from 15 (CH_3) to 106 (C_8H_{10}), particularly unsaturated and cyclic species are considered as important soot precursors in the present paper. These hydrocarbons may result from fuel decomposition steps (some of them are already presented above such as C_2H_4, C_3H_6, and C_4H_8), but they may also be products of build-up reactions that may yield unsaturated cyclic compounds known to play a very important role in the formation of polycyclic aromatic hydrocarbons (PAH). In all five studied flames, small stable hydrocarbon species with one and two carbon atoms were detected with high mole fractions, especially ethylene and acetylene ($\sim 3–4 \times 10^{-2}$), see Fig. 3 and Tables S1,S2, because they are decomposition products of several species. Peak mole fractions of these species are quite close to those obtained by Oßwald et al. [63] in a pure *n*-butane flame under similar conditions. In flames containing *n*-butanol or *n*-butane (pure or in mixture), C_3H_6 is the most abundant C_3 hydrocarbon species with mole fractions of $\sim 4–8 \times 10^{-3}$, whereas in the flame of pure DEE, allene and propyne (C_3H_4) are present at a slightly higher mole fraction ($\sim 6 \times 10^{-4}$) than C_3H_6 ($\sim 4 \times 10^{-4}$), compare Fig. 3 and Tables S1 and S2. Among C_4 hydrocarbon species in the pure *n*-butane flames and in those containing DEE, diacetylene (C_4H_2) is the most abundant one with mole fractions of $\sim 1.0–1.4 \times 10^{-3}$ (Tables S1,S2). However, when *n*-butanol is used as pure fuel, C_4H_8 becomes more abundant ($\sim 2.2 \times 10^{-3}$) (Fig. 3 and Tables S1,S2). The data obtained with EI-MBMS by Oßwald et al. [34] for an *n*-butanol flame at $\phi = 1.7$ exhibit the same trend. The consumption of C_4H_8 leads to the formation of C_4H_6 that is noted to importantly contribute to the formation of unsaturated cyclic species as discussed below. According to the GC analysis, 1,3-butadiene is the dominant C_4H_6 isomer in all five flames with some contributions of 1,2-butadiene, and 1- or 2-butyne. This trend was also observed in fuel-rich flames of pure *n*-butane and pure *n*-butanol [34,63]. Figure 5 exemplarily shows mole fraction profiles of the sums of C_5H_6 and C_6H_6 isomers as some important cyclic soot precursors; further species are reported in Tables S1 and S3. The most important formation pathways of these species will be presented in the detailed analysis of the pollutant formation in Section 4.3. PI-MBMS results are again included for the pure DEE and *n*-butane/DEE flames. From the PI-MBMS analysis in the flames containing DEE, C_5H_5 (not shown) and C_5H_6 are almost exclusively cyclopentadienyl and 1,3-cyclopentadiene, respectively (Table S3), and C_6H_6 is predominantly benzene, with minor contribution of fulvene (Fig. 5). Isomer identification for the *n*-butane and *n*-butanol flames is based on the previous work in [34,63]. The EI-MBMS signals of C_4H_6, C_5H_5, C_5H_6, and C_6H_6 were thus calibrated as the respective most abundant isomer. Results from both MBMS experiments are in reasonable agreement although the flame position in the PI-MBMS experiment is slightly shifted away from the burner surface as mentioned earlier. Larger species, such as C_7H_8 (toluene) and C_8H_{10} (ethylbenzene), were also measured, but with low amounts ($< 5 \times 10^{-6}$) (Tables S1–S3).

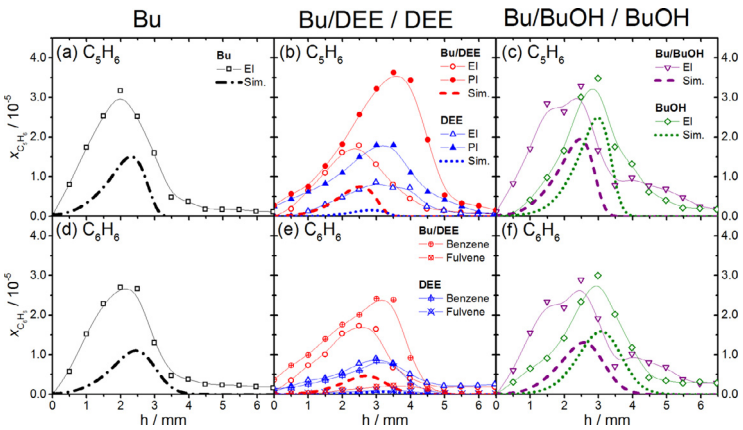

Fig. 5. Mole fraction profiles of some soot precursors. Left: *n*-butane flame, middle: *n*-butane/DEE and DEE flames, right: *n*-butane/*n*-butanol and *n*-butanol flames. Open symbols: EI-MBMS experiment, closed symbols: PI-MBMS experiment (only DEE and *n*-butane/DEE flames), thick lines: present model (using the temperature profiles measured in Bielefeld). Note that experimental results have been connected by a spline function (thin lines) to guide the eye.

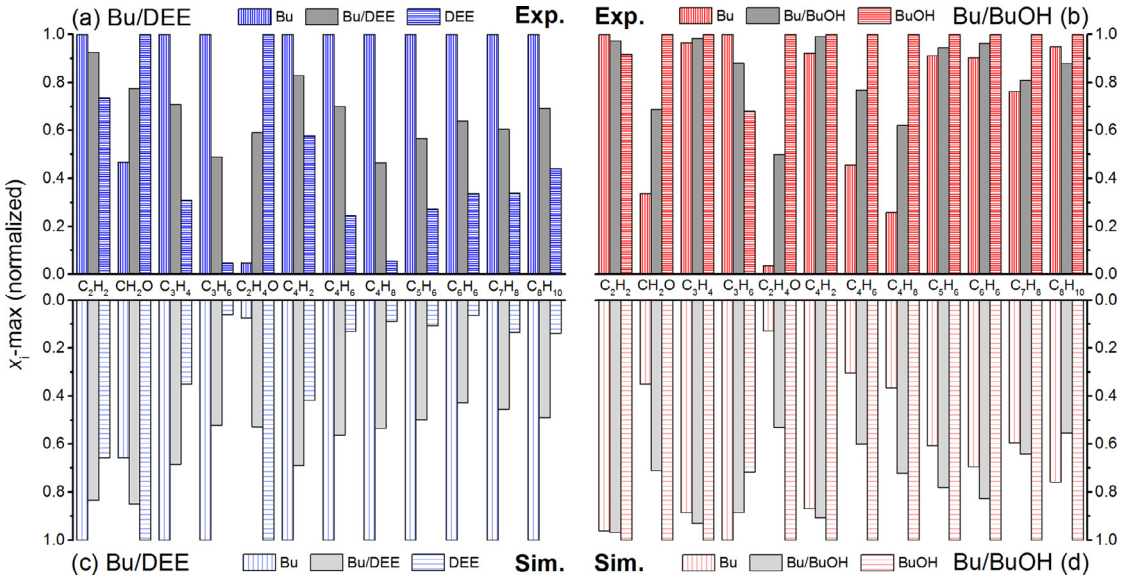

Fig. 6. Comparison of maximum mole fractions of selected soot precursors and aldehydes formed in the flame series of (a,c) *n*-butane, DEE-containing mixture, and DEE and of (b,d) *n*-butane, *n*-butanol-containing mixture and *n*-butanol. Top: experiment, bottom: simulation (lighter shading). For clarity, normalization by the highest value is performed, and mole fraction scales are inverted for the simulations.

4.3. Influence of DEE and n-butanol addition on pollutant formation

In previous sections, some trends were noted regarding the influence of DEE and *n*-butanol addition on the species pools. In this section we will discuss these effects more deeply with special emphasis on soot precursors and on aldehydes that may limit the use of these biofuels in terms of air quality improvement. Figure 6 presents comparisons between the *n*-butane, mixture, and oxygenated fuel flames, specifically comparing the measured and simulated peak mole fractions of toxic carbonyls including CH_2O (formaldehyde) and C_2H_4O (sum of acetaldehyde and vinyl alcohol), and of selected hydrocarbon species potentially involved in soot precursor formation including C_2H_2 (acetylene), C_3H_4 (sum of propyne and allene), C_3H_6 (propene), C_4H_2 (diacetylene), C_4H_6 (sum of 1,3-butadiene, 1,2-butadiene, and butyne), C_4H_8 (sum of 1-butene, 2-butene, and *iso*-butene), C_5H_6 (1,3-cyclopentadiene), C_6H_6 (sum of benzene and fulvene), C_7H_8 (toluene), and C_8H_{10} (ethylbenzene). To facilitate the identification of trends upon oxygenated fuel addition in both experiment and simulation, we have normalized the peak mole fractions by the respective highest values. Thus, Fig. 6a provides trends in the experimental mole fractions for sequential change from pure *n*-butane fuel via their 1:1 mixture to pure DEE, while Fig. 6b shows such trends in the experiment for the sequence from *n*-butane via their 1:1 mixture to *n*-butanol. Bars for *n*-butane are distinguished by vertical line patterns, those for the oxygenated fuels by horizontal-line patterns, and mixtures are coded in plain grey. The respective trends from the simulations (in lighter shades) are given in Fig. 6c and d below; mole fraction scales are inverted ("mirror image") to facilitate recognition of trends.

The formation of formaldehyde and acetaldehyde is observed to increase significantly upon the addition of both oxygenated fuels. This undesirable trend has been considered as common concern for the use of oxygenated biofuels [6]. As mentioned earlier, formaldehyde and acetaldehyde are specific species of DEE or *n*-butanol decomposition and can be produced from these fuels via a few steps. In the case of DEE, large parts of acetaldehyde are formed via the reaction pathway DEE→DEE-YL-2→$CH_3CHO+C_2H_5$ (Fig. 2), while formaldehyde mainly rises from the decomposition of the C_2H_5O radical formed via the reaction route DEE→DEE-YL-1→$C_2H_5O+C_2H_4$. In the case of *n*-butanol, acetaldehyde is mainly produced via tautomerization from vinyl

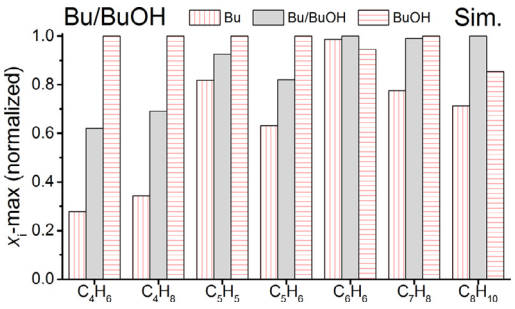

Fig. 7. Comparison of simulated peak mole fractions of C_4–C_8 hydrocarbons in the flames of *n*-butane, *n*-butane/*n*-butanol, and *n*-butanol. Simulations were performed using an identical equivalence ratio of $\phi = 1.7$ and the same temperature profile as in the *n*-butane flame. For clarity, normalization by the highest value is performed.

alcohol (C_2H_3OH). The formation of the latter species is predominantly via the most important consumption pathway of *n*-butanol ($NC_4H_9OH \rightarrow C_4H_8OH\text{-}1 \rightarrow C_2H_3OH + C_2H_5$). The second important consumption pathway of *n*-butanol ($NC_4H_9OH \rightarrow C_4H_8OH\text{-}3 \rightarrow C_3H_6 + CH_2OH$) contributes to a large part of formaldehyde via the reaction $CH_2OH + O_2 \rightarrow CH_2O + HO_2$ (Fig. 2).

Regarding hydrocarbon species involved in soot precursor formation, it is important to note that their peak mole fractions decrease significantly with DEE as neat fuel or additive (Fig. 6a), whereas *n*-butanol surprisingly shows no significant reduction effects or even higher formation of hydrocarbon species, especially in the C_4–C_8 range (Fig. 6b). Remember that the C/O and C/H ratios are the same for all flames. These tendencies have been experimentally observed and are also well predicted by the present model (Fig. 6c,d). While the decrease of soot precursor species in flames containing DEE is expected, because primary reactions of DEE mainly release small hydrocarbon species with one and two carbon atoms (Fig. 2), their increase upon adding *n*-butanol is undesirable and merits further explanations that will be presented in the next paragraph.

The formation of larger amounts of higher hydrocarbons in the flames containing *n*-butanol compared to the *n*-butane flame could result from several effects. To examine whether a higher equivalence ratio used for the *n*-butanol flame ($\phi = 1.8$ vs. $\phi = 1.7$ in the *n*-butane flame) is the reason for the noted trend, we performed additional simulations for the *n*-butane/*n*-butanol and *n*-butanol flames at an identical equivalence ratio of $\phi = 1.7$, using the same temperature profile as in the *n*-butane flame. Figure 7 displays the results of these simulations, with a focus on the C_4-C_8 species. These results again show no significant reduction effect or even higher mole fractions of these species in the flames containing *n*-butanol versus the *n*-butane flame.

The higher ability to form higher hydrocarbon species typically regarded as soot precursors in the flames containing *n*-butanol is most likely a result of the fuel structure, in which chemical groups and carbon-chain length are different from those of DEE. To examine this potential influence, an additional rate-of-production analysis was performed for the formation of selected soot precursors in the *n*-butane/*n*-butanol flame ($\phi = 1.75$) at $h \sim 2.5$ mm (near the peak mole fraction of unsaturated cyclic species), corresponding to a temperature of 1480 K, and presented in Fig. 8. The formation of benzene and fulvene (C_6H_6) is influenced by the *n*-butanol decomposition via the formation of propene (C_3H_6). The latter species can be produced partially from *n*-butanol via the C_4H_8OH-3 radical (Fig. 2), and reacts to form allyl (C_3H_5-A) by H-abstractions (Fig. 8). Recombination of C_3H_5-A and propargyl radicals (C_3H_3) is the main source of benzene formation. The formation of further unsaturated cyclic/aromatic soot precursors including cyclopentadienyl (C_5H_5), 1,3-cyclopentadiene (C_5H_6), toluene (C_7H_8), and ethyl

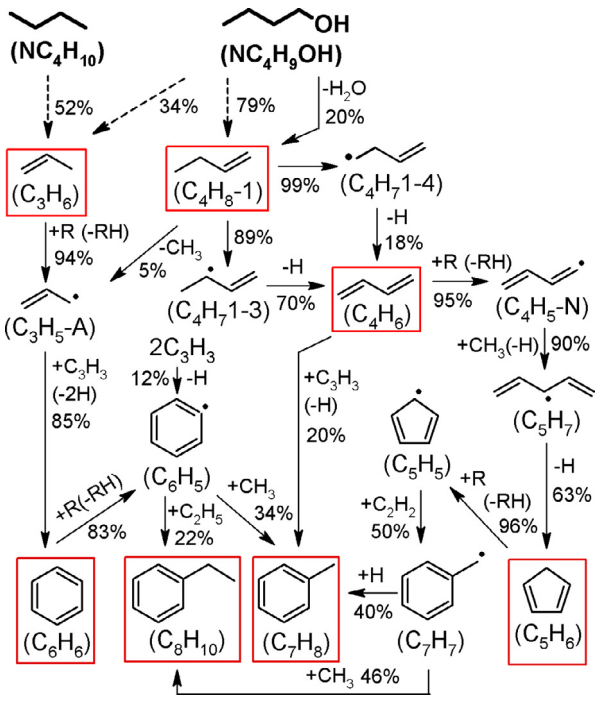

Fig. 8. Reaction-pathway analysis for the formation of selected soot precursor species in the *n*-butane/*n*-butanol flame ($\phi = 1.75$) for $h \sim 2.5$ mm corresponding to a temperature of ~1480 K. Percentages are relative rates of production of the given species. Dashed arrows represent a series of reactions in the present mechanism (details can be found in Fig. 2).

benzene (C_8H_{10}) is significantly affected by the formation of 1-butene (C_4H_8-1) (Fig. 8). The latter species is mainly formed from *n*-butanol via H-abstractions followed by C-O β-scission, and via a complex fission involving four-center elimination of water. When flames contain *n*-butanol, the formation of 1-butene is enhanced, and this induces an increase of those species with four or more carbon atoms including unsaturated cyclic species (Fig. 6b). Contrary to the case of *n*-butanol, this water elimination reaction cannot occur in the decomposition of DEE, and all important primary reactions of DEE lead to the formation of small hydrocarbon species with one or two carbon atoms as discussed previously (Fig. 2); therefore flames containing DEE produce significantly lower amounts of soot precursors in comparison to those blended with similar amounts of *n*-butanol. This difference in soot precursor formation between DEE and *n*-butanol results simultaneously from the difference of their chemical groups as well as in their carbon-chain length.

As a further interesting aspect regarding to the flames with hydrocarbon/oxygenated fuel mixtures, it may be essential to know whether interactions occur between the intermediate pools of both fuels. To analyze the situation for both experiment and simulation, we compare the peak mole fractions $x_{i,\mathrm{mix}}$ of intermediates in the mixture flames (*n*-butane/DEE or *n*-butane/*n*-butanol) with those calculated as mean values $x_{i,\mathrm{mean}}$ from the contributions of the pure fuels by Eq. (4).

$$x_{i,\mathrm{mean}} = x_{i,\mathrm{Bu}} \cdot 0.5 + x_{i,\mathrm{Ox}} \cdot 0.5 \tag{4}$$

where, $x_{i,\mathrm{Bu}}$ is the maximum mole fraction of species *i* in the pure *n*-butane flame and $x_{i,\mathrm{Ox}}$ is the maximum mole fraction of species *i* in the pure DEE (or *n*-butanol) flame. We assume that whenever $x_{i,\mathrm{mix}}$ deviates noticeably from $x_{i,\mathrm{mean}}$, the formation of species *i* may be influenced by the interaction of the intermediate pools and is not simply formed by both formation pathways of the two fuels individually. These deviations are shown in Fig. 9.

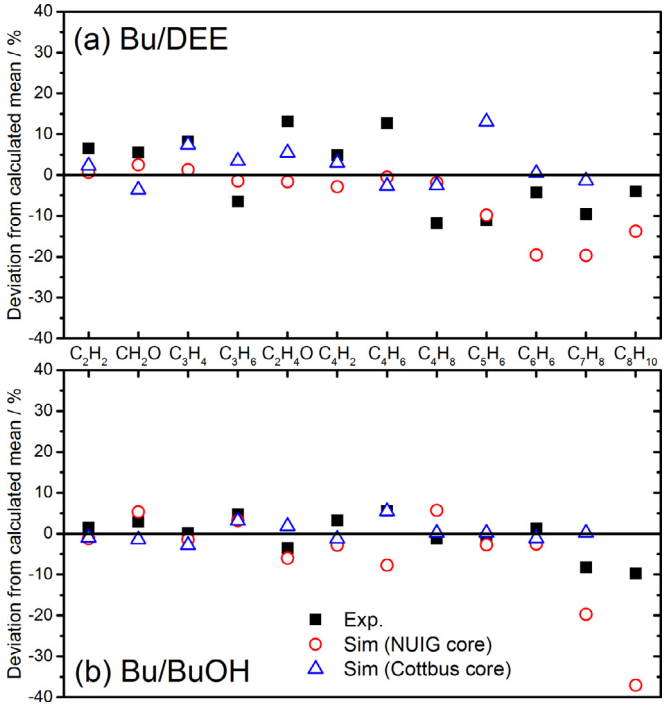

Fig. 9. Deviation of the peak mole fractions of selected hydrocarbon and carbonyl species of the mixture flames from those calculated by the mean value of the pure flames using Eq. (4). Positive values indicate a higher formation of the species in the mixture than what has been calculated by Eq. (4) and vice versa. Top: Mixture of *n*-butane and DEE, bottom: Mixture of *n*-butane and *n*-butanol. Results for the simulations are shown with different core models (NUIG or Cottbus). Note that ethylbenzene is not included in the Cottbus model.

It can be noted that although a good agreement between the experiment (squares in Fig. 9) and the simulations with the NUIG core model (circles in Fig. 9) for the relative trends is observed for several species, a conclusion regarding interactive effects on the formation of intermediates does not seem easy to give, because the deviation of $x_{i,\mathrm{mean}}$ and $x_{i,\mathrm{mix}}$ in the experiments is mostly quite close to the order of the estimated relative experimental error (~5%); moreover, the difference is more pronounced in the simulations for some species and vice versa. Note that relative errors in the model predictions are unknown. In the following, we thus only discuss species for which the difference between $x_{i,\mathrm{mean}}$ and $x_{i,\mathrm{mix}}$ in both experiment and the simulation with the used NUIG core model is higher than 5%. This criterion applies only to a few larger hydrocarbon species, including C_5H_6, C_6H_6, and C_7H_8 in the flames containing DEE, and C_7H_8 and C_8H_{10} in the flames containing *n*-butanol. These species are known as important soot precursors. Figure 9 shows that $x_{i,\mathrm{mix}}$ of these species in the mixture flames is lower than $x_{i,\mathrm{mean}}$. This trend, which is observed in both experiments and model predictions, could result from several effects including thermal, transport, and/or chemical effects. The latter influences could involve synergies between reaction pathways of both fuels, and more detailed modeling efforts will be needed for their analysis, especially in view of experimental uncertainties and unknown predictive quality of the kinetic models for these heavy species.

As one initial test, we have replaced the core model of the NUI-Galway group by another systematically constructed model recently reported by the Cottbus group in [64]. That reaction database contains species from C_0 to large polycyclic aromatic hydrocarbons such as naphthalene and 3-ring species, and it was validated against extensive experimental data as described in [64]. Results (triangles in Fig. 9) using the Cottbus core model indicated very limited deviations (≤5%) of $x_{i,\mathrm{mix}}$ from $x_{i,\mathrm{mean}}$ for all species presented in Fig. 9, with the exception of C_5H_6 in the flames containing DEE, for which the difference between $x_{i,\mathrm{mix}}$ and $x_{i,\mathrm{mean}}$ was ~10% with an opposite trend to that obtained experimentally and with the NUIG core model. Moreover, for larger species such as benzene and toluene, simulation using the NUIG core model predicts higher deviations of $x_{i,\mathrm{mix}}$ from $x_{i,\mathrm{mean}}$ (as mentioned earlier), while simulation using the Cottbus core model shows almost no deviation. Because of these differences noted with two established core models used to represent the chemistry of the *n*-butane base flame, such comparisons, while they might seem interesting, should be interpreted with utmost care. A rigorous analysis regarding the predictive capabilities of respective core models for such questions as well as high-quality experimental data, particularly for higher equivalence ratios where interactive reactions could be expected to be stronger, will be needed to answer the delicate question of interaction between fuel-specific species pools in prototypical hydrocarbon/oxygenated fuel mixtures.

5. Summary and conclusions

The influence of the addition of DEE and its isomer *n*-butanol to *n*-butane on the flame structure, intermediate species composition, and pollutant formation has been investigated by examining mole fraction profiles of species in five different fuel-rich *n*-butane flames (ϕ = 1.7–1.8) containing 0%, 50%, and 100% each of these oxygenated fuels, with keeping the same C/O ratio (0.52), argon dilution (25%), pressure (4 kPa), and gas velocity (73 cm s^{-1} at 333 K, 4 kPa). EI-MBMS-GC and SVUV-PI-MBMS were used to identify and quantify more than 40 stable and radical species in the range of C_0–C_8 in each flame. A kinetic model has been established to interpret the obtained results, by combining different sub-mechanisms available in the literature. The results demonstrate that the formation of toxic carbonyls, such as formaldehyde and acetaldehyde, is enhanced significantly in flames containing the oxygenated fuels. Mole fractions of hydrocarbon species involved in soot precursor formation are significantly reduced in flames containing DEE, while *n*-butanol shows no significant reduction effects or even higher formation of soot precursor species. This trend was observed in both experiment and model prediction and it remained valid when identical temperature profile and equivalence ratio were assumed in the simulation. The higher ability to form soot precursors could thus mainly be a consequence of the molecular structure of *n*-butanol and its associated combustion reactions. Particularly, H-abstractions followed by C-O β-scission or a complex fission involving four-center elimination of water lead to the formation of 1-butene which can play an important role in the formation of soot precursors including unsaturated cyclic species. Diethyl ether, which is mainly decomposed under formation of smaller hydrocarbon species with one or two carbon atoms, does not contribute similarly to such reactions and might thus be regarded as the potentially preferable biofuel isomer.

Acknowledgments

L.-S. Tran thanks the Alexander von Humboldt Foundation for a research fellowship. Partial support from the Deutsche Forschungsgemeinschaft under Project KO1363/31-1 is gratefully acknowledged. M. Zeng is grateful for the joint Ph.D. scholarship funded by the China Scholarship Council. F. Qi is grateful for funding support from Natural Science Foundation of China (U1332208).

Supplementary materials

Supplementary material associated with this article can be found, in the online version, at doi:10.1016/j.combustflame.2016.06.031.

References

[1] Exxonmobil 2012: The outlook for energy: a view to 2040, available at http://www.exxonmobil.com.

[2] A. Sydbom, A. Blomberg, S. Parnia, N. Stenfors, T. Sandström, S.-E. Dahlén, Health effects of diesel exhaust emissions, Eur. Respir. J. 17 (2001) 733–746.

[3] J.F. Mejía, S.L. Choy, K. Mengersen, L. Morawska, Methodology for assessing exposure and impacts of air pollutants in school children: data collection, analysis and health effects – a literature review, Atmos. Environ. 45 (2011) 813–823.

[4] A.A. Mehus, R.J. Reed, V.S.T. Lee, S.R. Littau, C.C. Hu, E.A. Lutz, J.L. Burgess, Comparison of acute health effects from exposures to diesel and biodiesel fuel emissions, J. Occup. Environ. Med. 57 (2015) 705–712.

[5] A.K. Agarwal, Biofuels (alcohols and biodiesel) applications as fuels for internal combustion engines, Prog. Energy Combust. Sci. 33 (2007) 233–271.

[6] K. Kohse-Höinghaus, P. Oßwald, T.A. Cool, T. Kasper, N. Hansen, F. Qi, C.K. Westbrook, P.R. Westmoreland, Biofuel combustion chemistry: from ethanol to biodiesel, Angew. Chem. Int. Ed. 49 (2010) 3572–3597.

[7] L.S. Tran, B. Sirjean, P.-A. Glaude, R. Fournet, F. Battin-Leclerc, Progress in detailed kinetic modeling of the combustion of oxygenated components of biofuels, Energy 43 (2012) 4–18.

[8] N. Miyamoto, H. Ogawa, N. Nurun, K. Obata, T. Arima, Smokeless, low NOx, high thermal efficiency, and low noise diesel combustion with oxygenated agents as main fuel, SAE Technical Paper 980506, 1998.

[9] T. Litzinger, M. Stoner, H. Hess, A. Boehman, Effects of oxygenated blending compounds on emissions from a turbocharged direct injection diesel engine, Int. J. Engine Res. 1 (2000) 57–70.

[10] C.K. Westbrook, W.J. Pitz, H.J. Curran, Chemical kinetic modeling study of the effects of oxygenated hydrocarbons on soot emissions from diesel engines, J. Phys. Chem. A 110 (2006) 6912–6922.

[11] D.C. Rakopoulos, C.D. Rakopoulos, E.G. Giakoumis, A.M. Dimaratos, Characteristics of performance and emissions in high-speed direct injection diesel engine fueled with diethyl ether/diesel fuel blends, Energy 43 (2012) 214–224.

[12] A. Paul, P.K. Bose, R. Panua, D. Debroy, Study of performance and emission characteristics of a single cylinder CI engine using diethyl ether and ethanol blends, J. Energy Inst. 88 (2015) 1–10.

[13] S. Imtenan, H.H. Masjuki, M. Varman, I.M. Rizwanul Fattah, H. Sajjad, M.I. Arbab, Effect of *n*-butanol and diethyl ether as oxygenated additives on combustion-emission-performance characteristics of a multiple cylinder diesel engine fuelled with diesel-jatropha biodiesel blend, Energy Convers. Manag. 94 (2015) 84–94.

[14] K. Sudheesh, J.M. Mallikarjuna, Diethyl ether as an ignition improver for biogas homogeneous charge compression ignition (HCCI) operation – an experimental investigation, Energy 35 (2010) 3614–3622.

[15] N.K. Miller Jothi, G. Nagarajan, S. Renganarayanan, Experimental studies on homogeneous charge CI engine fueled with LPG using DEE as an ignition enhancer, Renew. Energy 32 (2007) 1581–1593.

[16] K. Yasunaga, F. Gillespie, J.M. Simmie, H.J. Curran, Y. Kuraguchi, H. Hoshikawa, M. Yamane, Y. Hidaka, A multiple shock tube and chemical kinetic modeling study of diethyl ether pyrolysis and oxidation, J. Phys. Chem. A 114 (2010) 9098–9109.

[17] M. Werler, L.R. Cancino, R. Schiessl, U. Maas, C. Schulz, M. Fikri, Ignition delay times of diethyl ether measured in a high-pressure shock tube and a rapid compression machine, Proc. Combust. Inst. 35 (2015) 259–266.

[18] J. Hashimoto, K. Tanoue, N. Taide, Y. Nouno, Extinction limits and flame structures of 1-butanol and diethyl ether non-premixed flames, Proc. Combust. Inst. 35 (2015) 973–980.

[19] L.-S. Tran, J. Pieper, H.-H. Carstensen, H. Zhao, I. Graf, Y. Ju, F. Qi, K. Kohse-Höinghaus, Experimental and kinetic modeling study of diethyl ether flames, Proc. Combust. Inst. 36 (2016) (submitted for publication), doi:10.1016/j.proci.2016.06.087.

[20] F. Gillespie, W.K. Metcalfe, P. Dirrenberger, O. Herbinet, P.-A. Glaude, F. Battin-Leclerc, H.J. Curran, Measurements of flat-flame velocities of diethyl ether in air, Energy 43 (2012) 140–145.

[21] D.T. Jones, D.R. Woods, Acetone-butanol fermentation revisited, Microbiol. Rev. 50 (1986) 484–524.

[22] N. Qureshi, B.C. Saha, R.E. Hector, B. Dien, S. Hughes, S. Liu, L. Iten, M.J. Bowman, G. Sarath, M.A. Cotta, Production of butanol (a biofuel) from agricultural residues: Part II – use of corn stover and switchgrass hydrolysates, Biomass Bioenergy 34 (2010) 566–571.

[23] P. Dürre, Biobutanol: an attractive biofuel, Biotechnol. J. 2 (2007) 1525–1534.

[24] S. Szwaja, J.D. Naber, Combustion of *n*-butanol in a spark-ignition IC engine, Fuel 89 (2010) 1573–1582.

[25] X. Gu, Z. Huang, J. Cai, J. Gong, X. Wu, C.-F. Lee, Emission characteristics of a spark-ignition engine fuelled with gasoline-*n*-butanol blends in combination with EGR, Fuel 93 (2012) 611–617.

[26] M. Yao, H. Wang, Z. Zheng, Y. Yue, Experimental study of *n*-butanol additive and multi-injection on HD diesel engine performance and emissions, Fuel 89 (2010) 2191–2201.

[27] D.C. Rakopoulos, C.D. Rakopoulos, D.T. Hountalas, E.C. Kakaras, E.G. Giakoumis, R.G. Papagiannakis, Investigation of the performance and emissions of bus engine operating on butanol/diesel fuel blends, Fuel 89 (2010) 2781–2790.

[28] P. Saisirirat, F. Foucher, S. Chanchaona, C. Mounaïm-Rousselle, Spectroscopic measurements of low-temperature heat release for homogeneous combustion compression ignition (HCCI) *n*-heptane/alcohol mixture combustion, Energy Fuels 24 (2010) 5404–5409.

[29] P. Saisirirat, C. Togbé, S. Chanchaona, F. Foucher, C. Mounaïm-Rousselle, P. Dagaut, Auto-ignition and combustion characteristics in HCCI and JSR using 1-butanol/*n*-heptane and ethanol/*n*-heptane blends, Proc. Combust. Inst. 33 (2011) 3007–3014.

[30] K.A. Heufer, R.X. Fernandes, H. Olivier, J. Beeckmann, O. Röhl, N. Peters, Shock tube investigations of ignition delays of *n*-butanol at elevated pressures between 770 and 1250 K, Proc. Combust. Inst. 33 (2011) 359–366.

[31] S. Vranckx, K.A. Heufer, C. Lee, H. Olivier, L. Schill, W.A. Kopp, K. Leonhard, C.A. Taatjes, R.X. Fernandes, Role of peroxy chemistry in the high-pressure ignition of *n*-butanol – experiments and detailed kinetic modelling, Combust. Flame 158 (2011) 1444–1455.

[32] I. Stranic, D.P. Chase, J.T. Harmon, S. Yang, D.F. Davidson, R.K. Hanson, Shock tube measurements of ignition delay times for the butanol isomers, Combust. Flame 159 (2012) 516–527.

[33] N. Hansen, M.R. Harper, W.H. Green, High-temperature oxidation chemistry of *n*-butanol – experiments in low-pressure premixed flames and detailed kinetic modeling, Phys. Chem. Chem. Phys. 13 (2011) 20262–20274.

[34] P. Oßwald, H. Güldenberg, K. Kohse-Höinghaus, B. Yang, T. Yuan, F. Qi, Combustion of butanol isomers – a detailed molecular beam mass spectrometry investigation of their flame chemistry, Combust. Flame 158 (2011) 2–15.

[35] S.M. Sarathy, M.J. Thomson, C. Togbé, P. Dagaut, F. Halter, C. Mounaïm-Rousselle, An experimental and kinetic modeling study of *n*-butanol combustion, Combust. Flame 156 (2009) 852–864.

[36] W. Liu, A.P. Kelley, C.K. Law, Non-premixed ignition, laminar flame propagation, and mechanism reduction of *n*-butanol, *iso*-butanol, and methyl butanoate, Proc. Combust. Inst. 33 (2011) 995–1002.

[37] S.M. Sarathy, P. Oßwald, N. Hansen, K. Kohse-Höinghaus, Alcohol combustion chemistry, Prog. Energy Combust. Sci. 44 (2014) 40–102.

[38] D.C. Rakopoulos, Combustion and emissions of cottonseed oil and its bio-diesel in blends with either *n*-butanol or diethyl ether in HSDI diesel engine, Fuel 105 (2013) 603–613.

[39] D.C. Rakopoulos, Comparison of combustion, performance, and emissions of HSDI diesel engine operating on blends of diesel fuel with ethanol, *n*-butanol, or butanol isomer ether DEE, J. Energy Eng. 141 (2015) C4014001.

[40] U. Struckmeier, A. Lucassen, N. Hansen, T. Wada, N. Peters, K. Kohse-Höinghaus, Demonstration of a burner for the investigation of partially premixed low-temperature flames, Combust. Flame 157 (2010) 1966–1975.

[41] A. Lucassen, N. Labbe, P.R. Westmoreland, K. Kohse-Höinghaus, Combustion chemistry and fuel-nitrogen conversion in a laminar premixed flame of morpholine as a model biofuel, Combust. Flame 158 (2011) 1647–1666.

[42] M. Schenk, L. Leon, K. Moshammer, P. Oßwald, T. Zeuch, L. Seidel, F. Mauss, K. Kohse-Höinghaus, Detailed mass spectrometric and modeling study of isomeric butene flames, Combust. Flame 160 (2013) 487–503.

[43] F. Qi, R. Yang, B. Yang, C. Huang, L. Wei, J. Wang, L. Sheng, Y. Zhang, Isomeric identification of polycyclic aromatic hydrocarbons formed in combustion with tunable vacuum ultraviolet photoionization, Rev. Sci. Instrum. 77 (2006) 084101.

[44] F. Qi, Combustion chemistry probed by synchrotron VUV photoionization mass spectrometry, Proc. Combust. Inst. 34 (2013) 33–63.

[45] Y. Li, L. Zhang, Z. Tian, T. Yuan, J. Wang, B. Yang, F. Qi, Experimental study of a fuel-rich premixed toluene flame at low pressure, Energy Fuels 23 (2009) 1473–1485.

[46] Z. Zhou, X. Du, J. Yang, Y. Wang, C. Li, S. Wei, L. Du, Y. Li, F. Qi, Q. Wang, The vacuum ultraviolet beamline/endstations dedicated to combustion research, J. Synchrotron Radiat. 23 (2016) 1035–1045.

[47] J.C. Biordi, Molecular beam mass spectrometry for studying the fundamental chemistry of flames, Prog. Energy Combust. Sci. 3 (1977) 151–173.

[48] Photoionization Cross Section Database (Version 1.0), National synchrotron radiation laboratory, Hefei, China, 2011, available at http://flame.nsrl.ustc.edu.cn/database/.

[49] U. Struckmeier, P. Oßwald, T. Kasper, L. Böhling, M. Heusing, M. Köhler, A. Brockhinke, K. Kohse-Höinghaus, Sampling probe influences on temperature and species concentrations in molecular beam mass spectroscopic investigations of flat premixed low-pressure flames, Z. Phys. Chem. 223 (2009) 503–537.

[50] X. Yang, D. Felsmann, N. Kurimoto, J. Krüger, T. Wada, T. Tan, E.A. Carter, K. Kohse-Höinghaus, Y. Ju, Kinetic studies of methyl acetate pyrolysis and oxidation in a flow reactor and a low-pressure flat flame using molecular-beam mass spectrometry, Proc. Combust. Inst. 35 (2015) 491–498.

[51] Y. Li, J. Cai, L. Zhang, T. Yuan, K. Zhang, F. Qi, Investigation on chemical structures of premixed toluene flames at low pressure, Proc. Combust. Inst. 33 (2011) 593–600.

[52] S.M. Burke, W. Metcalfe, O. Herbinet, F. Battin-Leclerc, F.M. Haas, J. Santner, F.L. Dryer, H.J. Curran, An experimental and modeling study of propene oxidation. Part 1: Speciation measurements in jet-stirred and flow reactors, Combust. Flame 161 (2014) 2765–2784.

[53] S.M. Burke, U. Burke, R. Mc Donagh, O. Mathieu, I. Osorio, C. Keesee, A. Morones, E.L. Petersen, W. Wang, T.A. DeVerter, M.A. Oehlschlaeger, B. Rhodes, R.K. Hanson, D.F. Davidson, B.W. Weber, C.-J. Sung, J. Santner, Y. Ju, F.M. Haas, F.L. Dryer, E.N. Volkov, E.J.K. Nilsson, A.A. Konnov, M. Alrefae, F. Khaled, A. Farooq, P. Dirrenberger, P.-A. Glaude, F. Battin-Leclerc, H.J. Curran, An experimental and modeling study of propene oxidation. Part 2: ignition delay time and flame speed measurements, Combust. Flame 162 (2015) 296–314.
[54] W.K. Metcalfe, S.M. Burke, S.S. Ahmed, H.J. Curran, A hierarchical and comparative kinetic modeling study of C_1–C_2 hydrocarbon and oxygenated fuels, Int. J. Chem. Kinet. 45 (2013) 638–675.
[55] D. Healy, N.S. Donato, C.J. Aul, E.L. Petersen, C.M. Zinner, G. Bourque, H.J. Curran, *n*-Butane: ignition delay measurements at high pressure and detailed chemical kinetic simulations, Combust. Flame 157 (2010) 1526–1539.
[56] D. Healy, N. Donato, C. Aul, E.L. Petersen, C. Zinner, G. Bourque, H.J. Curran, Isobutane ignition delay time measurements at high pressure and detailed chemical kinetic simulations, Combust. Flame 157 (2010) 1540–1551.
[57] D. Healy, M.M. Kopp, N.L. Polley, E.L. Petersen, G. Bourque, H.J. Curran, Methane/*n*-butane ignition delay measurements at high pressure and detailed chemical kinetic simulations, Energy Fuels 24 (2010) 1617–1627.
[58] D. Healy, D.M. Kalitan, C.J. Aul, E.L. Petersen, G. Bourque, H.J. Curran, Oxidation of C1–C5 alkane quinternary natural gas mixtures at high pressures, Energy Fuels 24 (2010) 1521–1528.
[59] K.P. Somers, J.M. Simmie, W.K. Metcalfe, H.J. Curran, The pyrolysis of 2-methylfuran: a quantum chemical, statistical rate theory and kinetic modelling study, Phys. Chem. Chem. Phys. 16 (2014) 5349–5367.
[60] S.M. Sarathy, S. Vranckx, K. Yasunaga, M. Mehl, P. Oßwald, W.K. Metcalfe, C.K. Westbrook, W.J. Pitz, K. Kohse-Höinghaus, R.X. Fernandes, H.J. Curran, A comprehensive chemical kinetic combustion model for the four butanol isomers, Combust. Flame 159 (2012) 2028–2055.
[61] CHEMKIN-PRO 15092, Reaction design: San Diego, 2009.
[62] C. Morley. Gaseq V063, program for thermodynamic gas equation, 1999.
[63] P. Oßwald, K. Kohse-Höinghaus, U. Struckmeier, T. Zeuch, L. Seidel, L. Leon, F. Mauss, Combustion chemistry of the butane isomers in premixed low-pressure flames, Z. Phys. Chem. 225 (2011) 1029–1054.
[64] L. Seidel, K. Moshammer, X. Wang, T. Zeuch, K. Kohse-Höinghaus, F. Mauss, Comprehensive kinetic modeling and experimental study of a fuel-rich, premixed *n*-heptane flame, Combust. Flame 162 (2015) 2045–2058.

ANHANG E

Publikation 5

H. Jin[1], J. Pieper[1], C. Hemken, E. Bräuer, L. Ruwe, K. Kohse-Höinghaus

Chemical interaction of dual-fuel mixtures in low-temperature oxidation, comparing *n*-pentane/dimethyl ether and *n*-pentane/ethanol

Combustion and Flame, 2018
Zur Veröffentlichung akzeptiert.

Abstract

With the aim to study potential cooperative effects in the low-temperature oxidation of dual-fuel combinations, we have investigated prototypical hydrocarbon (C_5H_{12}) / oxygenated (C_2H_6O) fuel mixtures by doping *n*-pentane with either dimethyl ether (DME) or ethanol (EtOH). Species measurements were performed in a flow reactor at an equivalence ratio of ϕ=0.7, at a pressure of p=970 mbar, and in the temperature range of 450–930 K using electron ionization molecular-beam mass spectrometry (EI-MBMS). Series of different blending ratios were studied including the three pure fuels and mixtures of *n*-pentane containing 25% and 50% of C_2H_6O. Mole fractions and signals of a significant number of species with elemental composition $C_nH_{2n+x}O_y$ (n=1–5, x=0–(n+2), y=0–3) were analyzed to characterize the behavior of the mixtures in comparison to that of the individual components. Not unexpectedly, the overall reactivity of *n*-pentane is decreased when doping with ethanol, while it is promoted by the addition of DME. Interestingly, the present experiments reveal synergistic interactions between *n*-pentane and DME, showing a stronger effect on the negative temperature coefficient (NTC) for the mixture than for each of the individual components. Reasons for this behavior were investigated and show several oxygenated intermediates to be involved in enhanced OH radical production. Conversely, ethanol is activated by the addition of *n*-pentane, again involving key OH radical reactions. Although the main focus here is on the experimental results, we have attempted, in a first approximation, to complement the experimental observations by simulations with recent kinetic models. Interesting differences were observed in this comparison for both, fuel consumption and intermediate species production. The inhibition effect of ethanol is not predicted fully, and the synergistic effect of DME is not captured satisfactorily. The exploratory analysis of the experimental results with current models suggests that deeper knowledge of the reaction chemistry in the low-temperature regime would be useful and might contribute to improved prediction of the low-temperature oxidation behavior for

1 geteilte Erstautorenschaft

such fuel mixtures.

Chemical interaction of dual-fuel mixtures in low-temperature oxidation, comparing *n*-pentane/dimethyl ether and *n*-pentane/ethanol

Hanfeng Jin[1,2,#,*], Julia Pieper[1,#], Christian Hemken[1,3], Eike Bräuer[1], Lena Ruwe[1], Katharina Kohse-Höinghaus[1,*]

[1]*Department of Chemistry, Bielefeld University, Universitätsstraße 25, 33615 Bielefeld, Germany*

[2] *Now at: Center for Clean Combustion Research, KAUST, Thuwal 23955-6900, Saudi Arabia*

[3] *Now at: Physico Chemical Fundamentals of Combustion, RWTH Aachen University, Schinkelstraße 8, 52062 Aachen, Germany*

[#] They both contributed equally to this work.

*Corresponding authors:

Dr. Hanfeng Jin
Email: hanfeng.jin@kaust.edu.sa
Phone: +966 12 808 4745

Prof. Dr. Katharina Kohse-Höinghaus
Email: kkh@uni-bielefeld.de
Phone: +49 521 106 2052

Abstract: With the aim to study potential cooperative effects in the low-temperature oxidation of dual-fuel combinations, we have investigated prototypical hydrocarbon (C_5H_{12}) / oxygenated (C_2H_6O) fuel mixtures by doping *n*-pentane with either dimethyl ether (DME) or ethanol (EtOH). Species measurements were performed in a flow reactor at an equivalence ratio of ϕ=0.7, at a pressure of p=970 mbar, and in the temperature range of 450–930 K using electron ionization molecular-beam mass spectrometry (EI-MBMS). Series of different blending ratios were studied including the three pure fuels and mixtures of *n*-pentane containing 25% and 50% of C_2H_6O. Mole fractions and signals of a significant number of species with elemental composition $C_nH_{2n+x}O_y$ (n=1–5, x=0–(n+2), y=0–3) were analyzed to characterize the behavior of the mixtures in comparison to that of the individual components. Not unexpectedly, the overall reactivity of *n*-pentane is decreased when doping with ethanol, while it is promoted by the addition of DME. Interestingly, the present experiments reveal synergistic interactions between *n*-pentane and DME, showing a stronger effect on the negative

temperature coefficient (NTC) for the mixture than for each of the individual components. Reasons for this behavior were investigated and show several oxygenated intermediates to be involved in enhanced OH radical production. Conversely, ethanol is activated by the addition of *n*-pentane, again involving key OH radical reactions. Although the main focus here is on the experimental results, we have attempted, in a first approximation, to complement the experimental observations by simulations with recent kinetic models. Interesting differences were observed in this comparison for both, fuel consumption and intermediate species production. The inhibition effect of ethanol is not predicted fully, and the synergistic effect of DME is not captured satisfactorily. The exploratory analysis of the experimental results with current models suggests that deeper knowledge of the reaction chemistry in the low-temperature regime would be useful and might contribute to improved prediction of the low-temperature oxidation behavior for such fuel mixtures.

Keywords: Dual-fuel strategy, low-temperature oxidation, chemical interaction, *n*-pentane, dimethyl ether, ethanol, EI-MBMS, flow reactor

1. Introduction

Adverse effects on the environment and climate caused by the combustion of fossil fuels in conventional engines underline the need for more efficient and cleaner engine–fuel combinations [1,2]. Fuel additives as a component of intelligent fuel design can serve to control the ignition timing in advanced engine concepts using homogeneous charge compression ignition (HCCI), reactivity-controlled compression ignition (RCCI), and stratified-charge compression ignition (SCCI), with the prospect of cleaner burning processes and higher thermal efficiencies [3,4]. However, the operation of such engine–fuel combinations must rely on the fundamental knowledge of the combustion chemistry that drives the low-temperature auto-ignition of fuel mixtures. Such low-temperature combustion (LTC) strategies can involve mixtures of high-cetane and high-octane fuels with their synergistic combustion characteristics to achieve high thermal efficiencies, and several approaches have been demonstrated, *e.g.* using primary reference fuels with additives to achieve efficient engine control and ignition timing [5,6]. High-cetane fuels usually auto-ignite early, showing typical low-temperature heat release (LTHR) and high-temperature heat release (HTHR) characteristics. The addition of high-octane fuels suppresses the early LTHR, shifting more of the heat release from high-cetane fuels closer to the top dead center of engines, thereby improving the combustion efficiency in internal combustion engines.

Dual-fuel mixtures are a good basis to understand the chemistry of multi-component mixtures. In spite of its importance for practical applications in engines, however, detailed information regarding potential interactions between different fuel components in the LTC regime remains scarce. The auto-ignition of mixtures with simple molecular structures was investigated recently [7,8], including methane/dimethyl ether (DME) and propane/DME blends. These studies have profited from the numerous low-temperature oxidation investigations of light C_3–C_4 alkanes [8–18] as a substantial basis to examine dual-fuel interactions. Regarding heavier alkanes, *n*-heptane/ethanol (EtOH) blends were investigated by Saisirirat *et al.* [19,20] under HCCI and jet-stirred reactor (JSR) conditions, with a noted impact of *n*-heptane on ethanol consumption between 600 and 700 K. Their work mainly focused on ignition delay times, however, and only a few intermediates were observed which could not

illustrate the nature of the interaction between *n*-heptane and ethanol [19,20]. A challenge to fully understand such interactive effects for fuels of the size of *n*-heptane or *iso*-octane is the large number of isomeric structures that are formed in the low-temperature oxidation reactions *via* alkyl (R), peroxyalkyl (ROO), and hydroperoxyalkyl (QOOH) radicals. The identification and quantification of these radicals and their subsequent reaction products are often beyond the capability of commonly used diagnostic techniques. Furthermore, significant uncertainties exist in the pressure-dependent kinetic parameters of these reactions [21–25] which limit the further development of accurate kinetic models. As a reasonable compromise, we have therefore chosen *n*-pentane (C_5H_{12}), an alkane component in gasoline, as the primary fuel in this work to explore its interaction with fuel additives of different ignition reactivity.

As for lighter or heavier alkanes [8–18,21–25], a number of studies have been performed of the low-temperature oxidation of *n*-pentane, using rapid compression machine (RCM) [26–35], shock tube (ST) [34–36], and JSR [37–40] experiments. Most of the previous experimental work focused on the macroscopic auto-ignition behavior of *n*-pentane, with detailed speciation reported only in recent publications of Bugler *et al*. [39] and Rodriguez *et al.* [40]. Bugler *et al.* [39] have also developed a mechanism for the auto-ignition of pentane isomers which they examined against JSR data (500–1100 K, 1 and 10 atm) obtained by gas chromatography (GC), cavity ring-down spectroscopy (CRDS), and Fourier transform infrared spectroscopy (FTIR). Rodriguez *et al.* [40] complemented the atmospheric-pressure JSR experiments in the temperature range of Bugler *et al.* [39] with measurements using synchrotron vacuum ultraviolet photoionization mass spectrometry (SVUV-PIMS). Their experiment successfully identified and separated contributions of different isomers, especially of saturated, unsaturated, and carbonyl hydroperoxides. These recent investigations support the choice of *n*-pentane as base fuel for the present work.

DME and ethanol have been selected as isomeric fuel additives of different reactivity in this study. They are considered as potential or widely applied biofuels that could reduce the emission of air pollutants [1,41,42]. DME has been used as a fuel additive or alternative fuel in compression ignition

engines because of its excellent auto-ignition characteristics [43]. It has a high cetane number (CN=55) and was found to be an excellent ignition improver for HCCI engines [44,45]. The present knowledge on these two isomeric fuels' low-temperature oxidation reactions is more detailed for DME than for ethanol. Experimental investigations, including ignition delay [7,46] and speciation [41,47–54] measurements in JSRs and flow reactors have laid an extensive foundation for DME's reaction kinetics. Quantum chemical calculations were performed for both the first and second O_2 addition reactions, as well as the further reactions of the $CH_3OCH_2O_2$ (ROO) and CH_2OCH_2OOH (QOOH) intermediates [55]. The pressure-dependent description for these reactions is sensitive to the low-temperature oxidation of DME [56], which was well considered in the recently published DME models of Burke *et al.* [7] and Rodriguez *et al.* [57]. Very recently, Jiang *et al.* [58] determined ignition delay times of *n*-pentane/DME mixtures and their experimental results compared favorably to the pentane isomer model by Bugler *et al.* [35]. The situation for a detailed study including reactive intermediates of *n*-pentane/DME interactive mixture effects in the LTC regime attempted here should thus be considered favorable.

Ethanol is a commonly used additive to fossil transportation fuels. Different from DME, ethanol has a high research octane number (RON=109 [59]) and displays single-stage ignition. Compared to ample studies on the high-temperature combustion of ethanol, its low-temperature oxidation chemistry has attracted lesser attention [51,60–63]. Haas *et al.* [61] and Herrmann *et al.* [51] studied the oxidation of pure ethanol in flow reactor conditions with somewhat different results. Very weak negative temperature coefficient (NTC) behavior might have been observed for the rich ethanol/O_2/Ar mixture by Herrmann *et al.* [51] as evident from their figure 3a, but not in the work of Haas *et al.* [61]. The model of Cancino *et al.* [60] also showed a slight NTC behavior in the reproduction of Herrmann *et al.*'s data [51], but no further studies confirmed these results. Recognizing these difficulties, ethanol auto-ignition has been investigated very recently for ST and RCM conditions by adding DME as a radical initiator [64].

Regarding this background, it is to be expected that *n*-pentane will exhibit different global NTC

behavior when blended with either isomer of C_2H_6O, namely DME or ethanol. However, there is a lack of prior information on the detailed oxidation reactions and intermediate species mole fractions or on any potential interactions between the two fuels in such mixtures. We therefore provide speciation experiments in a flow reactor for both, the dual-fuel mixtures of *n*-pentane/DME and *n*-pentane/EtOH, at near-atmospheric pressure and in the temperature range of 450 to 930 K. The species composition along the reaction progress was analyzed using electron ionization molecular-beam mass spectrometry (EI-MBMS). The results for the mixtures were compared to the behavior of each individual fuel component. Temperature-resolved, extensive species information has thus been obtained systematically regarding synergistic or antagonistic effects between these fuels of different reactivity, and combined with an analysis of the detailed chemical oxidation pathways.

Although the main emphasis in the present work is on the experimental results, we have complemented the measured species data with initial simulations by two recent kinetic models. Specifically, we have used the model for pentanes of the Galway group [39] and the recent update of the Polimi mechanism [17]. Discrepancies between experiment and simulation were noted and are discussed in an attempt to improve the understanding of the low-temperature oxidation mechanisms for these mixtures including interactive effects.

2. Experimental and numerical approaches

2.1 Flow reactor experiment

The low-temperature oxidation reactions of *n*-pentane, DME, ethanol, and the respective dual-fuel mixtures were investigated in a flow reactor in the temperature regime of 450–930 K (step size ΔT=5 K), keeping several important parameters constant. The experiments were consistently performed at ϕ=0.7, 970 mbar, a total cold gas flow rate of 300 sccm (standard cubic centimeters per minute at 1 atm and 273.15 K), and an argon dilution of 90%. A lean stoichiometry was chosen due to the importance of lean and efficient burning and of the influences of high amounts of oxygen for the formation of oxygenated species. Electron ionization molecular-beam mass spectrometry was

employed to identify the species composition. A detailed description of the experimental set-up, including both the reactor and mass spectrometry technique, has been reported earlier [41,51,52] so that only some details of importance for the present experiment are given here.

The reactor is a fused silica tube with an inner diameter of 8 mm. Its total length is 1.4 m, with a heating area of 1.3 m that is divided into 8 independently regulated zones [65]. These are heated using an electrical furnace and are controlled by Ni-Cr/Ni thermocouples at the outside wall of the reactor. The exhaust gas from the reactor is extracted with a quartz nozzle (50 µm orifice) at the reactor exit and guided *via* a copper skimmer and a two-stage differential pumping system into the ionization chamber of the mass spectrometer. Molecules are then ionized by a 17 eV electron beam and detected by their time of flight with a resolution of $m/\Delta m \approx 2200$, enabling the separation of hydrocarbon and oxygenated species of the same nominal mass.

The inlet conditions for the oxidation experiments are listed in Table 1 and address the three individual fuels as well as two sets each of *n*-pentane mixtures with DME or EtOH. *n*-Pentane (≥99%) was supplied by ChemSolute, and ethanol (≥99.96%) was provided by VWR Chemicals. Gases were obtained from Linde AG, including dimethyl ether (≥99.9%), O_2 (≥99.5%), and Ar (≥99.996%). The fraction of *n*-pentane in the mixture is expressed as γ in Table 1. The delivery of *n*-pentane and ethanol relied on a dialysis pump (Protea PM-1000) providing flow rates in the µl/min range with uncertainties of 1%. To prepare the respective mixtures, gases were metered by calibrated mass flow controllers (MKS Instruments, uncertainty ~5%), and liquid fuels were vaporized, mixed with the gases, and then preheated to 423 K prior to the reactor inlet.

Table 1. Experimental conditions; γ is the fraction of *n*-pentane in the mixture: $\gamma = x_{C5H12}/(x_{C5H12}+x_d)$, *d*: DME or EtOH.

Fuel	Name	P (bar)	ϕ	γ	Gas flow rate (sccm), std. 273.15 K, 1 atm					
					Total	Ar	O_2	C_5H_{12}	DME	EtOH
n-Pentane (C_5H_{12})	P100	0.97	0.7		300.0	270.0	27.59	2.414		
Dimethyl ether (DME)	D100	0.97	0.7		300.0	270.0	24.32		5.676	
Ethanol (EtOH)	E100	0.97	0.7		300.0	270.0	24.32			5.676
C_5H_{12}/DME mixtures	PD75	0.97	0.7	0.75	300.0	270.0	27.18	2.114	0.705	
	PD50	0.97	0.7	0.50	300.0	270.0	26.61	1.694	1.694	
C_5H_{12}/EtOH mixtures	PE75	0.97	0.7	0.75	300.0	270.0	27.18	2.114		0.705
	PE50	0.97	0.7	0.50	300.0	270.0	26.61	1.694		1.694

Quantitative species mole fractions were determined whenever possible according to the procedure by Schenk *et al.* [66] using Ar as the reference. Following that work, the ratio of the integrated ion signal of a species to a reference signal is proportional to the ratio of their mole fractions, weighted by an energy-dependent calibration factor that includes a number of relevant experimental parameters. Here, the calibration factors for major species (C_5H_{12}, DME, EtOH, O_2, H_2O, CO, and CO_2) were determined from calibration with cold-gas samples and using the C, H, and O element balances at high-temperature equilibrium conditions. Intermediates were calibrated by simulating the signal ("convolution" method in [66]). The resulting uncertainties of mole fractions for major species are typically within 15%, and those for intermediate species are within a factor of 2, depending on the available cross section information from the literature. In cases where electron ionization cross sections or calibration information was not available as for some of the detected oxygenated species, relative species profiles are reported in terms of signal intensities normalized by the respective fuel inlet mole fraction to facilitate the analysis of trends between the behavior of individual mixture components and the mixtures. All experimental data reported in this work are provided in Supplementary Material 1 (SM1).

2.2 Numerical simulation

Simulations of the oxidation process in a laminar flow reactor have typically assumed a constant gas temperature or have relied on measured gas temperature profiles along the reactor, determined in non-reactive flows at identical reactor wall temperature [41,49,67]. Heat release in such reacting systems, typically approximated as negligible for highly diluted mixtures, is thus not considered, and consequently, negligible heat transfer between the reacting gas and the reactor wall is assumed, as no highly diluted conditions have been used here (10% reactive mixture). This limit may not be applicable for less diluted conditions, especially since temperature is a very sensitive parameter in the low-temperature oxidation process. An accurate physical model of a laminar flow reactor should consider mass convection, mass diffusion, heat release of the reacting gas, thermal conductivity, and thermal exchange with the wall of the reactor.

Since this work is mainly focused on reporting experimental results, we provide only a first approximation of model predictions for the investigated conditions. The simulation of the flow reactor using the OpenSMOKE++ package [68] follows procedures by Refs. [51,65]. A multi-zone approach was used, dividing the reactor into a pre-heating zone (14 cm), a reaction zone (111 cm), and a cooling zone (5 cm). A time-resolved non-isothermal solution was applied. The temperature profile of the non-reacting argon flow was measured along the reactor at different heating temperatures, and the heat transfer coefficient k for transfer between the heating furnace and the reacting gas through the flow reactor wall was evaluated by simulating a pure (non-reactive) argon flow. As a result, a coefficient of k=10 W m^{-2} K^{-1} was assigned for all reaction conditions. Details for the evaluation of k are provided together with the measured and simulated gas temperature profiles (Fig. S1) in Supplementary Material 2 (SM2). We acknowledge that this approach may reach its limits for the reactive mixtures with very temperature-sensitive chemistry, and suggest that the assumptions made here should be tested with more refined models in the future that might consider two-dimensional effects and changing heat transfer depending on reaction conditions.

For the initial simulation, two recent mechanisms were chosen to explore the interaction between

n-pentane and dimethyl ether or ethanol. The mechanism by Bugler *et al.* [39], here called the NUIG model, provides a low-temperature oxidation pentane sub-mechanism, which was improved based on their previous model [35] and examined against ignition delay times and JSR experimental data. The DME and ethanol sub-mechanisms in the NUIG model were also comprehensively investigated in their former kinetic studies [7,49,62]. Also, we have chosen the long-term developing and regularly updated model by Ranzi *et al.* [17], here called Polimi model. Their recent improvements in the low-temperature oxidation chemistry were focused on the reaction of carbonyl-hydroperoxides and peroxy radicals [17,21]. In any case, comparisons of our experimental data reported here with model simulations should be regarded as an initial exploration focused mainly on the trends observed for the mixtures, with the aim to detect substantial deviations between experiment and model that may serve to guide further model development.

3. Results and discussion

In this section, experimental results are presented for the dual-fuel mixtures and analyzed in consideration of those for the individual fuels. The main aim is to detect and contribute to understanding differences in reactivity and species formation in the low-temperature regime with *n*-pentane as the base fuel upon addition of each of the two oxygenated isomers. In addition, initial modeling is performed for the three individual fuels and the mixtures to examine, in particular, their capability to reproduce the trends in the low-temperature oxidation behavior. Generally, we will limit the model analysis to the NUIG model [39], with some additional results given for the Polimi model [17], especially to illustrate differences in the prediction for the fuel mixtures. A species list of the NUIG model with all species discussed in this work can be found in Table S1 in SM2 with formula, model name, nomenclature and structure.

Section 3.1 will present the conversion of the individual fuels and the dual-fuel combinations. Section 3.2 will provide more detailed insight into the reaction pathways for the different fuel components by reporting temperature-dependent profiles of intermediate species with an emphasis on

the behavior of the fuel mixtures. Section 3.3 will conclude with selected aspects of the low-temperature chemistry of these dual-fuel combinations.

3.1 Reactivity of dual-fuel mixtures

Selected experimental results for the low-temperature oxidation of all individual fuels and fuel combinations listed in Table 1 are given in Fig. 1. It shows the consumption of fuel and O_2 as well as the formation of H_2O and permits a first inspection of the temperature-dependent oxidation behavior. All major species profiles are presented in Figs. S2–S8 in SM2 together with simulations with the NUIG and Polimi models. The profiles in Fig. 1 are presented with the same scale, and a thin broken line at 616 K, the temperature for the low-temperature minimum of *n*-pentane consumption, is included to facilitate comparison.

As expected, both *n*-pentane and DME show a two-stage oxidation behavior (*n*-pentane: 616 K and 830 K, DME: 550 K and additional ignition at 750 K not in the focus here), while the consumption of ethanol starts only above 750 K. The low-temperature minimum of the fuel mole fraction near 550 K for DME is significantly lower than for *n*-pentane at 616 K. These temperatures compare quite well with the results of Herrmann *et al.* [51] for DME and ethanol (see also the Supplemental Material of that paper), and of Bugler *et al.* [39] for *n*-pentane, considering the slightly different conditions in those studies. Increasing addition of DME to *n*-pentane increases the reactivity and shifts the minimum to temperatures below that for pure *n*-pentane. Ethanol/*n*-pentane mixtures show some low-temperature reaction already for PE50 as particularly evident from the H_2O mole fraction with a peak near 625 K, and further increasing reactivity for PE75, with minima shifted to higher temperatures than for pure *n*-pentane.

In Fig. 2, the interaction effects are visualized in more detail, showing only the fuel consumption curves including predictions with both models. The four panels (a-d) consider these effects with *n*-pentane as the base fuel to which increasing amounts of DME (a,c) and ethanol (b,d) are added. Every profile is normalized by the inlet mole fraction of *n*-pentane in the specific mixture to ensure

comparability between the measurements. The bottom two panels (e,f) take an inverse perspective, with DME and ethanol as the respective basis and a corresponding normalization. Because of the normalization, identical profiles would be expected if no mixture effects occurred.

The enhancement of the reactivity of *n*-pentane by DME in panels (a,c) in Fig. 2 is quite well reproduced by both models. The experimental profiles are slightly shifted towards lower temperatures and may indicate a small trend of increasing low-temperature fuel conversion (conversion = 1 – consumption) that is, however, within the experimental uncertainty. In the NTC region, some differences are seen in the shape of the experimental profiles with increasing DME addition, and the recovery of the fuel mole fraction towards the initial value near 750 K is less pronounced for the PD50 mixture. The NUIG model reproduces the shape of the profile excellently for the pure *n*-pentane condition and catches the trends for all conditions quite well. With shifts to lower temperatures by about 12 K for PD75 and 22 K for PD50 and an increase in low-temperature fuel conversion, it slightly over-predicts the effect of DME on the reactivity. With the Polimi model, the predictions are closer to the experimental results, with shifts by about 8 K and 16 K to lower temperatures and almost identical fuel consumption in this regime, and a slightly better representation of the profiles also at higher temperatures. A tendency towards predicting two peaks can be noted in the NTC region for both the PD75 and PD50 mixtures. This effect is seen also in the major species curves in Figs. S5 and S6 in SM2. The reason for this behavior seems to be related to the representation of heat transfer in the numerical simulation (see Section 2.2), since exploratory modeling results for these two neat fuels and their mixtures without considering the heat release of the reacting gases (Figs. S9–S12 in SM2) do not show this two-peak behavior. As explained above in Section 2.2, the present modeling results should be considered as a first approximation, awaiting a more full description of two-dimensional effects and changing heat release that is, however, beyond the present study with a mainly experimental focus.

As seen in Fig. 2b,d, the addition of ethanol significantly inhibits the consumption of *n*-pentane in contrast to the effect of DME. It shifts the consumption temperature to a higher region, narrows the temperature window of the NTC zone, and significantly reduces the maximum fuel conversion. Both

models can well reproduce the *n*-pentane profile for the PE75 mixture but fail for PE50. The measured maximum conversion of *n*-pentane in PE50 is near 40%, while the NUIG model predicts only about 20% and the Polimi model shows only very weak low-temperature reaction.

Instead of focusing on *n*-pentane as the base fuel to which DME or ethanol is added, the opposite perspective is assumed in Fig. 2e,f which reports the consumption profiles for the oxygenated fuels. From this perspective, the addition of *n*-pentane inhibits the low-temperature behavior of DME but promotes that of ethanol. The strong effect evident from the experiments upon *n*-pentane addition to DME (Fig. 2e) is also reflected in the model predictions. The measured low-temperature consumption profiles are shifted to higher temperatures by 35 K for PD50 and 49 K for PD75. Both NUIG and Polimi models overestimate the reactivity of DME in the mixture conditions, and the NUIG model presents a wider temperature shift than the Polimi model. Also, differences are noted between experiment and model in the consumption around 725 K as a function of *n*-pentane addition, not well reflected in the NUIG model that apparently considers only weak interaction between both fuels and thus leads to negligible deviations between the PD75 and PD50 cases. The Polimi model results in a slightly better match with the experimental consumption curve in this region. A synergistic effect between DME and *n*-pentane is observed in the experiment, detecting somewhat higher conversion of these two active fuels in their mixtures than for each fuel individually. Trends in the two models differ in this respect.

The addition of *n*-pentane to ethanol enhances the ethanol reactivity in the low-temperature region (Fig. 2f). While inhibition of *n*-pentane consumption in this regime was already visible upon 50% ethanol addition (PE50, Fig. 2b,d), ethanol conversion in the PE50 mixture is negligible within the experimental uncertainty (therefore not included in Fig. 2f). A strong promotion tendency of *n*-pentane is seen for the PE75 mixture that shows a maximum low-temperature ethanol conversion of 35%. One reason why the ethanol mole fraction could decrease would be a dilution effect by *n*-pentane; the total moles of the reacting gas can expand due to the oxidation of *n*-pentane, leading to a reduction of the ethanol mole fraction. To confirm the reaction of ethanol near 650 K, the result of a simulation with

an assumed non-reactive ethanol species is provided in Fig. S13 in SM2 that shows the dilution effect to be negligible compared to the chemical reaction. The experimental observations for *n*-pentane addition to ethanol are reasonably well predicted by both models (Fig. 2f).

For a deeper understanding of the low-temperature reaction behavior of the fuel mixtures in consideration of the detailed reactions of the individual components, intermediate species formation along the fuel decomposition and oxidation reaction pathways will be presented with a focus on the experimental data, including discussion of simulation trends with the NUIG model.

3.2 Intermediate species formation

In the following, we will discuss the formation of key intermediate species observed in the low-temperature oxidation of the dual-fuel mixtures in view of the reaction pathways of the individual fuel components. Although the general structure of these LTC pathways is quite well known, schematic diagrams for the fuel-specific reactions in this study are presented for *n*-pentane in Fig. 3 and for the two oxygenated fuels in Fig. 4. They are intended to facilitate identification of intermediate species discussed in the text by their mass and molecular structure (compare also Table S1 in SM2) as well as by an assigned code number.

The following discussion is organized along the reaction pathways of *n*-pentane and will present the experimentally observed species profiles for this base fuel and the dual-fuel mixtures regarding important classes of low-temperature intermediates and changes upon DME and ethanol addition. Simulation results with the NUIG model are included for orientation.

Starting with the fuel *n*-pentane (RH, **P1**), H-abstraction forms the fuel radicals (R, **P2**) and the subsequent first oxygen addition yields pentylperoxy radicals (ROO, **P3**), not detectable in the present experiment, however. ROO can either form hydroperoxypentanes (**P4**) by H-addition or alkenes (**P5**) by HO_2-elimination or isomerize to QOOH radicals (**P6**). Along the reaction progress, the first stable, and thus detectable species are hydroperoxypentanes (**P4**) and alkenes (**P5**), discussed in Section 3.2.1. After isomerization of ROO (**P3**) ↔ QOOH (**P6**), a second O_2-addition step can occur leading to

O_2QOOH (**P7**) species. By OH-elimination the ketohydroperoxide (KHP, **P8**) is formed, which is the next stable and detectable intermediate, presented in Section 3.2.2, with consideration also of the ketohydroperoxide in the DME oxidation, hydroperoxymethyl formate (HPMF, **D8**). In Section 3.2.3, selected small oxygenated intermediates are provided including hydroperoxyalkanes, acids, and carbonyl compounds, accessible through further decomposition of the ketohydroperoxide, and Section 3.2.4 reports information on some further detected intermediates.

3.2.1 Hydroperoxypentanes (P4) and pentenes (P5)

Hydroperoxypentanes ($C_5H_{12}O_2$, P4)

Hydroperoxyalkanes are the products of ROO radicals *via* chain termination reactions, recognized as a competing channel to the ROO ↔ QOOH isomerization [12]. The signal of the stable species detected at a mass-to-charge ratio of m/z=104 with formula $C_5H_{12}O_2$ is therefore assigned here to hydroperoxypentanes (**P4**), without a possibility to discriminate between the **P4-1**, **P4-2**, and **P4-3** isomers in Fig. 3, however. Temperature-dependent $C_5H_{12}O_2$ profiles for the different conditions are provided in Fig. 5. The experimental profiles present the maximum for the base fuel *n*-pentane near 585 K in close agreement with the start of the fuel conversion. Small temperature shifts are observed when adding DME or ethanol to *n*-pentane. Modeling results, however, predict more important shifts, similarly to those observed for the *n*-pentane consumption profiles in Fig. 2. Quantification of hydroperoxypentanes (**P4**) was not possible because of lacking electron ionization cross sections, but the relative trends, namely higher conversion of C_5H_{12} → $C_5H_{12}O_2$ in the mixtures, are evident from the observed signal intensities, normalized to the inlet *n*-pentane mole fraction. As an indication for the probable concentration range, a mole fraction of about 3×10^{-5} has been observed by Rodriguez *et al.* [40] for the sum of hydroperoxypentanes in pure *n*-pentane oxidation under their lean JSR conditions. Hydroperoxypentane isomers (**P4**) are formed *via* the reaction of hydroperoxypentyl radicals ($C_5H_{11}O_2$, ROO, **P3**) and HO_2. Thus, the formation of hydroperoxypentane (**P4**) is determined by the efficiency of the pentyl (**P2**) production in the reacting system. DME oxidation provides an

enhanced amount of OH radicals already at lower temperatures, shifting hydroperoxypentane (**P4**) formation to lower temperatures and slightly increasing the amount. In contrast, ethanol reduces the production of hydroperoxypentanes (**P4**) and increases their formation temperature slightly. Particularly for the PE50 mixture, the signal is too weak to be detected in the experiment, thus only the modeling result is provided in Fig. 5. The NUIG model predictions show a slight tendency to overestimate the intensity of the influence of the oxygenated additive.

Pentenes (C_5H_{10}, P5)

Temperature-dependent profiles for C_5H_{10} (**P5**) are given in Fig. 6; the mole fraction represents the sum of 1-pentene and 2-pentene, with the C_5H_{10} signal calibrated as 1-pentene (with calibration based on 2-pentene, the total mole fraction would be 4.9% higher). The profiles reveal both low-temperature reactions as well as high-temperature formation from the fuel radicals (R, **P2**). Temperature shifts in both regimes are negligible for DME addition and minor upon ethanol addition, a trend that is also well captured by the model. Mixtures containing 75% *n*-pentane (PD75 and PE75) present similar pentene maxima to that in pure *n*-pentane (P100) oxidation, and reduction effects are only visible for the 50:50 mixtures (PD50 und PE50). Simulation results have been divided by a factor of 2 to fit the scale in Fig. 6 since the model over-predicts the mole fractions in all cases. For pure *n*-pentane oxidation, Bugler *et al.* [39] also show a tendency to over-predict especially 2-pentene concentrations under lean conditions at $\phi = 0.5$ and 1 atm.

3.2.2 Ketohydroperoxides (P8, D8)

Pentane ketohydroperoxide ($C_5H_{10}O_3$, P8)

Figure 7 presents the signal intensity for $C_5H_{10}O_3$ (**P8**), normalized by the different *n*-pentane inlet conditions. Note again that all profiles should be identical because of this normalization if no mixture effects would occur. The observed signal can be ascribed to the sum of C_5-ketohydroperoxide (**P8**), the three isomers of which have been identified by Rodriguez *et al.* [40]; from their SVUV-PIMS study

they reported a somewhat preferential formation of 3-hydroperoxy-pentanal (**P8-1**) and 1-hydroperoxy-3-pentanone (**P8-3**) over that of 2-hydroperoxy-4-pentanone (**P8-2**), which is kinetically favored, however, and provided mole fraction values of the order of 10^{-5} for the sum of the C_5-ketohydroperoxides for pure *n*-pentane oxidation under lean JSR conditions. Quantification is not possible here because electron ionization cross sections are lacking. The addition of DME (Fig. 7a) reduces the formation temperature, in agreement with the observed tendencies for *n*-pentane consumption and hydroperoxypentane formation (see above). The model represents the relative profile shape reasonably well for the pure *n*-pentane (P100) case. For the mixtures investigated here, the model overestimates the influence of DME. The reason may be lacking low-temperature-related reactions of the mixtures, as *e.g.*, $RO_2 + R'O_2 \rightarrow RO + R'O + O_2$ and H-abstraction of the RO_2 species of both fuels. With the addition of ethanol, the reactivity of the system is significantly reduced (Fig. 7b), and the profiles for the *n*-pentane/ethanol blends are shifted to higher temperature. The maximum signals decrease, in agreement with the lower consumption of *n*-pentane in Fig. 2b. The NUIG model can reproduce the tendencies for different conditions reasonably well, with the somewhat larger differences in the NTC region that were already evident in the fuel consumption profiles (Fig. 2b). For all five conditions, the experimental peak positions agree well with those for the hydroperoxypentanes (**P4**), as might be expected from the close relation of these species along the reaction pathway (Fig. 3), and those from the model again exhibit a larger spread in temperature.

DME ketohydroperoxide ($C_2H_4O_4$, HPMF, D8)

The general formation path of the ketohydroperoxide of DME proceeds similar to that of the pentane ketohydroperoxide (compare Fig. 4). In their experiments focused on low-temperature oxidation of DME in a JSR, Moshammer *et al.* [53,54] have identified the signal at *m/z*=92 corresponding to the sum formula of $C_2H_4O_4$ as hydroperoxymethyl formate (HPMF, **D8**). In the present work, HPMF (**D8**) was only detected for pure DME conditions due to its significant fragmentation and correspondingly,

low signal. CH_4O_3 at *m/z*=64 was confirmed by Moshammer *et al.* [53] to be a dominant fragment of HPMF (**D8**) by CO loss. They also performed theoretical calculations and assigned its structure as hydroxymethyl hydroperoxide ($HOOCH_2OH$, **D9**), clarifying earlier results of Wang *et al.* [41], who had also reported strong signals at this mass but assumed the species to be either hydroxymethyl hydroperoxide (**D9**) or trihydroxymethane. For the PD75 and PD50 mixtures, we thus consider the signal at *m/z*=64 to be representative of HPMF **(D8)** in light of the results of [53]. Figure 8 reports the results for *m/z*=92 (HPMF, **D8**) in the pure DME case (see insert top left) and *m/z*=64 (CH_4O_3, **D9**) for pure DME and the PD75 and PD50 mixtures. The temperatures of the maxima for both signals agree, supporting the assumption that the signal at *m/z*=64 can be used as an indicator for HPMF.

With the addition of a large amount of *n*-pentane, the concentration of HPMF **(D8)** decreases significantly, *e.g.,* a reduction of 90% for PD50 which can be partly due to diluting and chemical effects. Further reasons can include the shift towards higher temperatures that could enhance the decomposition of such labile species. Higher temperatures would also favor the reverse reaction of $R+O_2$, leading to a lower formation of ketohydroperoxide species and ultimately to reduced OH concentrations involved in forming fuel radicals. Nevertheless, the change seems more significant than that for the C_5-ketohydroperoxides (**P8**) in Fig. 7, and it may reveal information about the competition of the DME radical (CH_3OCH_2, **D2**) with the pentyl radical (**P2**) in the combination with O_2 molecules. Concerning the profile shapes, the NUIG model **(D8)** predicts a narrower temperature distribution of HPMF than the experiment for all conditions, with a width of only ~20 K versus ~50 K in the experiment, and it also provides smaller temperature shifts than the experiments with increasing *n*-pentane addition.

3.2.3 Selected small oxygenated intermediates

Hydroperoxymethane (CH_4O_2, P9-1) and hydroperoxyethane ($C_2H_6O_2$, P9-2)

Unlike hydroperoxypentanes (**P4**) that were discussed before, smaller hydroperoxyalkanes are

secondary oxidation products. Within the detection limit of the experiment of a few ppm, no quantifiable signals could be observed for hydroperoxybutane ($C_4H_{10}O_2$) and hydroperoxypropane ($C_3H_8O_2$). However, the smaller species hydroperoxymethane (CH_4O_2, **P9-1**) and hydroperoxyethane ($C_2H_6O_2$, **P9-2**) could be found. Methyl and ethyl radicals are derived from the decomposition of C_5-ketohydroperoxides (**P8**) and pentylperoxy radicals (ROO, **P3**), and their reactions with O_2 or HO_2 can lead to the formation of these smaller hydroperoxyalkanes. The profiles of CH_4O_2 (**P9-1**) and $C_2H_6O_2$ (**P9-2**) in Fig. 9 are normalized (in the *n*-pentane-containing mixtures) by the inlet mole fractions of *n*-pentane, and for the pure fuels, P100 shows higher conversion to these small hydroperoxyalkanes (**P9**) than DME.

Since doping with DME promotes the reactivity of the system and consequently, the formation of pentyl radicals (R, **P2**) and of typical intermediates derived from the fuel decomposition, it also enhances the formation of the hydroperoxyalkanes in Fig. 9a,c in the PD75 mixture. No significant further increase is observed with increased DME content for PD50, however. This behavior is different in the model for both, hydroperoxymethane (Fig. 9a,b) and hydroperoxyethane (Fig. 9c,d), especially for the formation of the latter in PD50. In the oxidation of DME, hydroperoxymethane (**P9-1**) is proposed to be formed along a sequence from the CH_3OCH_2OO radical (the ROO of DME, **D3**) via methyl formate (**D4**) and methyl radicals [54,69]. For pure DME (D100), hydroperoxymethane (**P9-1**) is indeed experimentally observed as shown in Fig. 9a, but the NUIG model predicts only insignificant amounts. Similar observations were noted by Moshammer *et al.* [54], who report a mole fraction for hydroperoxymethane of the order of 10^{-5} and point out large discrepancies between their DME JSR experiment and several models including the NUIG DME mechanism [7]. Ethanol can form neither of these hydroperoxyalkanes in its low-temperature reactions, so that in mixtures of *n*-pentane and ethanol they must be produced only from *n*-pentane. Their formation tendencies in P100, PE75, and PE50 (Fig. 9b,d) are similar to those of the hydroperoxypentanes (**P4**) (see Fig. 5b). The shift with ethanol to higher temperature is expected because of the decrease of the system in reactivity. The wider spread of the peak temperatures in the modeling results is similar to that shown before for the

C_5-ketohydroperoxides (**P8**). The NUIG model represents the observed tendencies for these mixtures reasonably well.

Formic acid (FAC)

Acids are important intermediates in the fuel oxidation process and lead to the formation of CO, CO_2, and esters. For the mixtures of *n*-pentane and DME, pentanoic, acetic, and formic acid are the most favorable products. Possible acid mass peaks, at *m/z*=102, 60, and 46 respectively, were detected in this work by EI-MBMS. However, in their investigation of *n*-pentane oxidation with SVUV-PIMS, Rodriguez *et al.* [40] identified the peak of *m/z*=102 as pentenylhydroperoxide, and their PIE curve did not indicate a slope at the ionization energy of pentanoic acid. The species of *m/z*=60 was identified as acetic acid by GC in the *n*-pentane oxidation study of Bugler *et al.* [39]. Here, we would need to consider not only acetic acid for *m/z*=60 but also methyl formate, since it dominates in the oxidation of DME [51]. With the used electron ionization, however, isomer identification was not possible. The signal at *m/z*=46 (CH_2O_2) is likely to be formic acid (**FAC**) as there are no other reasonable isomers, and is therefore calibrated as formic acid in this experiment. It is a typical DME-derived intermediate. *n*-Pentane also forms formic acid (**FAC**), but not in a similar amount as DME. Thus, **FAC** is selected as a typical species here to represent the interaction of *n*-pentane and DME. Figure 10a shows the experimental results for pure *n*-pentane, DME, and their mixtures, together with model simulations, while the complementary mixtures with ethanol, for which no significant interaction is noted, are presented in Fig. 10b.

Large temperature shifts are seen along the replacement of *n*-pentane with DME that are quite well matched by the model and correspond approximately to the consumption maxima in Fig. 2. Trends for the mixtures in the low-temperature region are quite well captured by the NUIG model that over-predicts **FAC** for P100, however, and under-predicts it for D100. This could be explained by the

lacking importance of a reaction producing formic acid as suggested by Wang *et al.* [70]. They showed that the isomerization reaction of $OCH_2OCHO \rightarrow HOCH_2OCO$ is predicted to be more dominant in most models than its reaction to form formic acid ($OCH_2OCHO \rightarrow HCOOH + HCO$) which has; however, a much lower energy barrier and should therefore be more dominant (see figure 3 of Ref. [70]). For the *n*-pentane/DME mixtures, the NUIG model reveals two formation pathways of formic acid to yield major contributions as shown in the rate of production (ROP) analysis in Fig. 11, where the reaction suggested in Ref. [70] is not considered.

From the ROP in Fig. 11 it can be seen that the pathway involving acetaldehyde (CH_3CHO, **AAL**) is important in the *n*-pentane oxidation, while the $HOCH_2O$ radical (**D12**) channel contributes for both fuels, but to a larger extent for DME oxidation. Over this channel, **FAC** is formed *via* the decomposition of HPMF (**D8**) for D100 (see Fig. 4), or the combination of OH and CH_2O *via* the intermediate radical of $HOCH_2O$ for P100 (see Fig. 3). The formaldehyde pathway becomes more important with the addition of DME. However, the rate constant of this channel estimated in the NUIG model is much faster than that from the theoretical investigation of Xu *et al.* [71], and its influence might thus be overestimated.

Carbonyl compounds

Formaldehyde (**FAL**), acetaldehyde (**AAL**), and butanone are important intermediates in *n*-pentane oxidation [39]. **AAL** is mainly formed *via* the decomposition of 2-hydroperoxy-4-pentanone (**P8-2**), which is, however, not the major ketohydroperoxide isomer in the *n*-pentane oxidation according to Rodriguez *et al.* [40], who measured only **P8-1** and **P8-3** in their experiment. However, **P8-2** is quite important in the formation of methyl radicals and impacts the formation of hydroperoxymethane (**P9-1**), formaldehyde (**FAL**) and even OH radicals *via* its subsequent reactions. The mole fractions of acetaldehyde and formaldehyde, normalized (in the *n*-pentane-containing mixtures) by the inlet mole

fraction of *n*-pentane, are given in Fig. 12; as stated before, changes observed are thus due to interactive effects in the mixtures.

As seen in Fig. 12a, the **AAL** mole fraction is not changed significantly upon blending with 25% DME, but it is notably reduced with 50% DME, while the model predicts a constant **AAL** mole fraction. With increasing ethanol addition (Fig. 12b), the pathway forming acetaldehyde from ethanol (compare Fig. 4) gains importance, as also seen in the ROP analysis in Fig. 13. Ethanol is activated by OH provided by the *n*-pentane oxidation. The ethanol radical (sC_2H_4OH**, E2-3**) that consumes ~70% of ethanol is the precursor of acetaldehyde.

Formaldehyde (**FAL**) as a typical oxidation intermediate is formed by different reactions for the three investigated fuels. CH_3 radical reactions provide major contributions to **FAL** for *n*-pentane, while the decomposition of CH_3OCH_2OO (ROO, **D3**) and CH_2OCH_2OOH (QOOH, **D6**) radicals are the main formation reactions of formaldehyde (**FAL**) in the oxidation of DME. For ethanol, the formation of **FAL** involves pathways *via* the methyl and the $O_2C_2H_4OH$ (**E3-1**) radicals. Figure 12c,d shows the normalized mole fractions of formaldehyde for all mixtures. Opposite tendencies are observed. With DME addition, the mole fraction increases compared to P100, but PD75 and PD50 show nearly the same amount. With the addition of ethanol, the mole fraction is similar for P100 and PE75, but lower for PE50.

The behavior of acetaldehyde (**AAL**) and formaldehyde (**FAL**) could be roughly explained by the enhanced H-abstraction of C_5-ketohydroperoxides (**P8**) according to the work of Ranzi *et al.* [17]. The common reaction pathway for the decomposition of ketohydroperoxide species is described as O-O scission and subsequent β-scission. Here, this reaction sequence would lead to the formation of acetaldehyde. However, the decomposition pathway by H-abstraction of the C_5-ketohydroperoxide and subsequent β-scission proposed by Ranzi *et al.* [17] would lead to pentadione and ketene. These recently proposed reaction classes are not included in the NUIG kinetic model, and their implementation could lead to a better prediction of acetaldehyde especially for PD50 compared to PD75 (see Fig. 12a). The ROP analysis for acetaldehyde (**AAL**) in Fig. 13 shows that $NC_5KET24O$

(**P10-2**) is the main pathway, with the caveat, however, that the used model does not include the competing channels. The ROP analysis for formaldehyde (**FAL**) in Fig. 13 shows another important formation channel from the CH_3COCH_2O radical (*via* the acetonyl radical) in the blends with ethanol. It is a product of the unimolecular decomposition of 2-hydroperoxy-4-pentanone (**P8-2**). Because of the reduced amount of OH by ethanol, it reduces the general efficiency of formaldehyde formation but favors the unimolecular decomposition of **P8-2**. The production of formaldehyde in the ethanol-containing blends is therefore altered to the reaction sequence 2-hydroperoxy-4-pentanone ($C_5H_{10}O_3$, **P8-2**) → 2-pentanoxide-4-one ($C_5H_9O_2$, **P10-2**) → CH_3COCH_2 (C_3H_5O, acetonyl) → CH_3COCH_2O ($C_3H_5O_2$) → CH_2O (**FAL**), compare also Fig. 3.

3.2.4 Further intermediates

While the previous analysis has focused on the fuel decomposition schemes and small oxygenated species, a number of further intermediates has also been detected, and selected species are presented in Fig. 14, with experimental results in panels (a,d) and predictions with the NUIG and Polimi models in panels (b,e and c,f). Again, all mole fractions (in the *n*-pentane-containing mixtures) have been normalized by the inlet mole fraction of *n*-pentane for the respective conditions. The maximum values of all species in the NTC zone are grouped in order to illustrate the selectivity of *n*-pentane reaction pathways impacted by the addition of DME or ethanol. Please note that full temperature-dependent mole fraction profiles over the entire range from 450–900 K are provided, together with simulations with the NUIG model, in Figs. S14–S21 in SM2. In general, the shapes of these profiles are reasonably well predicted. However, with an emphasis on the experiment and on the low-temperature reactions in the dual-fuel mixtures, we will limit the discussion here to some aspects in the LTC region. Due to the normalization, mole fraction values should agree if there were no interactive effects. Inspection of the patterns in Fig. 14 reveals some important differences between experimental and modeling results.

Figure 14a-c compares experiment and model predictions for selected oxygenated intermediates. Since acetic acid is the major acid produced in the oxidation of *n*-pentane [39], it is identified as the

dominant isomer of $C_2H_4O_2$ in P100, PE75, and PE50. However, methyl formate is the oxidation product of DME with the formula of $C_2H_4O_2$ [51,54], which is also observed in this experiment. Therefore, with the addition of DME, methyl formate becomes the major isomer of $C_2H_4O_2$. However, due to lacking EI cross sections of methyl formate, $C_2H_4O_2$ has been calibrated as acetic acid in all experiments. Hydroxyacetaldehyde would be another isomer, but there is no known pathway how it could be formed and it seems kinetically unlikely. Compared to the modeling results, this species is well-predicted by the Polimi model but highly under-predicted by NUIG model. Bugler *et al.* [39] also reported the under-prediction of their measurement of $C_2H_4O_2$ in the oxidation of *n*-pentane in a JSR.

The further species in Fig. 14a-c are single oxygenated species of the sum formula $C_nH_{2n}O$ that can be assigned to cyclic ethers, aldehydes, and ketones, and $C_nH_{2n-2}O$ that are probably ketenes. CH_2O can only be formaldehyde, C_2H_2O obviously is ketene, and C_3H_4O has been calibrated as methyl ketene. According to previous analysis with GC, CRDS, and FTIR [39], C_2H_4O was separated for oxirane and acetaldehyde, but is here calibrated only as acetaldehyde due to missing distinction of isomers. In Ref. [39], C_3H_6O was identified as propanal, acetone, 2-methyloxirane, and oxetane, here it is calibrated as acetone. In general, aldehyde compounds could be produced from the decomposition of the C_5-hydroperoxides or ketohydroperoxides by breaking the O-OH bond in the hydroperoxy group. Cyclic ethers are usually formed *via* the reactions of QOOH radicals. Looking at the tendencies in Fig. 14a-c in both experimental and modeling results, identical selectivity is observed in both experiment and Polimi model predictions among different $C_nH_{2n}O$ and $C_nH_{2n-2}O$ species under different inlet condition except for PE50. The NUIG model predictions for CH_2O, C_2H_4O and C_3H_6O are closer to the experimental values than those for the other shown species, with substantial deviations especially for C_2H_2O (ketene) and $C_2H_4O_2$ (acetic acid), see also Figs. S14 and S17 in SM2.

Figure 14d-f presents the experimental and modeling results for selected alkanes and alkenes. Pentene (C_5H_{10}, calibrated as 1-pentene), propene (C_3H_6), and ethene (C_2H_4) are major intermediates. Both models well predict the formation of pentene and ethene, but under-predict the formation of butene (C_4H_8, here calibrated as 1-butene) and propene. A uniform selectivity can be found among

these species in different conditions in Fig. 14d-f, except for ethane (C_2H_6), for which experiment and model reveal opposite tendencies with the addition of DME and ethanol. As observed in the formation of hydroperoxymethane (Fig. 9), the methyl radical formed in the decomposition of DME undergoes the recombination to ethane, but not the reaction with O_2. Since ethane is under-predicted by a factor of 100 in P100, a significant difference can be observed by the addition of DME for the modeling result, but not in the experiment.

3.3 Selected aspects influencing the reactivity

To inspect the reactivity of the dual-fuel mixtures further, the known major low-temperature oxidation cycles for the three individual fuels are shown schematically in Fig. 15. For all cycles, the solid thick arrows show reactions that produce OH radicals, while the solid thin arrows indicate OH-consumption. To obtain the maximum of OH being produced from one complete cycle, the solid thick arrows after the second O_2 addition (behind O_2QOOH) need to be considered as all other reactions producing OH before this step lead to a termination of the cycle.

As seen in Fig. 15a for *n*-pentane, the two-step O_2 addition reaction sequence from the fuel could yield three OH radicals (solid thick arrows after O_2QOOH), while it consumes only one OH radical in its pentyl radical production process *via* H-abstraction reactions (solid thin arrow). The α-step is the most important *n*-pentane consumption reaction, which may be in strong competition in the fuel blends or with other primary intermediates during the reaction process.

OH is the dominant initial radical for the recurrence of the branching process of DME. As shown in Fig. 15b, a maximum of two OH radicals could be produced through one cycle (solid thick arrows after O_2QOOH), while also only one OH is consumed by the DME radical formation (solid thin arrow). However, in the α-step, a strong competition from *n*-pentane impacts the consumption of OH radicals. When the more reactive fuel DME is added to *n*-pentane, OH radicals could be produced at lower temperatures, thus promoting the system's reactivity. However, the maximum conversion of *n*-pentane keeps almost the same with the addition of DME (compare Fig. 2a), which means that the consumption

of OH radicals by *n*-pentane does not significantly increase. This may be due to the similar concentration of OH radicals at identical equivalence ratio, or *n*-pentane taking advantage over DME in the competition of OH radical reactions.

Figure 15c shows the reactions of ethanol in the low-temperature region. The light-grey arrows indicate a fictitious second O_2 addition that cannot happen because of ethanol's molecular structure. Therefore, ethanol consumes one OH radical (solid thin arrow), and produces almost none in its reaction recurrence, as the ROO is very unlikely to be formed. Since ethanol plays the role of an OH radical consumer in *n*-pentane/ethanol mixtures, it sufficiently reduces the pool of active radicals and inhibits the general reactivity of the whole system.

As discussed above, the OH radical plays an important role in the H-abstraction of *n*-pentane, DME, and ethanol during the ignition progress in the low-temperature regime. H-abstraction reactions, especially with OH, are the first step turning RH (C_5H_{12}, DME, or EtOH) into the R radical. It is interesting to view the balance of OH and HO_2, another prominent radical associated with low-temperature reactions. Fig. 16 shows the simulated mole fraction ratio of OH/HO_2 for all fuel conditions. It is the ratio between the maxima of OH and HO_2 radicals along the flow reactor at each temperature point in the range of 475–750 K.

According to both, NUIG and Polimi models, the mole fraction of the OH radical is ~10^{-8} in the NTC zone, and that of the HO_2 radical is ~10^{-5} in that zone, corresponding to the high reactivity of OH in the H-abstraction reactions. For the neat fuels, the x_{OH}/x_{HO2} ratio is highest for DME at very low temperatures of 480–580 K. After a slow but steady rise in this region, a steep increase occurs around 540 K, coincident with the DME low-temperature consumption maximum (see Fig. 2e). With rising temperature, the low-temperature kinetics slows down and chain-terminating reactions become of increasing importance. After a steep increase in OH production at about 560 K for *n*-pentane, approximately in the zone where low-temperature fuel consumption accelerates (see Fig. 2a), a plateau is reached that represents the competing reactions in the NTC region. Similar approximately constant values of the x_{OH}/x_{HO2} ratio are also evident in the intermediate temperature range of about 570–670 K

for DME and the *n*-pentane/DME mixtures in Fig. 16b. As discussed before, ethanol shows a much lower relative OH production in the low-temperature regime, with a rise of the x_{OH}/x_{HO2} ratio only noted above 650 K with much lower values than for the other two fuels, and it should be remembered that no significant low-temperature fuel consumption was noted in this case (see Fig. 2f). Ethanol-containing mixtures with *n*-pentane exhibit a significantly increased OH production around 580 K for PE75 and 600 K for PE50, approximately near the respective start of fuel consumption; a plateau at higher temperatures up to 650 K can also be noted for these mixtures (Fig. 16c). The formation and consumption of OH radicals based on the reaction cycles in Fig. 15 can contribute to the understanding of the low-temperature system reactivity; more details on the efficiency of OH production following a similar analysis of Dames *et al.* [8] and Merchant *et al.* [18] for propane and propane/DME mixtures are also provided in Section S6 of SM2. They support the strong decrease in low-temperature reactivity for ethanol addition to *n*-pentane and show a small tendency of higher OH yield in the *n*-pentane/DME mixtures. It must be noted, however, that an assessment of the total OH production in the system may explain some features of the dual-fuel behavior, especially when systems with quite different low-temperature reactivity are considered. For the *n*-pentane/DME mixtures that show synergistic effects, these cannot be understood in terms of the OH balance alone but need to consider the formed fuel radicals and other early intermediates and their secondary reactions. For this reason, sensitivity analyses of OH were performed with the NUIG model for P100, PD75, and PD50 at 25% *n*-pentane conversion and are provided in Fig. 17.

The results also show the interaction of *n*-pentane and DME *via* the competition of the OH radical. In general, H-abstraction of *n*-pentane at the γ-site shows the highest negative coefficient, since for this radical it is most difficult to form new OH radicals in its further reactions. Upon DME addition, the abstraction reactions at the other two sites of *n*-pentane by OH radicals reduce their positive sensitivity or even turn to negative values. Second O_2-addition reactions have stronger sensitivities than the first O_2-addition step. The unimolecular decomposition reaction of the C_5-ketohydroperoxide (**P8**), forming one OH radical, becomes slightly less important with the doping of DME, whilst the

H-abstraction reaction of DME and the decomposition of HPMF (**D8**) become very sensitive reactions for the mixture conditions, of increasing importance with higher DME fraction. Especially the formation and decomposition reactions of the ketohydroperoxide of the respective fuel are thus important pathways in the formation of OH radicals influencing the overall reactivity of the system.

4. Summary and perspectives

The low-temperature oxidation of mixtures of *n*-pentane with the oxygenated C_2H_6O fuel isomers dimethyl ether and ethanol, including that of the three individual fuels, was experimentally investigated in a flow reactor at an equivalence ratio of 0.7 and atmospheric pressure, covering the temperature range of 450–930 K. Electron ionization molecular-beam mass spectrometry was used to provide a detailed species overview under all conditions, with quantitative evaluation as mole fraction profiles whenever possible. In cases where only relative signal intensities could be provided, trends between the individual fuels and the mixtures could be identified. The overall reactivity of the fuels and their mixtures was discussed, considering the very different low-temperature behavior of the three individual fuels. To emphasize interactive effects of the C_2H_6O isomers in the blends with *n*-pentane, normalization on the *n*-pentane inlet mole fractions was performed. Ethanol, as a fuel that exhibits only marginal low-temperature reactivity, is a significant consumer of active free radicals and thus inhibits the oxidation process in the mixtures, whilst the mixture of two reactive fuels, *n*-pentane and DME, presents noticeable synergistic effects where the maximum conversion of both *n*-pentane and DME is improved in the mixtures compared to the pure fuels.

For a deeper albeit preliminary understanding of the effects in the LTC of the dual-fuel mixtures, two current models, namely the NUIG and the Polimi models that can both be considered well examined for the individual fuels were adopted in simulations for all conditions. Both models were seen to perform reasonably well regarding the fuel consumption and major species formation for the individual fuels, but the predictions of temperature shifts and synergistic effects, especially in the oxidation behavior of the mixtures leave room for improvement. Such further developments can in

part be considered for the simulation of two-dimensional effects and heat transfer in the flow reactor with more refined models than used in these preliminary predictions, especially in zones with very temperature-sensitive reactions.

The oxidation chemistry in the fuel mixtures was analyzed in more detail on the basis of the reaction pathways of the individual fuel components by following the sequence of initial fuel decomposition products and their further reactions by means of intermediate species profiles. Mole fractions of oxygenated intermediates as well as selected hydrocarbon species were presented with an emphasis on the zone of the initial fuel conversion and NTC region in the mixtures, and trends between experiment and model were compared, resulting in an overall somewhat diverse picture. While many trends seen in the experiments upon blending of *n*-pentane with either one of the two isomers are quite well reproduced by these preliminary simulations, the magnitude of the effects is not always correctly predicted, and large discrepancies are seen for some intermediates.

Regarding the reactivity of the system, the OH balance as well as the ratio of OH and HO_2, both important intermediates in the low-temperature oxidation zone, were inspected to assist understanding of some aspects of the interactions for the dual-fuel mixtures. The OH competition between *n*-pentane and ethanol, two fuels with very different low-temperature reactivity, seems simpler than between *n*-pentane and DME that both show low-temperature reactions with different production cycles of OH. Secondary products such as alkyl radicals could participate in this OH competition by enhancement of O_2 addition reactions that in turn can contribute to OH radical production. Because they are involved in the formation of OH radicals, acetaldehyde, hydroperoxyethane, and especially hydroperoxymethane, could also be considered as indicative species of the reactivity of the fuel mixture. Interactive effects between the reactive species provided in the fuel mixtures may result in a higher maximum conversion of both fuels than found for each of them individually.

The work presented here suggests several areas for further work. As seen in some cases, the nature of the isomer composition might change for the fuel blends, with $C_2H_4O_2$ as one example that should be predominantly acetic acid for *n*-pentane and methyl formate for DME oxidation. Isomer-resolved,

quantitative species analysis over the critical temperature range between about 500 and 650 K for these dual-fuel mixtures is thus recommended as a further continuation of this work. It would be especially useful if it provided detailed data on first fuel decomposition products and highly oxygenated species. Furthermore, in spite of recent model development and ample knowledge on the oxidation of the three individual fuels in the literature, it seems that interactive effects cannot be fully captured and might need more accurate determination of critical reaction parameters in the low-temperature zone where the initial fuel consumption accelerates. Temperature dependences may need to be inspected with care. As one indicator for such needs, it is interesting to note that the rate expressions for the H-abstraction reactions by OH for the three individual fuels exhibit important differences in both tested models. Since reliable predictions for the oxidation behavior of mixtures of alkane fuels with ethanol or DME – or more generally of hydrocarbon with oxygenated fuels – are highly desirable, we hope that the presented experimental dataset will contribute to the further improvement of models for such dual-fuel mixtures.

Acknowledgements

The authors wish to thank the Deutsche Forschungsgemeinschaft (DFG) for support of this work under contract KO1363/31-1. HJ is grateful for a fellowship of the Alexander von Humboldt (AvH) Foundation that supported his research period in Bielefeld. Helpful discussions with Dr. Luc-Sy Tran, now at Lille University, during his research period as an AvH Fellow in Bielefeld are gratefully acknowledged. Furthermore, the authors wish to thank Prof. Yiguang Ju, Princeton University, USA, for his profound and continuous interest in this work, for insightful discussions and for hosting HJ for a research stay in his group.

References

[1] A.K. Agarwal, Biofuels (alcohols and biodiesel) applications as fuels for internal combustion engines, Prog. Energy Combust. Sci. 33 (2007) 233–271.

[2] W. Leitner, J. Klankermayer, S. Pischinger, H. Pitsch, K. Kohse-Höinghaus, Advanced biofuels and beyond: Chemistry solutions for propulsion and production, Angew. Chem. Int. Ed. 129 (2017) 5500–5544.

[3] X. Lu, D. Han, Z. Huang, Fuel design and management for the control of advanced compression-ignition combustion modes, Prog. Energy Combust. Sci. 37 (2011) 741–783.

[4] S. Kokjohn, R. Hanson, D. Splitter, J. Kaddatz, R. Reitz, Fuel reactivity controlled compression ignition (RCCI) combustion in light- and heavy-duty engines, SAE Int. J. Fuels Lubr. 4 (2011) 2011-01–0357.

[5] S. Saxena, I.D. Bedoya, Fundamental phenomena affecting low temperature combustion and HCCI engines, high load limits and strategies for extending these limits, Prog. Energy Combust. Sci. 39 (2013) 457–488.

[6] B. Prabhakar, S. Jayaraman, R. Vander Wal, A. Boehman, Experimental studies of high efficiency combustion with fumigation of dimethyl ether and propane into diesel engine intake air, J. Eng. Gas Turb. Power 137 (2015) 41505.

[7] U. Burke, K.P. Somers, P. O'Toole, C.M. Zinner, N. Marquet, G. Bourque, E.L. Petersen, W.K. Metcalfe, Z. Serinyel, H.J. Curran, An ignition delay and kinetic modeling study of methane, dimethyl ether, and their mixtures at high pressures, Combust. Flame 162 (2015) 315–330.

[8] E.E. Dames, A.S. Rosen, B.W. Weber, C.W. Gao, C.-J. Sung, W.H. Green, A detailed combined experimental and theoretical study on dimethyl ether/propane blended oxidation, Combust. Flame 168 (2016) 310–330.

[9] M. Cord, B. Husson, J.C. Lizardo Huerta, O. Herbinet, P.-A. Glaude, R. Fournet, B. Sirjean, F. Battin-Leclerc, M. Ruiz-Lopez, Z. Wang, M. Xie, Z. Cheng, F. Qi, Study of the low temperature oxidation of propane, J. Phys. Chem. A 116 (2012) 12214–12228.

[10] M. Cord, B. Sirjean, R. Fournet, A. Tomlin, M. Ruiz-Lopez, F. Battin-Leclerc, Improvement of the modelling of the low-temperature oxidaton of *n*-butane - Study of the primary reactions, J. Phys. Chem. A 116 (2012) 6142–6158.

[11] C. Bahrini, P. Morajkar, C. Schoemaecker, O. Frottier, O. Herbinet, P.-A. Glaude, F. Battin-

Leclerc, C. Fittschen, Experimental and modeling study of the oxidation of *n*-butane in a jet stirred reactor using cw-CRDS measurements, Phys. Chem. Chem. Phys. 15 (2013) 19686–19698.

[12] F. Battin-Leclerc, O. Herbinet, P.-A. Glaude, R. Fournet, Z. Zhou, L. Deng, H. Guo, M. Xie, F. Qi, Experimental confirmation of the low-temperature oxidation scheme of alkanes, Angew. Chem. Int. Ed. 49 (2010) 3169–3172.

[13] O. Herbinet, F. Battin-Leclerc, S. Bax, H. Le Gall, P.-A. Glaude, R. Fournet, Z. Zhou, L. Deng, H. Guo, M. Xie, F. Qi, Detailed product analysis during the low temperature oxidation of *n*-butane, Phys. Chem. Chem. Phys. 13 (2011) 296–308.

[14] D. Healy, N.S. Donato, C.J. Aul, E.L. Petersen, C.M. Zinner, G. Bourque, H.J. Curran, *n*-Butane: Ignition delay measurements at high pressure and detailed chemical kinetic simulations, Combust. Flame 157 (2010) 1526–1539.

[15] D. Healy, D.M. Kalitan, C.J. Aul, E.L. Petersen, G. Bourque, H.J. Curran, Oxidation of C1-C5 alkane quinternary natural gas mixtures at high pressures, Energy Fuels 24 (2010) 1521–1528.

[16] D. Healy, M.M. Kopp, N.L. Polley, E.L. Petersen, G. Bourque, H.J. Curran, Methane/*n*-butane ignition delay measurements at high pressure and detailed chemical kinetic simulations, Energy Fuels 24 (2010) 1617–1627.

[17] E. Ranzi, A. Cuoci, A. Frassoldati, M. Pelucchi, T. Faravelli, New reaction classes in the kinetic modeling of low temperature oxidation of n-alkanes, Combust. Flame 162 (2015) 1679–1691.

[18] S.S. Merchant, C.F. Goldsmith, A.G. Vandeputte, M.P. Burke, S.J. Klippenstein, W.H. Green, Understanding low-temperature first-stage ignition delay: Propane, Combust. Flame 162 (2015) 3658–3673.

[19] P. Saisirirat, C. Togbé, S. Chanchaona, F. Foucher, C. Mounaim-Rousselle, P. Dagaut, Auto-ignition and combustion characteristics in HCCI and JSR using 1-butanol/*n*-heptane and ethanol/*n*-heptane blends, Proc. Combust. Inst. 33 (2011) 3007–3014.

[20] P. Saisirirat, F. Foucher, S. Chanchaona, C. Mounaïm-Rousselle, Spectroscopic measurements of low-temperature heat release for homogeneous combustion compression ignition (HCCI) *n*-heptane/alcohol mixture combustion, Energy Fuels 24 (2010) 5404–5409.

[21] M. Pelucchi, M. Bissoli, C. Cavallotti, A. Cuoci, T. Faravelli, A. Frassoldati, E. Ranzi, A. Stagni, Improved kinetic model of the low-temperature oxidation of *n*-heptane, Energy Fuels 28 (2014) 7178–7193.

[22] D.M.A. Karwat, S.W. Wagnon, M.S. Wooldridge, C.K. Westbrook, Low-temperature speciation and chemical kinetic studies of *n*-heptane, Combust. Flame 160 (2013) 2693–2706.

[23] O. Herbinet, B. Husson, Z. Serinyel, M. Cord, V. Warth, R. Fournet, P.-A. Glaude, B. Sirjean, F. Battin-Leclerc, Z. Wang, M. Xie, Z. Cheng, F. Qi, Experimental and modeling investigation of the low-temperature oxidation of *n*-heptane, Combust. Flame 159 (2012) 3455–3471.

[24] R. Di Sante, Measurements of the auto-ignition of *n*-heptane/toluene mixtures using a rapid compression machine, Combust. Flame 159 (2012) 55–63.

[25] G.E. Bogin Jr., A. DeFilippo, J.Y. Chen, G. Chin, J. Luecke, M.A. Ratcliff, B.T. Zigler, A.M. Dean, Numerical and experimental investigation of *n*-heptane autoignition in the ignition quality tester (IQT), Energy Fuels 25 (2011) 5562–5572.

[26] M. Ribaucour, R. Minetti, L.R. Sochet, H.J. Curran, W.J. Pitz, C.K. Westbrook, Ignition of isomers of pentane: An experimental and kinetic modeling study, Proc. Combust. Inst. 28 (2000) 1671–1678.

[27] R. Minetti, A. Roubaud, E. Therssen, M. Ribaucour, L.R. Sochet, The chemistry of pre-ignition of n-pentane and 1-pentene, Combust. Flame 118 (1999) 213–220.

[28] C.K. Westbrook, H.J. Curran, W.J. Pitz, J.F. Griffiths, C. Mohamed, S.K. Wo, The effects of pressure, temperature, and concentration on the reactivity of alkanes: Experiments and modeling in a rapid compression machine, Proc. Combust. Inst. 27 (1998) 371–378.

[29] M. Ribaucour, R. Minetti, L.R. Sochet, Autoignition of *n*-pentane and 1-pentene: Experimental data and kinetic modeling, Proc. Combust. Inst. 27 (1998) 345–351.

[30] J.F. Griffiths, P.A. Halford-Maw, C. Mohamed, Spontaneous ignition delays as a diagnostic of the propensity of alkanes to cause engine knock, Combust. Flame 111 (1997) 327–337.

[31] R. Minetti, M. Ribaucour, M. Carlier, L.R. Sochet, Autoignition delays of a series of linear and branched chain alkanes in the intermediate range of temperature, Combust. Sci. Technol. 113–114 (1996) 179–192.

[32] A. Cox, J.F. Griffiths, C. Mohamed, H.J. Curran, W.J. Pitz, C.K. Westbrook, Extents of alkane combustion during rapid compression leading to single- and two-stage ignition, Proc. Combust. Inst. 26 (1996) 2685–2692.

[33] J.F. Griffiths, P.A. Halford-Maw, D.J. Rose, Fundamental features of hydrocarbon autoignition in a rapid compression machine, Combust. Flame 95 (1993) 291–306.

[34] B. Marks, O. Mathieu, R. Archuleta, E.L. Petersen, J. Bugler, A. Heufer, H. Curran, Ignition

delay time measurements and modeling of *n*-pentane and *iso*-pentane at elevated pressures, 51st AIAA Aerosp. Sci. Meet. (2013).

[35] J. Bugler, B. Marks, O. Mathieu, R. Archuleta, A. Camou, C. Grégoire, K.A. Heufer, E.L. Petersen, H.J. Curran, An ignition delay time and chemical kinetic modeling study of the pentane isomers, Combust. Flame 163 (2016) 138–156.

[36] V.P. Zhukov, V.A. Sechenov, A.Y. Starikovskii, Self-ignition of a lean mixture of *n*-pentane and air over a wide range of pressures, Combust. Flame 140 (2005) 196–203.

[37] A. Chakir, M. Bellimam, J.C. Boettner, M. Cathonnet, Kinetic study of *n*-pentane oxidation, Combust. Sci. Technol. 77 (1991) 239–260.

[38] V. Simon, Y. Simon, G. Scacchi, F. Baronnet, Étude expérimentale et modélisation des réactions d'oxydation du *n*-pentane et du cyclopentane, Can. J. Chem. 75 (1997) 575–584.

[39] J. Bugler, A. Rodriguez, O. Herbinet, F. Battin-Leclerc, C. Togbé, G. Dayma, P. Dagaut, H.J. Curran, An experimental and modelling study of n-pentane oxidation in two jet-stirred reactors: The importance of pressure-dependent kinetics and new reaction pathways, Proc. Combust. Inst. 36 (2017) 441–448.

[40] A. Rodriguez, O. Herbinet, Z. Wang, F. Qi, C. Fittschen, P.R. Westmoreland, F. Battin-Leclerc, Measuring hydroperoxide chain-branching agents during n-pentane low-temperature oxidation, Proc. Combust. Inst. 36 (2017) 333–342.

[41] Z. Wang, X. Zhang, L. Xing, L. Zhang, F. Herrmann, K. Moshammer, F. Qi, K. Kohse-Höinghaus, Experimental and kinetic modeling study of the low- and intermediate-temperature oxidation of dimethyl ether, Combust. Flame 162 (2015) 1113–1125.

[42] K. Kohse-Höinghaus, P. Oßwald, T.A. Cool, T. Kasper, N. Hansen, F. Qi, C.K. Westbrook, P.R. Westmoreland, Biofuel combustion chemistry: From ethanol to biodiesel, Angew. Chem. Int. Ed. 49 (2010) 3572–3597.

[43] W. Ying, Z. Longbao, Performance and emissions of a compression-ignition engine fueled with dimethyl ether and rapeseed oil blends, Energy Fuels 21 (2007) 1454–1458.

[44] Y. Tsutsumi, K. Hoshina, A. Iijima, H. Shoji, Analysis of the combustion characteristics of a HCCI engine operating on DME and methane, SAE Tech. Pap. 2007-65–41 (2007).

[45] M. Konno, Z. Chen, Ignition mechanisms of HCCI combustion process fueled with methane/DME composite fuel, SAE Tech. Pap. 2005-01–01 (2005).

[46] U. Pfahl, K. Fieweger, G. Adomeit, Self-ignition of diesel-relevant hydrocarbon-air mixtures

under engine conditions, Proc. Combust. Inst. 26 (1996) 781–789.

[47] N. Kurimoto, B. Brumfield, X. Yang, T. Wada, P. Diévart, G. Wysocki, Y. Ju, Quantitative measurements of HO_2/H_2O_2 and intermediate species in low and intermediate temperature oxidation of dimethyl ether, Proc. Combust. Inst. 35 (2015) 457–464.

[48] P. Dagaut, C. Daly, J. Simmie, M. Cathonnet, The oxidation and ignition of dimethylether from low to high temperature (500-1600 K): Experiments and kinetic modeling, Proc. Combust. Inst. 27 (1998) 361–369.

[49] H.J. Curran, S.L. Fischer, F.L. Dryer, The reaction kinetics of dimethyl ether. II: Low-temperature oxidation in flow reactors, Int. J. Chem. Kinet. 32 (2000) 741–759.

[50] H. Guo, W. Sun, F.M. Haas, T. Farouk, F.L. Dryer, Y. Ju, Measurements of H_2O_2 in low temperature dimethyl ether oxidation, Proc. Combust. Inst. 34 (2013) 573–581.

[51] F. Herrmann, B. Jochim, P. Oßwald, L. Cai, H. Pitsch, K. Kohse-Höinghaus, Experimental and numerical low-temperature oxidation study of ethanol and dimethyl ether, Combust. Flame 161 (2014) 384–397.

[52] F. Herrmann, P. Oßwald, K. Kohse-Höinghaus, Mass spectrometric investigation of the low-temperature dimethyl ether oxidation in an atmospheric pressure laminar flow reactor, Proc. Combust. Inst. 34 (2013) 771–778.

[53] K. Moshammer, A.W. Jasper, D.M. Popolan-Vaida, A. Lucassen, P. Diévart, H. Selim, A.J. Eskola, C.A. Taatjes, S.R. Leone, S.M. Sarathy, Y. Ju, P. Dagaut, K. Kohse-Höinghaus, N. Hansen, Detection and identification of the keto-hydroperoxide ($HOOCH_2OCHO$) and other intermediates during low-temperature oxidation of dimethyl ether, J. Phys. Chem. A 119 (2015) 7361–7374.

[54] K. Moshammer, A.W. Jasper, D.M. Popolan-Vaida, Z. Wang, V.S. Bhavani Shankar, L. Ruwe, C.A. Taatjes, P. Dagaut, N. Hansen, Quantification of the keto-hydroperoxide ($HOOCH_2OCHO$) and other elusive intermediates during low-temperature oxidation of dimethyl ether, J. Phys. Chem. A 120 (2016) 7890–7901.

[55] A.J. Eskola, S.A. Carr, R.J. Shannon, B. Wang, M.A. Blitz, M.J. Pilling, P.W. Seakins, S.H. Robertson, Analysis of the kinetics and yields of OH radical production from the CH_3OCH_2 + O_2 reaction in the temperature range 195−650 K : An experimental and computational study, J. Phys. Chem. A 118 (2014) 6773–6788.

[56] A.S. Tomlin, E. Agbro, V. Nevrlý, J. Dlabka, M. Vašinek, Evaluation of combustion mechanisms

using global uncertainty and sensitivity analyses: A case study for low-temperature dimethyl ether oxidation, Int. J. Chem. Kinet. 46 (2014) 662–682.

[57] A. Rodriguez, O. Frottier, O. Herbinet, R. Fournet, R. Bounaceur, C. Fittschen, F. Battin-Leclerc, Experimental and modeling investigation of the low-temperature oxidation of dimethyl ether, J. Phys. Chem. A 119 (2015) 7905–7923.

[58] X. Jiang, F. Deng, F. Yang, Y. Zhang, Z. Huang, High temperature ignition delay time of DME/n-pentane mixture under fuel lean condition, Fuel 191 (2017) 77–86.

[59] M. Eyidogan, A.N. Ozsezen, M. Canakci, A. Turkcan, Impact of alcohol-gasoline fuel blends on the performance and combustion characteristics of an SI engine, Fuel 89 (2010) 2713–2720.

[60] L.R. Cancino, M. Fikri, A.A.M. Oliveira, C. Schulz, Measurement and chemical kinetics modeling of shock-induced ignition of ethanol-air mixtures, Energy Fuels 24 (2010) 2830–2840.

[61] F.M. Haas, M. Chaos, F.L. Dryer, Low and intermediate temperature oxidation of ethanol and ethanol-PRF blends: An experimental and modeling study, Combust. Flame 156 (2009) 2346–2350.

[62] G. Mittal, S.M. Burke, V.A. Davies, B. Parajuli, W.K. Metcalfe, H.J. Curran, Autoignition of ethanol in a rapid compression machine, Combust. Flame 161 (2014) 1164–1171.

[63] M.S. Graboski, R.L. McCormick, Combustion of fat and vegetable oil derived fuels in diesel engines, Prog. Energy Combust. Sci. 24 (1998) 125–164.

[64] Y. Zhang, H. El-Merhubi, B. Lefort, L. Le Moyne, H.J. Curran, A. Kéromnès, Probing the low-temperature chemistry of ethanol via the addition of dimethyl ether, Combust. Flame 190 (2018) 74–86.

[65] C. Hemken, U. Burke, K.-F. Lam, D.F. Davidson, R.K. Hanson, K.A. Heufer, K. Kohse-Höinghaus, Toward a better understanding of 2-butanone oxidation: Detailed species measurements and kinetic modeling, Combust. Flame 184 (2017) 195–207.

[66] M. Schenk, L. Leon, K. Moshammer, P. Oßwald, T. Zeuch, L. Seidel, F. Mauss, K. Kohse-Höinghaus, Detailed mass spectrometric and modeling study of isomeric butene flames, Combust. Flame 160 (2013) 487–503.

[67] L. Cai, A. Sudholt, D.J. Lee, F.N. Egolfopoulos, H. Pitsch, C.K. Westbrook, S.M. Sarathy, Chemical kinetic study of a novel lignocellulosic biofuel: Di-*n*-butyl ether oxidation in a laminar flow reactor and flames, Combust. Flame 161 (2014) 798–809.

[68] A. Cuoci, A. Frassoldati, T. Faravelli, E. Ranzi, OpenSMOKE++: An object-oriented

framework for the numerical modeling of reactive systems with detailed kinetic mechanisms, Comput. Phys. Commun. 192 (2015) 237–264.

[69] S.L. Fischer, F.L. Dryer, H.J. Curran, The reaction kinetics of dimethyl ether. I: High-temperature pyrolysis and oxidation in flow reactors, Int. J. Chem. Kinet. 32 (2000) 713–740.

[70] Z. Wang, X. Zhang, L. Xing, L. Zhang, F. Herrmann, K. Moshammer, F. Qi, K. Kohse-Höinghaus, Experimental and kinetic modeling study of the low- and intermediate-temperature oxidation of dimethyl ether, Combust. Flame 162 (2015) 1113–1125.

[71] S. Xu, R.S. Zhu, M.C. Lin, Ab initio study of the OH+CH_2O reaction: The effect of the OH··OCH_2 complex on the H-abstraction kinetics, Int. J. Chem. Kinet. 38 (2006) 322–326.

Figures

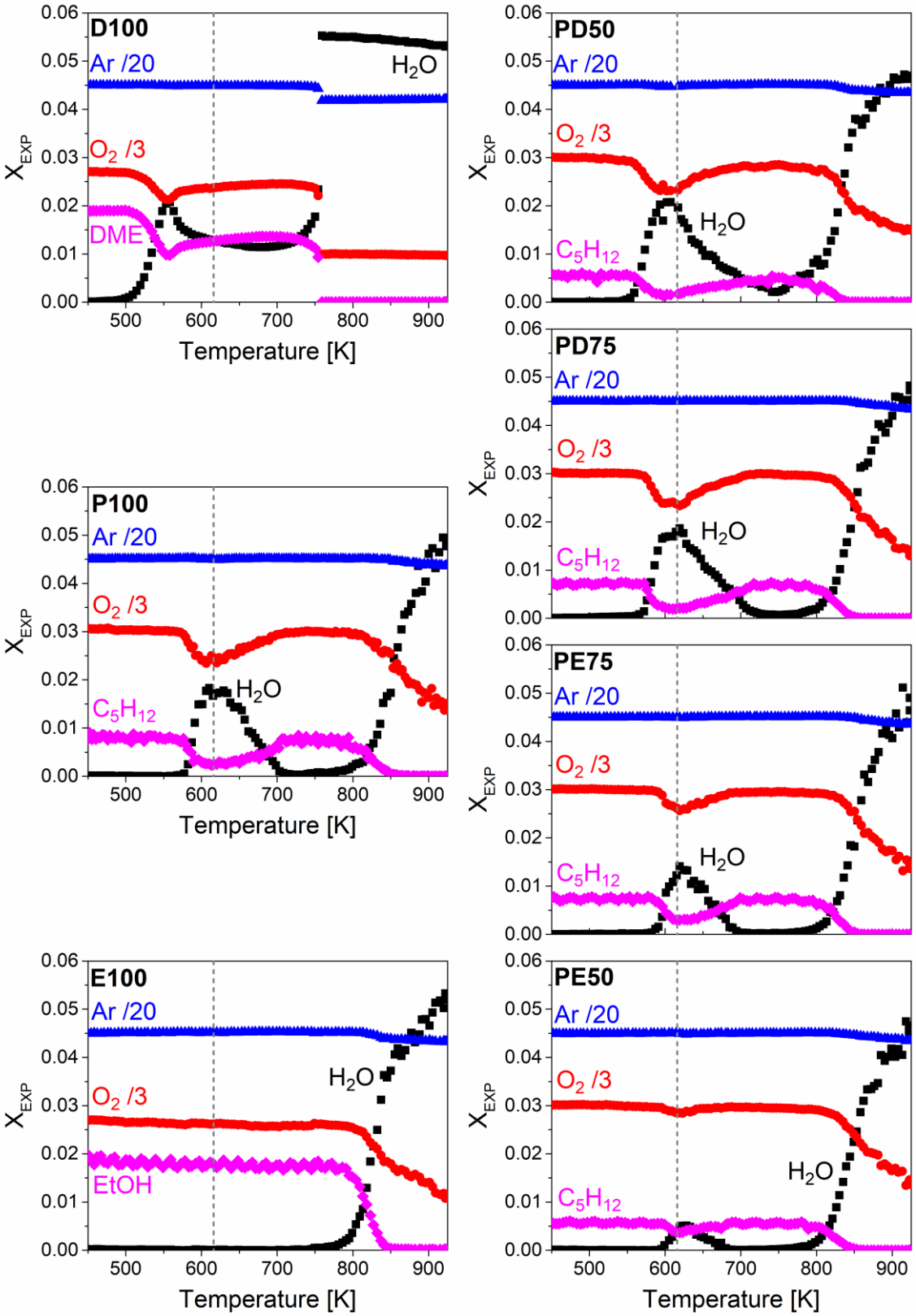

Fig. 1: Temperature-dependent species mole fraction profiles for Ar, fuel, O_2, and H_2O for pure DME (D100), *n*-pentane (P100), and ethanol (E100) as well as for mixtures of either oxygenated fuel with 75% (PD75, PE75) and 50% (PD50, PE50) of *n*-pentane. The broken line at 616 K is drawn to guide the eye. The temperature plotted on the x-axis is the set temperature at the outside wall of the reactor.

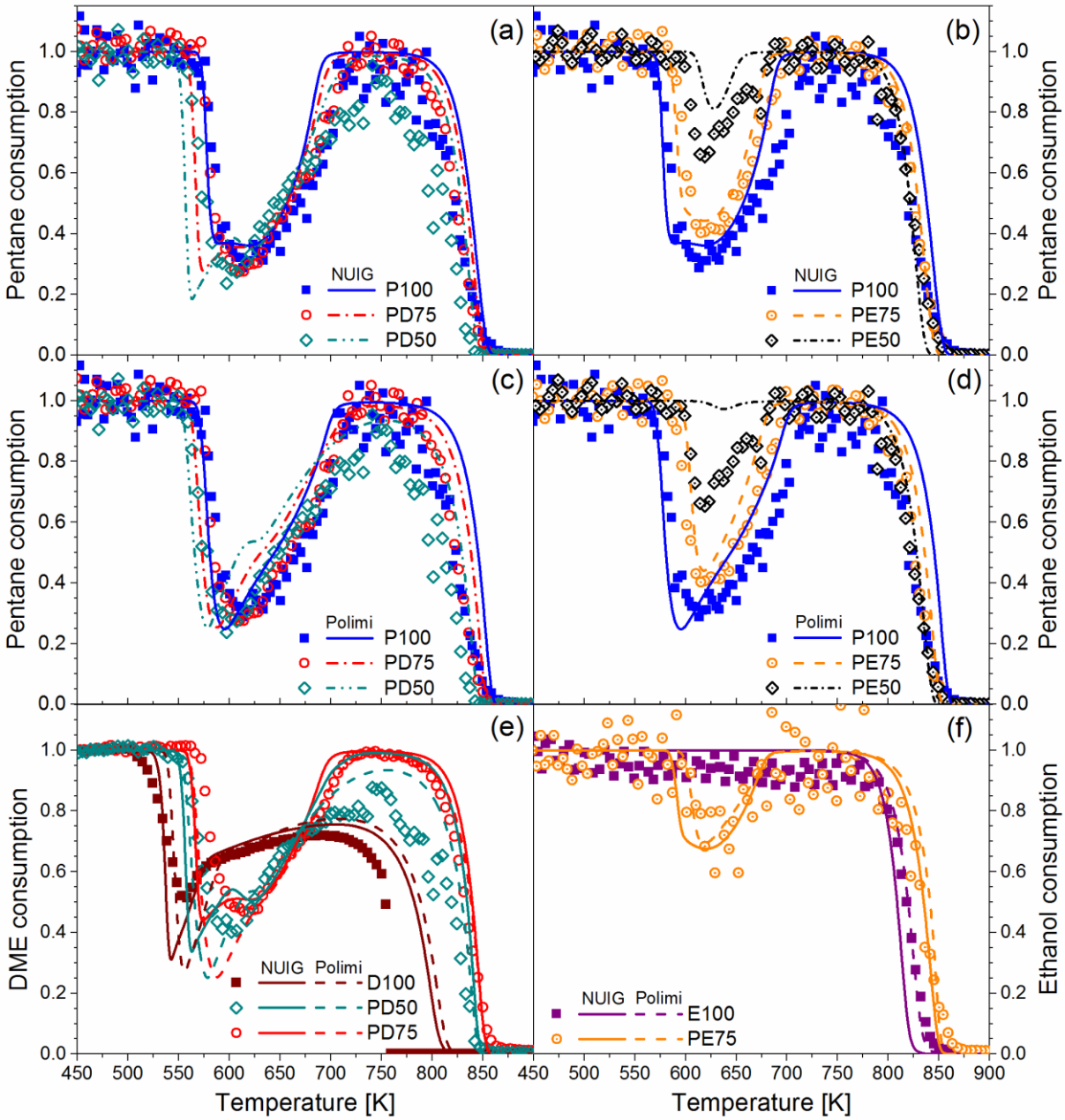

Fig. 2: Reactivity for neat fuels and dual-fuel mixtures. Experimental fuel consumption mole fraction profiles (*symbols*) are given as a function of temperature, together with model simulations (*lines*). **Panels (a-d):** *n*-Pentane consumption profiles for pure *n*-pentane fuel and for mixtures containing 75% and 50% *n*-pentane with DME (a,c) or EtOH (b,d); each profile is normalized by the inlet mole fraction of *n*-pentane. Simulation results for (a,b) were obtained with the NUIG model [39] and for (c,d) with the Polimi model [17]. **Panels (e,f):** Consumption profiles for DME (e) and EtOH (f) for different inlet conditions; each profile is normalized by the respective inlet fuel mole fraction. *Solid line:* NUIG model, *dashed line:* Polimi model. The profile for PE50 is not shown in (f) because of negligible low-temperature chemistry behavior.

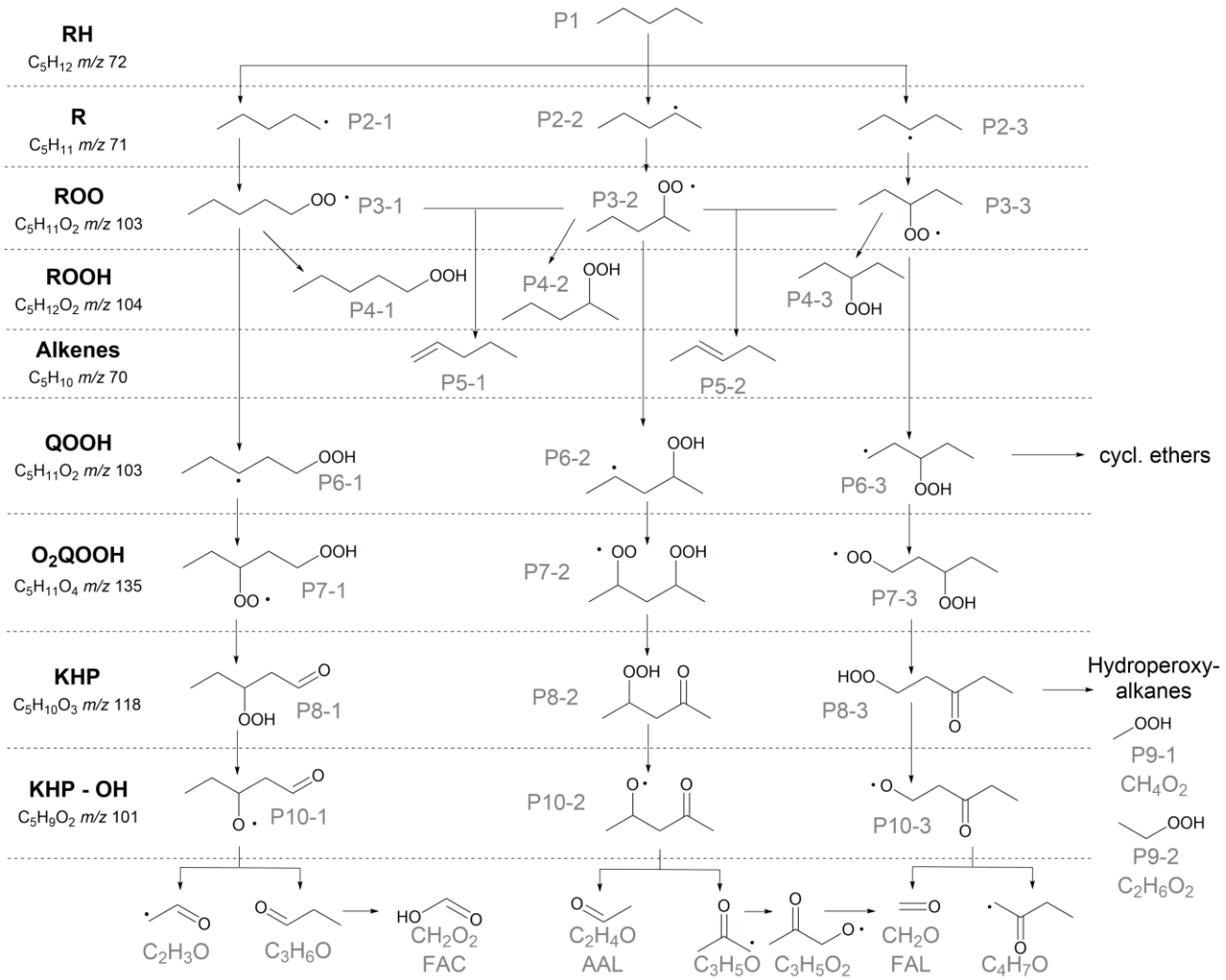

Fig. 3: Reaction pathway diagram for *n*-pentane. Species code starts with P, the first figure denotes the step along the reaction progress, and isomers are distinguished by the second figure (*e.g.*, **P2-3** identifies one of the three isomers of the fuel radical in the *n*-pentane oxidation). FAC: formic acid, AAL: acetaldehyde, FAL: formaldehyde.

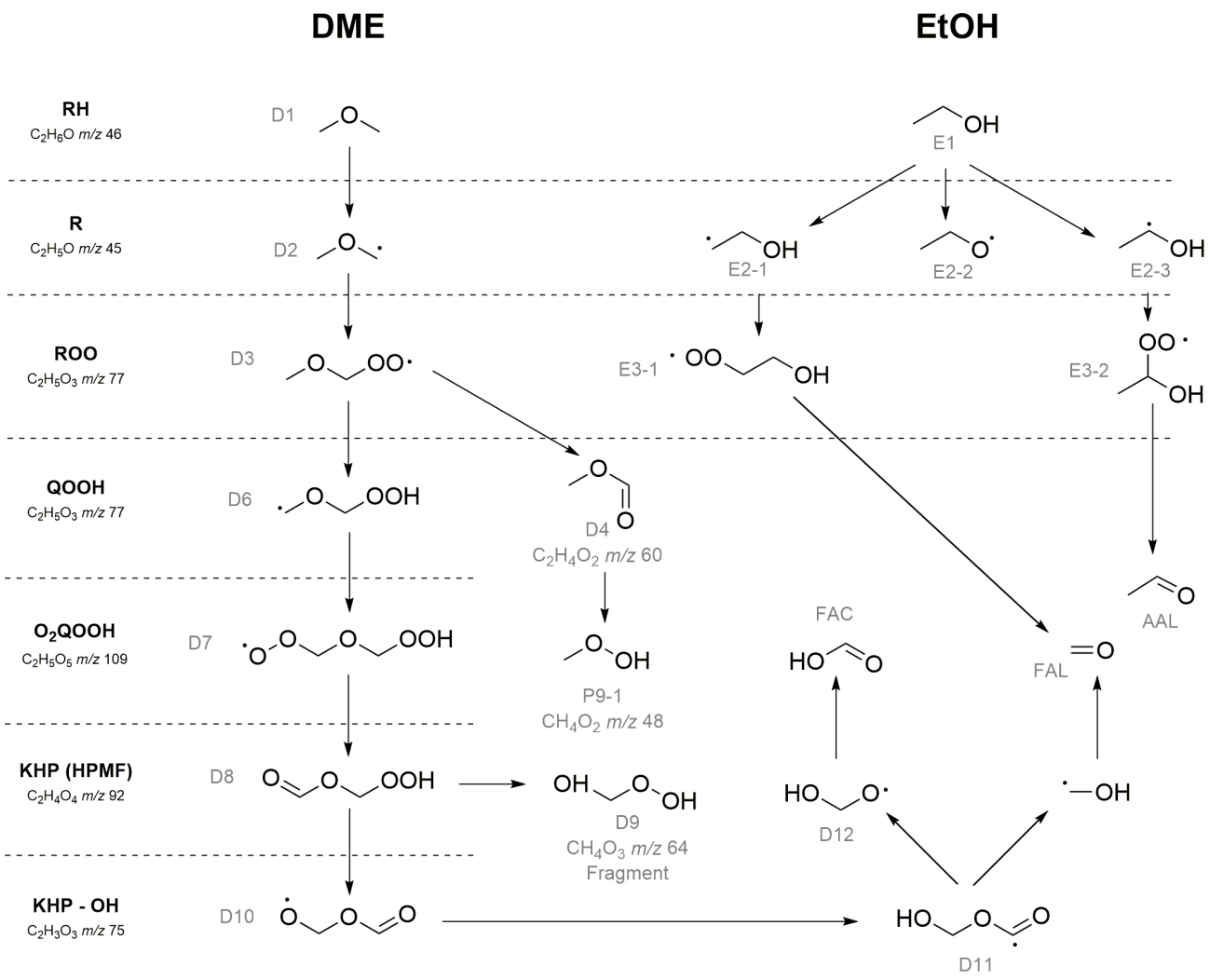

Fig. 4: Reaction pathway diagram for DME and ethanol. Species codes follow the same rules as in Fig. 3. FAC: formic acid, AAL: acetaldehyde, FAL: formaldehyde.

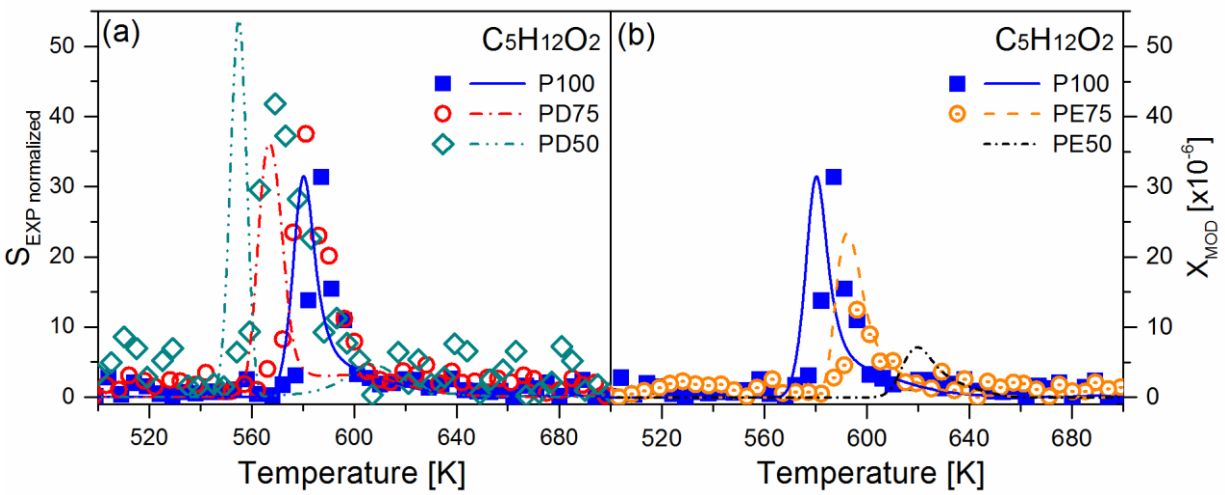

Fig. 5: Signal intensities (*left axis, arbitrary units*) of $C_5H_{12}O_2$, assigned to hydroperoxypentanes (**P4**), normalized by the different inlet mole fractions of *n*-pentane (*symbols*) and quantitative mole fractions (*right axis*) from NUIG model predictions (*lines*). (a) *n*-Pentane/DME, (b) *n*-pentane/EtOH. No experimental data of $C_5H_{12}O_2$ is observed in PE50 due to its low concentration, thus only the modeling result is provided.

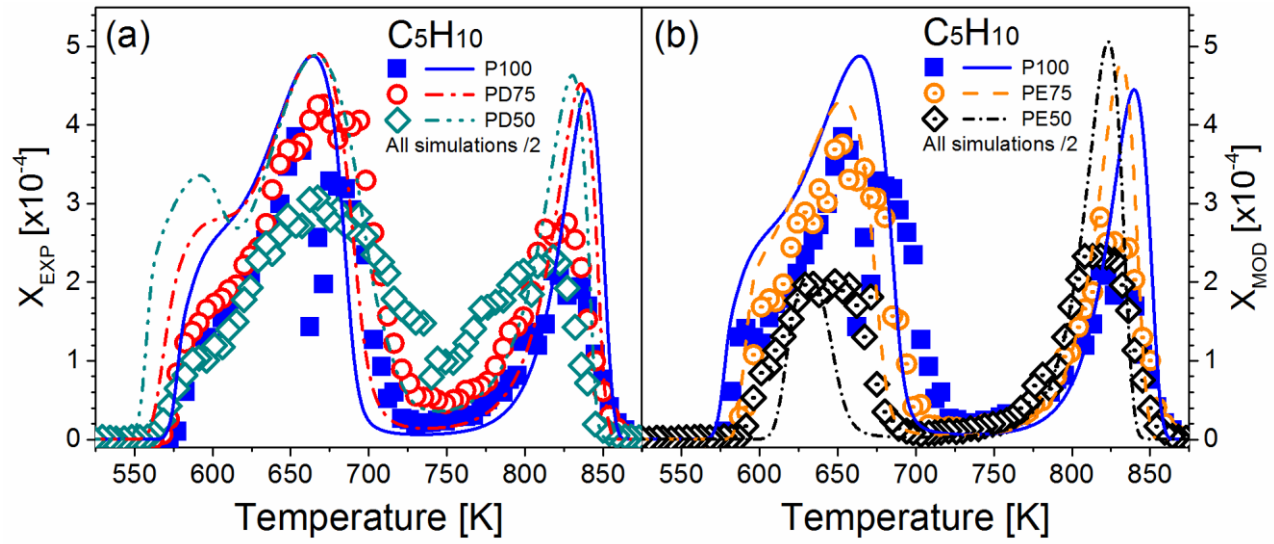

Fig. 6: Experimental mole fractions (*left axis*) of pentenes (sum of C_5H_{10}, **P5**, *symbols*), normalized (in the *n*-pentane-containing mixtures) by the different *n*-pentane inlet mole fractions, and NUIG model predictions (*right axis*) for the sum of 1-pentene and 2-pentene (*lines*). (a) *n*-Pentane/DME, (b) *n*-pentane/EtOH. Please note that all simulation results have been divided by a factor of 2.

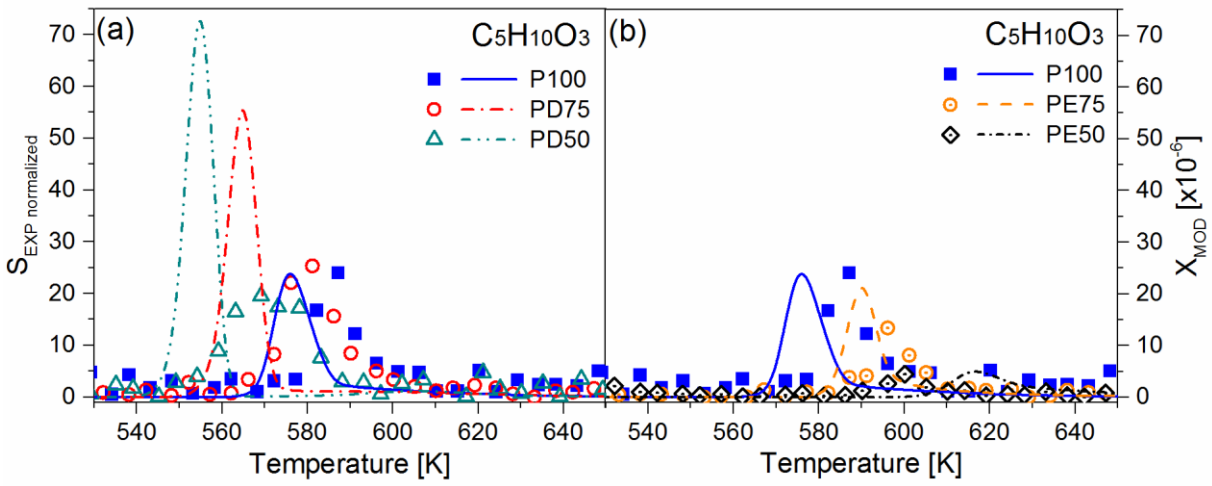

Fig. 7: Signal intensities (*left axis, arbitrary units*) for $C_5H_{10}O_3$ assigned to C_5-ketohydroperoxides (**P8**), normalized by the different inlet mole fractions of *n*-pentane (*symbols*), and quantitative mole fractions (*right axis*) from NUIG model prediction (*lines*). (a) *n*-Pentane/DME, (b) *n*-pentane/EtOH.

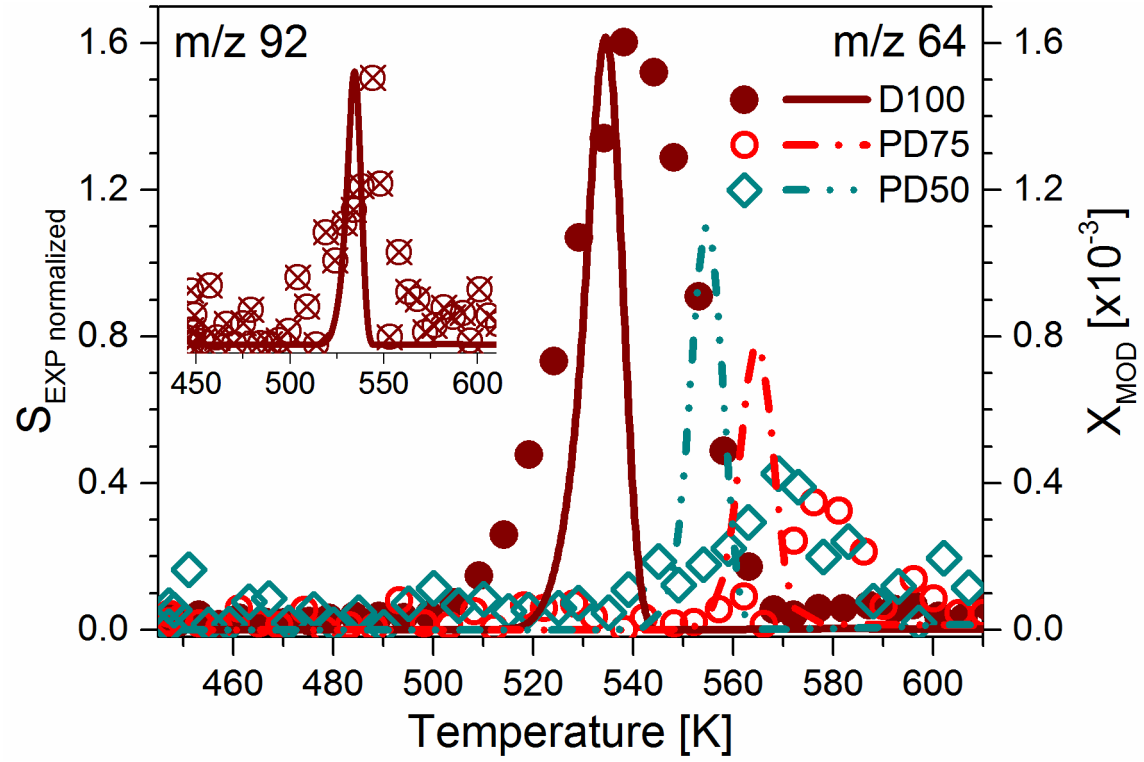

Fig. 8: Signal intensities (*symbols, left axis, arbitrary units*) of *m/z*=64 (CH_4O_3, **D9**) and (*insert top left*) of *m/z*=92 (HPMF, **D8**) for D100, together with quantitative mole fractions from NUIG model predictions for HPMF (*lines, right axis*). For D100 and *m/z*=64, both measured and modeled results are divided by a factor of 5. Profiles have been normalized by the different inlet mole fractions for DME.

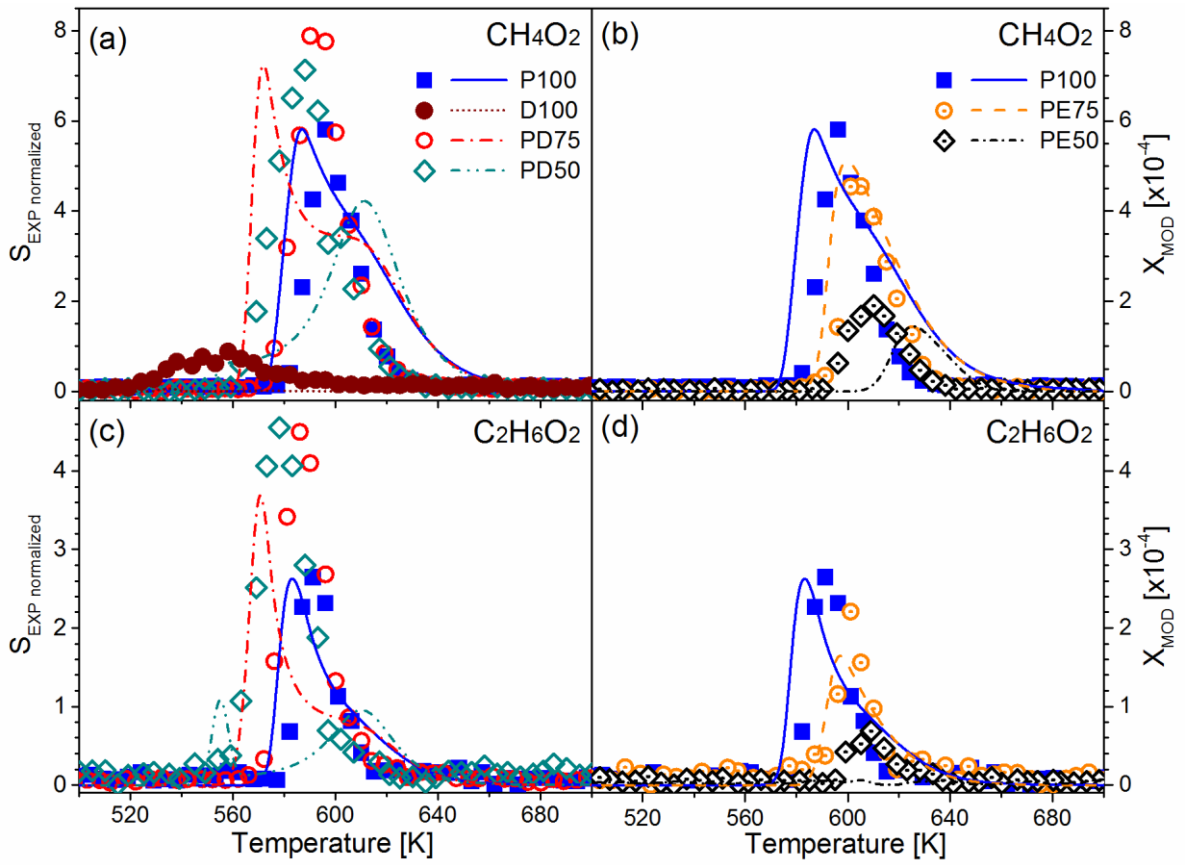

Fig. 9: Signal intensities (*symbols, left axes, arbitrary units*) of CH_4O_2 and $C_2H_6O_2$ assigned to hydroperoxymethane (**P9-1**) and hydroperoxyethane (**P9-2**), respectively, normalized (in the *n*-pentane-containing mixtures) by the different inlet mole fractions of *n*-pentane, and quantitative mole fractions from NUIG model predictions (*lines, right axes*). (a,c) *n*-Pentane/DME, (b,d) *n*-pentane/EtOH.

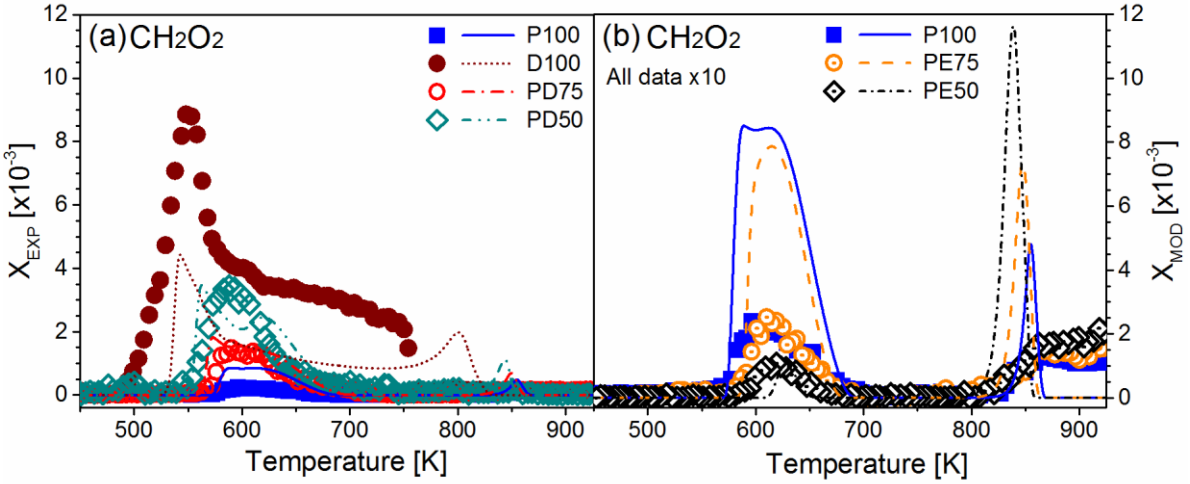

Fig. 10: Quantitative mole fractions of CH_2O_2, calibrated as formic acid (HCOOH, **FAC**), normalized (in the *n*-pentane-containing mixtures) by the different *n*-pentane inlet mole fractions. Symbols: experiment (*left axes*); lines: NUIG model predictions (*right axes*). (a) *n*-Pentane/DME, (b) *n*-pentane/EtOH.

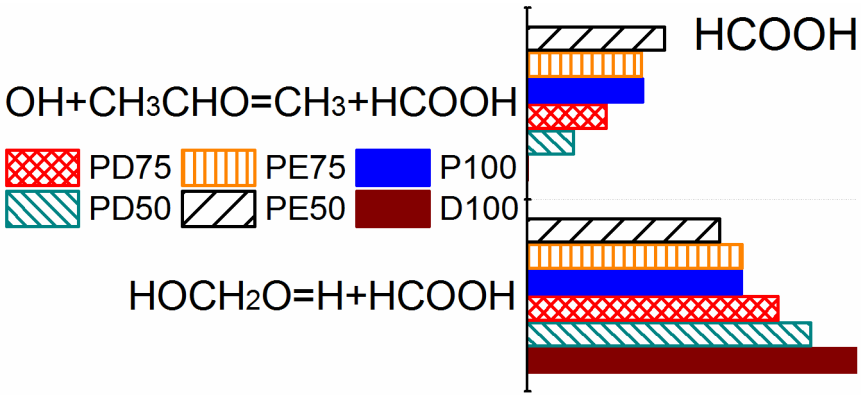

Fig. 11: Rate of production analysis of formic acid (HCOOH) for different inlet conditions modeled by the NUIG model at the temperatures of the respective maximum mole fraction (±5 K) in the NTC zone.

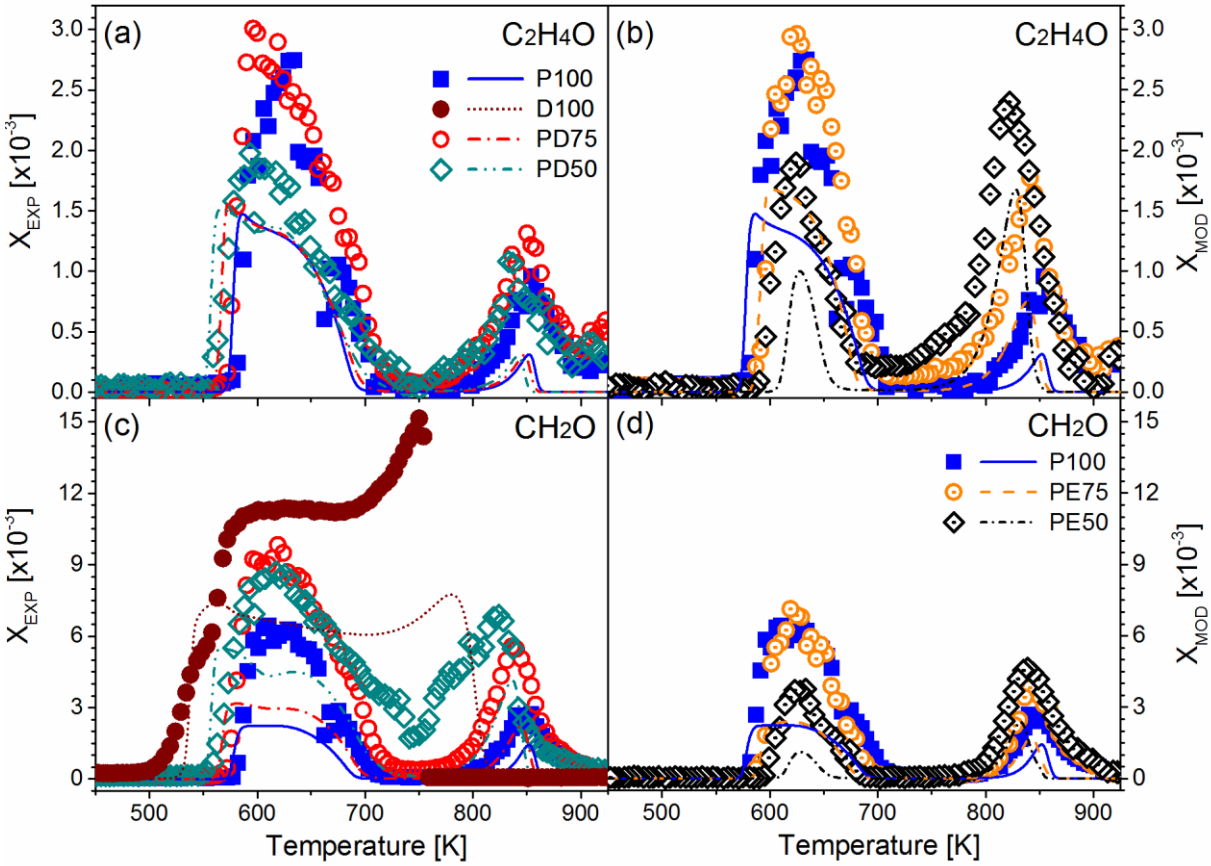

Fig. 12: Quantitative mole fractions of (a,b) acetaldehyde (**AAL**) and (c,d) formaldehyde (**FAL**), normalized (in the *n*-pentane-containing mixtures) by the different *n*-pentane inlet mole fractions. Symbols: experimental measurements (*left axes*); lines: NUIG model predictions (*right axes*). (a,c) *n*-Pentane/DME, (b,d) *n*-pentane/EtOH.

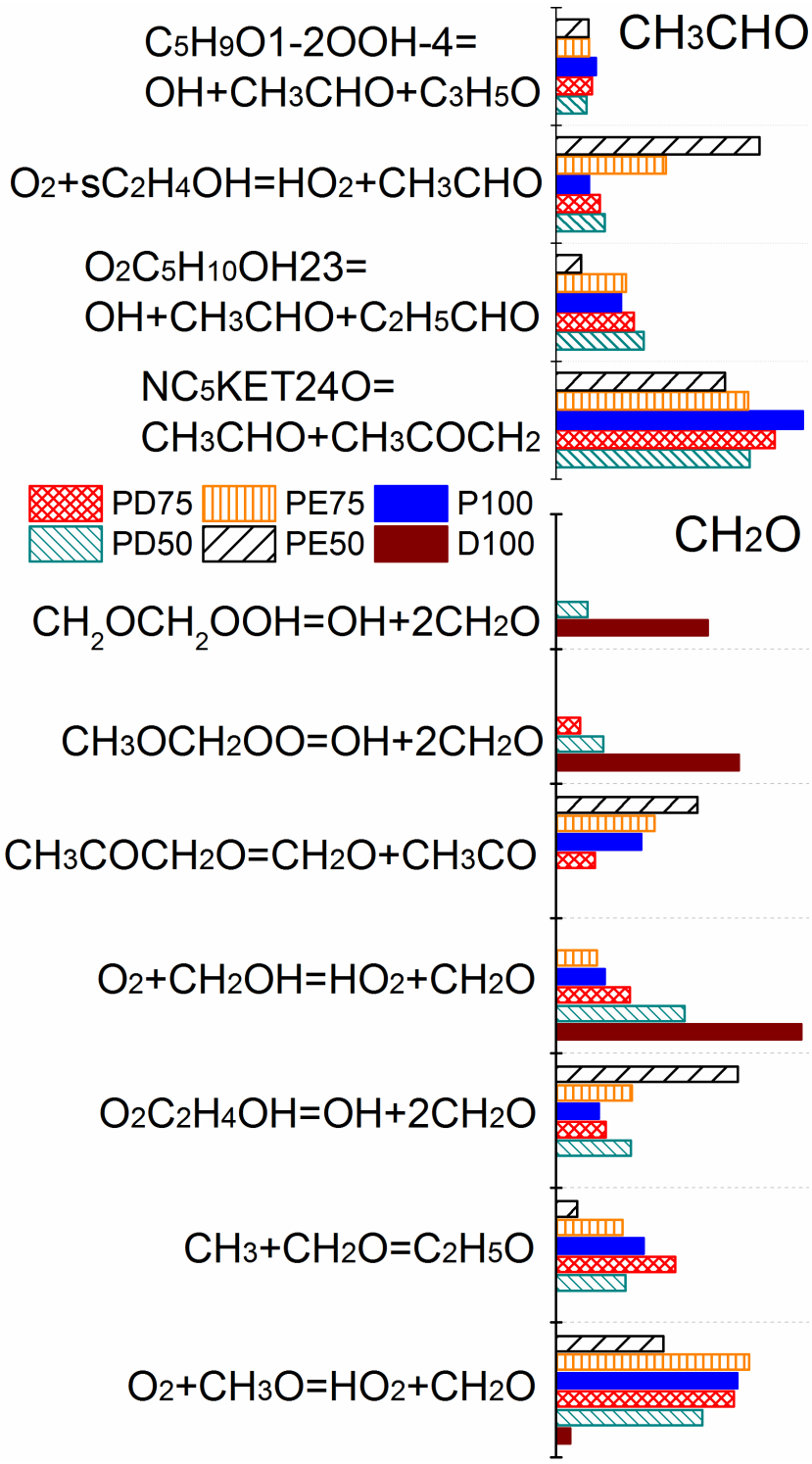

Fig. 13: Contributions of the main pathways in the formation of acetaldehyde (CH_3CHO, **AAL**) and formaldehyde (CH_2O, **FAL**) for the different inlet conditions. The results were obtained with the NUIG model at the respective maximum **AAL** and **FAL** mole fractions (±5 K) in the NTC zone. Abbreviations: C_5H_9O1-2OOH-4 is 2-hydroperoxy-4-methyltetrahydrofuran, $O_2C_5H_{10}OH23$ the pentan-3-ol-2-peroxy radical, $NC_5KET24O$ (**P10-2**) the 2-pentanoxide-4-one radical, and sC_2H_4OH (**E2-3**) the α-ethanol radical. (Compare also nomenclature and structures in Table S1 in SM2).

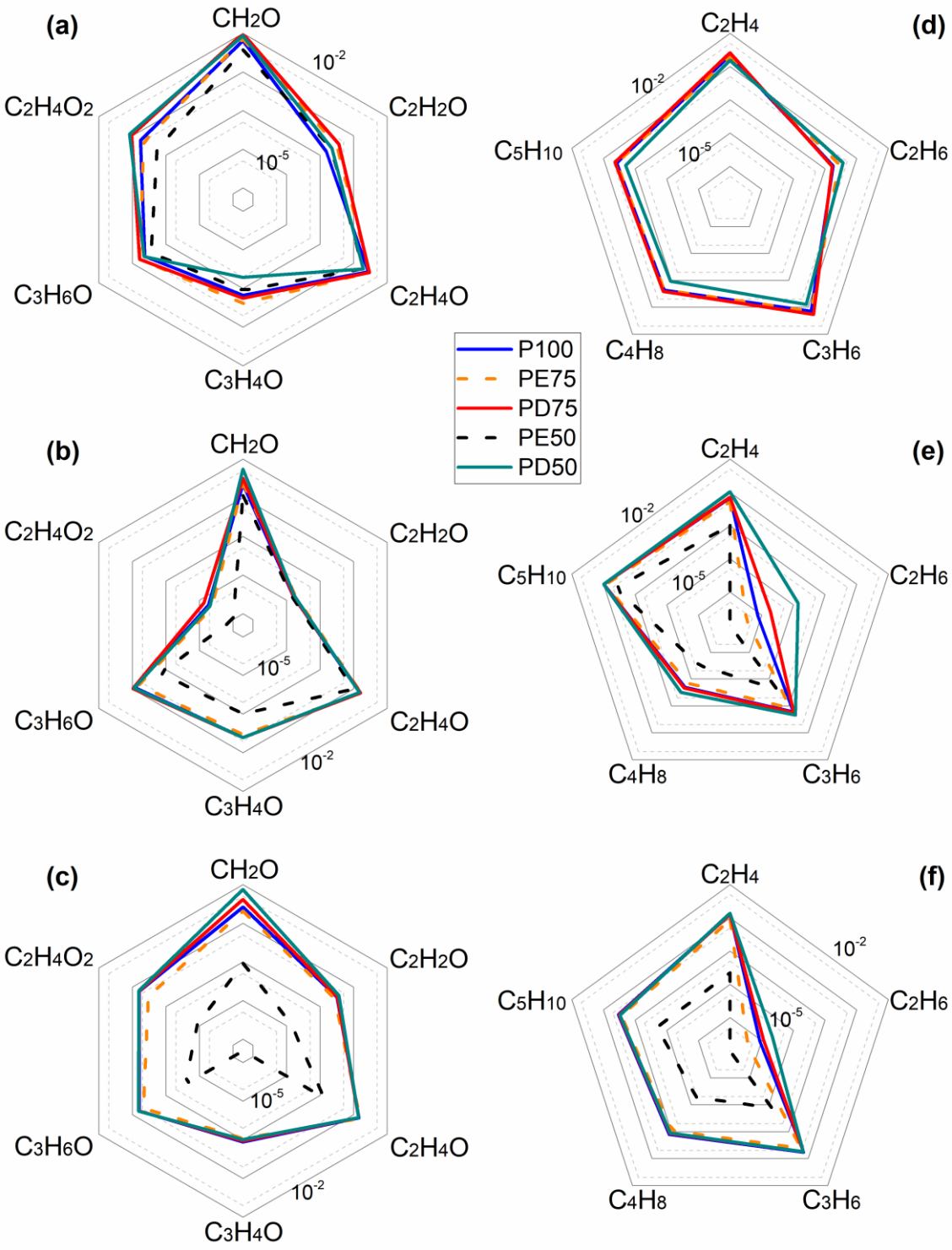

Fig. 14: Mole fractions of selected oxygenated and hydrocarbon intermediates at their respective maxima in the low-temperature regime (logarithmic scale); the mole fraction of each species is normalized by the inlet mole fraction of *n*-pentane for the respective condition. (a,d): experimental results; (b,e) predictions with the NUIG model; (c,f) predictions with the Polimi model.

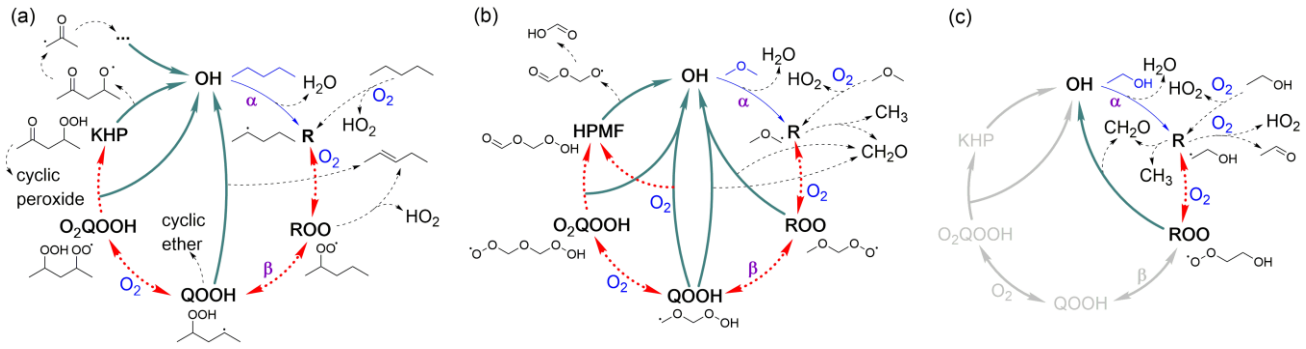

Fig. 15: Schematic diagram of the major reaction cycles of (a) *n*-pentane, (b) DME, and (c) ethanol in the low-temperature oxidation of fuel blends. Solid thick arrows: reactions that produce OH radicals; solid thin arrows: H-abstraction reactions of the respective fuel; thick dashed arrows: reactions that promote the chain branching cycle; solid light-grey arrows: fictitious chain branching pathways of ethanol; thin dashed arrows: other products during the oxidation procedure. Abbreviations: KHP: ketohydroperoxide of *n*-pentane, HPMF: hydroperoxymethyl formate.

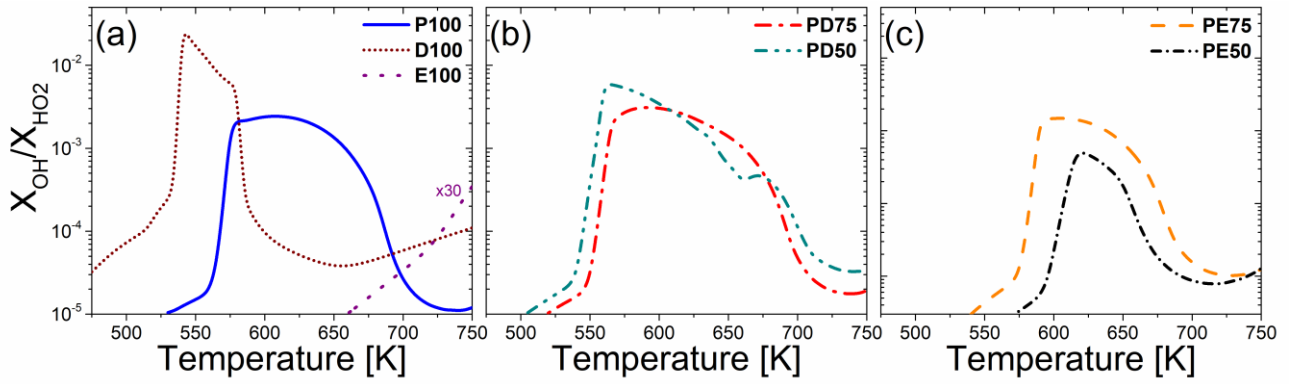

Fig. 16: Ratio of maximum mole fractions of OH and HO_2 radicals x_{OH}/x_{HO_2} along the flow reactor at each temperature point, predicted by the NUIG model for (a) the pure fuels, (b) the mixtures of *n*-pentane and DME, and (c) the mixtures of *n*-pentane and ethanol.

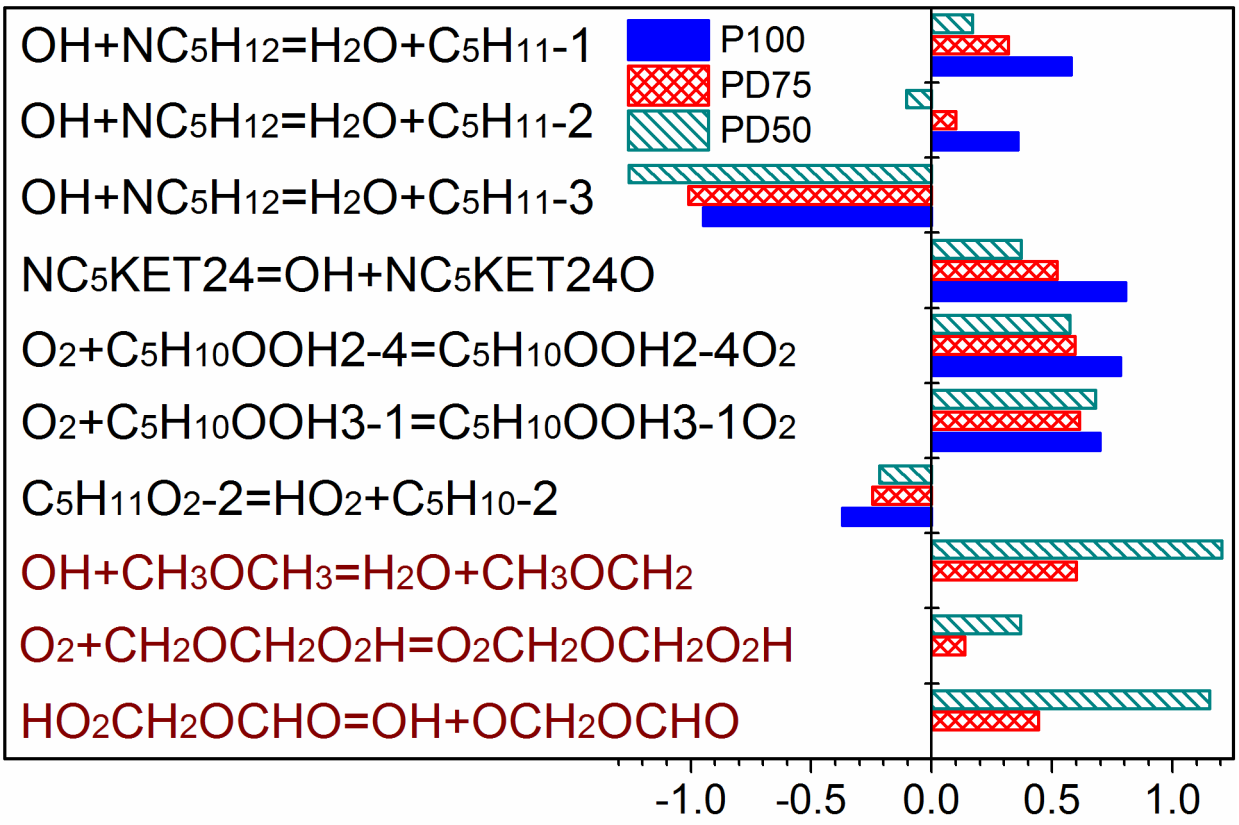

Fig. 17: Sensitivity coefficient for OH to reaction rate pre-exponential factors at 25% *n*-pentane conversion (NUIG model). Abbreviations: NC_5KET24 is 2-hydroperoxy-4-pentanone (**P8-2**), $NC_5KET24O$ is the 2-pentanoxide-4-one radical (**P10-2**), $C_5H_{10}OOH2\text{-}4$ is the 2-hydroperoxy-4-pentyl radical, $C_5H_{10}OOH2\text{-}4O_2$ is the 2-hydroperoxy-4-pentylperoxy radical, $C_5H_{10}OOH3\text{-}1$ is the 3-hydroperoxy-1-pentyl radical, $C_5H_{10}OOH3\text{-}1O_2$ is the 3-hydroperoxy-1-pentylperoxy radical, $C_5H_{11}O_2\text{-}2$ is the 2-pentylperoxy radical (**P3-2**), and $C_5H_{10}\text{-}2$ is 2-pentene (**P5-2**); compare also nomenclature and structures in Table S1 in SM2.

ANHANG F

Publikation 6

J. Pieper, C. Hemken, R. Büttgen, I. Graf, N. Hansen, K.A. Heufer, K. Kohse-Höinghaus

A high-temperature study of 2-pentanone oxidation: experiment and kinetic modeling

Proceedings of the Combustion Institute, 2018
Eingereicht, positiv begutachtet.

Abstract

Small methyl ketones are known to have high octane numbers, impressive knock resistance, and show low emissions of soot, NO_x, and unburnt hydrocarbons. However, previous studies have focused on the analysis of smaller ketones and 3-pentanone, while the asymmetric 2-pentanone (methyl propyl ketone) has not gained much attention before. Considering ketones as possible fuels or additives, it is of particular importance to fully understand the combustion kinetics and the effect of the functional carbonyl group. Due to the higher energy density in a C_5-ketone compared to the potential biofuel 2-butanone, the flame structure and the mole fraction profiles of species formed in 2-pentanone combustion are of high interest, especially to evaluate harmful species formations. In this study, a laminar premixed low pressure (p=40 mbar) fuel rich (ϕ=1.6) flat flame of 2-pentanone has been analyzed by vacuum-ultraviolet photoionization molecular-beam mass-spectrometry (VUV-PI-MBMS) enabling isomer separation. Quantitative mole fraction profiles of 47 species were obtained and compared to a model consisting of an existing base mechanism and a newly developed high-temperature sub-mechanism for 2-pentanone. High-temperature reactions for 2-pentanone were adapted in analogy to 2-butanone and *n*-pentane, and the thermochemistry for 2-pentanone and the respective fuel radicals was derived by *ab initio* calculations. Good agreement was found between experiment and simulation for the first decomposition products, supporting the initial branching reactions of the 2-pentanone sub-mechanism. Also, species indicating low-temperature chemistry in the preheating zone of the flame have been observed. The present measurements of a 2-pentanone flame provide useful validation targets for further kinetic model development.

A high-temperature study of 2-pentanone oxidation: experiment and kinetic modeling

Julia Pieper[1], Christian Hemken[2], Rene Büttgen[2], Isabelle Graf[1], Nils Hansen[3], K. Alexander Heufer[2,*], Katharina Kohse-Höinghaus[1,*]

[1] Department of Chemistry, Bielefeld University, Universitätsstraße 25, D-33615 Bielefeld, Germany.
[2] Physical Chemical Fundamentals of Combustion (PCFC), RWTH Aachen University, Schinkelstraße 8, D-52062 Aachen, Germany.
[3] Combustion Research Facility, Sandia National Laboratories, CA 94551, USA.

* Corresponding authors:
K. Alexander Heufer, Physical Chemical Fundamentals of Combustion (PCFC), RWTH Aachen University, Schinkelstraße 8, D-52062 Aachen, Germany, E-mail: heufer@pcfc.rwth-aachen.de
Katharina Kohse-Höinghaus, Department of Chemistry, Bielefeld University, Universitätsstraße 25, D-33615 Bielefeld, Germany, E-mail: kkh@uni-bielefeld.de

Abstract

Small methyl ketones are known to have high octane numbers, impressive knock resistance, and show low emissions of soot, NO_x, and unburnt hydrocarbons. However, previous studies have focused on the analysis of smaller ketones and 3-pentanone, while the asymmetric 2-pentanone (methyl propyl ketone) has not gained much attention before. Considering ketones as possible fuels or additives, it is of particular importance to fully understand the combustion kinetics and the effect of the functional carbonyl group. Due to the higher energy density in a C_5-ketone compared to the potential biofuel 2-butanone, the flame structure and the mole fraction profiles of species formed in 2-pentanone combustion are of high interest, especially to evaluate harmful species formations. In this study, a laminar premixed low-pressure (p = 40 mbar) fuel-rich (ϕ = 1.6) flat flame of 2-pentanone has been analyzed by vacuum-ultraviolet photoionization molecular-beam mass-spectrometry (VUV-PI-MBMS) enabling isomer separation. Quantitative mole fraction profiles of 47 species were

obtained and compared to a model consisting of an existing base mechanism and a newly developed high-temperature sub-mechanism for 2-pentanone. High-temperature reactions for 2-pentanone were adapted in analogy to 2-butanone and *n*-pentane, and the thermochemistry for 2-pentanone and the respective fuel radicals was derived by *ab initio* calculations. Good agreement was found between experiment and simulation for the first decomposition products, supporting the initial branching reactions of the 2-pentanone sub-mechanism. Also, species indicating low-temperature chemistry in the preheating zone of the flame have been observed. The present measurements of a 2-pentanone flame provide useful validation targets for further kinetic model development.

Keywords: 2-pentanone, laminar premixed flame, photoionization molecular-beam mass-spectrometry, kinetic modeling, thermochemistry

1. Introduction

With a rising energy demand and the objective to reduce global warming, a transition from the combustion of fossil fuels in the transport sector to second-generation biofuels is desired, because it may eventually contribute to a reduced net carbon emission. As representatives of this category of fuels, small methyl ketones like acetone (RON = 110-117 [1,2]) and 2-butanone (RON=117 [3]) show impressive knock resistance. 2-butanone, for example, was tested in a SI engine as neat fuel and showed low emissions of soot, NO_x, and unburnt hydrocarbons compared to a RON 95 fuel blend, ethanol, and 2-methylfuran [3]. Nonetheless, studies investigating the combustion behavior and properties of 2-pentanone (methyl propyl ketone, MPK) are scarce, while the symmetric conformer 3-pentanone (diethyl ketone, DEK) gained more attention [4–6]. Compared to 2-butanone and 3-pentanone with one or two ethyl side chains, respectively, 2-pentanone has a propyl side chain, which could lead to changes in the underlying kinetics and to a lower effect of the carbonyl group. With a higher energy density, C_5-ketones could be preferred in engine applications, while the formation of toxic and harmful species is unknown. In a premixed flame study [7], it was shown that 2-butanone exhibits very low emissions of oxygenated intermediates and soot precursors. With a linear alkyl chain of three carbon atoms in 2-pentanone, the formation of soot precursors like C_3H_3 could be increased. Minwegen et al. [8] measured the ignition delay times of a series of small linear ketones, including 2-pentanone, at 20 and 40 bar in a shock tube. High temperature measurements of reactions of small linear ketones with OH were performed at 1-2 atm by Lam et al. [9]. Furthermore, Badra et al. [10] experimentally investigated the H-abstraction by OH of a series of larger ketones. In theoretical work by Hudzik and Bozzelli [11], the thermochemistry and bond dissociation energies of ketones were calculated.

In this study, a laminar premixed low-pressure (40 mbar) fuel-rich (ϕ = 1.6) flat flame of 2-pentanone was quantitatively analyzed by vacuum-ultraviolet photoionization molecular-beam mass-spectrometry (VUV-PI-MBMS). For the first time, 47 species were measured, quantified and isomers were separated whenever possible. Complementing the experimental data set, a kinetic model, representing the high-temperature chemistry, is presented here. For this kinetic model, the

thermochemistry (heat of formation, entropy, and heat capacity) of the fuel and the corresponding fuel radicals was determined by *ab initio* quantum mechanical calculations.

2. Experiments

A laminar premixed fuel-rich flame of 2-pentanone/oxygen/argon (0.093/0.407/0.500) was investigated at 40 mbar, equivalence ratio of 1.6 and cold gas velocity of 73.85 cm/s (at inlet conditions of 333 K and 40 mbar, 2.574 cm/s at 298 K and 1 atm) by VUV-PI-MBMS [12,13] at the Advanced Light Source (ALS) in Berkeley. Gas flow rates of oxygen and argon were metered by calibrated mass-flow controllers with a precision of 5%, while liquid 2-pentanone was injected into a heated vaporizer system (~400 K) by a syringe pump (0.5% precision) and transported by an argon flow. The components were mixed and transferred into a McKenna burner (60 mm diameter), and flame gases were sampled via a two-stage expansion (~10^{-4} mbar, ~10^{-6} mbar) by a quartz nozzle (500 μm orifice, 40° opening angle) and a nickel skimmer forming the molecular beam that was then crossed with the tunable VUV beam. This setup features a mass resolution of $m/\Delta m$~4000 combined with an energy resolution of E ~ 0.05 eV, enabling the separation of C/H/O composition and isomeric species by their ionization energy (IE). Species profiles were recorded at different positions of the sampling nozzle using 16 fixed soft ionization energies between 8.7 and 16.65 eV for low fragmentation and separation of isomeric species. Furthermore, photoionization efficiency (PIE) curves were obtained at a distance from the burner of h = 4 mm tuning the photon energy between 8 and 11.5 eV (ΔE = 0.05 eV). For quantification, routines described previously [14,15] were applied using photoionization cross sections (PICS); errors were 30-40% if measured and a factor 2-4 if estimated cross sections were used [16]. More details on the experimental setup and procedures can be found in Refs. [12,13].

The temperature profile was determined as described in [17] using the recorded first-stage pressure profile of the flame. Calibration was performed in the exhaust gas at h = 20 mm with a temperature of 2290 ± 50 K obtained by planar laser-induced fluorescence of OH, using the setup and procedure described in [18]. Due to pressure uncertainties, the measured temperature profile was slightly

smoothed (4pt moving average) to achieve a faster convergence and remove non-physical temperature discontinuities in the modeling.

The data of all evaluated mole fraction profiles and the temperature profile are provided in Supplemental Material 1.

3. Kinetic model and flame simulations

The presented kinetic model is based on the latest AramcoMech 2.0 [19] updated with the high-temperature sub-mechanism of 2-butanone by Hemken et al. [20] and a small-aromatic sub-mechanism by Zhang et al. [21]. This model represents the high-temperature kinetics of 2-pentanone, consists of 520 species and 2960 reactions and is provided in Chemkin format in Supplemental Material 2. The high-temperature reactions include the unimolecular decomposition of the fuel, H-atom abstraction, and fuel radical decomposition, which are adapted in analogy to 2-butanone and *n*-pentane. Unimolecular decompositions were included from calculations for 2-butanone of Thion et al. [22] and from Bugler et al. [23] for the alkyl rest (MPK↔CH_3+$CH_2CH_2COCH_3$). The most important decomposition takes place adjacent to the carbonyl group (MPK↔CH_3CO+C_3H_7), and its rate coefficient was increased by a factor of four to match the ignition delay times of Refs. [8,24]. While such a modification of the coefficient is outside the uncertainty of the quantum mechanical calculations, a higher rate coefficient can be expected due to the larger molecule size of 2-pentanone and thus the collision probability is increased. Consistently, the other decomposition rate coefficients were increased, too. The methyl group at the propyl side chain, which is not close to the carbonyl group, is treated as in *n*-pentane [23] for all reaction classes. H-atom abstraction reactions as well as the following β-scission reactions are included by the rates of Thion et al. [22] for 2-butanone and Bugler et al. [23] for *n*-pentane. Detailed information on reactions, applied factors, and sources are given in the mechanism files in Supplemental Material 2.

The thermochemistry for 2-pentanone as well as for the four fuel radicals was derived by *ab initio* calculations. The method is described in detail by Burke et al. [25]. G4 model chemistry [26] as implemented in Gaussian09 package [27] was used to calculate the enthalpies of formation.

Temperature dependencies of heat capacities, enthalpies, and entropies were determined using TAMkin [28] with correction of 1D hindrance potentials. Accuracy in the entropies of formation and heat capacity data was increased by one-dimensional hindered rotor treatment for all single bonds connecting nonlinear molecular groups. All calculations have been performed at B3LYP/6-31G(2*df,p)* level that was also used for geometry optimization in the G4 method. C-H and C-C bond strengths are shown in Fig. 1 and compared to those of Hudzik and Bozzelli [11]. They agree within 0.5-1.1 kcal/mol, which fits the uncertainty of the method. Transport data was estimated by group additivity with RMG [29].

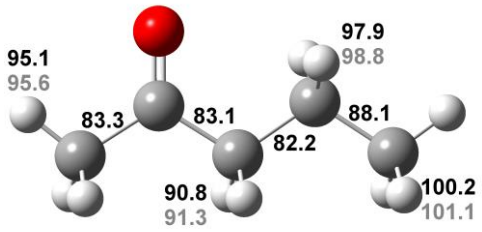

Figure 1: Calculated C-H and C-C bond strengths in kcal/mol for 2-pentanone; black: this work, grey: work by Hudzik and Bozzelli [11].

Simulations in this work were performed using the LOGEsoft [30] premixed burner-stabilized module, including the experimentally determined temperature profile. The kinetic model was also validated against high-temperature shock tube data by Minwegen et al. [8] at elevated pressures of 20 and 40 bar, as well as against highly diluted shock tube data of Lam et al. [24], and the results are presented in Supplemental Material 3 (see Figs. S1-S2).

4. Results and discussion

The following section provides the results of the measurements and the comparison with the simulations using the present model. First, the main species occurring during the combustion of 2-pentanone will be discussed and then the primary intermediates will be presented along with the fuel decomposition scheme. Finally, some species indicating low-temperature chemistry will be discussed

which normally are not observable in the hot flame. Because only selected mole fraction profiles are shown here, several further profiles are available in Supplemental Material 3 (see Figs. S3-S5).

4.1 Main species

Figure 2 presents the mole fractions of the main species (H_2, H_2O, CO, O_2, Ar, CO_2, 2-pentanone) during the combustion of 2-pentanone together with the measured temperature profile. Mole fractions in the exhaust gas agree well with the calculated equilibrium values shown as open symbols at 32 mm. Good agreement can be noted between the experimental results and the simulated mole fractions with only slight deviations for H_2 due to high noise in the H_2-signal.

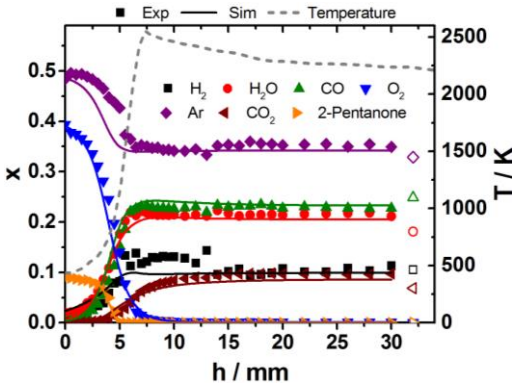

Figure 2: Main species profiles in a rich premixed low-pressure 2-pentanone flame. Filled symbols: experimental results, open symbols: calculated equilibrium values, lines: simulation, dashed line: measured temperature profile.

4.2 Fuel decomposition and primary intermediates

Figure 3 shows a flux analysis for 2-pentanone with the present model. The respective net percentage consumptions (h = 0-3.3 mm, corresponding to a fuel consumption of 0-20%) are shown next to the arrows. In the first step, 2-pentanone is consumed via H-abstraction reactions by H and OH forming the respective four fuel radicals (C_5H_9O). 2-pentanon-1-yl is consumed almost equally *via* C-C β-scission forming ketene and the propyl radical (42%) and radical isomerization to the 2-pentanon-3-yl radical (45%). This radical is almost completely decomposed by C-C β-scission between C4 and C5 resulting in CH_3 and methyl vinyl ketone (99.9%). The other β-scission between C1 and C2 forming ethylketene and CH_3 is only predicted with 0.01%. The reaction rate coeffecient

of the β-scission reaction at the alkyl side is more than 2 orders of magnitude higher than the respective one at the carbonyl site as a result of a much lower activation energy for the latter. The 2-pentanon-4-yl radical mostly forms propene and the acetyl radical (91.5%), while further H-abstraction forming 3-penten-2-one is predicted with only 8.5%. This reaction is predicted to be even less important for the 2-pentanon-5-yl radical leading to 4-penten-2-on (0.5%). The preferred reaction here is also the β-scission forming ethene and the acetonyl radical (97%).

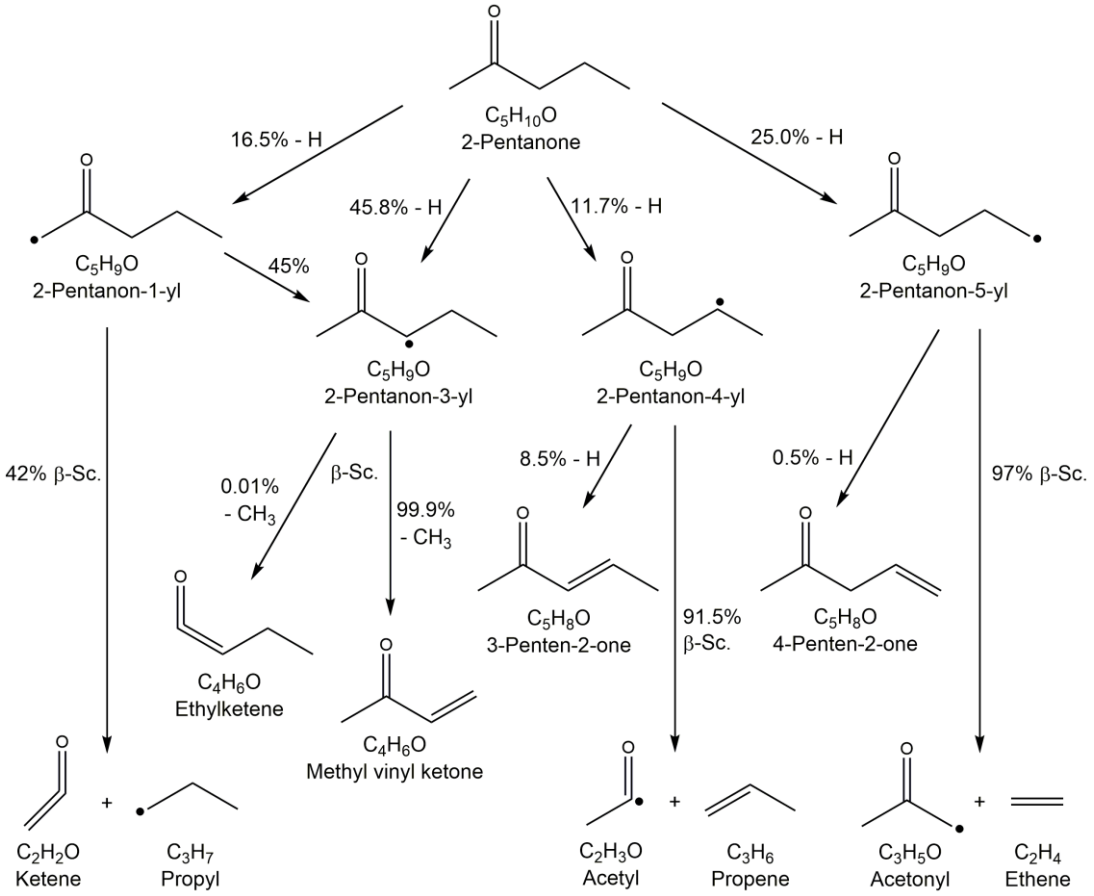

Figure 3: Reaction flux analysis for the 2-pentanone flame conditions with the net consumption from the simulation in the range of h = 0-3.3 mm (representing up to 20% fuel consumption) shown as percentages next to the arrows.

As the first H-abstraction products cannot be detected and quantified with the present PI-MBMS experiment, the primary decomposition products from the subsequent β-scissions are analyzed in the experiment. Figure 4 shows the stable products from the 2-pentanon-1-yl, -4-yl, and -5-yl radicals, namely ketene (a), propene (b), and ethene (c). Ketene and propene show mole fractions in the range of $2\text{-}3\cdot10^{-3}$, while that of ethene is about one order of magnitude higher ($2.4\cdot10^{-2}$). The simulation agrees excellently with the profiles of propene and ethene, while ketene is overestimated by a factor

of 2. The prediction shows the same trends as for the 2-butanone flame [7]. Ketene is mainly formed by the decomposition of the acetonyl radical (CH_3COCH_2) that is a decomposition product of 2-pentanone-5-yl, and by the direct decomposition of 2-pentanon-1-yl. However, the results indicate that the acetone chemistry in the base mechanism might require further development, which can also be seen by the underprediction and the shift of acetone in Fig. S5. Similarily Minwegen et al. [8] recommended a revision of the acetone submechansim as a result from their study. However, the good prediction of ethene and propene (s. Fig. 4b,c) indicates that the branching of the fuel radicals is reasonable and that the underlying sub-mechanisms are working.

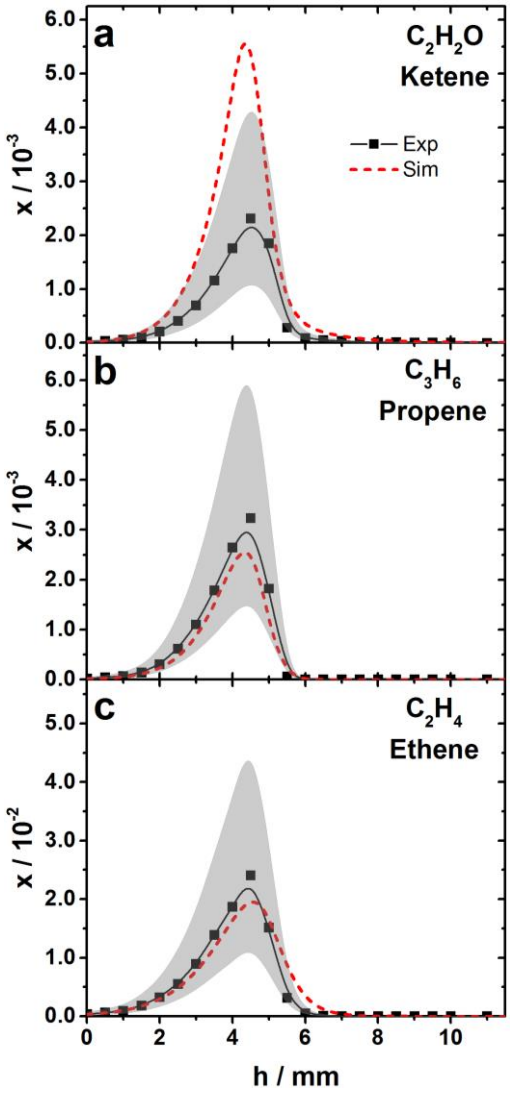

Figure 4: Mole fraction profiles of selected primary intermediates after H-abstraction and β-scission. Symbols: experimental results (an error range of factor 2 is indicated in grey), solid lines: spline to guide the eye, dashed lines: simulation.

Looking at the 2-pentanon-3-yl radical, it seems interesting whether the simulation can predict the drastic ratio between the two pathways leading to methyl vinyl ketone (MVK) and ethylketene (EK) correctly. Unfortunately, for the evaluation of EK no photoionization cross sections (PICS) could be found in the literature. However, a photoelectron spectrum of this species, measured by Bock et al. [31], could be integrated and scaled with a value of 24 Mb at 10.35 eV in analogy to the PICS of ketene from Yang et al. [32]. Clearly, a higher uncertainty is therefore connected to the evaluation of the mole fraction of EK, probably in the range of a factor of 5-10. Nevertheless, this estimate enables a comparison of the C_4H_6O isomers. Figure 5a shows the evaluated mole fractions for MVK and EK, the latter multiplied by a factor of 25 as it is about a factor of 100 lower ($1.6 \cdot 10^{-5}$) than that of MVK ($2.4 \cdot 10^{-3}$). Therefore, the higher error in the quantification of EK is still much lower than the difference between both species. This ratio can also be validated by the PIE curve, which is shown in Fig. 5b (squares). The circles show the same PIE curve for C_4H_6O, but multiplied by a factor of 25 to emphasize the slope at lower energies, most likely belonging to EK with an ionization energy (IE) of 8.80 eV [31]. The change of the slope can be assigned to MVK with an IE of 9.64 eV [32]. In addition, the PICS of EK and MVK are shown in comparison to the experimental data. Both PICS excellently fit the slopes in the PIE curves and lead to a ratio of 99.4% of MVK and 0.6% EK, which correlates perfectly to the mole fraction ratio from Fig. 5b (99.3% MVK, 0.7% EK). These experimental results excellently confirm the prediction from the simulation.

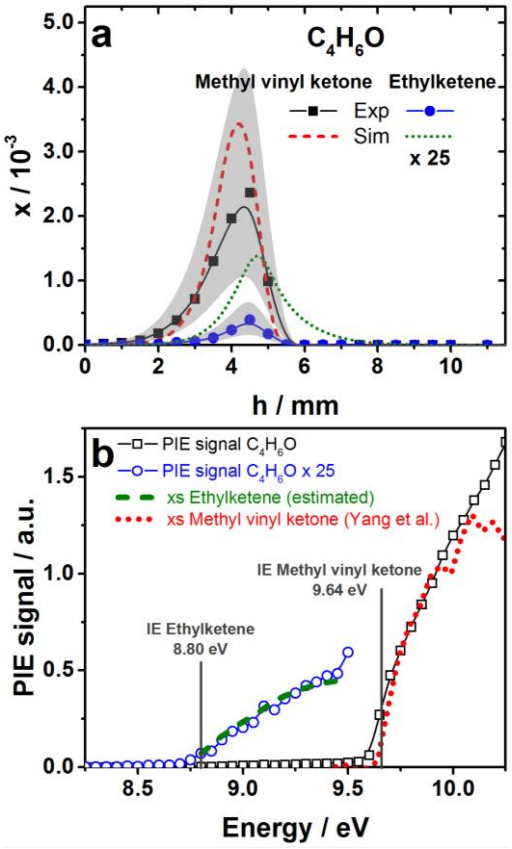

Figure 5: a) Mole fraction profiles of the detected C_4H_6O isomers, symbols: experimental results (an error range of factor 2 is indicated in grey), solid lines: spline to guide the eye, dashed/dotted lines: simulation; note that experimental results and simulation are multiplied by a factor of 25 for ethylketene. b) PIE signal of C_4H_6O (squares) and again shown, but multiplied by a factor of 25 (circles), to emphasize the slope for lower energies. The PICS of ethylketene (estimated) and methyl vinyl ketone [32] are scaled and shown for comparison. The IEs of ethylketene [31] and methyl vinyl ketone [32] are shown as vertical lines.

4.3 Low-temperature species

Several species that are connected to low-temperature chemistry were detected in the present flame. Figure 6a shows formaldehyde, a typical oxygenated species that is also related to low-temperature reactions. A shift towards later reaction times is seen in the simulation in Fig. 6a, which could be one aspect to indicate that oxygen addition reactions could occur in the preheating zone of the flame. Formaldehyde is mainly produced by the reaction of CH_3 with O, while CH_3 is formed via several reactions, including the decomposition of 2-pentanone-3-yl in the early phase of the flame as well as through the decomposition of propyl, ethyl, and acetonyl radicals. Further indications of low-temperature reactions are presented by the detection of C_5H_8O (Fig. 6b) and the signal of m/z = 100.052, which is identified as $C_5H_8O_2$ (Fig. 6c) with the high mass resolution of the setup. This

sum formula can be assigned to a dione or a cyclic ether structure that is typically formed via O_2 addition and isomerization to QOOH. No PICS or IEs are tabulated for these species, but the PIE curve shows a slope corresponding to an IE in the range of 9.1-9.3 eV for $C_5H_8O_2$. That O_2 addition reactions can take place in the early flame at lower temperatures has been shown by Seidel et al. [33] and Hemken et al. [7]. Nonetheless, due to the rather low flux of these species into low-temperature pathways, the general performance of this high-temperature model is very satisfying.

Figure 6b shows the fragment-corrected signal profile of C_5H_8O, which can be assigned to 3-pentene-2-one and 4-pentene-2-one, for which no PICS were found in the literature. These species can either be formed by C-H β-scission from 2-pentanone-3yl, -4yl, and -5yl or by O_2 addition to the fuel and concerted HO_2 elimination reactions. The comparison of the qualitative signal profile and the model predictions indicates that such reactions already happen early in the flame, with a maximum earlier than that of the $C_5H_8O_2$ signal (compare Fig.6c). Shape and peak position can obviously not yet be correctly predicted by the present kinetic model, maybe due to the neglected low-temperature reactions. Thus, a complete implementation of the low-temperature chemistry could also slightly influence the branching ratio of the fuel radicals due to a change in the available radical pool. However, the profile position of 4-pentene-2-one indicates that probably not only low-temperature-related reactions are needed to improve the prediction. Here, further experimental and theoretical work is encouraged to enlighten these pathways.

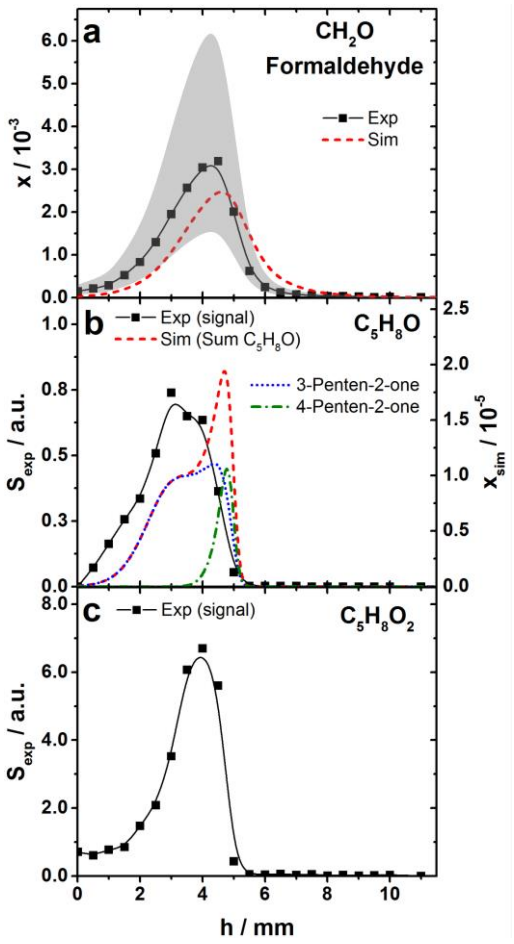

Figure 6: Profiles of selected oxygenated species related to low-temperature chemistry. For formaldehyde (a) the mole fraction profile is shown (an error range of factor 2 is indicated in grey), while for C_5H_8O (b) and $C_5H_8O_2$ (c) only the corrected signals are presented due to missing PICS for quantification. Symbols: experimental results, solid lines: spline to guide the eye, dashed, dotted, and dash-dotted lines: simulation.

5. Summary and conclusions

Mole fraction profiles for 47 species from a laminar premixed low-pressure flame fueled by 2-pentanone were obtained by VUV-PI-MBMS including isomer separation. A new high-temperature sub-mechanism has been developed for 2-pentanone and has been coupled to an existing base mechanism. High-temperature reactions for 2-pentanone were adapted in analogy to 2-butanone and *n*-pentane, and the thermochemistry for 2-pentanone and the fuel radicals was derived by *ab initio* calculations.

A flux analysis has been performed for the 2-pentanone flame conditions, showing the first decomposition reactions of the fuel by H-abstractions and β-scissions and their respective probabilities. For the first β-scission products ketene, propene, ethene, methyl vinyl ketone, and ethylketene, good

agreement between experiment and simulation was found permitting the conclusion that the initial branching reactions are reasonably captured in the model. With the isomer distinction enabled by the PI-MBMS experiment, it was possible to confirm that more than 99% of the 2-pentanon-3-yl radical is decomposed by C-C β-scission between C4 and C5 forming CH_3 and methyl vinyl ketone, while the β-scission between C1 and C2 forming CH_3 and ethylketene is about a factor of 100 lower in both the experiment and the simulation.

Furthermore, some species assigned to low-temperature reactions were observed in the flame. Especially the detection of a $C_5H_8O_2$ signal, here potentially assigned to cyclic ethers formed by O_2 addition to the fuel and subsequent isomerization to the QOOH species, supports the assumption of low-temperature reactions taking place in the preheating zone of the flame. Further confirmation of this observation might be the mole fraction profile of formaldehyde that rises earlier than the simulation predicts, potentially due to missing reactions of fuel radicals with HO_2 forming the related alkoxy (RO) species [7]. This reaction path could additionally be enhanced by the concerted HO_2 elimination reactions of RO_2 species, forming 3- and 4-pentene-2-one, which is supported by the early rise of the C_5H_8O profile. Except for these low-temperature reactions in the early flame zone that are not yet included in the model, most profile shapes and positions were captured quite well by the simulations.

In comparison to the smaller ketone 2-butanone, 2-pentanone might be preferred in applications because of its higher energy density; however, a similar amount of toxic species and pollutants was found to be formed in its combustion. For the particularly toxic species methyl vinyl ketone the mole fraction was observed to be even five times higher in 2-pentanone combustion compared to 2-butanone [7].

The present data, providing quantitative and isomer-separated mole fraction profiles whenever possible with good agreement with the high-temperature model, may be helpful in further critical examination of the related reaction chemistry. In the next steps, additional calculations should be performed to integrate a low-temperature sub-mechanism into the model.

List of Supplemental Material

SMM1 Experimental data (Excel file)

SMM2 Mechanism for 2-Pentanone (CHEMKIN file)

Thermodynamic properties (CHEMKIN file)

Transport properties (CHEMKIN file)

SMM3 Additional information (pdf file)

Acknowledgements

The authors thank all participants of the ALS “Flame Team” for their contribution to the PI-MBMS measurements. The Advanced Light Source is supported by the Director, Office of Science, Office of Basic Energy Sciences, of the U.S. Department of Energy under contract DE-AC02-05CH11231. NH was supported by the U.S. Department of Energy (DOE), Office of Science, Office of Basic Energy Sciences. Sandia National Laboratories is a multimission laboratory managed and operated by National Technology and Engineering Solutions of Sandia, LLC., a wholly owned subsidiary of Honeywell International, Inc., for the U.S. Department of Energy’s National Nuclear Security Administration under contract DE-NA0003525. CH, RB, and KAH acknowledge the support of the cluster of excellence “Tailor Made Fuels from Biomass”, which is funded by the Excellence Initiative of the German federal and state governments to promote science and research at German universities. The authors greatly acknowledge Lars Seidel from LOGE for helpful discussions and support with their software package, Ultan Burke from NUI Galway, and Prajakta Parab and Heiko Minwegen from PCFC for the preparation of the thermochemical data.

References

[1] A. Elfasakhany, Eng. Sci. Technol. Int. J. 19 (2016) 1224–1232.

[2] Y. Li, L. Meng, K. Nithyanandan, T.H. Lee, Y. Lin, C.-F. Lee, S. Liao, Energy 121 (2017) 43–54.

[3] F. Hoppe, U. Burke, M. Thewes, A. Heufer, F. Kremer, S. Pischinger, Fuel 167 (2016) 106–117.

[4] A.M. Scheer, A.J. Eskola, D.L. Osborn, L. Sheps, C.A. Taatjes, J. Phys. Chem. A 120 (2016) 8625–8636.

[5] E.E. Dames, K.-Y. Lam, D.F. Davidson, R.K. Hanson, Combust. Flame 161 (2014) 1135–1145.

[6] Z. Serinyel, N. Chaumeix, G. Black, J.M. Simmie, H.J. Curran, J. Phys. Chem. A 114 (2010) 12176–12186.

[7] C. Hemken, U. Burke, I. Graf, L. Ruwe, S. Park, S.M. Sarathy, K.A. Heufer, K. Kohse-Höinghaus, Proc. Combust. Inst. 36 (2017) 1175–1183.

[8] H. Minwegen, U. Burke, K.A. Heufer, Proc. Combust. Inst. 36 (2017) 561–568.

[9] K.-Y. Lam, D.F. Davidson, R.K. Hanson, J. Phys. Chem. A 116 (2012) 5549–5559.

[10] J. Badra, A.E. Elwardany, A. Farooq, Phys. Chem. Chem. Phys. 16 (2014) 12183–12193.

[11] J.M. Hudzik, J.W. Bozzelli, J. Phys. Chem. A 116 (2012) 5707–5722.

[12] T.A. Cool, A. McIlroy, F. Qi, P.R. Westmoreland, L. Poisson, D.S. Peterka, M. Ahmed, Rev. Sci. Instrum. 76 (2005) 94102.

[13] N. Hansen, T.A. Cool, P.R. Westmoreland, K. Kohse-Höinghaus, Prog. Energy Combust. Sci. 35 (2009) 168–191.

[14] K. Moshammer, S. Vranckx, H.K. Chakravarty, P. Parab, R.X. Fernandes, K. Kohse-Höinghaus, Combust. Flame 160 (2013) 2729–2743.

[15] L. Ruwe, K. Moshammer, N. Hansen, K. Kohse-Höinghaus, Combust. Flame 175 (2017) 34–46.

[16] D. Felsmann, K. Moshammer, J. Krüger, A. Lackner, A. Brockhinke, T. Kasper, T. Bierkandt, E. Akyildiz, N. Hansen, A. Lucassen, P. Oßwald, M. Köhler, G.A. Garcia, L. Nahon, P. Hemberger, A. Bodi, T. Gerber, K. Kohse-Höinghaus, Proc. Combust. Inst. 35 (2015) 779–786.

[17] U. Struckmeier, P. Oßwald, T. Kasper, L. Böhling, M. Heusing, M. Köhler, A. Brockhinke, K. Kohse-Höinghaus, Z. Phys. Chem. 223 (2009) 503–537.

[18] X. Yang, D. Felsmann, N. Kurimoto, J. Krüger, T. Wada, T. Tan, E.A. Carter, K. Kohse-

Höinghaus, Y. Ju, Proc. Combust. Inst. 35 (2015) 491–498.

[19] Y. Li, C.W. Zhou, K.P. Somers, K. Zhang, H.J. Curran, Proc. Combust. Inst. 36 (2017) 403–411.

[20] C. Hemken, U. Burke, K.-Y. Lam, D.F. Davidson, R.K. Hanson, K.A. Heufer, K. Kohse-Höinghaus, Combust. Flame 184 (2017) 195–207.

[21] Y. Zhang, K.P. Somers, M. Mehl, W.J. Pitz, R.F. Cracknell, H.J. Curran, Proc. Combust. Inst. 36 (2017) 413–421.

[22] S. Thion, P. Diévart, P. Van Cauwenberghe, G. Dayma, Z. Serinyel, P. Dagaut, Proc. Combust. Inst. 36 (2017) 459–467.

[23] J. Bugler, B. Marks, O. Mathieu, R. Archuleta, A. Camou, C. Grégoire, K.A. Heufer, E.L. Petersen, H.J. Curran, Combust. Flame 163 (2016) 138–156.

[24] K.-Y. Lam, W. Ren, Z. Hong, D.F. Davidson, R.K. Hanson, Combust. Flame 159 (2012) 3251–3263.

[25] U. Burke, J. Beeckmann, W.A. Kopp, Y. Uygun, H. Olivier, K. Leonhard, H. Pitsch, K.A. Heufer, Combust. Flame 168 (2016) 296–309.

[26] L.A. Curtiss, P.C. Redfern, K. Raghavachari, J. Chem. Phys. 126 (2007) 84108.

[27] M.J. Frisch et al., Gaussian 09 Revision D.01 Gaussian Inc., Wallingford CT, 2009.

[28] A. Ghysels, T. Verstraelen, K. Hemelsoet, M. Waroquier, V. Van Speybroeck, J. Chem. Inf. Model. 50 (2010) 1736–1750.

[29] C.W. Gao, J.W. Allen, W.H. Green, R.H. West, “Reaction Mechanism Generator: automatic construction of chemical kinetic mechanisms.”, Computer Physics Communications, 2016.

[30] LOGEsoft, available at http://loge.se/Products/LOGE_Products.html, 2017.

[31] H. Bock, T. Hirabayashi, S. Mohmand, Chem. Ber. 114 (1981) 2595–2608.

[32] B. Yang, J. Wang, T.A. Cool, N. Hansen, S. Skeen, D.L. Osborn, Int. J. Mass Spectrom. 309 (2012) 118–128.

[33] L. Seidel, K. Moshammer, X. Wang, T. Zeuch, K. Kohse-Höinghaus, F. Mauss, Combust. Flame 162 (2015) 2045–2058.